PREPARATION AND CHARACTERIZATION OF METAL OXIDE
SUPPORTED GROUP 9B METAL NANOPARTICLES AND THEIR USE AS
ELECTROCATALYSTS IN WATER SPLITTING

A THESIS SUBMITTED TO
THE GRADUATE SCHOOL OF NATURAL AND APPLIED SCIENCES
OF
MIDDLE EAST TECHNICAL UNIVERSITY

BY

MERVE AKBAYRAK

IN PARTIAL FULFILLMENT OF THE REQUIREMENTS
FOR
THE DEGREE OF DOCTOR OF PHILOSOPHY
IN
CHEMISTRY

SEPTEMBER 2022

Approval of the thesis:

PREPARATION AND CHARACTERIZATION OF METAL OXIDE SUPPORTED GROUP 9B METAL NANOPARTICLES AND THEIR USE AS ELECTROCATALYSTS IN WATER SPLITTING

submitted by **MERVE AKBAYRAK** in partial fulfillment of the requirements for the degree of **Doctor of Philosophy** in **Chemistry, Middle East Technical University** by,

Prof. Dr. Halil Kalıpçılar
Dean, Graduate School of **Natural and Applied Sciences**   _____

Prof. Dr. Özdemir Doğan
Head of the Department, **Chemistry**   _____

Prof. Dr. Ahmet M. Önal
Supervisor, **Chemistry, METU**   _____

Examining Committee Members:

Prof. Dr. Emren Nalbant
Chemistry, METU   _____

Prof. Dr. Ahmet M. Önal
Supervisor, Chemistry, METU   _____

Prof. Dr. Seha Tirkeş
Chemical Engineering, Atılım University   _____

Prof. Dr. Ali Çırpan
Chemistry, METU   _____

Prof. Dr. Atilla Cihaner
Chemical Engineering, Atılım University   _____

Date:02.09.2022

I hereby declare that all information in this document has been obtained and presented in accordance with academic rules and ethical conduct. I also declare that, as required by these rules and conduct, I have fully cited and referenced all material and results that are not original to this work.

Name Last name : Merve Akbayrak

Signature :

ABSTRACT

PREPARATION AND CHARACTERIZATION OF METAL OXIDE SUPPORTED GROUP 9B METAL NANOPARTICLES AND THEIR USE AS ELECTROCATALYSTS IN WATER SPLITTING

Akbayrak, Merve
Doctor of Philosophy, Chemistry
Supervisor: Prof. Dr. Ahmet M. Önal

September 2022, 215 pages

Hydrogen has been regarded as a crucial energy carrier due to its high energy density. Therefore, there is an increasing attention for the production of hydrogen. Among the hydrogen production methods, water splitting is one of the well-known environmentally friendly methods for the production of hydrogen. Although a large variety of catalysts have been tested in water splitting, the development of efficient and long-lived electrocatalysts is still an important issue. This thesis covers the preparation, characterization and the catalytic use of metal oxide supported group 9B metal nanoparticles (Co, Rh, Ir) in water splitting. Metal nanoparticles were formed on the surface of various metal oxides such as titania, zirconia and ceria by a simple impregnation method and the catalysts were characterized by advanced analytical techniques. The electrocatalytic activity and stability of the catalysts on glassy carbon electrode for both oxygen and hydrogen evolution reactions in water splitting were investigated.

The onset potential and overpotential of Ir/CeO_2 were found as -13.0 and -23.0 mV, respectively. Moreover, among the other Rh and Co based catalysts, Ir/CeO_2 provided lower Tafel slope (38.7 $mV.dec^{-1}$), higher turnover frequency (1.95 s^{-1}) and higher exchange current density (2.69 $mA.cm^{-2}$). Ir/CeO_2 shows superior stability even after 20 000 cycle in acidic environment which makes Ir/CeO_2 as a promising electrocatalyst for HER.

On the other hand, Co/CeO_2 exhibited impressive performance for the oxygen evolution reaction in an alkaline environment with low overpotential (0.368 V), low Tafel slope (63.0 $mV.dec^{-1}$), and high TOF value. Although the commercial Co_3O_4 loses its activity to a great extent after the stability test, for the Co/CeO_2 no noticeable change was observed in Tafel slopes and overvoltages.

Keywords: Transition Metals Nanoparticles, Metal Oxides, Water Splitting, Hydrogen Evolution Reaction, Oxygen Evolution Reaction

ÖZ

METAL OKSİTLERLE DESTEKLENMİŞ GRUP 9B METAL NANOPARÇACIKLARININ HAZIRLANMASI, TANIMLANMASI VE ELEKTROKİMYASAL KATALİZÖRLER OLARAK SUYUN AYRIŞMASINDA KULLANILMASI

Akbayrak, Merve
Doktora, Kimya
Tez Yöneticisi: Prof. Dr. Ahmet M. Önal

Eylül 2022, 215 sayfa

Hidrojen sahip olduğu yüksek enerji yoğunluğundan dolayı önemli bir enerji taşıyıcısı olarak düşünülmektedir. Bu nedenle hidrojen üretimi oldukça dikkat çekmektedir. Hidrojen üretim yolları arasında suyun ayrışması iyi bilinen çevre dostu hidrojen üretim metotlarından biridir. Suyun ayrışmasında çok çeşitli katalizörler test edilmesine rağmen, uzun ömürlü ve etkili eletrokatalizörlerin geliştirilmesi halen önemli bir araştırma konusudur. Bu tez metal oksitlerle desteklenmiş grup 9B metal nanoparçacıklarının (Co, Rh, Ir) hazırlanması, tanımlanması ve suyun ayrışmasında kullanılmasını kapsamaktadır. Metal nanoparçacıkları titanya, zirkonya ve serya gibi çeşitli metal oksit yüzeylerinde basit impregnasyon metodu ile oluşturulup hazırlanan katalizörler gelişmiş analitik tekniklerle tanımlanmıştır. Camsı karbon elektrotları üzerindeki katalizörlerin elektrokatalitik aktiviteleri ve dayanıklılıkları suyun ayrışmasında gerçekleşen oksijen ve hidrojen üretim tepkimelerinde araştırılmıştır.

Polarizasyon eğrilerine göre, Ir/CeO$_2$'nin başlangıç potansiyeli ve aşırı potansiyeli sırasıyla -13.0 ve -23.0 mV olarak bulunmuştur. Ayrıca, diğer Rh ve Co bazlı katalizörler arasında, Ir/CeO$_2$ daha düşük Tafel eğimi (38.7 mV.dec^{-1}), daha yüksek devir frekansı (1.95 s^{-1}) ve daha yüksek değişim akımı yoğunluğu (2.69 mA.cm^{-2}) sağladı. Ek olarak, Ir/CeO$_2$, asidik ortamda 20.000 döngüden sonra bile üstün stabilite gösterdi ve bu da Ir/CeO$_2$'yi HER için umut verici bir elektrokatalizör yaptı.

Öte yandan, Co/CeO$_2$ düşük aşırı potansiyel (0.368 V), düşük Tafel eğimi (63.0 mV.dec^{-1}), ve yüksek TOF değerleri ile alkali bir ortamda oksijen oluşumu reaksiyonu için etkileyici performans sergiledi. Ticari Co$_3$O$_4$, stabilite testi sonrasında aktivitesini büyük ölçüde kaybetmesine rağmen, Co/CeO$_2$'nın Tafel eğiminde ve aşırı geriliminde gözle görülür bir değişiklik gözlenmedi.

Anahtar Kelimeler: Geçiş metalleri nanoparçacıkları, Metal Oksitler, Suyun Ayrışması, Hidrojen Üretim Reaksiyonları, Oksijen Üretim Reaksiyonları

To my most precious one, Zehra

ACKNOWLEDGMENTS

I would like to express my deepest appreciation to my supervisor Prof. Dr. Ahmet M. Önal for his guidance, support, encouragement and patience. I am profoundly grateful to him for teaching me how to become a good scientist and for helping me in many ways. It was an honor to work with him.

I would like to express my gratitude to my thesis monitoring committee members Prof. Dr. Emren Nalbant and Prof. Dr. Seha Tirkeş for their support, help and understanding throughout my PhD studies.

I would like to thank to B24 lab members for their kind friendship and support.

I would like to thank the esteemed staffs of our department, especially Nizamettin Kavut, Erdal Şaşık, Şaban Geliş, and Cafer Kaya, for helping me whenever I needed at every stage of my PhD.

I want to express my deepest gratitude to my mother Ayşe Erkan, my father İshak Erkan and my brother R. Emre Erkan for making my life easier during my PhD adventure, being understanding towards my every behavior, standing behind me in my every decision, raising me with faith, teaching me that the honesty is more important than anything else in life. I am grateful for their endless love.

The two people I owe my biggest thanks to; my daughter Zehra Akbayrak and my dear husband Serdar Akbayrak.

Even when I was pregnant to her, she suffered from exam stress with me, she was exposed to the stress of my doctoral process from the moment she was born, but despite her young age, she was always understanding towards me and loved me the most. I sincerely believe that one day when she grows up, she will understand me. She is my light of life.

Words are not enough to express my endless gratitude to Serdar Akbayrak, for believing in me and giving me endless support. Without his love, understanding and encouragement, everything would have been much more difficult for me. I want to thank him for making my life more meaningful and for always being there for me.

TABLE OF CONTENTS

LIST OF TABLES

LIST OF FIGURES

FIGURES

xx

LIST OF ABBREVIATIONS

ABBREVIATIONS

HER:	Hydrogen Evolution Reaction
OER:	Oxygen Evolution Reaction
NPs:	Nanoparticles
TMO:	Transition Metal Oxides
LSV:	Linear Sweap Voltammetry
CV:	Cyclic Voltammetry
EIS:	Electrochemical Impedance Spectroscopy
UPD:	Under Potential Deposition
C_{DL}	Double Layer Capacitance
SEM:	Scanning Electron Microscopy
TEM:	Transmission Electron Microscopy
ICP:	Inductively Coupled Plasma
EDX:	Energy Dispersive X-ray Spectroscopy
XRD:	X-ray Diffraction

CHAPTER 1

INTRODUCTION

1.   The role of hydrogen and fuel cells in the global energy system

Concern about climate change and exhaustible sources of fossil fuels has led to the need for alternative and renewable energy sources and carriers.[1] Most of our energy comes from fossil fuels, but fossil fuels are non-renewable, not environmentally friendly because they are carbon monoxide pollutants, and have limited resources. There are some alternative and renewable energy sources such as solar, wind, wave, hydro, bio and geothermal energies to improve local air quality by reducing global carbondioxide emissions and to create new industrial and technological energy bases for future economic prosperity.

Hydrogen as an energy carrier has attracted significant attention because it has the highest gravimetric energy density of any known fuel.[2] Hydrogen is a lightest, colourless, odourless and non-toxic gas which has the highest specific energy content of all conventional fuels and is the most abundant element in the universe. [3,4] Hydrogen may be used as fuel in almost any application, where fossil fuels are used presently – particularly for motorising the vehicles, which would offer immediate benefits in terms of reduced pollution and cleaner environment[5]. Currently hydrogen is being used for synthesis of ammonia and other nitrogenized fertilizers, refining and desulphurisation (hydrogenation reactions, hydrodesulphurization); hydrogenation of hazardous wastes (dioxins, PCBs); chemical plants, food preparation; synthesis of methanol, ethanol, dimethyl ether (DME); alternative fuels synthesis by Fischer–Tropsch (FT) process; gas to liquid (GTL) synthesis technology; rocket fuel; IC engine fuel; high temperature industrial furnaces fuel.[6]

Although the advantages of hydrogen over fossil fuels are unquestionable when considered at the local level, producing hydrogen by the current methods may have disadvantages which outweigh the benefits when considered on a global level.

Most hydrogen is produced on an industrial scale from natural gas, and naphtha -LPG by catalytic steam reforming, and from heavy oil fractions by partial oxidation.[7] Carbon dioxide is generated in large amounts in the production of hydrogen by the steam reforming of hydrocarbons. The environmental benefits of a hydrogen-based energy system may therefore be questionable if the demand for hydrogen has to be covered by intensive use of fossil resources because this process is clearly a net contributor to carbon dioxide emissions.[8]

The true potential of a hydrogen-based energy system may only be achieved if hydrogen is made available from renewable resources such as biomass and also by water splitting either through electrolysis using electricity generated by renewable energy sources (e.g. sunlight, wind, wave or hydro-power) or directly by photo-catalysis.
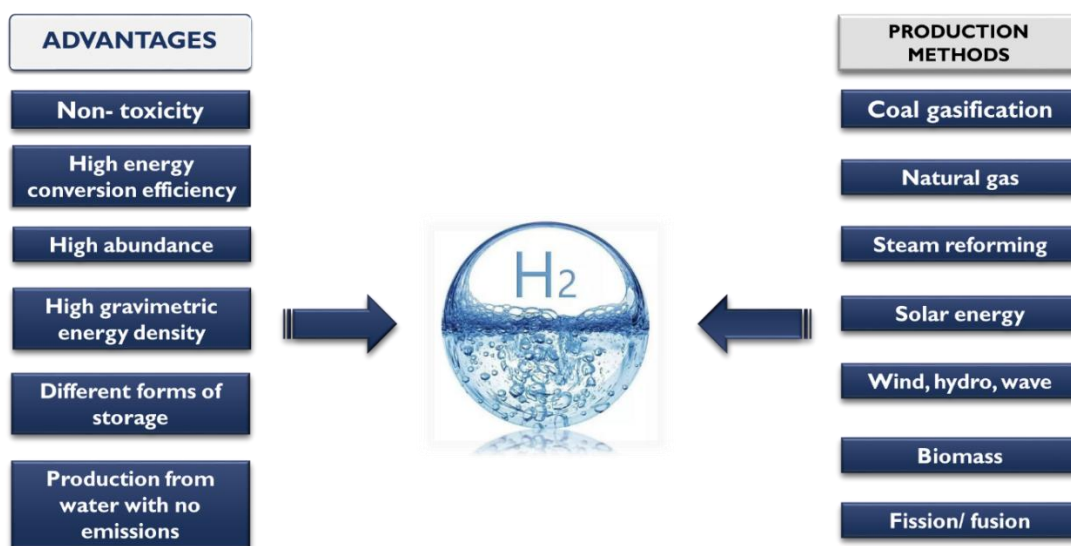
Figure 1. Advantages of hydrogen gas and its production methods

1.2. Hydrogen production by water splitting

Thermochemical, photochemical and electrochemical water splittings are the types of hydrogen production techniques. In thermochemical water splitting, high temperatures are used to produce hydrogen and oxygen from water. High temperatures can be obtained from nuclear or solar power. In photochemical water splitting, light absorbing semiconducting materials are used as an anode or a cathode and electrolysis can be driven by photochemically created holes and electrons. Reduction reaction are carried out by the electrons in the conduction band and oxidation reaction could be achieved by the electron holes in the valance band. In this method water can be directly splitted into hydrogen and oxygen by ultraviolet (UV) light from sunlight. This method is one of the most environmentally friendly methods because it produces no greenhouse gas emissions. However, UV light is harmful for all living things. In electrochemical water splitting, reactions are conducted in an electrolysis cell consisting of electrodes, electrolyte, an electronic conductor and an ionic conductor. When an external voltage is applied, water split into hydrogen at the cathode and oxygen at the anode compartment. Although obtaining pure hydrogen is a great advantage, electrolytic water splitting has also some disadvantages such as high cost and high energy consumption. Many researches have been conducted and catalysts have been designed to decrease the cost and energy consumption and increase the efficiency of reaction.

1.3. Water electrolysis

1.3.1. Historical background of water electrolysis

English researchers William Nicholson and Anthony Carlisle started research on the first real electrolysis of water with copper electrode in 1780 (a few weeks after Volta's invention of voltaic piles) and after a month, hydrogen and oxygen collected separately by German researcher Johann Wilhelm Ritter. [9,10] In the years 1833-1834, British scientist Michael Faraday established a quantitative relationship between the mass of the substances (converted in the electrolysis process) and the amount of electricity (passing through the electrode/electrolyte interface) and discovered the main laws of electrolysis.

3

In 1889, Walther Hermann Nernst initiated the development of electrochemical/electrolysis thermodynamics and in 1905 Julius Tafel developed the first kinetic approaches.[11] The Tafel equation was an empirical equation, and John Alfred Valentine Butler in 1924, Max Volmer and Tibor Erdey-Grúz in 1930, and later Alexander Naumovich Frumkin developed the theoretical background of this equation.[12]

1.3.2. Types of water electrolysis

When a voltage is supplied, hydrogen is formed on the cathode and oxygen is formed on the anode. Since pure water has a poor electrical conductivity (0.05 µS/cm) with an ion concentration of only 10^{-7} M, water electrolysis takes a long time in neutral water at room temperature. As a result, acid, base, or salts are commonly added to increase the conductivity of the electrolyte. Water electrolysis is classified into many forms based on electrolytes employed and the methods used to separate the reactions such as alkaline, acidic, polymer electrolyte membrane (PEM) and solid oxide electrolyte (SOE) water electrolysis. Because of the high temperature, solid oxide water electrolysis necessitates a large amount of energy. PEM-based water splitting is conducted under acidic conditions and with PEM. This state offers a few benefits over others, including decreased gas permeability and increased proton conductivity.[13] It has a high energy efficiency and a rapid rate of hydrogen generation. However, the requirement of acidic media limits the OER electrocatalysts.[14] For the alkaline electrolysis cell, water splitting is performed under alkaline condition. In comparison with cells using acidic media, water splitting in alkaline media broadens the selection of the electrocatalysts to non-noble metals or metal oxides. However, the activity of HER in alkaline media is usually 2–3 orders of magnitude lower than the activity of HER in acidic media.[15] Therefore, the design of optimal electrocatalysts suitable for the different media with low-cost, high catalytic activity, and good durability for electrolytic water splitting is very challenging.

1.3.3. Thermodynamics of electrolytic water splitting

Electrochemical water splitting reaction divided into two half reactions: hydrogen evolution reaction (HER, water reduction) at the cathode compartment and oxygen evolution reaction (OER, the water oxidation) at the anode part. [16]

At standard conditions (298 K, 1 bar) when the water is liquid, the water splitting reaction is described by

$$H_2O_{(liq)} \rightarrow H_{2\,(g)} + \tfrac{1}{2}\,O_{2(g)} \qquad (1)$$
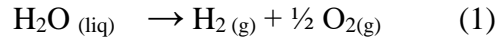
Theoretically, the minimum required potential to split water into hydrogen and oxygen is the thermodynamic reversible potential of the reaction, which is related to the change in Gibbs free energies of the involved reactants and products. The minimum voltage can be calculated as

$$E^0_{rev,T} = \frac{1}{2F}\,(G^0_{H2} + 0.5\,G^0_{O2} - G^0_{H2O(l)})_T \qquad (2)$$

Where G^0 is the standard molar Gibbs free energy; F is the Faraday constant, T is the temperature (25 °C -200 °C). According to LeRoy and Bowen reversible reduction potential can be calculated as followed[17];

$$E^0_{rev,T} = 1.5184 - 1.5421 \times 10^{-3}T + 9.523 \times 10^{-5}T\,\ln T + 9.84 \times 10^{-8}T^2 \qquad (3)$$

At standard pressure (1 bar) and 298 K, the minimum thermodynamic reversible potential value is 1.229 V. By using this value minimum Gibbs energy can be found as 237.18 kJ mol^{-1}.[18]

Cathode reaction (HER) $4e^- + 4H_2O_{(l)} \rightarrow 4OH^-_{(aq)} + 2H_2$ (4) $E^0_c = 0$ V vs. RHE

Anode reaction (OER) $4OH^-_{(aq)} \rightarrow 4e^- + 2H_2O_{(l)} + O_2$ (5) $E^0_a = 1.23$ V vs. RHE

Overall reaction $2H_2O_{(l)} \rightarrow 2H_{2(g)} + O_{2(g)}$ (6) $E^0 = E^0_a - E^0_c = 1.23$ V vs. RHE
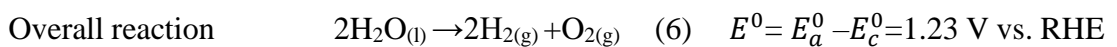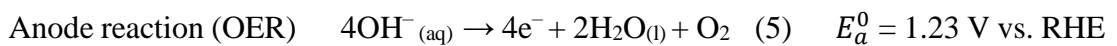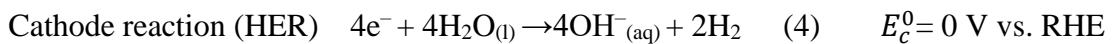
To split the water into hydrogen and oxygen successfully and get a significant current density, a higher thermodynamic operational voltage than the thermodynamic equilibrium voltage (1.23 V) is needed. Overpotential, η, is the excess potential at a certain current density and used for overcoming the intrinsic activation barriers (anodic (η_a), cathodic (η_c) overpotentials and solution resistance and contact resistance (η_{other} = IR ohmic drop)). The total voltage required for water splitting can be formulated as follows:

$$E_{total}=1.23 \text{ } V +\eta_a+|\eta_c|+ IR \quad (7)$$

The main reasons which cause the overpotentials are charge transfer resistance at both anode/electrolyte and cathode/electrolyte interfaces, resistance of electrolyte and resistance due to the Ohmic losses in electrodes and cable wiring.

1.3.4. Mechanism and kinetics of the hydrogen evolution reaction

In acidic electrolyte HER occurs via proton reduction (eqn. 8) and in basic electrolyte hydrogen gas is produced by water reduction (Eqn. 9).[19]

Acidic condition

$$\text{Cathode: } 2H^+ + 2e^- \rightarrow H_2, \text{ } E_c=0 \text{ } V \quad (8)$$

$$\text{Anode: } 2H_2O \rightarrow O_2 + 4H^+ + 4e^-, \text{ } E_a=1.23 \text{ } V$$

Alkaline condition

$$\text{Cathode: } 2H_2O+2e^- \rightarrow H_2 + 2OH^-, \text{ } E_c=-0.83 \text{ } V \quad (9)$$

$$\text{Anode: } 4OH^- \rightarrow O_2 + 2H_2O+4e^-, \text{ } E_a=-0.40 \text{ } V$$
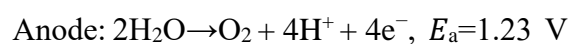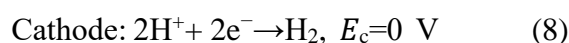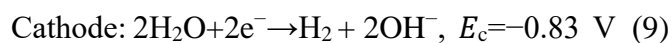
The hydrogen evolution reaction is thought to involve three possible reaction steps[20]:

1) Volmer step (electrochemical hydrogen ion adsorption)

$$H_2O + e^- + M \leftrightharpoons MH_{ads} + OH^- \text{ (alkaline conditions)}$$

$$H_3O^+ + e^- + M \leftrightharpoons MH_{ads} + H_2O \text{ (acidic conditions)}$$
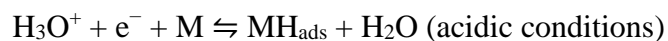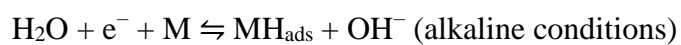
2) Heyrovsky step (electrochemical desorption)

$$MH_{ads} + H_2O + e^- \leftrightharpoons M + OH^- + H_2 \text{ (alkaline conditions)}$$

$$MH_{ads} + H_3O^+ + e^- \leftrightharpoons M + H_2 + H_2O \text{ (acidic conditions)}$$
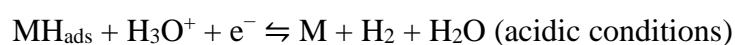
3) Tafel step (chemical desorption)

$$2MH_{ads} \leftrightharpoons 2M + H_2$$
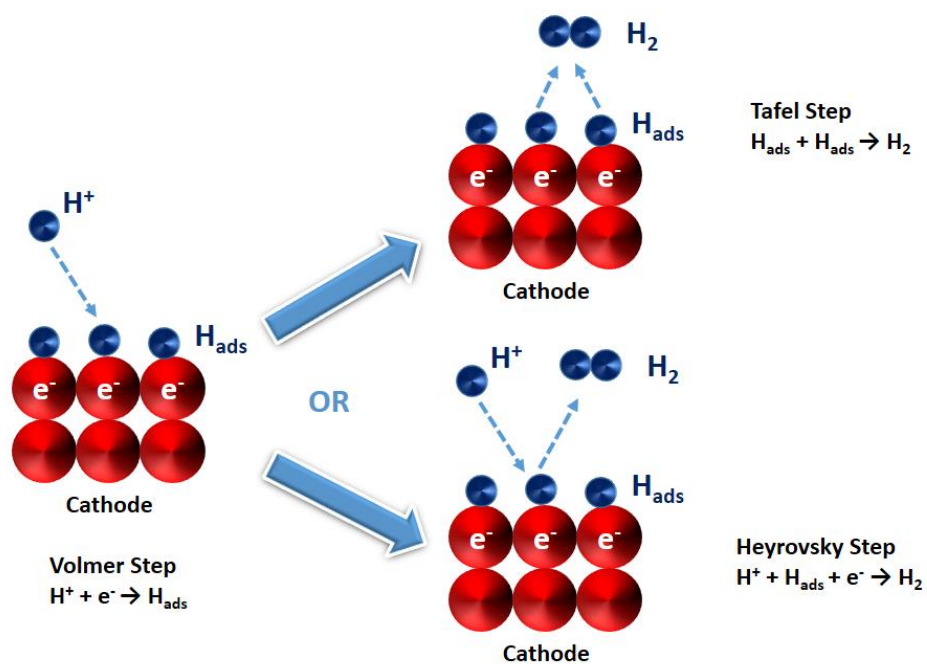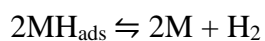
Figure 2. Schematic representation of possible reaction steps for HER

Noble metal based catalysts are extensively used to perform HER from water splitting efficiently. In fact, these catalysts are required to trigger proton reduction with minimal overpotential.[21] Metal-hydride (M-H) bond strength which affects both the adsorption of reactants and the desorption of products is a critical parameter for an ideal catalyst used for HER.[22] The rate of the reaction is mostly determined by interaction between the adsorbed hydrogen and metal. This interaction could be estimated by hydrogen adsorption free energy (ΔGH_{ads}). [23,24, 25] Trasatti performed an experimental plot in acidic media for HER, this volcano shape plot (see Figure 3) shows the logarithm of the exchange current densities (J_0) against the energy of chemisorption of hydrogen on different metals (H_{ads}– M).[26] If the metals with large and negative ΔGH_{ads} are used than strong adsorption of hydrogen onto the metal surface occur, which restricts the recombination or protonation steps and overall rate is determined by the slow desorption step (Heyrovski/Tafel). If the metals with negative ΔG_{Hads} are used, weak adsorption of hydrogen onto the metal surface will occur and the adsorption (Volmer) step will be the rds for HER (Figure 4). [27,28]

Therefore, Volcano plot that shows M–H bond strength is an excellent guide designing an efficient catalyst for HER. Platinum (Pt) which is at the top of Volcano plot is found to be the most efficient catalyst for HER because of its neither too strong nor too weak hydrogen binding energy with near zero ΔG_{Hads}.[29] Platinum group metals (PGMs, including Pt, Ru, Rh, Ir and Pd) are also the best known HER electrocatalysts located close to the apex of the volcano plot. The use of platinum, however, raises issues linked to cost and stability.[30] Recently, non-precious-metal-based catalysts have been reported, but these are susceptible to acid corrosion and are typically much inferior to Pt-based catalysts, exhibiting higher overpotentials and lower stability.[31,32]
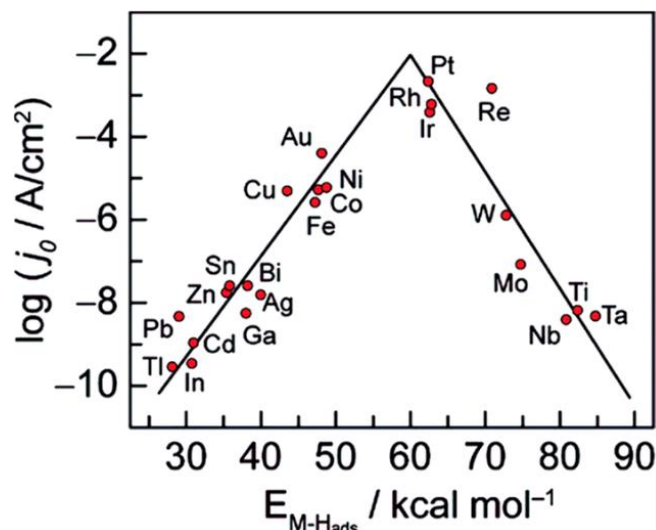
Figure 3. Trassati's volcano plot for the hydrogen evolution reaction in acid solutions[19]. Reprinted (adapted) with permission from ref (19). Copyright (2010) American Chemical Society.
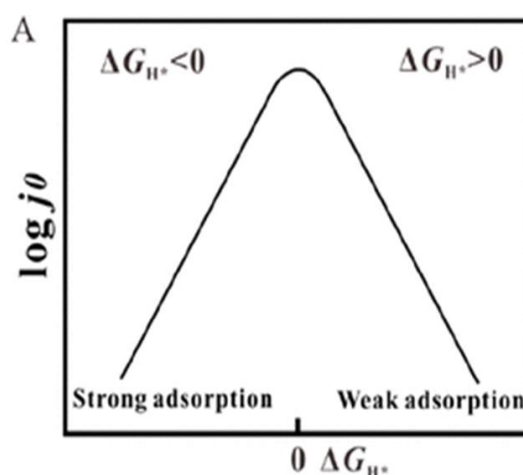
Figure 4. Relationship between j_0 and ΔG_{H*}. Reprinted (adapted) with permission from ref (23). Copyright (2020) American Chemical Society

According to the Sabatier's principle, cost-effective Rh and Ir have a very small ΔG, similar to Pt.[33] Therefore, the design and synthesis of efficient Rh and Ir based catalysts for HER have captured increasing attention.[34] Although Rh and Ir have limited resources and high price tags, they show higher catalytic activity than that of non-noble metal nanocatalysts even at a very low metal concentration. To overcome the problems caused from high cost and low abundance, nanostructured electrocatalysts with large surface to volume ratio have been designed.

9

1.3.5. Mechanism and kinetics of the oxygen evolution reaction

An oxygen evolution reaction (OER) occurs at the anode, and O_2 gas is generated by the oxidation of water.[35] As compared with HER, OER has more sluggish kinetic with the four-electron transfer. M-OH, M-O, and M-OOH (where M represents the active sites on the surface) adsorption intermediates occur during the reaction in an alkaline environment.[36] Electrochemical water splitting kinetic is seriously slow down due to high energy barriers causing from OER with four-electron transfer reactions. [37]

The mechanism of oxygen evolution reaction on anode electrocatalysts in alkaline medium was proposed by Krasil'shchikov as the following reaction path:

$$M + OH^- \rightarrow M–OH + e^- \qquad (1)$$

$$M–OH + OH^- \rightarrow M–O^- + H_2O \qquad (2)$$

$$M–O^- \rightarrow M–O + e^- \qquad (3)$$

$$2M–O \rightarrow 2M + O_2 \qquad (4)$$
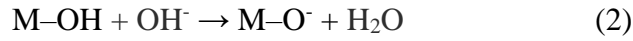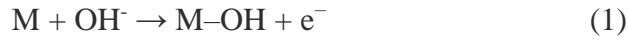
Where active site of electrocatalyst was represented as M. [38, 39, 16]

Another modified Krasil'shchikov scheme: [40,41]

$$M + OH^- \rightarrow M–OH + e^- \qquad (1)$$

$$M–OH + OH^- \rightarrow M–O^- + H_2O \qquad (2)$$

$$M–O^- + OH^- \rightarrow M–O\text{-}O\text{-}H^- + e^- \qquad (3)$$

$$M–O\text{-}O\text{-}H^- + OH^- \rightarrow M + O_2 + H_2O + 2e^- \qquad (4)$$
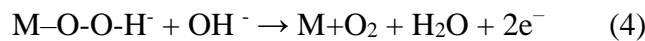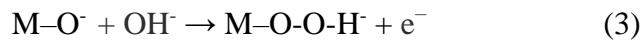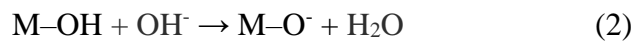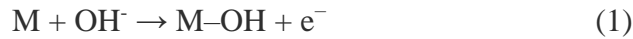
The bond strength of M–O in the intermediate states, which is similar to the HER principle determine the catalytic activity of materials for OER.

Matsumoto and Sato[42] reviewed various possible oxygen evolution mechanism in acid and alkaline environments presented by numerous research groups [43-48] (Table 1). All of the mechanisms show M–OH formation steps in the initial stage by attachment of OH^- ions at the active site, followed by other intermediate formations in the basic condition.

Table 1. The OER mechanism summarized by Matsumoto and Sato. Reproduced with permission ref 42 Copyright 1986, Elsevier.

Acid environment	Alkaline environment
Electrochemical oxide path[43] $M + H_2O \rightarrow MOH + H^+ + e^-$ $M\text{-}OH \rightarrow MO + H^+ + e^-$ $M\text{-}O + M\text{-}O \rightarrow 2M + O_2$	**Electrochemical oxide path**[43] $M + OH^- \rightarrow M\text{-}OH + e^-$ $M\text{-}OH + OH^- \rightarrow M\text{-}O + H_2O + e^-$
Oxide path[44] $M + H_2O \rightarrow M\text{-}OH + H^+ + e^-$ $M\text{-}OH + M\text{-}OH \rightarrow M\text{-}O + H_2O + M$ $M\text{-}O + M\text{-}O \rightarrow 2M + O_2$	**Oxide path**[44] $M + OH^- \rightarrow M\text{-}OH + e^-$ $M\text{-}OH + M\text{-}OH \rightarrow M\text{-}O + H_2O + M$ $M\text{-}O + M\text{-}O \rightarrow 2M + O_2$
Wade and Hackerman's path[45] $2M + 2H_2O \rightarrow M\text{-}O + M\text{-}H_2O + 2H^+ + 2e^-$ $M\text{-}O + 2M\text{-}OH^- \rightarrow 2M + M\text{-}H_2O + O_2 + 2e^-$	**Yeager's path**[46,47] $M + OH^- \rightarrow M\text{-}OH + e^-$ $M^z\text{-}OH \rightarrow M^{z+1}\text{-}OH + e^-$ $2M^{z+1}\text{-}OH + 2OH^- \rightarrow 2M + 2H_2O + O_2$
	Bockris path[48] $M + OH^- \rightarrow M\text{-}OH + e^-$ $M\text{-}OH + OH^- \rightarrow M{-}H_2O_2 + e^-$ $M\text{-}H_2O_2 + OH^- \rightarrow M\text{-}OOH^- + H_2O$ $M\text{-}H_2O_2 + M\text{-}OOH^- \rightarrow H_2O + OH^- + O_2$

OER process takes place in multistep reactions with single-electron transfer at each step. Obviously, the accumulation of energy needed at each step to overcome high kinetic energy barriers leads to slow kinetics resulting in a large overpotential.[49] That is why, developing an efficient, long-lived, and cost-effective electrocatalyst to decrease the overpotential and increase the rate of OER is still a challenging issue. Many oxide type electrocatalysts based on noble metals and earth-abundant metals were reported to catalyze the OER.[50] The OER activities of these metal oxides are related to the electronic structure and the types of metal-oxygen bonds.[51] RuO_2 and IrO_2 are well-known efficient noble metals containing benchmark electrocatalysts for OER in an acidic medium. [52] On the other hand, in an alkaline environment, highly abundant and inexpensive non-noble metal oxides [53,54] especially nickel (Ni) [55] and cobalt (Co) based materials are widely used to increase the slow kinetic of OER due to their high stability to corrosion[56], variable oxidation state such as Co^{3+} and Co^{4+} (form only during the reaction)[57, 58] and controllable morphology with various synthetic methods.[59,60] However, low conductivity and the low number of active sites limit the OER performance of earth-abundant metal oxides.[61] To overcome this problem electrocatalysts impregnated on conductive support materials were synthesized by this way number of electrochemically active surface areas also increase with decreasing the particle size.

1.4. Catalyst

1.4.1. Brief definition of catalyst

Catalysts increase the reaction rate by offering energetically more preferable alternative pathways. (Figure 5) The catalyzed reaction has lower activation energy than uncatalyzed reaction which increase the rate of reaction significantly. In catalyzed reaction, the effective molecular collisions that have lower energies can pass over the new activation energy barrier so reaction rate can be improved. Although the rate of reaction increases, the equilibrium constant of the reaction does not affected because rate of forward and reverse reactions increase the same extent which means that the catalyst has an effect on the kinetics of the reaction, but it has no effect on thermodynamics. [62]
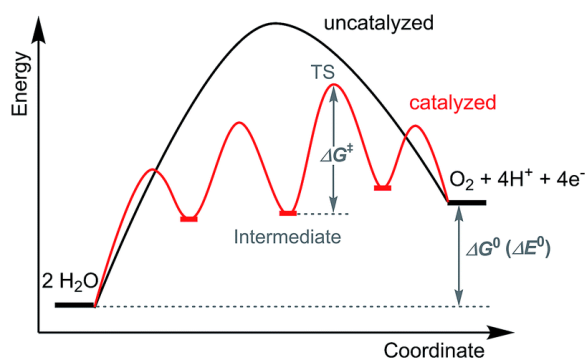
Figure 5. Representative energy diagram for the uncatalyzed and catalyzed OER reaction. Reproduced from Ref. 62 with permission from the Royal Society of Chemistry.

1.4.2. Sabatier's catalyst law

Sabatier's catalyst law has been fully validated by modern molecular understandings of the action of a catalyst and could be summarized as an ideal catalyst have to bind to the reactant at an intermediate strength, neither too strong nor too weak.[63] Reactants form intermediate complexes with the surface of the catalyst in a catalytic reaction. If these complexes are too unstable then reactants will not be activated, so surface reactant intermediate complexes will not be formed. If they are too stable they will not decompose and product formation cannot be achieved. In a catalytic reaction, firstly, molecules adsorb onto the catalyst surface and form intermediate reaction complexes to rearrange and recombine. Later, desorption of the product molecules from catalyst surface occurs and final product could be achieved. Figure 6 shows that the rate is maximum at optimum adsorption strength. To the right of the Sabatier optimum, the rate has a negative order in reactant concentration, and to the left it has a positive order.
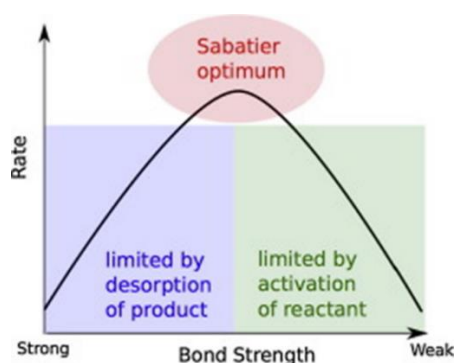
Figure 6. Volcano plot that illustrate the Sabatier principle. Reprinted from ref 28, Copyright (2015), with permission from Elsevier.

13

1.4.3. Classification of catalysts

Catalystis can be classified into three main groups;

1. Homogeneous catalyst (Organometallic complexes)
2. Heterogeneous catalyst (Supported metals, bulk metals, transition metal nanoparticles or nanocluster)
3. Biocatalysts (Enzymes)

Homogeneous catalysts occupy the same phase as the reaction mixture, while heterogeneous catalysts are not in the same phase as the reactants.[64] In homogeneous catalysis, primary benefit is that all of the active sites of catalysts are available and due to the high homogeneity of catalyst and reactants, high interaction occur between them which results in high reactivity and selectivity under mild condition. However, homogeneous catalysts show poor stability and product separation is difficult from the reaction medium.[65] In heterogeneous catalysis, reaction occurs at the interface between the surface of the catalyst and the reaction mixture. Reactants are temporarily adsorbed on the catalyst's surface and due to the weakness of the transient bond linkage the desired product desorbed after the reaction.[66] With the ease of separation and recovery of the catalyst, heterogeneous catalysts play an important role in industrial processes.[67, 68] In biocatalysis, enzymes (natural proteins) or nucleic acids are used to catalyze the chemical reactions outside the living cells.

1.4.4. Transition metal nanoparticles (TMNPs) in catalysis

Solid materials in the size interval of 1-100 nm are defined as nanoparticles. TMNPs for catalysis have gain great attention due to their advantageous characteristics compared to their larger counterparts. It is known that intrinsic properties of materials and properties of nanoparticles remarkably change with particle size. TMNPs with smaller particle size have larger surface area per unit mass than their bulk counterparts and which provides a large number of active sites. More active sites promote faster reactions and increase product yield. The magnetic properties, and electrochemical behaviours (dependent of Fermi level on the nanoparticle diameter) are also dependent the size of TMNPs.[69]

The increase in the number of metal atoms in nanoparticles increases the number of bonding and antibonding electronic levels, thus decreasing the energy band gap between electronic levels.[70] The band gap affects the (i) charge separation, (ii) charge migration, (iii) charge recombination and (iv) surface redox reactions and determines the electrochemical and magnetic properties of a catalyst.[71] Moreover that, the catalytic activity and selectivity of MNPs are dependent on the atomic arrangement of the surface, which can arrange adsorption energies and the geometries of substrate molecules and intermediates during a molecular transformation. [72]

1.4.5. Preparation and stabilization of TMNP catalysts

There are two approach for the preparation of TMNPs; "top-down" and "bottom-up". Top-down approach is a physical method in which bulk material is exposed to an external force and cut into nanoscale pieces. Electron beam lithography and ball milling techniques are used to break up large particles.[73] With this approach, it is difficult to synthesize monodisperse TMNPs and broad particle size distribution is obtained. On the other hand, monodispersed TMNPs with the controllable particle size could be achieved by bottom-up methods. The bottom-up approach is a chemical method in which monodispersed nanoparticles are obtained based on the reduction of metal ions in the solution to atoms by using the appropriate reducing agent.[74] In the chemical synthesis, metal salt, reducing agent, solvent, stabilizing agent and temperature are some important factors that determine the particle size and dispersion.[75] For the colloidal TMNPs impregnation method is mostly used. In the impregnation method, required metal and supporting material are dissolved in the solvent and a thick paste like substance is obtained. After the reduction, solvent is removed and TMNPs could be achieved. The particle size of the obtained TMNPs depends on mostly the metal loading, surface area of support, and post treatment conditions (such as annealing). A support which has a high surface area combined with a low metal loading promotes the greater dispersion with generation of smaller size of TMNPs. Different from the impregnation method, chemical reduction of transition metal complexes, sol-gel technique, thermal or photochemical decomposition, are some different chemical approaches for the preparation of TMNPs (Figure 7). [76]
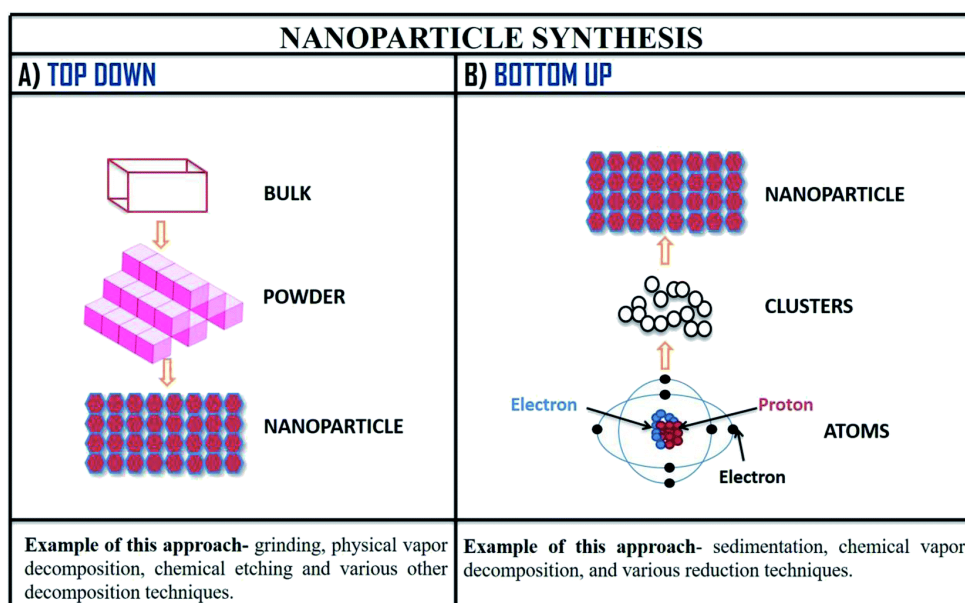
Figure 7. Method of nanoparticle synthesis; (A) top-down approach and (B) bottom-up approach of nanoparticle synthesis with examples. Reproduced from Ref. 76 with permission from the Royal Society of Chemistry.

It is well known that catalytic activity of metal nanoparticles (NPs) is highly dependent on their dispersion and the particle size. TMNPs have high surface energy because of their high surface area to mass ratio which tends to aggragation into large particle. Agglomeration decreases not only their active surface area but also their activities and cause the instability and short life time.[77] This problem can be avoided by using suitable supporting material such as capping agents including, metal oxides[78], carbon black and metal-organic frameworks (MOFs). [79]

1.4.6. Significance, characteristics and types of the supporting materials in heterogeneous catalysis

Metal NPs play an important role in heterogeneous catalysis due to the unique characteristics arise from their shape, size and composition. Many strategies have been developed to control these properties. To decrease metal amount, increase the active surface area, increase the stability and control the distribution of metal, supporting materials have been widely used. The performance of the TMNPs catalysts can be improved by preventing agglomeration using suitable supporting material.

The selection of the appropriate support material is an important criterion when preparing the catalyst for the desired reaction. There are some necessities for an ideal support which are high purity, well defined chemical composition, surface chemistry, porosity and pore size distribution, high temperature and corrosion resistance, and facile separation from the reaction mixture. The required chemical properties of the ideal supporting material are summarized as follows[80]:

- High stability under reaction conditions
- High specific activity/selectivity
- Being non-reactive to undesirable reactions
- Protection of the catalyst against sintering
- Minimizing catalytic poisoning

Some physical properties of the material to be a good supporting material are also given below[80]:

- It has a high active surface area.
- It has high mechanical strength.
- Optimizes bulk density
- Optimizes catalyst porosity
- Optimizes metal crystal and particle size

As shown in Figure 8, supporting materials can be classified in three main catagories; Oxide supports, highly ordered porous supports and carbonacous materials.
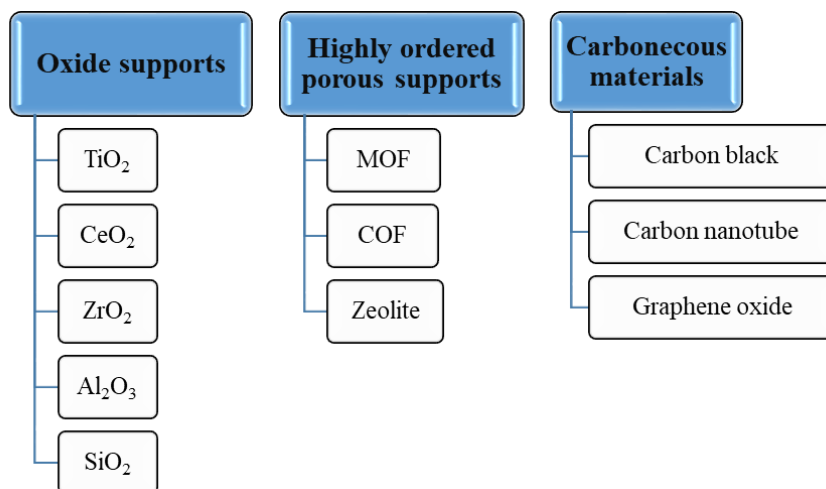
Figure 8. Types of supporting materials which used to prevent agglomeration of MNPs

1.4.6.1. Metal oxides as supporting materials

Oxides can be divided into two main classes, depending on their chemical behavior: nonreducible and reducible oxides. Nonreducible oxides consist of materials that do not easily lose oxygen due to the intrinsic resistance of the corresponding metal cations to change oxidation state. Since oxygen is formally in a '−2' oxidation state, the excess electrons that are left on the material by the removal of a neutral O atom cannot be accommodated in the cation empty states which lie too high in energy, contributing to the formation of the conduction band of the material. [81] Oxides such as SiO_2, MgO, Al_2O_3, and many other main-group oxides belong to this class. Usually these materials are characterized by a very large band gap (typically >3 eV) separating the valence band (VB) from the conduction band (CB). The excess electrons left on the material when oxygen is removed in the form of O_2 or H_2O are trapped in specific sites (e.g., an oxygen vacancy) and give rise to new defect states in the band gap.[82] This process is energetically very costly, and these as-prepared materials are highly stoichiometric, stable, and chemically inert.[83] The group of reducible oxides, in contrast, is characterized by the capability to exchange oxygen in a relatively easy way. This is because the lowest empty states available on the material (CB) consist of cation d orbitals which lie at not overly high energy with respect to the VB. These oxides usually have semiconductor character, with band gaps lower than 3 eV. The removal

of oxygen results in excess electrons that are redistributed on the cation empty levels, thus changing their oxidation state from M^{n+} to $M^{(n-1)+}$. Transition-metal oxides such as TiO_2, WO_3, NiO, Fe_2O_3, CeO_2, etc., just to mention a few, belong to this category.[81]

In this thesis, two strategies were adopted to increase the performance of the metals for water splitting. The first one is to improve the charge transfer using conductive support materials (charge transfer from support to metal). The second one is to increase the number of electrochemically active surface areas by decreasing the particle size. Metal oxides such as TiO_2,[84,85] ZrO_2,[86] and CeO_2[87] with the corrosion-resistance, chemical inertness, and homogeneous dispersion properties, are widely used as supporting materials to increase charge transfer, the surface to volume ratio, and the electrochemically active sites.[35] These metal oxides have been widely used in many electrochemical reactions such as HER [88,89], OER,[90] formic acid oxidation[91], and hydrogen generation from ammonia borane,[92] which encourages to use TiO_2, ZrO_2, and CeO_2 as supporting materials in this thesis.

➢ **Titania :** Among the various metal oxides, Titanium dioxide (TiO_2) is a widely used supporting material in the catalyst field because of its high availability, low cost, high chemical and thermal stability, nontoxic and noncorrosive properties and robust interaction with metal nanoparticles [93,94]. TiO_2 with a large surface area ranging from 10 to 300 $m^2\,g^{-1}$ can be used as a support to prevent the aggregation of metal nanoparticles. There are two most widely used types of TiO_2 which are anatase and rutile. The anatase-TiO_2 powder is well known and frequently utilized commercial material as a catalyst support for metal heterogeneous catalyst due to its high specific surface area and strong interaction with metal nanoparticles.[93] According to the literature, anatase-TiO_2 is widely used in many applications such as solar energy storage, water splitting, hydrogen generation reaction from ammonia borane and as a catalyst in the synthesis of organic compounds.[95] There are only a few studies reporting a rutile catalyst support which resulted in higher catalytic activity compared to anatase, such as the oxidation of toluene, xylene, and benzene over rutile supported Cu catalyst. It is reported that rutile and anatase vary substantially in their capability to attach metal particles onto their respective surfaces; although anatase often exhibits a strong metal support interaction, rutile does not.[93]

➢ **Zirconia:** Because of its weak acid and basic sites and durability in both oxidizing and reducing environments, zirconium oxide (ZrO_2) has received interest as a catalyst support.[96] Moreover that, ZrO_2 has high thermal stability and corrosion resistance, even in harsh reaction conditions. Zirconia is a polymorphic material and can be found in three forms: cubic, monoclinic, and tetragonal. The monoclinic phase is stable at room temperatures up to 1170°C. [97] The structure of monoclinic zirconia provides a more versatile surface than that of other polymorphs (cubic, tetragonal) due to a less symmetrical lattice.

➢ **Ceria:** Cerium usually has two types of oxides named as cerium dioxide (CeO_2/Ceria) and cerium sesquioxide (Ce_2O_3), but CeO_2 is more frequently used due to higher stability over Ce_2O_3.[98] Cerium(IV) oxide is typically crystallised in the most stable form of fluorite structure with a face centred cubic lattice (fcc).[99] Cerium, which is electropositive in nature, exists in dual oxidation modes, Ce^{3+} and Ce^{4+}.[100] The Ce^{4+} oxidation state is usually considered more stable than 3^+ due to Ce^{4+} electronic structure $[Xe]4f^0$ being more stable state than $[Xe]4f^1$ for Ce^{3+}. The relative ease of switching between these two states is the essential factor for its catalytic activity.[101] The rapid change of oxidation state is related to its ability to store and release oxygen, a property measured by the oxygen storage capacity (OSC).[101] The process of oxygen storage and transport in ceria can be described by the defect mechanism, and there are two types of defects involved in this process. One is the intrinsic defects and the other is the extrinsic defects. The intrinsic defects are due to the oxygen anion vacancies created upon the reduction of ceria. The extrinsic defects are due to the oxygen anion vacancies created by the charge compensation effect of foreign cations which have a valence lower than that of the host cerium ions they substitute.[102]

CeO_2 possesses reversible surface oxygen ion exchange, good electronic/ionic conductivity, and high oxygen storage capacity because of the flexible transition between the Ce^{3+} and Ce^{4+} oxidation states as a result of variations in oxygen concentration.[103] In addition, the multivalence of CeO_2 can generate strong metal-ceria electron interactions, and accordingly can enhance catalytic performances. CeO_2 is widely used supporting metal oxide because it affects the catalyst performance in many applications such as solid oxide fuel cells,[104] carbon monoxide (CO) oxidation[105], degradation of toxic pollutant[106],hydrolysis of ammonia borane[107], etc.

Some of the advantages of CeO_2 are given below:

- affect the dispersion of supported metals;
- increase the thermal stability of the support;
- promote noble metal reduction and oxidation;
- form surface and bulk vacancies;
- form intermetallic M-Ce compounds.[108]

1.4.7. Significance of Pt group metals in heterogeneous catalysis

The platinum group metals (PGMs) are widely used as catalysts in the automobile sector, industrial chemical production (e.g., fine chemicals, ammonia synthesis), environmental (gas remediation), electronics (hard disk manufacture, multilayer capacitor devices) petroleum refining, and medicine (pacemakers (Pt-Ir)), implantable defibrillators (Pt-Ir), catheters, treatment of Parkinson's disease (Brain pacemaker))[109] . PGMs contains six d-block metals which are ruthenium (Ru), osmium (Os), rhodium (Rh), iridium (Ir), palladium (Pd), and platinum (Pt) from periods 5 and 6 of groups 8, 9 and 10. The chemical similarity of these elements is based on the 4d electron shells of the metals Ru, Rh and Pd or the 5d shells of the metals Os, Ir and Pt.

Electronic configuration of Pt group metals;

Light PGM	**Heavy PGM**
Ru: [Kr] $4d^7 5s^1$	Os: [Xe] $4f^{14} 5d^6 6s^2$
Rh: [Kr] $4d^8 5s^1$	Ir: [Xe] $4f^{14} 5d^7 6s^2$
Pd: [Kr] $4d^{10}$	Pt: [Xe] $4f^{14} 5d^9 6s^1$

Pt-group metals are widely used industrially as heterogeneous catalysts for hydrogenation reactions[110], CO oxidation[111], selective catalytic reduction of NO by hydrocarbons,[112] hydrogen and oxygen generation reaction and also used as industrial three-way catalysts as main active components. Because the metal components mainly exist as nanoparticles, developing new catalysts with smaller metal crystalline size and higher activity as well as the introduction of non-noble metals to save the use of noble metals is an active research field.[70]

1.4.8. Metal support interaction in the heterogeneous catalyst

Electronic, structural or/and chemical interactions are the possible interactions between a PGMs and supporting metal oxides.[113] Charge transfer between metal and metal oxide can result in electronic interactions. On the other hand, chemical interactions occur as a result of a chemical reaction such as a redox reaction between metal and supporting metal oxide. Structural interaction can also arise and assume predominant interaction if either the supporting metal oxide structure or the structure of metal is altered in some way.[81, 102,114] The reducibility of the support and the catalytic performance (activity and selectivity) of precious metal are usually affected by the interaction between a metal and supporting metal oxide. [115,116]

Tauster used the term "strong metal–support interaction" (SMSI) to characterize the significant changes in the chemisorption characteristics of group 8 metals supported by reducible metal oxides before and after a high-temperature reductive treatment in hydrogen in 1978.[117] SMSI was further broadened to encompass interactions between an active metallic component and any support materials that display similar phenomena to Tauster's observations. SMSI reduces the high surface energy of metal nanoparticles by encapsulating them in support suboxide particles under reducing environment.[118] Three specific characteristics must be fulfilled for a metal–support interaction to be classified as "strong": 1) At low reduction temperatures, the catalyst exhibits conventional chemical behavior; 2) as the reduction temperature rises, the chemisorption capability of the dispersed metal phase towards "classic" probe molecules such as hydrogen or carbon monoxide is disrupted, along with significant changes in its catalytic behavior; and, most importantly, 3) the phenomenon has to be completely reversible, that is, reoxidation at a proper temperature followed by mild rereduction re-establishes the catalytic behavior before entering the SMSI state. Although the term "strong metal-support interaction" is very misleading and should be avoided, its structural and electrical effects provide a convenient way to discuss the intrinsic complexity of oxide-supported intermetallic complexes.[119] Metal–support interaction (MSI) can broadly be defined as any influence on the performance of a supported metal catalyst caused by a support material during the synthesis process or during a catalytic reaction.[120] Because of its enormous influence on the geometric structures and electric characteristics of metal catalysts, the discovery of MSI has prompted highly important research topics in the catalysis field. [70, 121- 123]

It is just as vital to design the support structure as it is to design the active components. Surfaces and interfaces are at the heart of nanoarchitectured catalyst fabrication; their characteristics affect the size, shape, and spatial distribution of particles, and charge transfer processes between support materials and metal nanoparticles.

1.4.9. Characterization of transition metal nanoparticles in the catalyst

1.4.9.1. Physical characterization

It is necessary to analyze the composition, structure, size and morphology of TMNPs to obtain valuable information about their behavior in specific applications. Various analytical techniques can be utilized for the characterization purposes.

To get information about distribution, size, and the shape of nanoparticles, *transmission emission microscopy* (TEM) is most commonly used technique. TEM gives chemical information from solid materials over a wide range of magnification, to a level of spatial resolution that is unapproachable by most other techniques. *Scanning electron microscopy* (SEM) could also be utilized to obtain information about morphology, topography of surface and composition based on backscattered electron. For the elemental composition of TMNPs *transmission emission microscopy energy dispersive X-Ray analysis* (TEM-EDX) or *scanning electron microscopy energy dispersive X-Ray analysis* (SEM- EDX) can be used. However, EDX gives semi quantitative analysis and can only provide which elements rich in particles. For quantitative elemental composition analysis, it is better to use inductively couple plasma optical emission spectroscopy (ICP-OES) which gives precise and accurate results to obtain mass percentage of metals in nanocatalysts. ICP-OES is based on exciting the metal atoms of the nanocatalysts using a plasma and analyzing the emission wavelength of the electromagnetic radiation, which is typical of that particular metal.

Another important characterization technique is *X-Ray diffraction* (XRD) which provides information regarding the crystalline structure, lattice parameters, nature of the phase and crystalline grain size. The standard database (JCPDS database) for XRD pattern is used for phase identification for a large variety of crystalline phases in the nanomaterials. XRD were used in this thesis to check whether the crystallinity of supporting material used in the nanocatalysts are preserved or not after the impregnation of metal nanoparticles.

To gain information about electronic structure, elemental composition, and oxidation states of nanoscale materials *X-ray photoelectron spectroscopy* (XPS) is the most widely used analytical technique. Its basic physical principle is the photoelectric effect. The existence of metal nanoparticles on the surface of metal oxides could be proven by the XPS spectra of full scanning survey.

1.4.9.2   Electrochemical characterization

Electrochemistry is an important tool to understand reactions involving the transfer of electron. Two electrode or three electrode systems can be used for electrochemical studies. Electrochemical cells which have three electrodes are frequently used and counter, reference and working electrodes are immersed in an electrolyte solution and connected to a potentiostat for electrochemical measurements. There are many electrochemical techniques which are used to evaluate the performance of catalysts some of them are linear sweep voltammetry, chronopotentiometry, chronoamperometry, bulk electrolysis, electrochemical impedance spectroscopy, and under potential deposition.

1.4.9.2.1. Linear Sweep Voltammetry (LSV)

LSV is commonly used potentiodynamic electrochemical technique. In LSV fixed potential range is applied. The characteristics of the LSV depend on the rate of the electron transfer reactions, the chemical reactivity of the electroactive species and the voltage scan rate. In LSV measurements the current response is plotted as a function of potential rather than time. (Figure 9)

Although CV and LSV are quite similar, CV does not end with a single sweep over a certain potential range. For example, if the potential range is E_1 to E_2, when E_1 to E_2 is reached, it will switch back to E1.
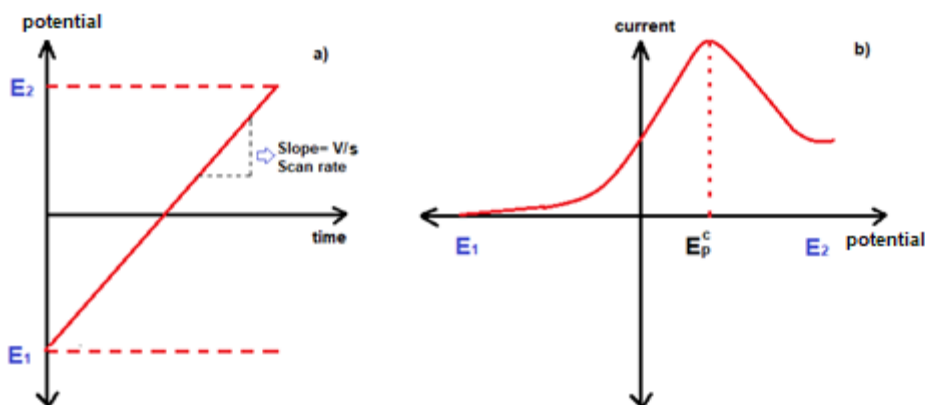
Figure 9. a) Potential vs. time and b) current vs. potential graphs for linear sweep voltammetry.

1.4.9.2.2. Chronopotentiometry and chronoamperometry

Chronoamperometry is a time-dependent technique where a square-wave potential is applied to the working electrode and which is used to study the kinetics of chemical reactions, adsorption and diffusion processes. Generally the working electrode is held at a potential at which there is no electrode reaction to one corresponding to the mass-transport-limited current, and the resulting current–time transient is recorded as a function of time. The chronoamperometry is mostly used for the deposition of metals, electrolysis, and the study of the stability over time of electrochemical systems.[124]

In chronopotentiometry, a constant current is applied to the working electrode and the potential changes to a value at which the flux of the electroactive species is sufficient to supply the applied current. After a certain time, the flux of redox species to the surface cannot sustain this current and the potential changes rapidly to a new value at which another species (often solvent or electrolyte) is reduced (or oxidized).[124]

1.4.9.2.3. Bulk Electrolysis

Bulk electrolysis is also known as potentiostatic coulometry or controlled potential coulometry. In the bulk electrolysis, constant potential is applied to working electrode for a long time (minutes to hours) and resulting current monitored over time. Even though the experiment measures electric current (amps) over time, the results of a bulk electrolysis are displayed as the total coulombs (total electric charge) passed plotted against time in seconds. Current efficiency or faradaic efficiency of a given process determined by a bulk electrolysis experiment.[125]

1.4.9.2.4. Electrochemical Impedance Spectroscopy (EIS)

Impedance (Z) can simply be defined as the measure of the opposition to alternating current of a circuit or a part of electrical circuit. All circuits and their components have impedance and the impedance works according to Ohm's Law (V= I*R) in ideal cases. However, deviation from Ohms Law can be observed due to the components of impedance which is composed of a resistance (real part) and a reactance (imaginary part-capacitive and inductive part). Electrochemical impedance spectroscopy (EIS) is an important electrochemical technique based on the interfacial reaction at the electrode surface.[126] There are three fundamental sources of voltage loss in an electrochemical reaction: kinetic losses (charge-transfer activation), ohmic losses (ion and electron transport), and mass transfer losses (concentration).[127] EIS can be used to distinguish and quantify these losses. When AC voltage is applied to an electrochemical cell, the current response is monitored by EIS and resistance, capacitance and inductance could be measured by this technique.[128] The results of the EIS can be represented by Nyquist or Bode plot as shown in Figure 10. Nyquist plot shows the imaginary and real parts of impedance using Cartesian coordinates and Bode plot represents the magnitude changes and phase shift in the applied frequency range.[129] The Nyquist plot provides insight into the possible mechanism in an equivalent circuit model system. Hu and his coworkers propose the idea that mechanism of the water splitting could be acquired by using EIS measurement (Nyquist plot) and the results can purely reflect the charge transfer kinetic of the electrode reaction excluding the contribution from catalyst resistance.[130]

26
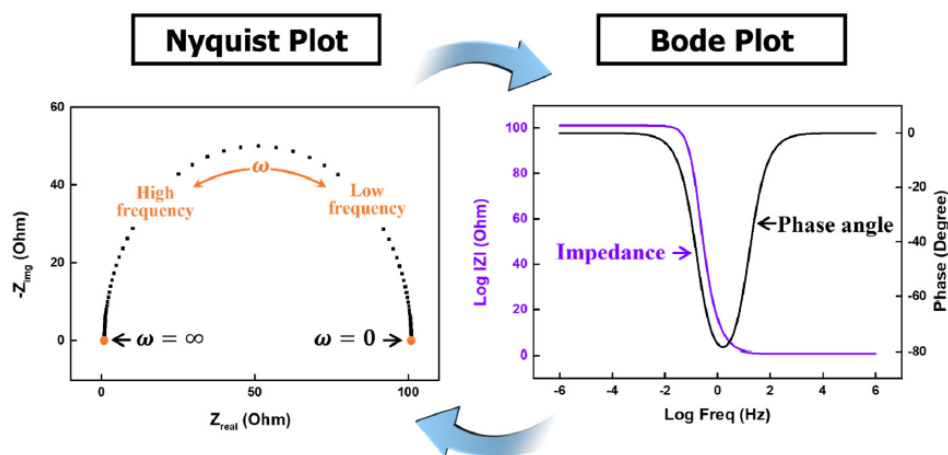
Figure 10. Nyquist and Bode plots for representation of electrochemical impedance spectroscopy. Reprinted from ref 131, Copyright (2020), with permission from Journal of Electrochemical Science and Technology.

To examine the EIS data correctly, using an appropriate model is important. The models consist of simple electrical circuit elements including resistors (R), capacitors (C) and inductor (L). Appropriate electrical components that represent the entire system should be used to create an accurate circuit model that is physically meaningful and minimizes the number of variables. In this thesis, the equivalence circuit model shown in Figure 11 was used to represent the EIS data. Constant phase elements (CPE) were used to fit the experimental data instead of capacitors (C) due to overcome the different degrees of surface roughness and a nonuniform distribution of surface reaction sites of solid electrodes.[132] Nyquist plots given in this thesis consist of two semicircles at low and high frequency regions. This model implies that the semicircles at high frequency region is potential independent (CPE_2 and R_2) and most probably arise from the contact between the GCE and the catalyst surface (porosity or adsorbed species on GCEs).[131] On the other hand, the semicircles at low frequency region are potential dependent and could be attributed to charge transfer process.[131] While CPE_1 represents the interfacial capacitance between oxide and electrolyte (the double layer capacitance, (C_{DL})), R_1 represents the charge transfer resistance (R_{CT}) and Rs refers to the uncompensated solution resistance.
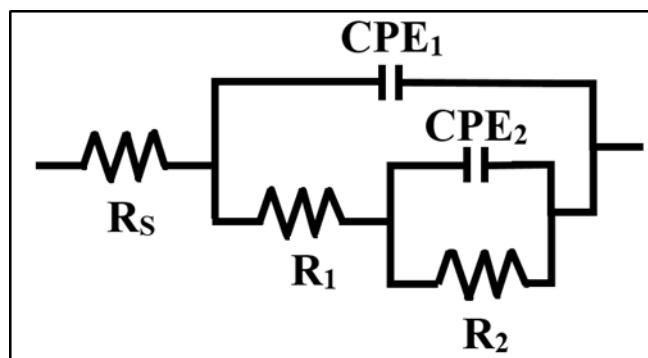
Figure 11. Equivalent circuit for EIS measurements

Double-layer capacitance is the important characteristic of the electrical double layer which appears, for example, at the interface between a conductive electrode and an adjacent liquid electrolyte. At this boundary two layers of charge with opposing polarity form, one at the surface of the electrode, and one in the electrolyte.[133] These two layers, electrons on the electrode and ions in the electrolyte, are typically separated by a single layer of solvent molecules that adhere to the surface of the electrode and act like a dielectric in a conventional capacitor.[134,135] The amount of electric charge stored in double-layer capacitor depends on the applied voltage. The double layer capacitance (C_{DL}) affect the activity can be calculated both from the EIS and CV measurements. C_{DL} was utilized to find electrochemically surface area (ECSA). The electrode with high ECSA shows a high electrocatalytic activity. ECSA could be calculated by dividing C_{DL} to the specific capacitance of flat electrode ($C_s \approx 40$ μFcm^{-2}).[136]

$$\text{ECSA} = \frac{C_{DL}}{C_S} = \frac{i_c}{\nu C_S} \qquad \textbf{(eqn. 1)}$$

where the C_{DL} is in mF. The i_c represents the charging current (mA), ν is the scan rate (V s^{-1}) and Cs is the specific capacitance of the catalyst (mF.cm^{-2}).

1.4.9.2.5. Under potential deposition

Electrodeposition of a metal adsorbate on a conductive solid surface is an important electrochemical method for purposes such as electroplating and inhibition of corrosion.[137] In some cases, metal overlayers could be electro-deposited onto a different metal substrate at a less negative potential than the Nernst potential (necessary for bulk deposition). Underpotential deposition (UPD) is important tool to reproducibly and quantitatively control the coverage of metal in the sub-monolayer to monolayer or multilayer regime.[138] In this thesis, UPD of copper on metal surface was applied for qualifying the active sites. In this approach, the number of active sites (n) were calculated based on the UPD copper stripping charge (Q_{Cu}, $Cu_{upd} \rightarrow Cu^{2+} + 2e^-$) with the following equation. The area under the oxidative wave, or Cu-UPD stripping charge (Q_{Cu}, Cu_{UPD}), was determined and used for the calculation of the number of active sites:

$$n = \frac{Q_{Cu}}{2F} \quad \textbf{(Eqn 2)}$$

1.4.10. Key parameters used to evaluate the catalytic activity

In electrochemical water splitting, many activity evaluation parameters are used such as overpotential at 10 mA cm^{-2}, Tafel slope, exchange current density, turnover frequency (TOF), stability, and Faradaic efficiency.

1.4.10.1. Some electrochemical terms about the electrocatalytic activity

i) Faradaic Process: In an electrochemical reaction, Faradaic and non-Faradaic processes occur at the surface of electrode. In the Faradaic process, charges or electrons (responsible for oxidation reduction) are transferred at the electrode electrolyte interface. The process is defined as Faradaic process because such reactions are ruled by Faradays law. According to the Faraday's law the amount of chemical reaction caused by the flow of current is proportional to the amount of electricity passed.[139] As can be understood from Figure 12 in a faradaic process, a species need to be transported through diffusion, migration or convection for any reaction at an electrode interface.
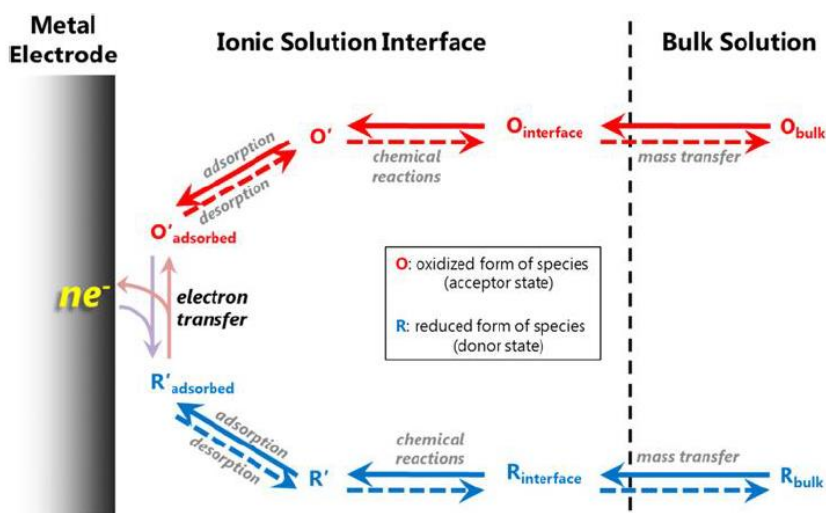
Figure 12. Pathway of a Faradic process. Reproduced with permission from ref. [140, 141]. Copyright © 2016, IOP Publishing Ltd.

ii) Equilibrium Potential: When a metal electrode immersed in a liquid electrolyte, metal ions will cross the electrode/electrolyte interface. The direction of the ions will be from the phase where electrochemical potential of ions is large to phase with smaller electrochemical potential.[142] The condition in which the chemical driving force equal to opposing electrical force is called equilibrium condition and equilibrium potential difference at this condition occur because of the potential difference of metal and solution phases.[143] Instead of the measuring this potential directly, electrode potentials are measured against a reference electrode because there is no way to make an electrical connection to the solution phase without setting up another electrode potential.[143] The equilibrium potential can be calculated by using Nernst equation. The Nernst equation relates potential to the concentration of electroactive species. For example, the free energy of the reduction of oxidized species, O, with n electrons (gives a reduced species, R, (Eqn. 3)) can be written as in Eqn 4.

$$O + ne^- \rightleftharpoons R \qquad \text{(Eqn. 3)}$$

$$\Delta G = \Delta G^o + RT \ln \frac{a_R}{a_O} \quad \text{or} \quad -\Delta G = -\Delta G^o + RT \ln \frac{a_O}{a_R} \qquad \text{(Eqn. 4)}$$

where $-\Delta G$ is the free energy change indicating the tendency for the reaction to go to the right; R is the gas constant (8.317 J mol^{-1} K^{-1}), T is the temperature (K), and the quantity ΔG^0 is the free energy change of the half reaction when the activities of the reactant and product have values of unity and is directly proportional to the standard half-cell potential for the reaction.

The free energy of this half reaction is related to the electrode potential, moreover it is a measure of the equilibirium constant for the half reaction. E^0 values are valid only under equilibrium conditions and for $a_O=a_R=1$. In practice, this condition is not fulfilled. The free energy can be expressed as follows:

$$-\Delta G = nFE^o \qquad \text{(Eqn. 5)}$$
$$-\Delta G = RT \ln K \qquad \text{(Eqn. 6)}$$

When these two reactions are combined, Nernst equation can be obtained (Egn. 7)

$$E = E^o + \frac{RT}{nF} \ln \frac{a_R}{a_O} \qquad \text{(Eqn. 7)}$$

At standard pressure (1 bar) and 298 K, the thermodynamic equilibrium potential for hydrogen evolution reaction reference to reversible hydrogen electrode (RHE) can be calculated by using following equations:

$$E_{HER} = E^0{}_{H2/H^+} - \frac{RT}{F} \ln \frac{a_{H+}}{P_{H2}^{1/2}} = -0.059 \times (pH) \text{ V vs. NHE} \qquad \text{(Eqn. 8)}$$

$$E^0{}_{H2/H^+} = 0 \text{ V vs. RHE (Eqn. 9)}$$

The potential is pH-dependent and shifts linearly by -59 mV for each pH unit increase and this dependance can be canceled by reference to RHE. The thermodynamic equilibrium potential for HER is straightforward and equals zero on the RHE scale, regardless of electrolytes used.[32]

1.4.10.2. Overpotential (η)

The overpotential (η) at a certain current density is one of the most important indicators when evaluating the performance of electrocatalysts. The overpotential is defined as the difference between the equilibrium potential (also called the thermodynamic potential) for a given reaction and the potential at which the catalyst operates at a given current under certain conditions.[144] (Eqn. 10) Overpotential is needed because of the reaction energy barriers.

$$\eta = E - E_{eq} \text{ (Eqn. 10)}$$

The measured overpotential mainly consists of three parts: i) activation overpotential depending on the intrinsic property of catalyst, ii) concentration overpotential caused from sudden concentration drop near the interface and iii) system overpotential due to uncompensated resistance.[145] Using electrolyte with a high concentration or stirring during the reaction can minimize concentration overpotential. On the other hand, system overpotential could be eliminated by iR-compensation (Ohmic drop). iR-compensation can be done by system setting of potentiostat or manually. The overpotential at 10 mAcm^{-2} (geometrical surface area) is considered a standard value for assessing the stated catalytic efficiency since the current density of 10 mA cm^{-2} is roughly in the range of most PV systems that provide enough voltage to separate water, and corresponds to 12.3% of solar to hydrogen efficiency under one sun illumination[146,147] A catalyst which has solar-to-hydrogen energy conversion efficiency of less than 10%, require improvements for real-world applications. The overpotentials at higher current densities such as 50 and 100 mA/cm^2 are also used as alternate activity parameters. A lower η of an electrocatalyst in the system indicates its superior electrocatalytic ability for the target reaction.

1.4.10.3. Exchange current density (J_0) and Tafel slope (η)

Exchange current density (j_0) is an important parameter in electrochemistry and used in the electrochemical kinetic expressions such as Butler Volmer equation and Tafel equation. The current which is created in the absence of net electrolysis at zero overpotential is called the exchange current and can be considered as a background current to normalize the net current observed at non zero overpotential. For a redox reaction written as a reduction at the equilibrium potential, the charges (electrons) cross the electrode-electrolyte interface in both directions, and the current density is only created by the flow of these electrons. A balance is established between the cathodic current and the anodic current. The current, continuing in both directions, is defined as the exchange current density and under equilibrium conditions which represent the catalyst's intrinsic activity.[148] Nature of the electrode such as roughness of surface, adsorbed species and passivating oxide on the surface, solvent and temperature can significantly affect the exchange current density.[149]

Butler-Volmer equation (Eqn. 11) can be used to approximetly describe the the kinetic of electrochemical reaction.

$$j = j_0 [e^{\frac{\alpha_a nF\eta_a}{RT}} - e^{\frac{\alpha_c nF\eta_c}{RT}}] \quad \text{(Eqn. 11)}$$

Where j: electrode current density, j_0: exchange current density, α:charge transfer coefficient at anode or cathode (sum of them is equal 1 and usually $\alpha_a = \alpha_c = 0.5$), n: transferred electron number (for the OER n=4 and for HER n=2), F: Faraday constant (96485 C/mole), η : overpotential, R: universal gas constant, and T: temperature (K).

At the large overpotential region (e.g., η > 15 mV) Butler–Volmer equation can be simplified to Tafel equation (Eqn. 12):

$$\eta = -(\frac{2.303RT}{\alpha F}) \log j_0 + (\frac{2.303RT}{\alpha F}) \log j \quad \text{(Eqn. 12)}$$

$$\mathbf{\eta = a + b\log(j)} \quad \text{(Eqn. 13)}$$

The eqn 13 is called Tafel equation and which shows a linear relationship between overpotential and log j. In the equation a is constant and b is the Tafel slope with the formula:

$$b = \frac{2.303RT}{\alpha F}$$

The Tafel equation is a convenient way to reveal the mechanism of the reaction and the rate-determining step (rds) at the liquid-solid interface.[150] Moreover that, comparison of the activities of different electrode and electrocatalyst is possible with Tafel analysis. Tafel slope (b) changes with increasing potential, which can be attributed to a change in the rds or potential variation on the adsorption of reaction intermediates.[39] For HER there are three possible rate determination step in acidic media, Volmer step, Heyrovski step and Tafel step.

1- Volmer (electrochemical hydrogen ion adsorption) reaction;

$$H_3O^+ + e^- \leftrightharpoons H_{ads} + H_2O$$
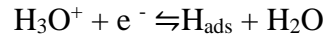
$$b = \frac{2.303RT}{\alpha F} \approx 120 \text{ mV.dec}^{-1} \quad \text{(Eqn. 13)}$$

2- Heyrovsky (electrochemical desorption) reaction;

$$H_{ads} + H_3O^+ + e^- \leftrightharpoons H_2 + H_2O$$
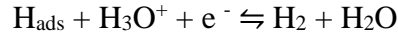
$$b = \frac{2.303RT}{\alpha F} \approx 40 \text{ mV.dec}^{-1} \quad \text{(Eqn. 14)}$$

3- Tafel (chemical desorption) reaction;

$$H_{ads} + H_{ads} \leftrightharpoons H_2$$
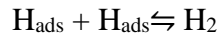
$$b = \frac{2.303RT}{\alpha F} \approx 30 \text{ mV.dec}^{-1} \quad \text{(Eqn. 15)}$$

When the Volmer reaction is the rate-determining step (rds) then Tafel slope is 120 mV/dec. For the Volmer-Tafel mechanism or Volmer-Heyrovsky mechanism Tafel slope is 30mV/dec and 40 mV/dec, respectively. [151]

The electrochemical OER mechanism is more complex and consists of many consecutive reactions steps both chemical steps such as association or dissociation reaction and electron transfer steps. Transfer coefficient value is important indicator for the determination of rate determining step (RDS) of the OER mechanism. The transfer coefficients (α) could be calculated for different temperatures by using the formula: $b = 2.303RT/\alpha F$ where; b is the Tafel slope (mV.dec^{-1}), R is the universal gas constant constant (J.K^{-1} mol^{-1}), T is the temperature (K), F is the Faraday constant (96485 C).[39]

Bockris and Reddy[152] derive also the transfer coefficient as $\alpha_a = (n_b/\upsilon) + (n_r\beta)$ for a multiple electron reaction where n_b represents the number of electrons transferred back to the electrode before the RDS, υ is the number of RDSs taken place in the overall reaction, n_r is the number of transferred electrons in each occurance of the RDS and β is symmetry factor (β is generally assumed 0.5). If the rate-determining step is the first electron transfer reaction, the values of both υ and n_b are equal to 0 while β and n_r are 0.5 and 1, respectively. The transfer coefficient is calculated to be 0.5 and the corresponding Tafel slope is 120 mV dec^{-1}.

If the chemical reaction after a one electron transfer reaction is RDS, the value of n_r is equal to 0 and the values of n_b and υ are 1. Hence, transfer coefficient become unity and Tafel slope is 60 mV.dec^{-1}.[16] If the rate-determining step is the 3rd electron transfer step in some systems such as OER (a four-electron transfer system), υ and n_b are equal to 1 and 2 (n_r and β are 0), respectively. This yields a transfer coefficient of 2 and a Tafel slope of 30 mV dec^{-1}.

If the remaining other parameters are constants, the Tafel slope is inversely proportional to the charge transfer coefficient (α). This indicates that a catalyst with a high charge transfer ability should possess a small Tafel slope. [150] This is the reason why the Tafel slope is often used as a primary activity parameter in determining the catalytic activity. The Tafel plot of an electrocatalytic process is generally obtained by replotting the polarization curve (e.g., LSV as a plot of log(j) versus η). However, there are several issues that can lead to misinterpretation of catalytic activity when using this route. In general, the LSV obtained with a high scan rate yields a high experimental inaccurate Tafel slope. LSV should be performed with the lowest possible scan rate. If the catalysts is highly capacitive, the scan rate used for LSV becomes a serious problem and can leads to large error when determining exchange current density because j_0 is generally found by extrapolating the linear fit toward the corresponding logaritmic current density at zero overpotential. In theory, a high exchange current density calculated from Tafel equation means that electron transfer across the catalytic interface will be easy and requires a very low activation energy and the result should have a low overpotential, however, in the results obtained, a catalyst with a high overpotential will have a large j_0 and it is not possible.[153]

Moreover that, capacitive current in the Faradaic region is not completely true because it is not the steady state current and this also cause experimental inaccuracy to determine Tafel slope. Hu and co-workers proposed a new method to determine more accurate Tafel slope and used different overpotentials and the slope of the plot of log (R_{CT}) vs η is obtained as a Tafel slope.[130] Solution resistance is excluded in this method and Tafel slope of the catalyst depends only on the charge transfer ability of the catalyst which results in an exact Tafel slope. To find the Tafel slope of an electrocatalyst, either LSV or EIS methods may be preferred depending on the requirements and conditions.

Among the Tafel slope, exchange current density, and overpotential, overpotential at a fixed current density can be considered the best activity parameter of the catalyst and j_0 is frequently used as an activity parameter in HER because which has less complex mechanism than OER.

1.4.10.4. Turnover frequency (TOF)

Turnover frequency (TOF) is another important activity parameter in the literature and can be defined in different ways. The electron transport rate per metal atoms on the surface per second[154] or the ratio of evolved product molecules per surface metal atom, per electrochemically active site, or per number of total metal atoms[147, 155] are some of the definitions of TOF. Under defined reaction conditions, TOF quantifies the specific activity of a catalytic centre for a special reaction by the number of molecular reactions or catalytic cycles occurring at the centre per unit time. Since TOF reveals the intrinsic electrocatalytic activity of a catalyst, in this thesis TOF values were determined by copper underpotential deposition (Cu-UPD) method for acidic conditions as explained below. In this approach, the number of active sites (n) were calculated based on the UPD copper stripping charge Q_{Cu}, **$Cu_{upd} \rightarrow Cu^{2+} + 2e^-$** with the following equation $n = Q_{Cu}/2F$ and then, the TOF (s^{-1}) were calculated with the following equation[156]:

$$TOF = \frac{I}{2nF} \quad \text{(Eqn. 16)}$$

For the alkaline conditions, the values of TOF were estimated by using the following formula[157]:

$$TOF = \frac{j \, S_{geo}}{4nF} \quad \text{(Eqn. 17)}$$

j: current density ($A.cm^{-2}$), n: the number of moles of metal atoms on the electrode surface, the number 4 : 4 electrons transferred per mole of O_2, F: the Faraday constant (96485 $C.mol^{-1}$) and S_{geo} :geometric surface area (cm^2). By using this formula TOF values of catalysts can be calculated for different current densities.

1.4.10.5. Stability

One of the most important parameters in using the electrocatalyst for a particular reaction is its stability or durability. The stability of electrocatalyst can be measured using a combination of voltammetry, chronoamperometry, or chronopotentiometry. If cyclic voltammetry is used to test stability of electrocatalyst than it is subjected to repetitive cycling at certain potential ranges. Before and after the stability test, LSV curves are recorded separately and the difference between the onset potentials, overvoltages and current densities obtained from these curves are examined to determine whether the electrocatalyst are stable or not and the results are compared with the literature. Other methods used for stability measurement are to apply a constant current or constant potential to the catalyst. After applying constant current for a certain time, the catalyst is stable if the potential obtained is close to the initial potential or if no change in potential is observed. Similarly, if the current obtained does not change or a slight change is observed when a constant potential is applied, the catalyst is also considered stable.

1.4.10.6. Faradaic Efficiency

Faradaic efficiency can be defined as the ratio of the actual mass of a substance produced during the reaction by the passage of a current to the theoretical mass produced according to Faraday's law.[139] It was calculated using water displacement method via Hoffmann apparatus (Figure 13). In this method, two electrode system and chronopotentiometry method are generally used, however, herein Hoffmann apparatus was modified and silver wire was integrated into the system as a pseudo reference electrode to control the applied potential.
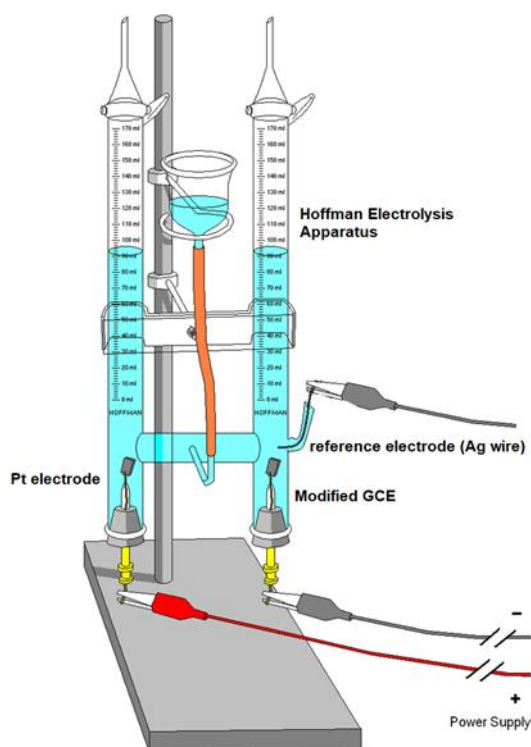
Figure 13. Hoffman electrolysis apparatus.

Constant potential was applied to system and the amount of gas measured by controlled potential coulometry method. The experimentally produced gas volume and the theoretical volume of produced gas are compared at certain potential vs. Ag wire which corresponds to a certain current in Hoffmann cell. To calculate Faradaic efficiency for hydrogen evolution reaction, the theoretical volume of hydrogen gas is calculated using Faraday's relation ($Q = i*t$). By calculating the quantity of electricity that passes through the system, number of moles of generated hydrogen can be determined experimentally. Theoretical volume of hydrogen gas is calculated as follows:

$$P.V_{H2} = n_{H2}.R.T$$

where; P is the atmospheric pressure during the experiment, n is the mole number calculated from Faraday's relation, R is the universal gas constant, 0.082 L.atm.mol^{-1}K^{-1}, and T is temperature recorded during experiment (K), V_{H2} is the theoretical volume of produced hydrogen gas. Faradaic efficiency of oxygen evolution reaction is also calculated by following same steps.

38

1.5. Motivation of the Dissertation

For the sustainable hydrogen production, electrochemical water splitting plays an important role. The conversion of water to hydrogen and oxygen provides an environmentally benign, carbon-free alternative for H_2 production. Noble and non-noble metal based catalysts are extensively used to perform HER and OER, respectively to lower the overpotential. [158] Electrochemical water splitting kinetic is seriously slow down due to considerable energy barriers causing from HER with two electron transfer and OER with four-electron transfer reactions.[159] That is why, developing an efficient, long-lived, and cost-effective electrocatalyst to decrease the overpotential and increase the rate of HER and OER is still a challenging issue.

Recently, a large variety of catalysts containing noble metals (i.e. Ru, Rh) and non noble metals (i.e. Ni, Cu) have been developed for HER. [160] 7.16 wt. % IrHNC, [161] 11 wt. % IrP_2@NC, [162] 23.8 wt. % Ir@CON, [163] 5.9 wt. % Ir/g-C_3N_4/NG, [164] 17% Ir/SiNW,[165] Rh Nanowires,[166] Rh/Si,[167] Rh-Au-SiNW-2,[168] Rh Hollow Nanoparticles,[169] Rh_2P/NC,[170] Rh_2P/C,[171] in situ- Rh/C,[172] Rh_2P[173] exhibit high electrocatalytic activity in terms of over potential values or Tafel slopes. In addition that, many oxide type electrocatalysts based on earth-abundant metals were also reported to catalyze the OER. [174] There are many studies including Co based catalysts for OER in alkaline medium such as $Cu_{0.3}Co_{2.7}P$/NC,[175] $CoCr_2O_4$/CNS,[176] Fe_3O_4@Co_9S_8/rGO-2,[177] CoP hollow polyhedrons,[178] $SrNb_{0.1}Co_{0.7}Fe_{0.2}O_{3-\delta}$,[179] and Co_9S_8@NOSC-900°C[180]. However, in the synthesis of most of the reported catalyst for HER and OER, harsh catalyst preparation conditions containing environmentally unfriendly chemical reagents and high temperatures were required such as calcination (400-600 ºC), carbonization (800–900 ºC), pyrolization(310-540 ºC), solvothermal treatment (600 ºC), annealing (300- 600ºC). The high metal amount used in the catalysts and usage of binding agent such as nafion which blocks the active sites are other disadvantages of the catalysts reported in the literature. [181]

The aim of this thesis was to synthesize low cost, highly active and stable electrocatalysts with enviroment friendly synthesis method to be used for HER and OER. Group 9B metals were chosen and combined with various metal oxides as supporting materials to decrease metal amount and particle size while increasing dispersion and charge transfer.

CHAPTER 2

EXPERIMENTAL

2.1. Materıals

Rhodium (III) chloride trihydrate (99.9% metal basis), iridium(III) chloride hydrate ($IrCl_3.xH_2O$) (trace metal basis 99.9%), cobalt(II) chloride hexahydrate ($CoCl_2.6H_2O$, 98%), cobalt(II,III) oxide (< 50 nm particle size), titania (TiO_2 particle size ≈ 25 nm) (99.9%), zirconia ($ZrO_2 \approx 100$ nm) (99.9%), ceria (99.9%) (CeO_2 particle size ≈ 25 nm), Pt/C (10 wt. %), nafion perfluorinated resin (5.0% wt. in lower aliphatic alcohols and water, contains 15-20% water) and sodium borohydride (98%), dimethyl formamide (DMF) and potassium hydroxide (KOH, 98%) were supplied from Sigma Aldrich. Unless otherwise stated, all the above chemicals were used as received without further purification.

2.2. Synthesis of metal oxide containing catalysts

Desired amount of supporting metal oxide (MO_2, M=Ce, Ti and Zr) powders and the desired amount of metal salts were mixed in 100 mL distilled water and the mixtures were stirred for 24 h at room temperature. Then, 10 mL of the $NaBH_4$ solutions were added to these slurries drop wise in 1:5 mole of metal:moles of $NaBH_4$ solutions ratio (for Ir containing catalysts 1:40 mole of metal:moles of $NaBH_4$ solutions ratio was used) and the mixtures were stirred for 60 min (Ir containing catalysts 3h stirring was applied). After this period, Rh, Ir or Co nanoparticles on supporting metal oxide were obtained and separated from the solutions via centrifugation at 8000 rpm for 10 min. In order to remove residues coming from the solution, the obtained catalysts were washed with 50 mL water and dried under vacuum at 60°C for 12 h (Figure 14). Metal content of our catalysts were determined by using ICP-OES (Table A1) .
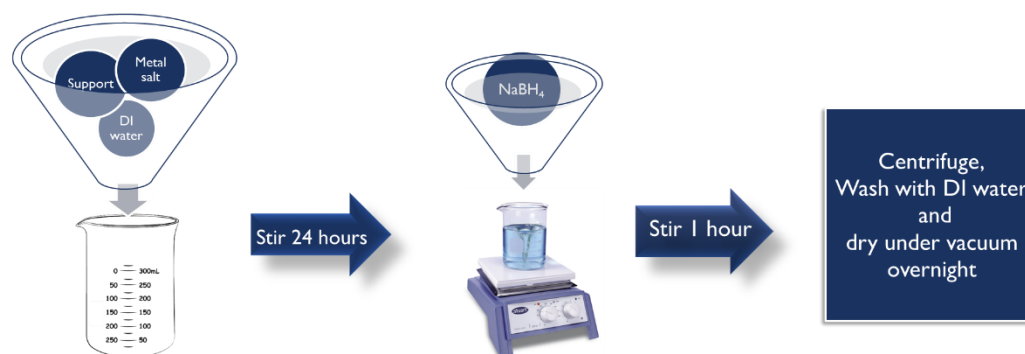
Figure 14. Synthesis scheme of the catalysts

The amount of metal salts were calculated using the following formula:

$$\text{Percent loading} = \frac{\frac{weight\ of\ metal\ salt}{molecular\ weight\ of\ metal\ salt}\ x\ molecular\ weight\ of\ metal}{weight\ of\ metal\ salt + weight\ of\ supporting\ material}\ x100$$

2.3. Electrode preparation and electrochemical studies for HER and OER

2.3.1. Electrochemical set-up

Gamry PCI4/300 potentiostat–galvanostat was used for all electrochemical studies. A three-electrode system consisting of a working (GCE, d=3.00 mm), a reference (Ag/AgCl in 3 M NaCl solution for HER or Hg/HgO in 3.0 M KOH solution for OER), and a counter (Graphite rod for HER or Pt wire for OER) electrodes were used for the electrochemical measurements. Alumina polishing suspension was used to clean GCEs prior to their use. The electrochemical cell and its components used during electrochemical measurements are shown in Figure 15.
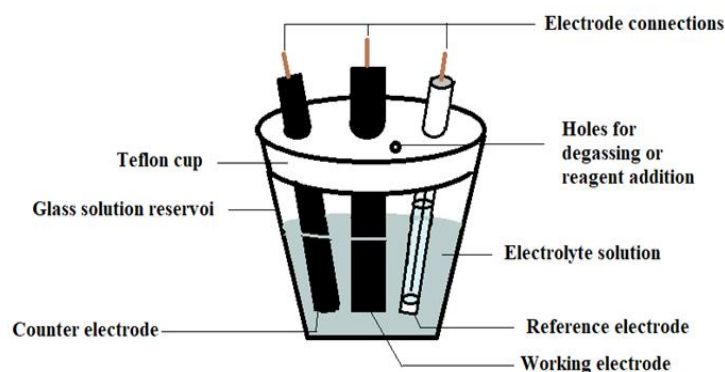
Figure 15. The electrochemical cell and its components used during electrochemical measurements.

2.3.2. Electrode preparation

GCEs were modified with as-prepared catalysts to determine the electrochemical HER activities of them. To modify the GCEs desired amount of Rh or Ir containing catalyst was sonicated for 1 h in 500.0 μL isopropanol and 2.0 μL aliquot of this dispersion was dropped onto previously cleaned GCE. The suspension was dried on GCE at room temperature for 1 h. For comparison Pt/C on GCE was also prepared by following the same procedure given above using 15.0 mg of commercial Pt/C. Note that the amount of metal content (Ir and Rh) on the GCE was kept constant as 85.7 $\mu g.cm^{-2}$ for all measurements.

To determine the electrochemical activities of the synthesized OER catalysts, the working electrodes were obtained by modifying 0.07 cm^{-2} GCE with catalyst inks. For the ink solutions, 445.0 μL of DMF, 5.0 μL of Nafion, and desired amount of catalyst were mixed and further dispersed via 1 h ultrasonication. Subsequently, the prepared ink solution was drop cast on the GCE and dried at room temperature overnight. Loading densities were kept constant as 51.58 $\mu g.cm^{-2}$ for all three Ir catalysts and 107.0 $\mu g.cm^{-2}$ for all three Co catalysts. The cobalt containing working electrodes were treated by oxidative constant current (0.07 $mA.cm^{-2}$) electrolysis for 10 s and the iridium containing working electrodes were pretreated during 100 s with constant current (-6×10^{-4} A) just before the measurements started. After conditioning, the surface is covered with thin oxide layer. Therefore, Co/MO_2 can be considered as CoO_x/MO_2.

43

2.3.3. Electrochemical measurements

LSV was utilized to investigate the electrochemical activity of the modified electrodes in 0.5 M H_2SO_4 solution at 5 mV/s scan rate. The obtained potentials were optimized with respect to reversible hydrogen electrode (RHE) by using the following equation ($E_{vs\ RHE} = E_{vs\ Ag/AgCl} + 0.210 + 0.059$ pH) V [182]. The electrochemical impedance spectroscopy (EIS) measurements were performed at various potentials in the frequency range of 0.1–100,000 Hz with an amplitude of 5 mV. The electrocatalytic stability of catalysts on GCE were tested by recording cycling voltammogram (CV) in 0.5 M H_2SO_4 solution in the range of -0.50 to +0.50 V vs. Ag/AgCl at a 50 $mV.s^{-1}$ scan rate.

The electrochemical activities of the synthesized OER catalysts were studied in a three-electrode setup. Hg/HgO was used as a reference electrode and Pt wire as a counter electrode. Linear sweep voltammograms (LSV) were recorded in the range of 0.0- 1.0 V vs. Hg/HgO with a scan rate of 20 $mV.s^{-1}$. All the potentials were converted to the reversible hydrogen electrode at pH =14 ($E_{vs\ RHE} = E_{vs\ Hg/HgO} + 0.915$) [183], and the LSV data were given after compensation for IR drop. The stability experiments were conducted by chronopotentiometry method in 1 M KOH solution at a constant current density of 10.0 mA cm^{-2}. Note that details of synthesis, characterization and electrochemical preparation of MO_2 (M= Ti, Zr, Ce) supported rhodium, iridium and cobalt nanoparticles were represented in Appendix A.

2.4. Instrumentation

The metal content was determined by using inductively coupled plasma optical emission spectrometry (ICP−OES) (Leeman-Direct Reading Echelle). Powder X-ray diffraction (XRD) patterns were acquired on a Rigaku MiniFlex Xray diffractometer (radiation source Cu Kα, $\lambda = 0.15418$ nm, and scanning rate = 2 min−1). Transmission electron microscopy (TEM) images were taken on a JEOL JEM-2100F electron microscope. X-ray photoelectron spectroscopy (XPS) was performed on a Physical Electronics' 5800 spectrometer (Al Kα radiation of 1486.6 eV).

CHAPTER 3

RESULTS AND DISCUSSIONS

3.1. Electrocatalytic activity of MO_2 (M= Ti, Zr, Ce) supported rhodium, iridium and cobalt nanoparticles towards HER

3.1.1. Electrocatalytic activity of Rh NPs supported on MO_2

At the beginning of the detailed investigations of the catalysts, the factors affecting the activity of rhodium nanoparticles towards hydrogen evolution reactions were examined under four main headings. The counter electrode effect, the effect of the supporting metal oxide, the effect of the loading amount and the effect of the loading density on the working electrode are the main topics mentioned above and going to be explained below.

3.1.1.1. Effect of counter electrode on the performance of Rh catalyst

Pt wire and graphite rod were used comparatively as counter electrodes in the electrochemical cell to observe whether there was metal dissolution in acidic media. Electrocatalytic activity of 0.5 % Rh/TiO_2 modified GCE was investigated by recording polarization curves in 0.5 M H_2SO_4 solution. First of all, the Pt wire was used as a counter electrode. Since the electrocatalytic activity of the modified electrode was found to be improved gradually after potential cycling between -0.5 and 0.5 V vs. Ag/AgCl when using Pt wire, Rh/TiO_2 modified GCE was subjected to the potential cycling until no more change was noted in the onset potential. This point was reached after 2000 cycles of CV treatment in 0.5 M H_2SO_4 solution. There were Pt dissolution and deposition on surface of the Rh/TiO_2 during 2000 cycle pretreatment.

To check the activity of the deposited Pt without Rh, the same pretreatment was applied to the bare GC electrode and bare TiO_2 on GCE. After applying the same

treatment, the obtained Pt deposited TiO_2 and GC electrode did not show any promising electrocatalytic activity as compared to the treated Rh/TiO_2. The onset potentials, the overpotentials and the Tafel slopes of bare GCE, bare TiO_2, initial 0.5% Rh/TiO_2, Pt deposited bare GCE and bare TiO_2 and Pt deposited Rh/TiO_2 were given in Table 2 to see how the presence of very low amount of Rh helps the improvement of electrode.

Table 2. Onset potentials, Tafel slopes and overpotential values of bare GCE, TiO_2 and Rh/TiO_2 for the initial state and after 2000 cycles treatment. (With IR compensation.)

	initial				after 2000 cycles treatment			
	η_0 (mV vs. RHE)	Tafel slope (mV/dec)	η (mV vs. RHE)	j_0 (mA.cm^{-2})	η_0 (mV vs. RHE)	Tafel slope (mV/dec)	η (mV vs. RHE)	j_0 (mA.cm^{-2})
Bare GCE	660	--	--	-	267	106	274@-10 mA/cm^2	0.028
TiO$_2$	498	464	--	-	93	87	104@-10 mA/cm^2	0.631
Rh/TiO$_2$	322	115	356@-10 mA/cm^2	0.009	28	32	37@-10 mA/cm^2	0.686

The observed improvements in the electrochemical activities of Rh/TiO_2 during the treatment (Table 2, Figure 16 (a) and (b)) were attributed to cathodic deposition of Pt originating from anodic dissolution of Pt counter electrode.[184, 185, 186] For the detail studies to understand how the bimetallic interaction affects the catalyst activity, GCE modified with 0.5% Rh/TiO_2 catalyst was chosen as the working electrode when Pt was used as the counter electrode. In the cell, the electrodes were not separated and the acidic electrolyte is continuously stirred, so that platinum from the dissolution of the counter electrode could easily reach the working electrode.
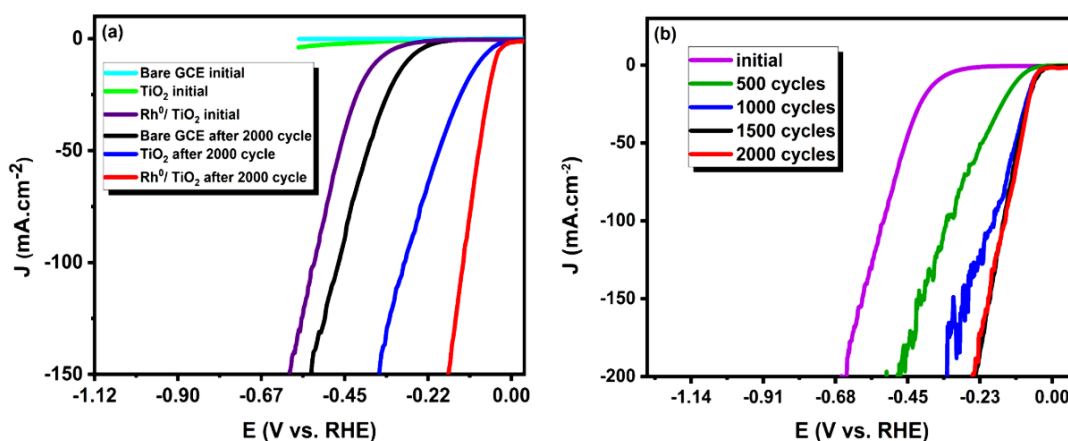
Figure 16. (a) The comparison of polarization curves of bare GCE, TiO_2 and Rh/TiO_2 catalyst on GCE before and after treatment in 0.5 M H_2SO_4 at a scan rate of 20 mV.s^{-1} (b) Polarization curves for the initial, 500, 1000, 1500 and 2000 cycle treated Rh/TiO_2 catalyst on GCE in 0.5 M H_2SO_4 at a scan rate of 20 mV.s^{-1}.

The dissolution of noble metals in acid solution by anodic scanning is a well-known and studied subject in the literature. [184, 185, 187 - 192,] Pt was used instead of graphite rod as a counter electrode in order to make cathodic deposition of the anodically dissolving metal and to observe the change of catalyst activity by reducing the metal amounts. Generally, Pt counter electrode contamination can be summarized as oxidation-dissolution-deposition process. As understand from the reactions in Table 3, under anodic potentials, the surfaces Pt atoms adsorb oxygenated species followed by O-penetration into sub-layers to form oxidized $Pt-O_{ex}$, which is unstable to be dissolved.[187] After dissolution, the Pt ions in the solution redeposit onto the working electrode under cathodic potentials.

Table 3. Oxidation-dissolution-deposition process of Pt in acidic medium

Under anodic potential	Under cathodic potential
$Pt + H_2O \rightarrow PtO + 2H^+ + 2e^-$	
	$Pt^{2+} + 2e^- \rightarrow Pt_{(s)}$
$PtO + H_2O \rightarrow PtO_2 + 2H^+ + 2e^-$	
$Pt-O_{ex} + 2H^+ \rightarrow Pt^{2+} + H_2O$	
	$Pt^{4+} + 4e^- \rightarrow Pt_{(s)}$
$Pt-O_{2ex} + 4H^+ \rightarrow Pt^{4+} + 2H_2O$	

As it is known, dissolution and electrodeposition of platinum is a slow process and the amount of Pt deposited on GCE increases with the increasing number of CV cycles. After 2000 cycle, there is no noticeable change in the onset potential, the Tafel slopes and overpotential values at 10 mA.cm^{-2} (Table 4). The amount of Pt deposited on Rh/TiO$_2$-GCE after 500, 1000 and 2000 cycles, were determined as 0.52, 6.38 and 17.94 mole/mole ratio, respectively by using ICP-MS (please see Appendix for the details of instrumentation).

Table 4. Onset potentials, Tafel slopes and overpotential values of initial Rh/TiO$_2$ and Rh/TiO$_2$ after 500, 1000 and 10000 cycle treatment. (With IR compensation.)

	η_0 (mV vs. RHE)	Tafel slope (mV/dec)	η_{10} (mV vs. RHE)
initial	317.0	115.0	352.7
500 cycle	83.0	55.0	103.0
1000 cycle	46.0	38.0	52.0
2000 cycle	28.0	32.0	37.0
10000 cycle	29.0	33.1	40.0

For the bimetallic catalyst, besides metal-support interaction metal-metal interactions are also important in HER. Therefore, the observed improvement in the electrocatalytic activity of Rh/TiO$_2$ can be attributed not only to Pt deposition but also Rh-Pt interaction.[193] By using very low amount of Rh, highly good results can be obtained and these results are due to the bimetallic relationship of Pt with Rh. The name of the bimetallic catalyst obtained after 2000 cycles treatment was updated as Rh/TiO$_2$-2000 to avoid any ambiguity

Rh/TiO$_2$-2000 shows superior electrocatalytic activity in 0.5 M H$_2$SO$_4$ solution for HER with ultralow mass loading of Rh (3.79 µg.cm^{-2}). The polarization curves belonging to bare GCE, TiO$_2$ and Rh/TiO$_2$-2000 modified GCE after CV treatment (2000 cycle) were presented in Figure 17 (a) and corresponding Tafel curves were given in Figure 17 (b). Tafel slopes of bare GCE, TiO$_2$ and Rh/TiO$_2$-2000 modified GCE were calculated as 106, 87, and 32 mV.dec^{-1}, respectively (Figure 17 (b)).
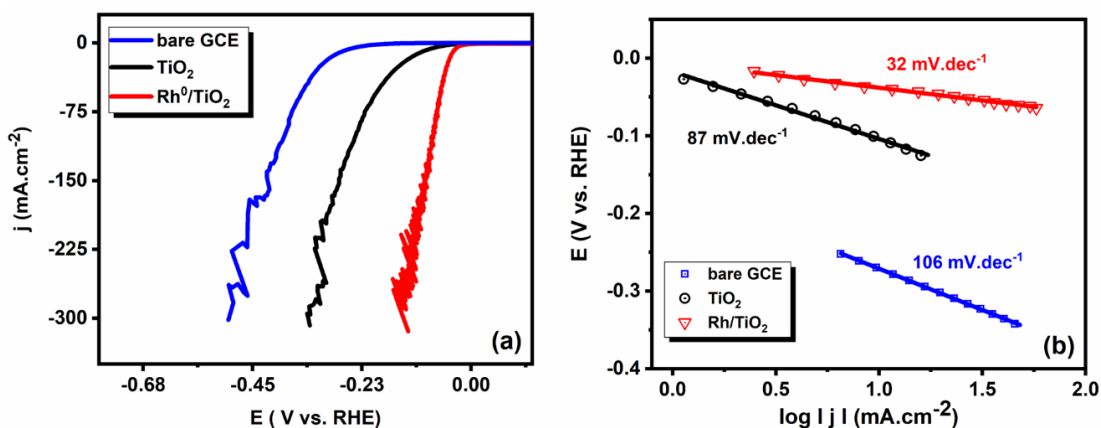
Figure 17. (a) Polarization curves of the treated electrodes (bare GCE, TiO_2 and Rh/TiO_2 catalyst on GCE) at 20 mV.s^{-1} scan rate in 0.5 M H_2SO_4 and (b) corresponding Tafel curves.

The Pt counter electrode was replaced by graphite electrodes and the LSV graph is shown below (Figure 18). There is no improvement after treatment when using graphite rod as a counter electrode and catalyst lost some of its electrochemical activity. In the continuation of the thesis, graphite electrode was used as a counter electrode in order to prevent platinum contamination and to evaluate the HER performance of group 9B metals in the acidic environment. Characterization and detailed investigation of Rh/TiO_2 and Rh/TiO_2-2000 were also presented in Appendix B.
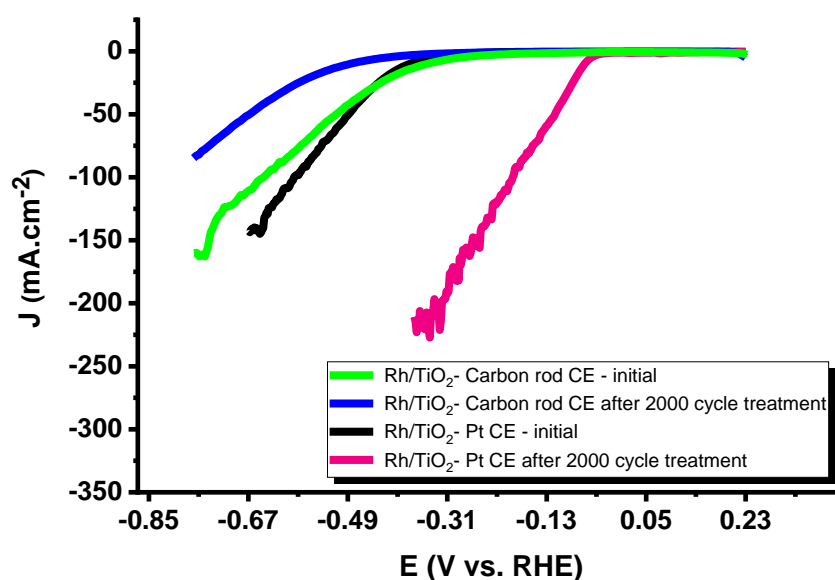
Figure 18. The electrocatalytic activities of untreated and treated Rh/TiO_2 with graphite and Pt counter electrode. (CE: counter electrode)

3.1.1.2. Effect of metal oxides on the performance of Rh catalysts

At the beginning of the experiment, different supporting materials combined with Rh metal with 0.5 % loading percent to find the best Rh containing catalyst towards hydrogen evolution reaction. According to the LSV curves in Figure 19, ceria was found to the best supporting material among titania, zirconia, alumina, hafnia and silica. Rh/CeO_2 exhibits the best activity, Rh/TiO_2 and Rh/ZrO_2 show moderate activity and Rh/Al_2O_3, Rh/HfO_2 and Rh/SiO_2 show no activity when considering the onset potentials, overpotentials, and Tafel slopes (Table C1). In fact, the switch between Ce^{3+} and Ce^{4+} oxidation states in CeO_2 provides generation of strong electronic interactions with other species, which enables CeO_2 to enhance the performance of electrocatalysts by improving charge transfer efficiency during water splitting. After this finding, Rh/CeO_2 was selected for detailed examination.
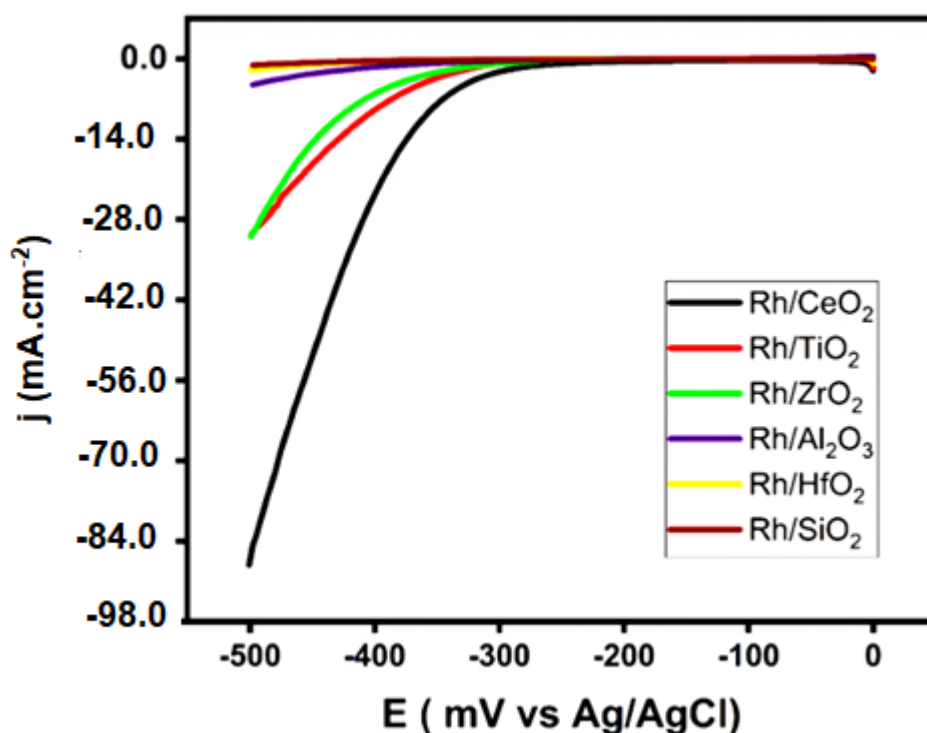
Figure 19. Polarization curves of the Rh containing catalysts in 0.5 M H_2SO_4

3.1.1.3. Effect of loading on the performance of Rh/CeO$_2$ catalysts

In order to observe the effect of the metal amount on the performance of the catalyst, four different catalysts were prepared by keeping the amount of support material constant and changing the amount of Rh metal. After the preparation of 2.0%, 3.0%, 4.0% and 5.0% Rh/CeO$_2$ catalysts, all of them were tested for the HER in 0.5 M H$_2$SO$_4$ by keeping the amount of Rh on the electrode surface constant. According to polarization curves belonging to these catalysts in Figure 20, it was found that changing the loading amount between 2.0% and 5.0% did not cause a large difference on the activity of the catalysts. However, 4.0% Rh/CeO$_2$ exhibits slightly better performance than the other catalysts with different loadings when considering its onset potential, Tafel slope and overpotential values together.
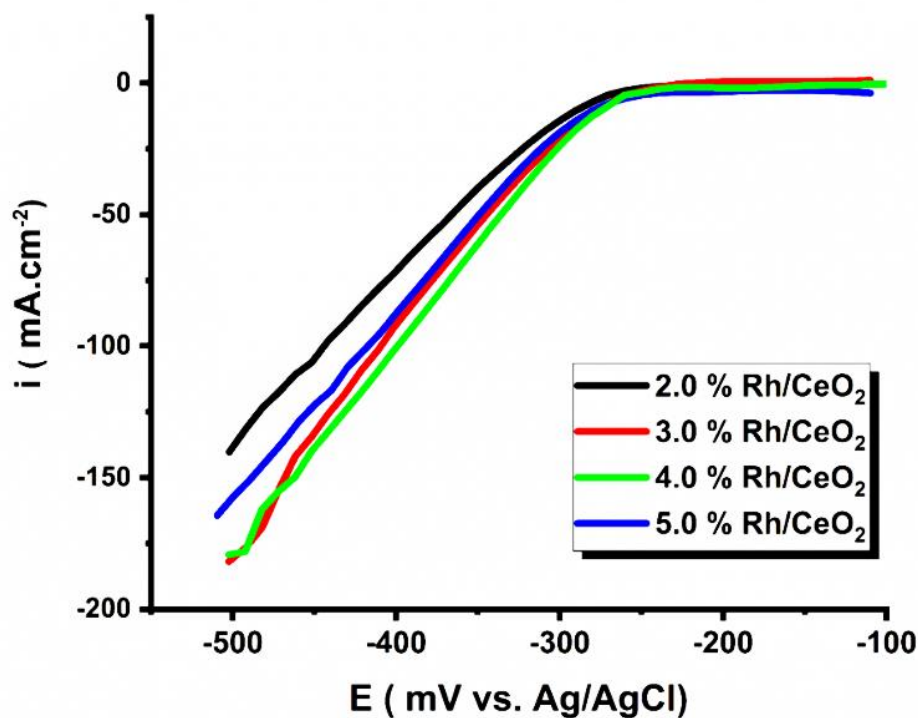
Figure 20. Polarization curves of Rh/CeO$_2$ catalysts with different loading amounts.

3.1.1.4. Effect of loading density on the performance of Rh/CeO₂ catalysts

The effect of loading density was also investigated. Electrochemical studies were carried out by changing the loading density on the electrode and the results were given in the Table 5. Accordingly, the best performance was obtained when the loading density was equal to 85.7 $\mu g.cm^{-2}$ for 4% Rh/CeO₂. When the 5% Rh/CeO₂ with 257.1 $\mu g.cm^{-2}$ loading density was used as a working electrode, similar results were obtained however the electrode could not maintain its activity even in the second measurement.

Table 5. Activity results of Rh/CeO₂ catalysts at different loadings and loading densities.

LOADINGS	Loading Densıty ($\mu g/cm^2$)	Onset Potential (mV vs. Ag/AgCl)	Overpotential at 10 mA/cm² (mV vs. Ag/AgCl))	Tafel Slope (mV.dec⁻¹)
2%	85.7	265	275	46
	171.4	278	296	54
	257.1	257	274	48
	342.8	267	293	50
3%	85.7	260	269	46
	171.4	261	300	45
	257.1	250	280	52
	342.8	285	302	52
4%	**85.7**	**256**	**263**	**37**
	171.4	246	265	44
	257.1	262	327	48
	342.8	218	309	54
5%	85.7	230	270	47
	171.4	215	263	38
Not stable	257.1	225	255	34
	342.8	240	275	45

Findings

➢ Ceria is better supporting material than TiO_2, ZrO_2, HfO_2, Al_2O_3, and SiO_2 towards HER in acidic media. Activity order is $CeO_2 > TiO_2 > ZrO_2 > Al_2O_3 > HfO_2 > SiO_2$.

➢ % Loading (2% -5%) does not affect the catalytic activity significantly if loading density is kept constant.

➢ When loading density increases, pouring of the catalyst increases and the stability decreases.

➢ Considering the onset potential, overpotential at 10 $mA.cm^{-2}$ and Tafel slope, 4% loading and 85.7 $\mu g.cm^{-2}$ was chosen.

3.1.1.5. Characterization of Rh/CeO$_2$

Ceria supported Rh nanoparticles, Rh/CeO$_2$, was prepared by the reduction of Rh^{3+} ions on CeO$_2$ surface at room temperature in aq. NaBH$_4$ solution and characterized by TEM, ICP-OES, XPS and XRD. According to TEM images (Figure 21 (a)-(b)), the particle sizes of Rh on the surface of CeO$_2$ was determined as in the range 1.2–4.2 nm. Mean particle size of highly dispersed Rh NPs was found as 2.60 ± 0.54 nm (Figure 21 (d)). The existence of Rh, Ce and O in Rh/CeO$_2$ catalyst were confirmed via TEM-EDX analysis (Figure 21 (c)).
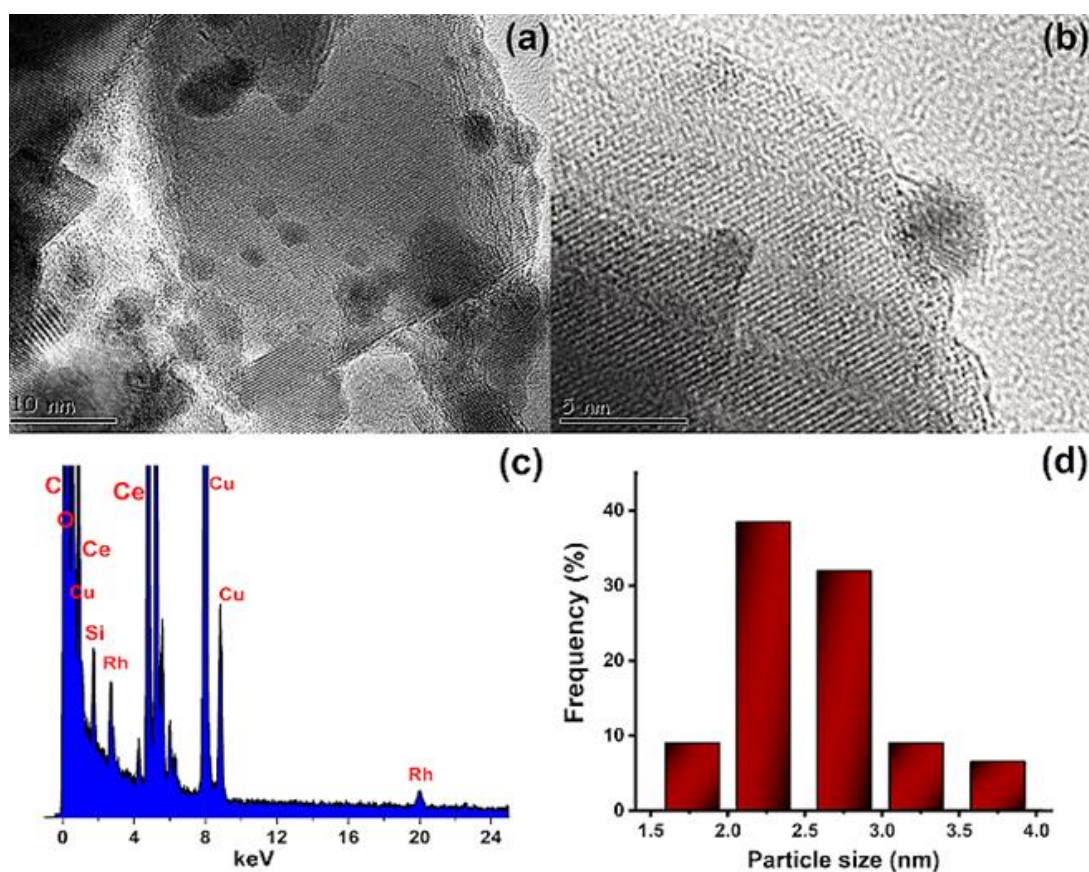
Figure 21. a, b) TEM images and, c) the corresponding EDX spectrum of Rh/CeO$_2$ and d) the particle size distribution histogram.

The diffraction peaks observed at 2 theta (degree) of 28.66, 33.13, 47.50, 56.42, 59.25, 69.45, 76.80 and 79.21 correspond to (111), (200), (220), (311), (222), (400), (331), and (420) planes, respectively, (JCPDS file No: 81–0792)[194]. The comparison of XRD patterns of Rh/CeO_2 (Figure 22 (a)) and CeO_2 catalyst (Figure 33b) shows that there is no change in the framework lattice of CeO_2 after the rhodium loading. However, due to the low rhodium loading there is no peak indicating the Rh NPs in Figure 22 (a). Note that the strong and sharp diffraction peaks are attributed to the high crystallinity of CeO_2.
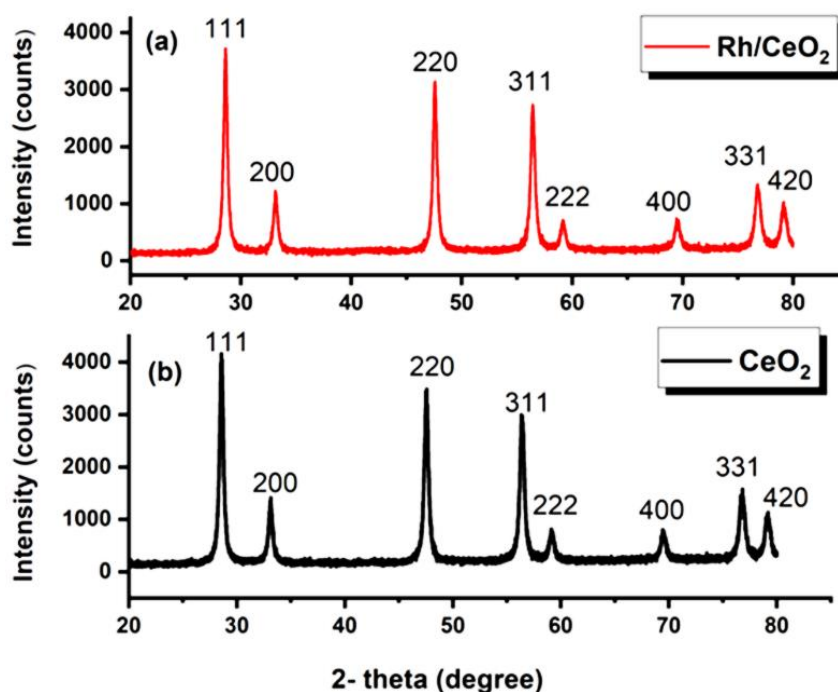
Figure 22. Powder XRD pattern of a) Rh/CeO_2 (4.0% wt. Rh) and b) bare CeO_2. (JCPDS file No: 81–0792).

The XPS spectra of full scanning survey between 0 and 1200 eV given in Figure 23 (a) also proves the existence of Rh nanoparticles on the surface of ceria. For the peak differentiating and imitating (PDI) analysis, C1s peak at 284.4 eV [195] used as a reference. The binding energy of Rh 3d was calibrated by subtracting the difference of theoretical and experimental (285.65 eV) values of C1s peak. XPS spectrum of Rh 3d bands of Rh/CeO$_2$ was shown in Figure 23 (a). Rh 3d$_{5/2}$ peak at 307.1 eV and Rh 3d$_{3/2}$ peak at 309.2 eV were attributed to metallic rhodium[196,197] The other peaks at 311.7 eV and 313.6 eV show the oxides species of rhodium. [198]
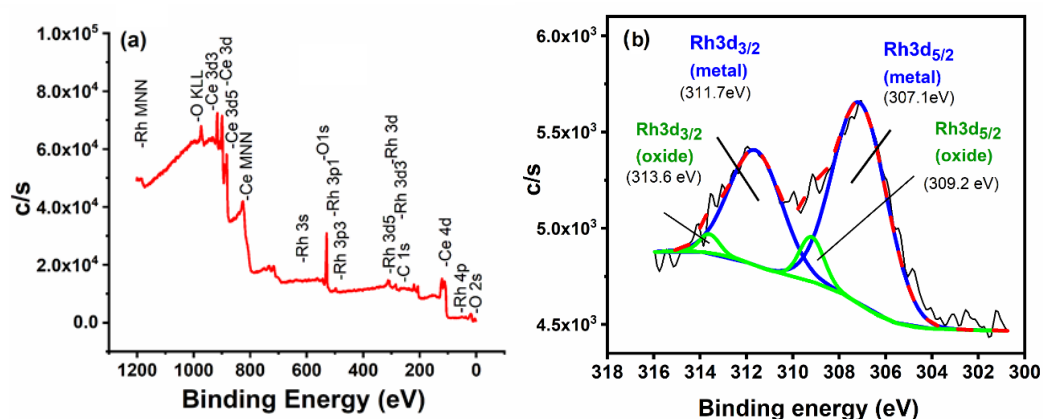
Figure 23. (a) The survey-scan XPS spectrum of Rh/CeO$_2$, (b) XPS spectrum of Rh 3d bands.

3.1.1.6. Electrochemical studies of Rh/CeO$_2$

Prior to the investigation on the electrocatalytic activity of Rh/CeO$_2$, to understand whether bare glassy carbon electrode (GCE) or CeO$_2$ without rhodium show any electrocatalytic activity under the same experimental conditions, control experiments were also carried out. For this purpose, 2.0 µL Rh free aliquot was dropped onto a cleaned GCE and this electrode was used to check catalytic activity of CeO$_2$. Polarization curve obtained by using Rh/CeO$_2$ modified GCE is given in Figure 24 together with polarization curves recorded by using bare GCE, CeO$_2$ modified GCE and Pt/C modified GCE. As seen from the Figure 24 both ceria modified GCE and bare GCE show no electrochemical activity for HER in 0.5 M H$_2$SO$_4$ solution. However, Rh/CeO$_2$, exhibited reasonably high electrocatalytic HER activity with low Tafel slope of 34 mV.dec^{-1} in the same electrolytic solution (Figure 24).
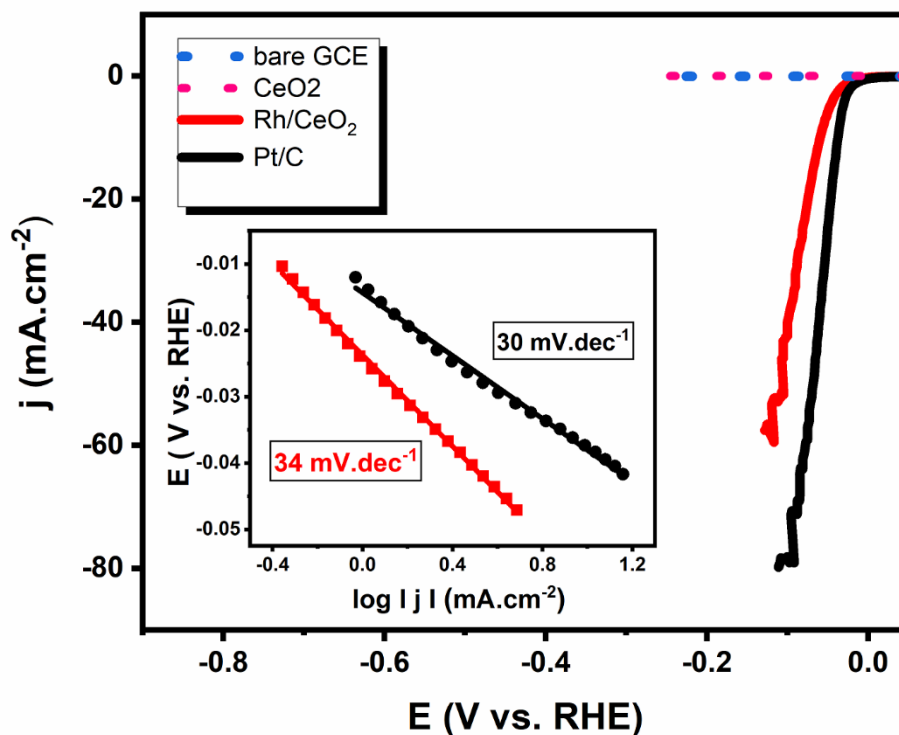
Figure 24. Polarization curves obtained in 0.5 M H_2SO_4 (voltage scan rate=5 mV.s^{-1}) for the unmodified GCE, CeO_2 modified GCE, Rh/CeO_2 and Pt/C modified GCEs. (Inset: Tafel plots for Rh/CeO_2 and Pt/C obtained from polarization curves for HER.)

The onset potential (η_0) of Rh/CeO_2 catalyst (-25 mV vs. RHE) was found to be not only lower than most of the reported values but also very close to η_0 of Pt/C electrode (-19 mV). It is also noteworthy that the overpotential value (η) of the Rh/CeO_2-GCE was only η = 42 mV vs. RHE (at j = 10 mA.cm^{-2}) which is also lower than most of the other reported catalysts (Table 6) such as Rh/Si[199], Rh_2S_3[200], Pt_2Si[201], $Rh_3Pb_2S_3$/C[202], Rh-Ag/SiNW[203], and Rh[204].

Table 6. Summary of recently reported electrocatalysts using for HER in 0.5 M H_2SO_4 reaction medium. Data were recorded [a] with and [b] without IR compensation. (Note that for the IR compensation, solution resistance (Rs) was calculated from EIS and the effect of Rs were corrected by using positive feedback IR compensation.)

	Loading density ($\mu g.cm^{-2}$)	Size (nm)	η_0 vs. RHE (mV)	η (mV)	Tafel Slope ($mV.dec^{-1}$)	j_0 ($mA.cm^{-2}$)	stability	Ref.
Rh Nanowires[a]	--	2	-140	>-100	23	--	1 hour	205
Rh/Si [b]	193	1.6	--	83.3@-10	24	0.00858	130 hours	199
Rh-Au-SiNW-2[a]	255	20	--	62@-10	24	0.0479	2 hours	206
Rh Hollow Nanoparticles[a]	2.26	3.89±1.24	~-20	28.1@-10	24	--	1 hour	207
Rh_2P/NC[b]	700	100	0	9@-10	26	2.5	1000 cycles	208
Rh_2P/C[a]	3.79	5-20	--	5.4@-5	--	--	2000 s	209
in situ- Rh/C[a]	--	--	~25	30@-10	28.4	--	1000 cycles	34
10% Pt/C[a]	85.7	--	-19	37@-10	30	0.424	1000 cycles	in this work
Rh_2P[b]	133	--	--	14@-10	31.7	--	1000 cycles	210
Rh@CeO$_2$[a]	**85.7**	**2.61 ± 0.5**	**-25**	**42@-10**	**34**	**0.527**	**10000 cycles (55.5 hours)**	**This Work**
Rh@CeO$_2$[a] (after 10000)	**85.7**	**2.61 ± 0.5**	**-25**	**48@-10**	**38**	**0.487**		**This Work**
Rh_2S_3[b]	153	--	--	122@-10	44	--	10000 cycles	200
$Rh_3Pb_2S_2/C$[a]	28	--	**--**	87.3@-10	45.6	--	10000 cycles	202
Rh–Ag/SiNW-2[b]	140	--	--	120@-10	51	0.0871	12 hours	206
Rh Nanoislands[b]	--	--	--	--	55	--	-	211
Rh[a]	169	--	-19	190@-10	92	0.190	2000 cycles	204

Tafel slopes were found by fitting the linear regions of Tafel plots (inset of Figure 24) derived from LSV curves and Tafel slopes values of 34 mV.dec^{-1} and 30 mV.dec^{-1} were obtained for Rh/CeO$_2$ and Pt/C modified GCEs, respectively. The value obtained for Rh/CeO$_2$ (34 mV.dec^{-1}) indicates that the rate-limiting step of electrocatalytic HER is the desorption of H$_2$ from the electrode surface and the Volmer−Tafel mechanism[212] could be used for hydrogen evolution. It was found that Rh/CeO$_2$ has 0.527 mA.cm^{-2} of j$_0$ value which is comparable that of Pt/C modified GCE (j$_0$=0.424 mA.cm^{-2}). These kinetic parameters obtained for Rh/CeO$_2$ are tabulated in Table 6, together with similar electrocatalysts reported in the literature for comparison sake. A close inspection of Table 6 reveals that the Tafel slope (34 mV.dec^{-1}), exchange current density (0.527 mA.cm^{-2}) and onset value of Rh/CeO$_2$ (-25 mV vs. RHE) are comparable or even better than the other reported catalysts given in the Table 6.
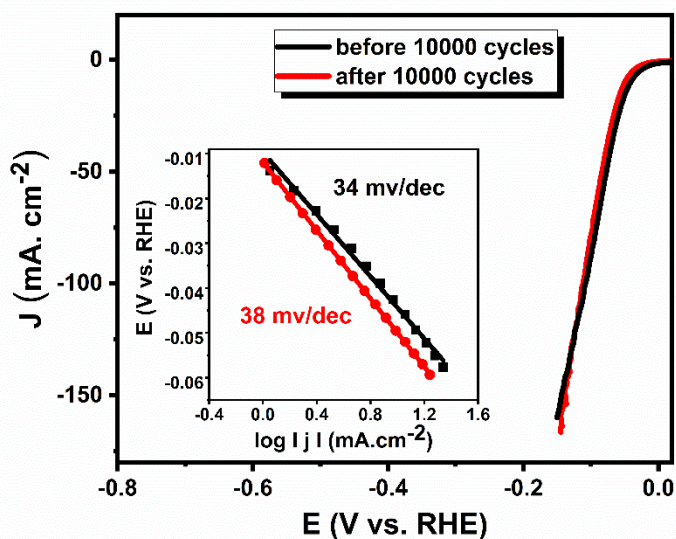
Figure 25. The polarization curves of Rh/CeO$_2$ in 0.5 M H$_2$SO$_4$ before and after 10000 cycles which correspond to 55.5 h.

To check the long term stability the Rh/CeO$_2$ was subjected to repetitive potential cycling in the range of -0.50 to 0.50 V vs. Ag/AgCl at a 50 mV/s scan rate in 0.5 M H$_2$SO$_4$ aqueous solution. As can be seen from Figure 25, there was no change in the onset potential before and after 10 000 scans (-25.0 mV). On the other hand, a slight increase in the Tafel slope (from 34 to 38 mV.dec^{-1})was noted. These results suggest that Rh/CeO$_2$ is highly durable electrocatalyst. Considering all these results one can conclude that Rh/CeO$_2$-GCE possess reasonably higher electrocatalytic activity and

superior long term stability in HER as compared to the other reported catalysts. For example, $Rh_2P@NC$[208] was found to retain its activity after 1000 CV cycles in 0.5 M H_2SO_4 solution, on the other hand, Rh_2P[209] showed a slight increase in the overpotential to afford a current density of 10 mA.cm^{-2} after 1000 CVs. Such a small negative shift was also reported by Chen. et. al. for Ru/ GLC[213] after 1000 cycles. Pu. et. al. and Nguyen. et al. reported small cathodic shifts in the overpotential values after 3000 for $RuP_2@NPC$[214] and after 2000 CV cycles for Ni_1Rh_3 nanosponge[204], respectively.

In all these examples, less than 5000 CV cycles were used to examine the stability of modified electrodes and there are only few examples in which 10 000 CV cycles were applied to investigate the long term stability. Kim et.al.[204] applied 10 000 cycle scans between −0.3 V and 0.1 V (vs. RHE) with a scan rate of 50 mV s^{-1} and reported a very small increase in the overpotential of $Rh_3Pb_2S_2$ after the stability test. Although this electrocatalyst exhibits long term stability, the kinetic parameters such as Tafel slope and overpotential at 10 mA.cm^{-2} are higher than most of the catalysts listed in Table 6. Furthermore, preparation of $Rh_3Pb_2S_2$ nanocages requires toxic organic solvents.

In the case of Rh/CeO$_2$, only 6 mV increase in the η at 10 mA.cm^{-2} and 6 mV.dec^{-1} increase in the Tafel slope after 10 000 cycle were observed. Moreover, preparation of our catalyst is environmental friendly and includes no toxic material. In fact, Rh/CeO$_2$ was even attached on GCE without using any binders such as nafion which cause lower catalytic activity by blocking active sites and pores.[215]
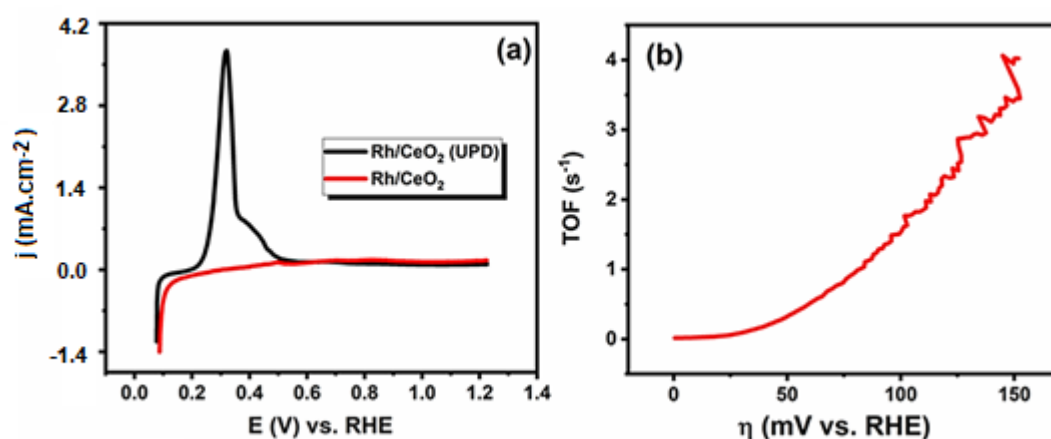
Figure 26. a) Copper UPD of Rh/CeO$_2$ in 1 M H$_2$SO$_4$ solution and b) corresponding TOF vs overpotential graphs.

To get more information about the electrocatalytic activity of Rh/CeO$_2$, TOF values were calculated by using the estimated number of active sites which were obtained via underpotential deposition (UPD) of copper onto Rh/CeO$_2$ in acidic solution (Figure 26 (a)). Figure 26 (b) shows that the calculated TOF values for Rh/CeO$_2$ in 1 M H$_2$SO$_4$ at 50 and 100 mV (vs. RHE) are 0.35 and 1.56 s^{-1}, respectively.
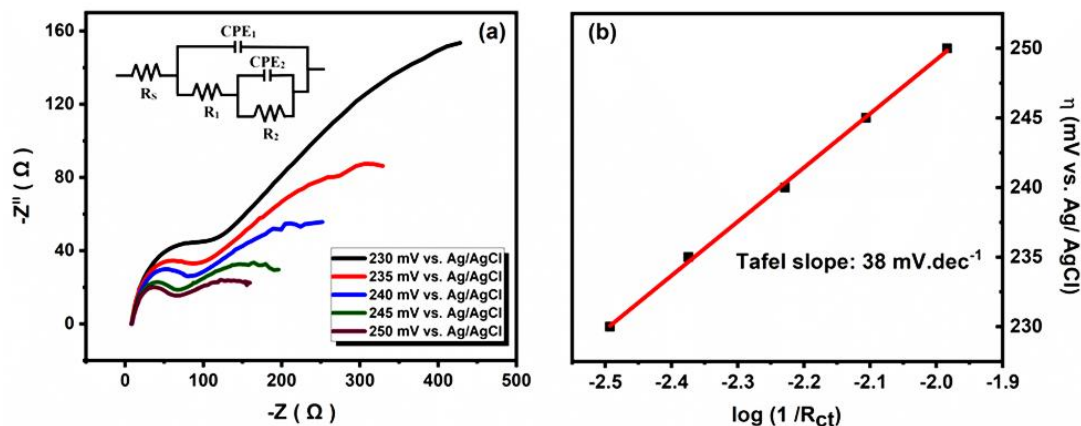
Figure 27. a) The Nyquist plots for Rh/CeO$_2$ at different overpotentials b) Tafel plot of Rh/CeO$_2$-GCE, obtained using RCT from the EIS.

The electrocatalytic HER performance of Rh/CeO$_2$ was also investigated by conducting electrochemical impedance spectroscopy (EIS) measurements at various overpotentials in 0.5 M H$_2$SO$_4$ solution. The resulting Nyquist plots are shown in Figure 27 (a) and inset of Figure 27 (a) shows equivalent circuit model used to fit the experimental data. Nyquist plots given in the Figure 27 (a) consist of two semicircles at low and high frequency regions. While the one at low frequency region can be attributed to charge transfer process, the latter might be due to the mass transfer processes of the adsorbed species[202] on GCEs. According to Figure 27, R$_{CT}$ values decrease with increasing overpotentials which indicates that HER kinetic increases at high over potential values. Double layer capacitance (C$_{DL}$) was found as 0.296 mF at the onset potential by using EIS which is consistent with the value obtained from CV experiments at different scan rates (C$_{DL}$=0.270 mF) (Figure 27). Note that C$_{DL}$ value of Rh/CeO$_2$ is comparable to that of commercial Pt/C-GCE (C$_{DL}$= 0.247 mF, Appendix). The electrochemically active surface area (ECSA) of Rh/CeO$_2$ was calculated from the obtained C$_{DL}$ (0.270 mF) (Figure 28) and was found as 6.75 cm^2. It should be noted that a very close Tafel slope value (38 mV.dec^{-1}) to the one obtained from LSV (34 mV.dec^{-1}) was obtained from EIS measurements (Figure 27 (b)).
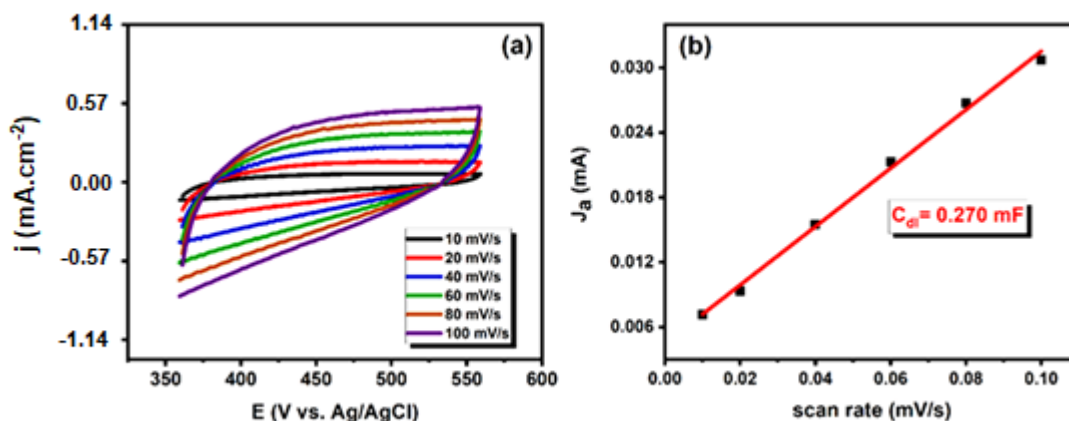
Figure 28. (a) Representative multi CV experiment at different scan rates for C_{DL} determination in 0.5 M H_2SO_4; (b) capacitive current at 0.45 V (vs Ag/AgCl) versus scan rates for Rh/CeO$_2$. ECSA = 6.75 cm^2

The volume of the evolved H_2 gas from the water electrolysis was measured in a Hoffman electrolysis cell and followed as a function of time. A constant potential coulometry was applied at 25°C in 0.5 M H_2SO_4 and Faradaic efficiency was obtained by comparing the theoretical and experimental results. As it is seen in the volume of generated H_2 vs. time plots shown in Figure 29, the experimental volume of the gas is so close to the theoretical volume and the Faradaic efficiency of Rh/CeO$_2$ catalyst was calculated as 89.8%.
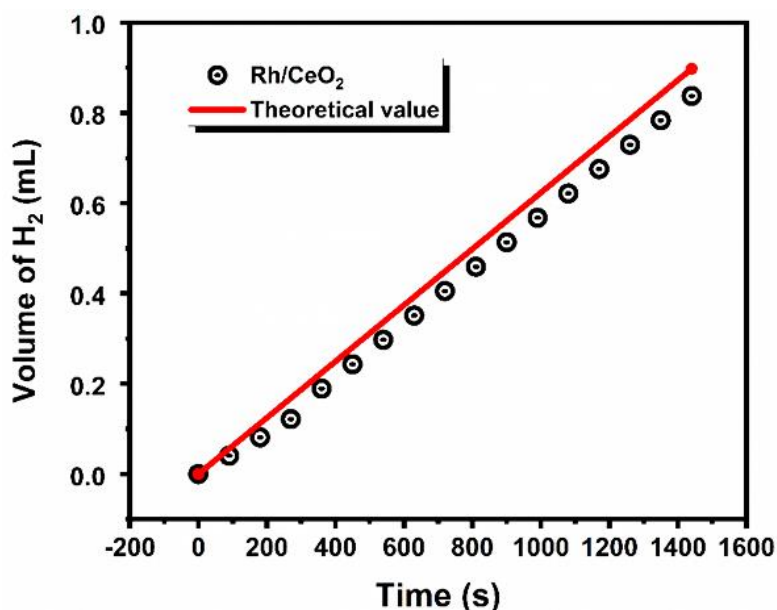
Figure 29. Generated H_2 volume versus time graph for Rh/CeO$_2$ during the electrolysis of water in 0.5 M H_2SO_4. Theoretical value was obtained from ideal gas equation and Faraday's relation.

3.1.1.7. Outlook of the synthesis, characterization and electrochemical studies of

Rh/CeO$_2$

Rhodium NPs were successfully formed on the surface of CeO$_2$ by simple impregnation technique and characterized by TEM, TEM-EDX, XRD and ICP-OES. Rh/CeO$_2$ was attached on GCE without using any binder such as nafion solution and used as an electrocatalyst for HER in acidic environment. Rh/CeO$_2$ provides a low Tafel slope value (34 mV.dec^{-1}) and high exchange current density (0.527 mA.cm^{-2}) with a low overpotential of 42 mV at j = 10 mA.cm^{-2}. Rh/CeO$_2$ with a very low mass loading 85 μg.cm^{-2} provides also exceptional electrocatalytic activity and durability even after 10 000 cycles.

3.1.2.   Electrocatalytic activity of Ir NPs supported on MO$_2$

3.1.2.1. Effect of metal oxides on the performance of Ir catalysts

Before starting the detailed investigation, different supporting materials combined with Ir metal to find the best Ir containing catalyst towards HER. According to the LSV curves in Figure 30, ceria was found to best supporting material among titania, zirconia and ceria. Although Ir/CeO$_2$, Ir/ZrO$_2$ and Ir/TiO$_2$ were prepared using the same amount of supporting materials by following the same procedure, it was observed that iridium adhered better to the ceria surface based on the ICP results. Ir content of the prepared catalysts was determined as 2.44%, 1.13% and 0.63% wt. Ir for Ir/CeO$_2$, Ir/ZrO$_2$ and Ir/TiO$_2$, respectively. The decrease in ICP results from ceria to titania from 2.44 to 0.63% reveals the importance of metal oxides for iridium. Ceria was used as a supporting material in detailed studies for iridium. Although the ratios during synthesis of Ir/CeO$_2$ were the same as Rh/CeO$_2$, the iridium content of the iridium catalyst prepared as 4% was found to be 2.44%. This may be due to the fact that the iridium salt used is very humid, which affects the weighing. Although Ir/CeO$_2$ was 2.44%, loading density was kept the same as in Rh/CeO$_2$ studies for comparison purposes.
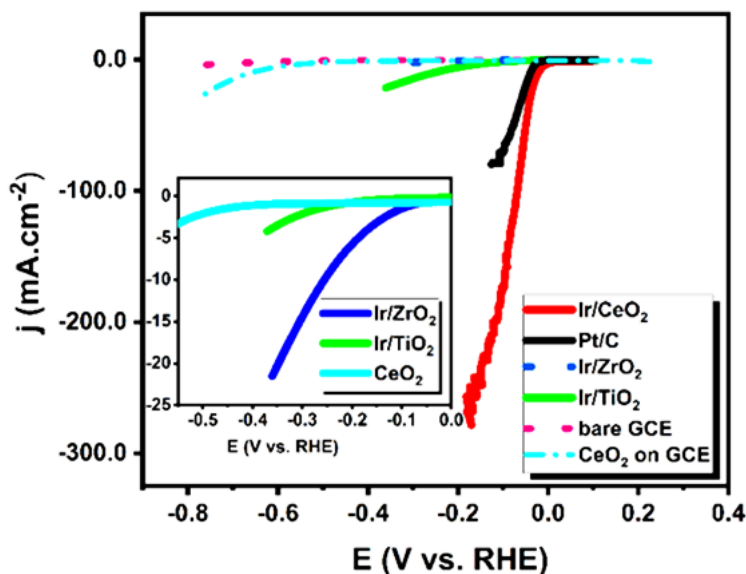
Figure 30. LSV curves for Ir/CeO_2, Ir/ZrO_2, Ir/TiO_2 and CeO_2 on GCE, Pt/C and bare GCE in 0.5 M H_2SO_4 (inset; the curves zoomed on onset potential of Ir/ZrO_2, Ir/TiO_2, CeO_2 on GCE)

3.1.2.2. Effect of loading on the performance of Ir/CeO_2 catalysts

To investigate the effect of loading on catalyst performance, four different Ir/CeO_2 catalysts with 2, 3, 4, and 5% mass percent iridium were prepared. When the prepared catalysts were characterized by ICP-OES, their Ir percentages were found as 1.21, 1.97, 2.44 and 3.55, respectively. By keeping the amount of Ir on the electrode surface constant, LSV measurements were carried out using catalysts containing less than or even more than 2.44% Ir by mass (Figure 31). The results indicate that 2.44 % is the optimum amount (Table 7). As it is expected, the catalytic performance of Ir/CeO_2 shows variations (i.e Tafel slope, onset potential etc.) with increasing Ir content. However, there is no significant enhancement in the electrocatalytic activity of Ir/CeO_2 when the iridium amount increased more than the optimum amount. For this reason, the Ir/CeO_2 catalyst, which is prepared at 4 % but actually has an iridium of 2.44% by mass, has been examined in detail in the thesis.
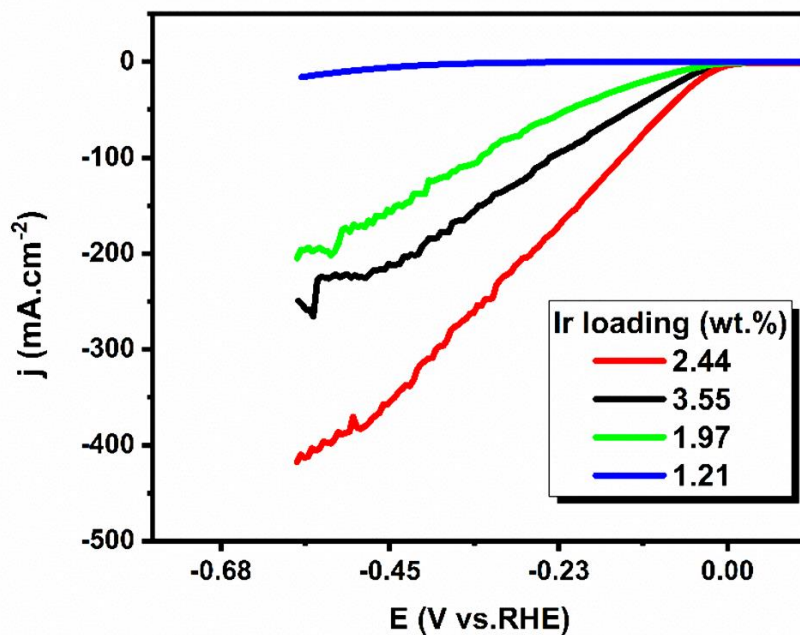
Figure 31. LSV curves for the Ir/CeO$_2$ catalysts with different Ir loadings

Table 7. Overpotential, Tafel slope and onset potential values of Ir/CeO$_2$ catalysts with different Ir loading

Ir loading (wt.%)	Overpotential @-10 mAcm^{-2} (mV vs. RHE)	Tafel Slope (mV.dec^{-1})	Onset potential (mV vs. RHE)
2.44	-23.0	38.7	-13.0
3.55	-38.0	48.0	-23.0
1.97	-59.0	57.0	-22.0
1.21	-434.0	212.0	-187.0

3.1.2.3. Characterization of Ir/CeO$_2$

The size and dispersion of impregnated Ir nanoparticles on the surface of ceria were investigated by TEM analysis. The TEM images given in Figure 32 (a) and (b) prove the high dispersion of Ir NPs with the particle size range from 1.6 to 3.4 nm (Figure 32 (c)) on CeO$_2$. The mean particle size of Ir was found as 2.25 ± 0.41 nm. The presence of Ir, Ce and O in the catalyst content were confirmed by TEM-EDX (Figure 32 (d)). The TEM analysis of Ir/TiO$_2$ and Ir/ZrO$_2$ were given in appendix Figure C.4 and Figure C.5 and the mean particle size of Ir was found as 2.83 ± 0.44 nm and 3.15 ± 0.77 nm, respectively.
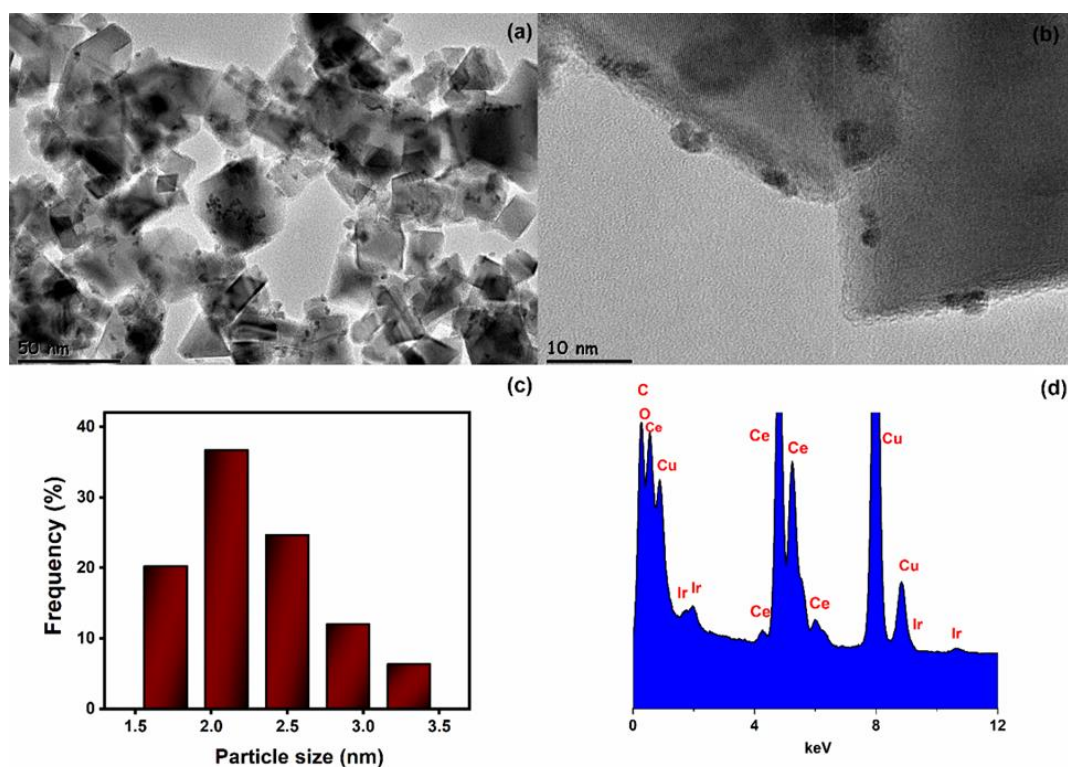
Figure 32. a, b) TEM images, c) the histogram and d) the corresponding TEM-EDX spectrum of Ir/CeO$_2$.

According to the XRD analysis given in Figure 33 (a) and (b) , the diffraction peaks of ceria observed at 2 theta (degree) of 28.66 ((111) plane), 33.13 ((200) plane), 47.58 ((220) plane), 56.40 ((311) plane), 59.17 ((222) plane), 69.59 ((400) plane), 76.82 , ((331) plane) and 79.22 ((420) plane) (JCPDS file No: 81–0792).[182] The strong and sharp diffraction peaks in the XRD patterns of Ir/CeO$_2$ (Figure 33 (a)) and CeO$_2$ (Figure 33 (b)) reveals that the good crystallinity of the CeO$_2$ nanoparticles were preserved after impregnation of Ir nanoparticles. On the other hand, due to low Ir loading no peaks indicating the presence of Ir NPs were observed in Figure 33 (a).
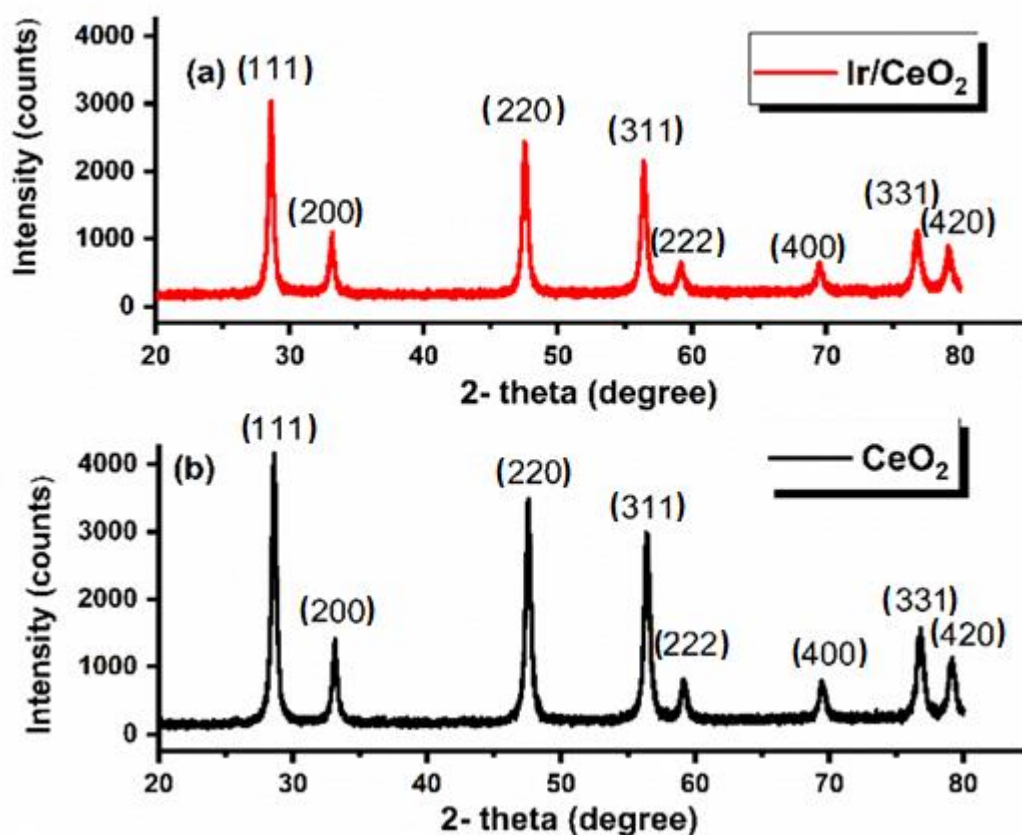
Figure 33. Diffraction pattern of a) Ir/CeO$_2$ (2.44% wt. Ir) and b) CeO$_2$.

3.1.2.4. Electrochemical studies of Ir/CeO$_2$

The electrocatalytic performance of the catalysts was evaluated by the onset and Tafel slope values. The prepared iridium catalysts were tested in HER. Before the test reaction, the activity of bare GCE and the supporting materials (CeO$_2$, TiO$_2$, ZrO$_2$) without iridium were checked and no electrocatalytic activity of these samples were observed. To study the activity of the catalysts for HER, Ir/CeO$_2$, Ir/ZrO$_2$ and Ir/TiO$_2$ nanoparticles and Pt/C were loaded onto polished GCE with 85.7 µg/cm^2 metal loading density by drop casting method.
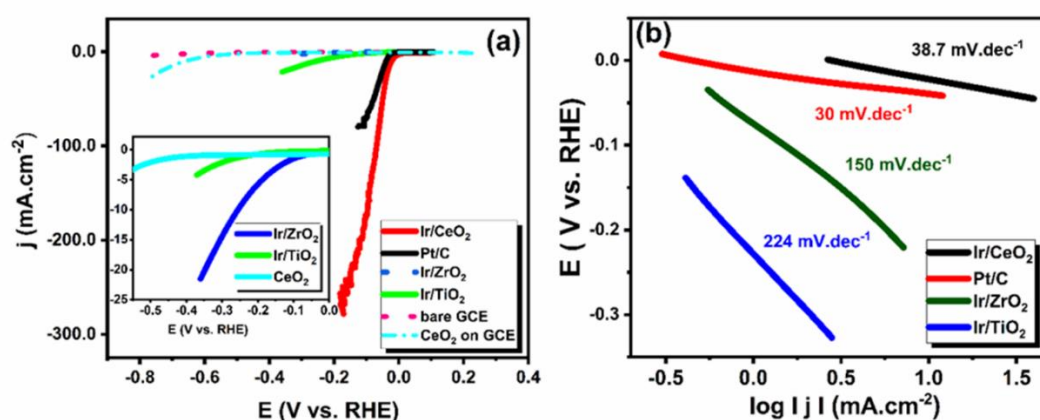
Figure 34. (a) LSV curves for Ir/CeO$_2$, Ir/ZrO$_2$, Ir/TiO$_2$ and CeO$_2$ on GCE, Pt/C and bare GCE in 0.5 M H$_2$SO$_4$ (inset; the curves zoomed on onset potential of Ir/ZrO$_2$, Ir/TiO$_2$, CeO$_2$ on GCE), (b) corresponding Tafel slopes of Ir/CeO$_2$, Ir/ZrO$_2$, Ir/TiO$_2$ and Pt/C.

The polarization curves belong to the catalysts, ceria and bare GCE are given in Figure 34 (a) with the inset Figure which was zoomed on the onset potential of Ir/ZrO$_2$ and Ir/TiO$_2$ and CeO$_2$ without Ir. Although the loading density of the catalyst on the GCE surface was kept constant to maintain the same amount of metal, the onset potentials show variation depending on the metal oxide. The onset potential of Ir/CeO$_2$ (-13 mV) was found pretty much lower than that of Ir/ZrO$_2$ (-55 mV) and Ir/TiO$_2$ (-130 mV). Moreover, the Tafel slope of Ir/ZrO$_2$ (-150 mV.dec^{-1}) and Ir/TiO$_2$ (224 mV.dec^{-1}) were found quite higher than that of Ir/CeO$_2$ (38.7 mV.dec^{-1}) (Figure 34 (b)).

The higher electrocatalytic activity of Ir/CeO_2 can be attributed to reducible nature of ceria which promotes both the activity and metal-support interaction which is a well-known phenomenon in the literature.[108] The electrocatalytic activity of Ir/CeO_2 was also compared with the benchmark Pt/C catalyst in our system. The Tafel slope and onset potential values for Pt/C catalyst were determined as 30 $mV.dec^{-1}$ and -19 mV, respectively, which are comparable with the values of Ir/CeO_2. Exchange current density 'j_0' describes the intrinsic catalytic activity of the electrode material under equilibrium conditions and can be evaluated by assuming η is zero. The j_0 values of Ir/CeO_2, Pt/C, Ir/ZrO_2 and Ir/TiO_2 modified GCEs are found as 2.69, 0.39, 0.32, 0.096 $mA.cm^{-2}$, respectively. Among them Ir/CeO_2 has the highest exchange current density indicating higher reaction rate at the equilibrium potential.[245]

On the other hand, it was found that Ir/CeO_2, Pt/C, Ir/ZrO_2 and Ir/TiO_2 modified GCEs produce cathodic current density (j) of -10 mA cm^{-2} at η = 23 mV, η = 37 mV, η = 255 mV and η < 500 mV, respectively. Ir/CeO_2 has very low η value which is even lower than the η value of Pt/C. These results show that Ir/CeO_2 shows superior electrocatalytic activity for HER as compared to Pt/C, Ir/ZrO_2, Ir/TiO_2 and most of the other reported iridium based catalysts given between entry 12 and 52 in Table 8. Although 7.16 wt. % IrHNC (entry 1), 11 wt. % IrP_2@NC(entry 2), 23.8 wt. % Ir@CON (entry 3), 5.9 wt. % $Ir/g-C_3N_4/NG$ (entry 4), 17% Ir/SiNW (entry 5) exhibit higher electrocatalytic activity than 2.44 wt. % Ir/CeO_2 in terms of over potential value, Ir/CeO_2 has more advantages over those reported catalysts which include high temperature (800-900ºC) annealing procedures and harsh catalyst preparation conditions containing environmentally unfriendly chemical reagents. In fact, Ir/CeO_2 can be reproducibly prepared following a facile method which consists of just a simple impregnation and reduction procedure. Moreover, herein; electrocatalytic measurements were performed without nafion which is extensively used polymer to attach the catalyst on GCE. Ir/CeO_2 was attached on GCE by simple drop casting method. This is the first binder free study including metal oxide supported Ir NPs used for HER. Considering the high stability, facile preparation method and low iridium loading (2.44wt. %), Ir/CeO_2 is a promising electrocatalyst among the reported ones given in Table 8.

Table 8. Literature survey of some reported HER electrocatalysts in 0.5 M H_2SO_4 reaction medium.

Entry	Catalyst	η (mV)	Tafel Slope (mV.dec^{-1})	η_0 vs. RHE (mV)	j_0 (mA.cm^{-2})	Loading density (μg.cm^{-2})	Size (nm)	Stability	Ref.
1	IrHNC	-4.5@-10	10	-	-	18	2.1	10000 cycles	242
2	IrP$_2$@NC	-8@-10	28	-	-	700	-	1000 cycles	216
3	Ir@CON	-13.6@-10	27	-	1.15	60	-	10000 cycles	217
4	Ir/g-C$_3$N$_4$/NG	-22@-10	22	-	-	6.7	-	2000 cycles	218
5	Ir/SiNW	-22@-10	20	-	0.946	~339	2.17	13.9 hours	248
6	**Ir/CeO$_2$**	**-23@-10**	**38.7**	**-13**	**2.69**	**85**	**2.25 ± 0.41**	**20000 cycles (111 hour during CV)**	**This work**
7	IrCo NPs	-24@-10	27.1	-	-	285	-	5.55 hours	219
8	IrCo@NC-500	-24@-10	23	-	-	285	-	10000 cycles	220
9	/IrO$_2$NFs-300 (1M H$_2$SO$_4$)	-27@-50	30.1	~0	-	-	-	5 hours	221
10	Ir-SA@Fe@NCNT	-26@-10	31.8	-	-	1.14	-	5000 cycles	222
11	Ir NP/PC	-30@-10	35	-	-	57.6	0.96 ± 0.13	1000 cycles	223
12	Ir$_6$Ag$_9$ NTs/C	-34@-10	27.5	--	-	13.3	20.9 ± 0.4	1000 cycles	224

Table 8 (continued).

13	IrNi-600	35@-10	18	-	-	285	-	12 hours	225
14	3D-IrO$_2$/N@C	-35@-10	31	0	0.996	120	-	12 hours	226
15	10% Pt/C	-37@-10	30	-19	0.424	85	-	-	237
16	Ir-Au-Si NCs	-38.2@-10	24	-	-	58.89	-	16.6 hours	227
17	IrNiCu HCSA	-41@-10	21.4	-	-	10.0	-	20 hour	228
18	Ir_VG	-47@-10	43	-	-	50	-	1000 cycles	229
19	IrCo@NC-800	-52@-10	75	-	-	285	-	-	220
20	Ir/Si	-59@-10	30	-	-	24.92	-	1000 cycles	230
21	Ir$_{0.5}$W$_{0.5}$@NC	-65@-10	48	-	-	5	-	10 hours	231
22	Ir@NC	-75@-10	43	-	-	-	-	10 hours	231
23	IrO$_2$–Fe$_2$O$_3$	-78@-10	36.2	-	0.27	125	1 µm	600 cycles	232
24	Ir$_{25}$Ni$_{33}$Ta$_{42}$/Si	-99@-10	35	-	-	8.14	--	1000 cycles	230
25	Rh Nanowires	>-100	23	-140	-	--	2	1 hour	205
26	IrO$_2$-TiO$_2$	−107@-10	46.8	-	-	-	-	1000 cycles	233
27	$_2$Si$_2$O$_7$:IrO$_2$−5 cube	-130@-10	49	−76	0.06	15000	-	2000 cycles	234
28	Ir/ZrO$_2$	-255@-10	150	-55	3.167	85	3.15	-	this work
29	Ir/TiO$_2$	-500<	224	-130	0.096	85	2.83	-	this work
30	r_2Si$_2$O$_7$:IrO$_2^{-1}$	-620 @-10	70	−360	3x10^{-3}	15000	-	2000 cycles	234

The stability of Ir/CeO$_2$ was also investigated in HER. It is noteworthy that herein we used graphite rod as a counter electrode instead of Pt counter electrode by which platinum leaching is inevitable in acidic reaction medium and the true life-time measurement cannot be performed. Since the CV technique is generally used for the determination of stability we performed 20000 CV cycles on Ir/CeO$_2$ (Figure 35 (a)). Note that Ir/CeO$_2$ has -13.0 mV onset potential, -23.0 mV overpotential at 10 mA/cm^2 and 38.7 mV.dec^{-1} Tafel slope value before the stability test. The results show that there are small shifts in the onset potential (-25.0 mV), overpotential at 10mA/cm^2 (-34.0 mV) and Tafel slope (40.1 mV.dec^{-1}) values after 20000 CV cycles in acidic medium. Such shifts are commonly observed in the literature even for less number of cycles. For example, a 5.5 mV shift at a current density of 10 mAcm^{-2} was observed for Ir@CON[217] after 10 000 CV cycles in acidic conditions. It is noteworthy that the onset potential (-25.0 mV) of Ir/CeO$_2$ is still very close to Pt/C even after 20000 CV cycles. Taking all these results together, one can conclude that Ir/CeO$_2$ modified GCE possess reasonably higher electrocatalytic activity and superior stability in HER as compared to the other reported catalysts in literature such as IrCo@NC-800[220], Ir-Au-Si NCs[227], IrO$_2$–Fe$_2$O$_3$[232] and Ir@NC[231].
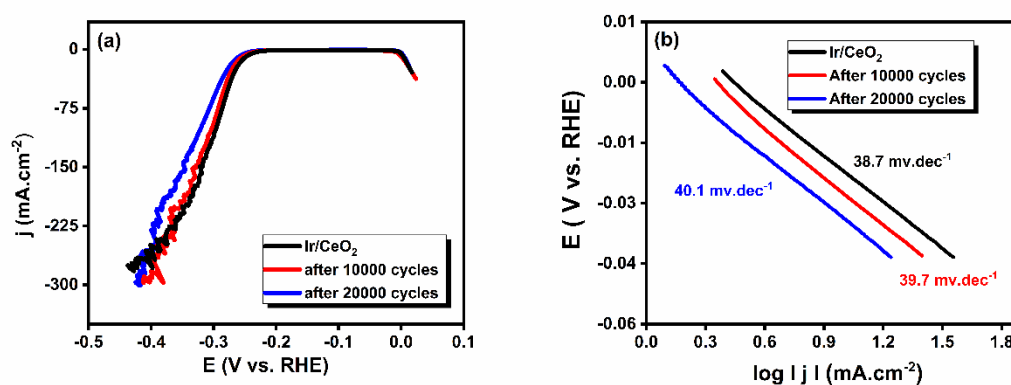
Figure 35. (a) The polarization curves of Ir/CeO$_2$ at the beginning, after 10000 and 20000 cycle in 0.5 M H$_2$SO$_4$ (20000 cycles correspond to 111 h) (b) The corresponding Tafel plots.

Since the turnover frequency reveals the intrinsic electrocatalytic activity of a catalyst, the TOF values of Ir/CeO_2 in acidic condition were determined according to the results of copper underpotential deposition (Cu-UPD) method (Figure 36 (a)). The TOF values for Ir/CeO_2 in 0.5 M H_2SO_4 at 0, 25, 50, 75 and 100 mV (vs. RHE) were determined as 0.10, 0.28, 0.72, 1.28 and 1.95 s^{-1}, respectively (Figure 36 (b)). TOF values of 10% Pt/C were also calculated and found as 0.36 s^{-1} and 1.18 s^{-1} at 50 mV at 100 mV overpotential values, respectively.[237] Ir/CeO_2 has relatively high TOF values compared to the benchmark Pt/C, which indicates higher amount of H_2 could be generated at the same overpotential by using Ir/CeO_2.
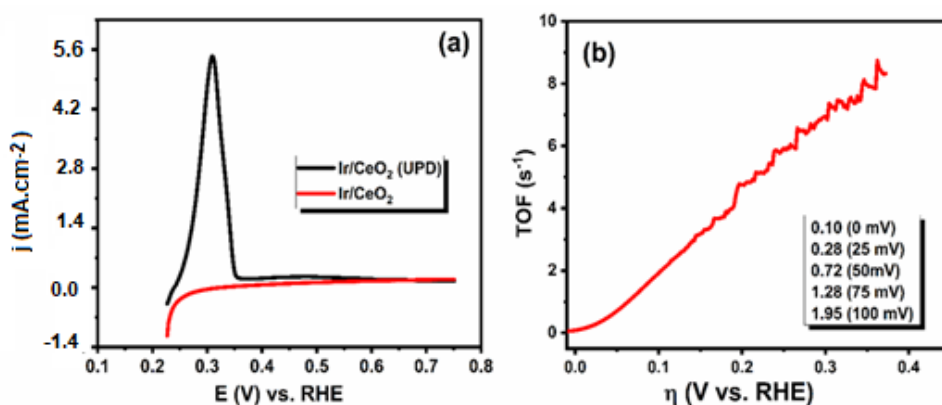
Figure 36. a) Linear sweep voltammograms of Ir/CeO_2 before and after Cu-UP in 1.0 M H_2SO_4 and b) TOF (s^{-1}) vs η (V) graph of Ir/CeO_2 in 0.5 M H_2SO_4.

The electrocatalytic activity of Ir/CeO_2 was also studied by electrochemical impedance spectroscopy method. EIS studies were conducted at the potential from 210 mV to 250 mV with 10 mV interval in 0.5 M H_2SO_4 (Figure 37 (a)). Two semicircles at low and high frequency regions can be observed from the resulting Nyquist curves which were fitted the model which is inset of Figure 37 (a). As it is seen from the Figure, R_{CT} values decrease with increasing overpotential values (i.e. from 314 ohm at 17 mV vs RHE to 32 ohm at -23 mV vs RHE) indicating increasing charge transfer kinetics. Hu and his coworkers propose the idea that the Tafel slope could also be acquired by using EIS measurement and the results can purely reflect the charge transfer kinetic of the electrode reaction excluding the contribution from catalyst resistance.[130] Therefore, the Tafel slope was also calculated from the overpotential vs. log ($1/R_{CT}$) graph (Figure 37 (b)) and found as 40 $mV.dec^{-1}$ which is highly consistent with the value derived from LSV voltammogram.

The mechanism of HER could be determined by the value of Tafel slope. If the hydrogen adsorption on the surface of catalyst is very weak, the Volmer step controls the overall rate and for this case the Tafel slope is found as ~120 mV.dec^{-1}. If the adsorption of hydrogen is very strong, then the desorption of hydrogen (Tafel or Heyrovsky reactions) controls the overall rate.[246] According to the population of adsorbed hydrogen (H_{ads}) on the catalyst surface, Tafel or Heyrovsky mechanism will determine the rate of hydrogen evolution. The Tafel mechanism can be rate determining step (rds) when the H_{ads} population are high, in which two adjacent adsorbed hydrogen atoms combine and produce H_2 gas. In this situation, the Tafel slope is found as ~ 30 mV.dec^{-1}.

If the H_{ads} population is low on the surface of catalyst, the proton in the environment will attack to H_{ads} and generate hydrogen gas. For this case, Heyrovsky reaction is rds and Tafel slope is equal to ~40 mV dec^{-1}.[243] The strong tendency to form a chemical bond between Ir and H would hinder hydrogen desorption and decreases the reaction rate of HER.[235] As mentioned before, the Tafel slope of the Ir/CeO$_2$ is in the range of 38.7 – 40.0 mV dec^{-1} which confirms that Volmer-Heyrovsky reaction mechanism is preferable for the HER with Ir/CeO$_2$ and the electrochemical reaction of H_{ads} and H_3O^+ to form hydrogen and its desorption is the rate-determining step.
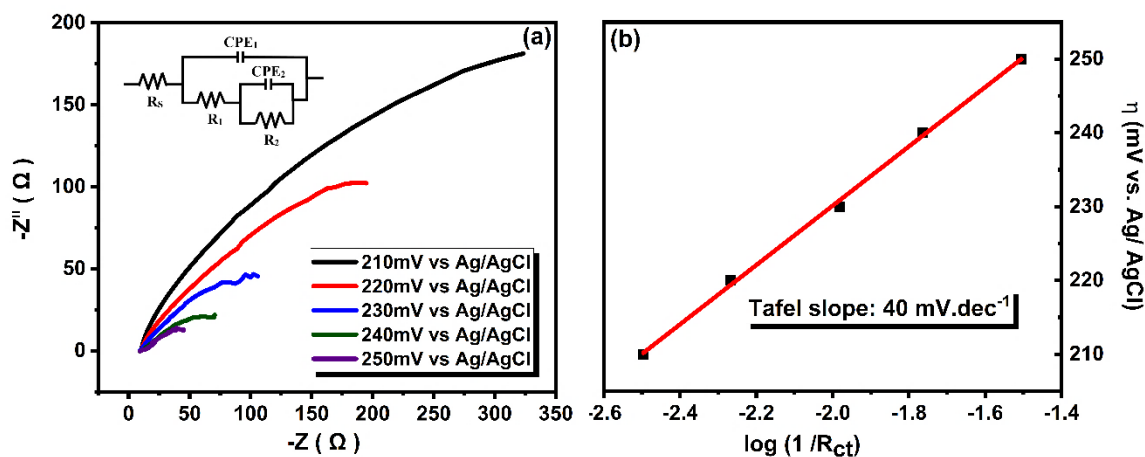
Figure 37. a) The Nyquist plots of Ir/CeO$_2$ at different overpotentials and b) Tafel plot obtained using R$_{CT}$ from the EIS.

Other important parameter that affects the activity is the double layer capacitance (C_{DL}). The values of C_{DL} were found as 0.651 mF and 0.671 mF from the non- faradic region of CV curves (Figure 38) and the EIS measurement at the onset potential, respectively. ECSA values were calculated as 16.275 and 16.775 cm^2 by using these C_{DL} values obtained from CV and EIS, respectively.
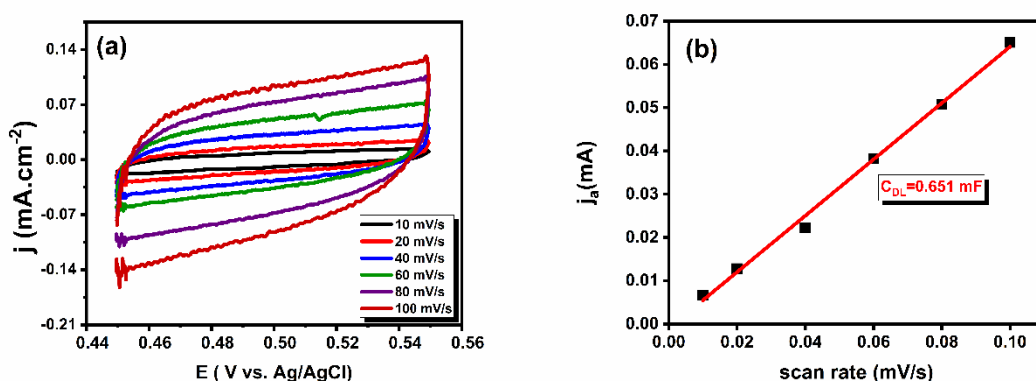
Figure 38. (a) Multi CV experiment for determination of C_{DL} at different scan rates in 0.5 M H_2SO_4 and (b) capacitive current at 0.50 V (vs Ag/AgCl) versus scan rates for Ir/CeO$_2$.

The electrocatalytic activity of Ir/CeO$_2$ was also performed in both basic and neutral media (Figure 39). The results show that Ir/CeO$_2$ is more efficient in acidic medium.
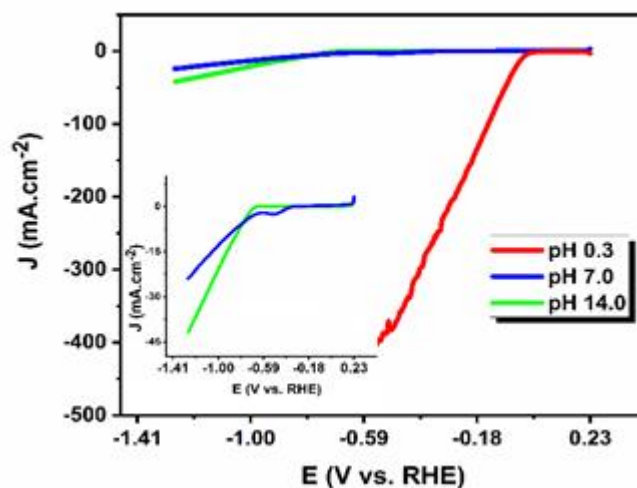
Figure 39. LSV curves of Ir/CeO$_2$ in 0.5 M H_2SO_4 solution (pH= 0.3), buffer solution (disodium hydrogen phosphate/ potassium dihydrogen phosphate, pH= 7.0) and 1M KOH solution (pH= 14.0) (Inset Figure: The magnified image at lower current density for basic and neutral medium)

Further electrocatalytic tests for Ir/CeO$_2$ was also performed at different reaction temperatures (Figure 40). The activation energy for the Ir/CeO$_2$ was obtained from the polarization curves taken at different temperatures ranging from 293 to 323 K in 0.5 M H$_2$SO$_4$. Tafel curves of Ir/CeO$_2$ were derived from their corresponding LSV curves and shown in Figure 40 (a). As the temperature increases, the activity of Ir/CeO$_2$ increases for HER, i.e., decreasing overpotentials and enhancing current densities. Apparent thermal activation energy (ΔG^o) can be calculated from the slope of the log j$_0$ vs. 1/T plot.[248] By using the j$_0$ values at different temperatures, corresponding Arrhenius plot in Figure 40 (b) was obtained and ΔG^o was calculated as 1.94 kJ/mol which indicates that Ir/CeO$_2$ has a smaller thermal activation energy than most of the catalysts in literature such as Ir/SiNW[248], Rh-Au-SiNW-2 [206] and Pt(111)/TiO$_2$[236].
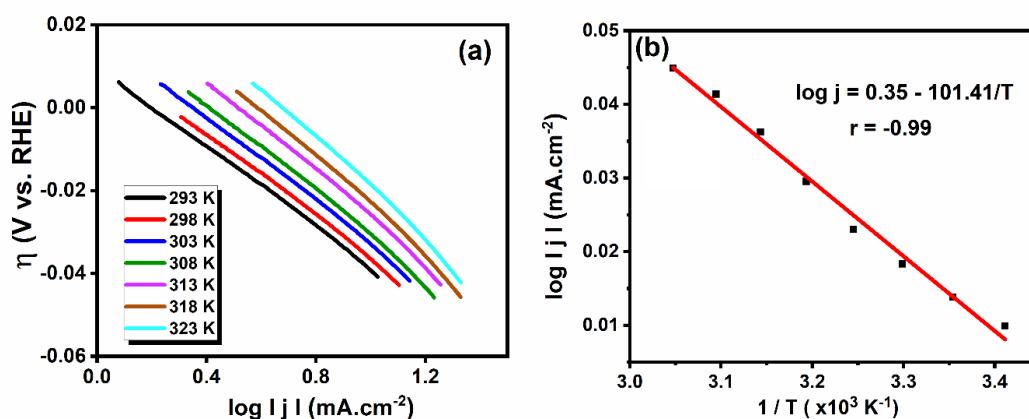
Figure 40. (a) Tafel curves of the Ir/CeO$_2$ catalyst at different temperatures in 0.5 M H$_2$SO$_4$ and (b) corresponding Arrhenius plot.

The Faradaic efficiency during hydrogen production was also determined using Ir/CeO$_2$ modified GCE. Constant potential was applied to system and the amount of gas measured by controlled potential coulometry method. The experimentally produced gas volume and the theoretical volume of H$_2$ gas were compared at 1.2 V vs. Ag wire (which is equal to 172 mA.cm^{-2} in Hoffmann cell). For this test, a current density of 172 mA cm^{-2} and 71 mA cm^{-2} (0.8 V vs. Ag wire) were applied to the system and the amount of generated H$_2$ gas was calculated at different times. Finally, Faradaic efficiency was obtained by comparing the theoretical and experimental results. As it is seen in the volume of generated H$_2$ vs. time plots shown in Figure 41, the experimental volume of gas is so close to theoretical volume and faradaic efficiency is about 90.9%.
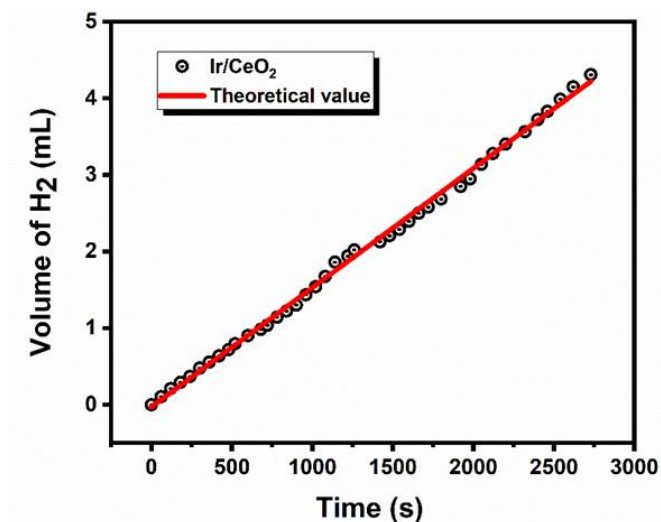
Figure 41. Generated H$_2$ volume versus time graph for Ir/CeO$_2$ during the electrolysis of water in 0.5 M H$_2$SO$_4$. Theoretical value was obtained from ideal gas equation and Faraday's relation.

3.1.2.5. Outlook of the synthesis, characterization and electrochemical studies of Ir/CeO$_2$

Ir based catalysts including Ir/TiO$_2$, Ir/ZrO$_2$ and Ir/CeO$_2$ were successfully prepared and tested for HER in acidic media. Among these catalysts, Ir/CeO$_2$ has been found very efficient in this reaction. Electrochemical tests were performed without using any binder such as nafion[242] and graphene. Ir/CeO$_2$ provides -13 mV onset potential, -23 mV overpotential at 10 mA.cm^{-2}, 2.69 mA.cm^{-2} exchange current density and 38.7 mV.dec^{-1} Tafel slope values which were better than the ones obtained for Ir/TiO$_2$ and Ir/ZrO$_2$. Ir/CeO$_2$ shows higher intrinsic electrocatalytic activity (TOF= 1.95 s^{-1} at 100 mV) and stability than that of commercial Pt/C (TOF= 1.18 s^{-1} at 100 mV).[237] The electrocatalytic stability test shows that Ir/CeO$_2$ exhibits an outstanding stability for HER in 0.5 M H$_2$SO$_4$ even after 20000 CV cycles. The Tafel slopes determined before and after stability test are found to be nearly the same. Considering the high stability, facile preparation method and low iridium loading (2.44 wt. %), binder free Ir/CeO$_2$ is a promising electrocatalyst for hydrogen evolution from water splitting.

3.1.3. Electrocatalytic activity of CoNPs supported on MO_2

3.1.3.1. Effect of metal oxides on the performance of Co catalysts

As with Rh and Ir, ceria shows better performance as a supporting material for Co in the hydrogen evolution reaction. As summarized in Table 9, when the loading densities were kept as 85.7 $\mu g.cm^{-2}$, Co/CeO_2 performed better than Co/TiO_2 and Co/ZrO_2 (Figure 42), however, its performance remained lower than iridium and rhodium derivatives with its 384 mV vs. RHE onset potential, -432.6 mV overpotential, 188 $mV.dec^{-1}$ Tafel slope and 0.0034 $mA.cm^{-2}$ exchange current density values.
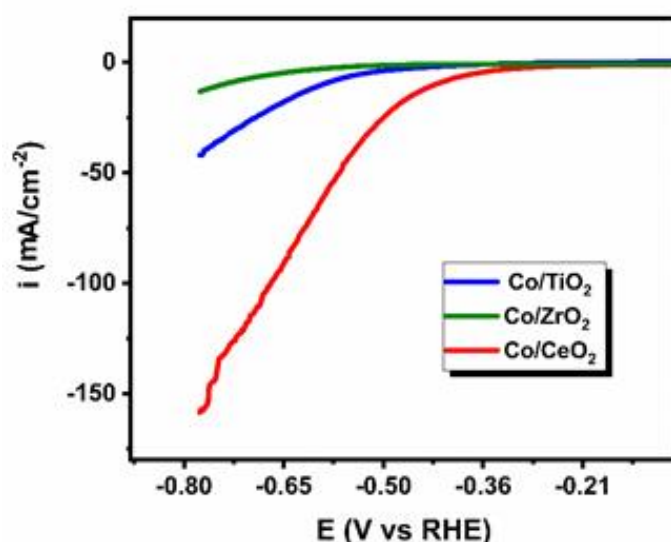
Figure 42. Polarization curves of the Co containing catalysts in 0.5 M H_2SO_4

Table 9. Onset potential, overpotential, Tafel slope and exchange current density values of Co containing catalysts with different supporting materials.

Catalyst	Loading Density ($\mu g.cm^{-2}$)	η_0 (mVvs. RHE)	η (mV@-10 $mA.cm^{-2}$)	Tafel Slope ($mV.dec^{-1}$)	j_0 ($mA.cm^{-2}$)
Co/CeO_2	85.7	-384	-432.6	188.0	0.0034
Co/ZrO_2	85.7	-526	-736.3	279.0	0.0032
Co/TiO_2	85.7	-506	-589.0	210.0	0.0013

3.1.3.2. Characterization of Co/CeO₂

The particle size distribution of Co NPs in Co/CeO$_2$ was investigated by TEM analyses and shown in Figure.43 (a) and (b). The mean particle size of highly dispersed Co NPs were found as 2.8 ± 0.4 nm (Figure 43 (c)). The content of the Co/CeO$_2$ catalysts was confirmed by TEM-EDX (Figure 43 (d)), and the existence of Co, Ce, and O were proven.
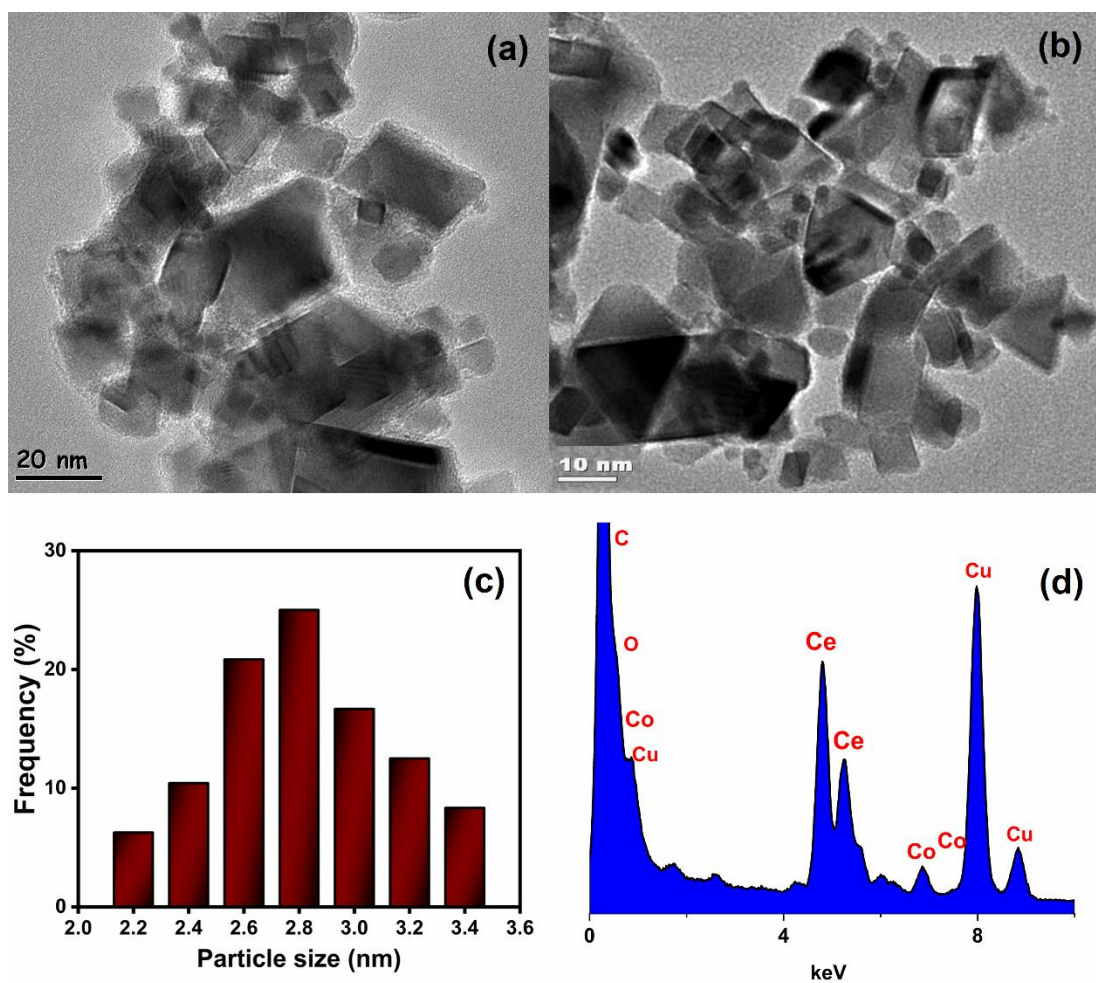
Figure 43. a and b)TEM images, c) particle size histogram and d)TEM-EDX spectra of Co/CeO$_2$.

The crystal structures of bare cerium oxide and the Co/CeO_2 were investigated by XRD. Figure 44 shows the XRD patterns of Co/CeO_2, and CeO_2. In Figure 44 (b), the miller indices were indicated onto diffraction peaks. The XRD pattern of the Co/CeO_2 and CeO_2 show that the crystal structure of CeO_2 nanoparticles is face-centered cubic and the high-intensity peaks are in good agreement with the JCPDS file No: 81-0792.[238] According to the XRD patterns of Co/CeO_2 and CeO_2, due to the low cobalt loading, there is no signal indicating the Co NPs. The crystallinity of CeO_2 does not change after the impregnation of cobalt nanoparticles.
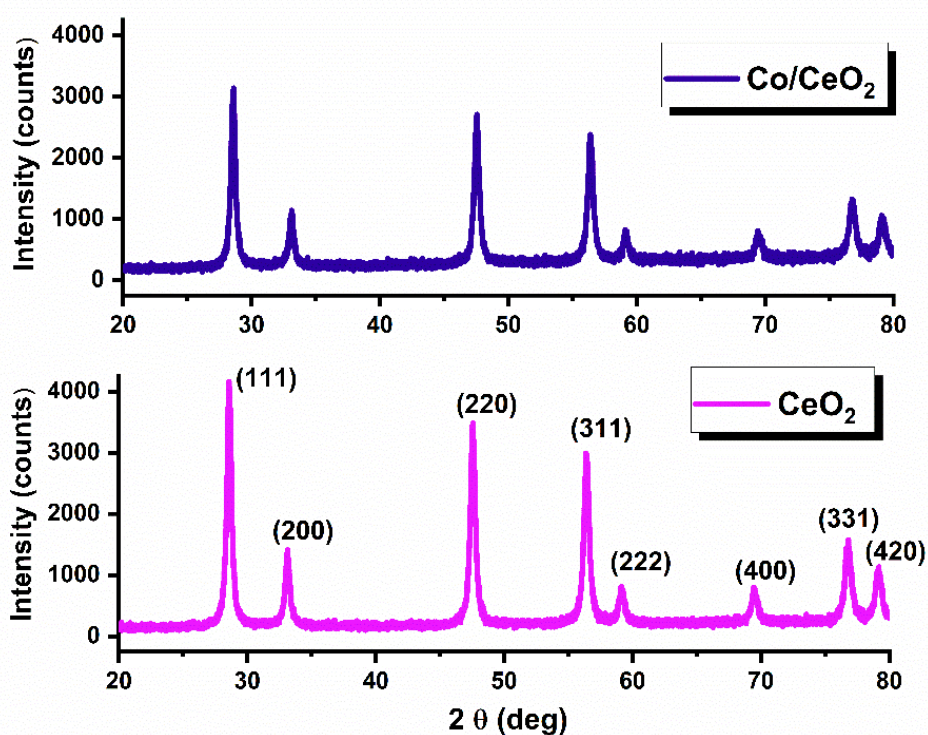
Figure 44. XRD patterns of Co/CeO_2 and bare cerium oxide.

3.1.3.3. Electrochemical studies of Co/CeO$_2$

Although Co/CeO$_2$ showed better activity than Co/ZrO$_2$ and Co/TiO$_2$, it was observed that it could not maintain this activity. Co/CeO$_2$ lost its activity to a large extent even in the 2nd and 3rd LSV measurements taken consecutively (Figure 45). The reason of this activity loss could be explained via corrosion or dissolution of non-noble metal electrocatalysts under strong acidic conditions.[239,240] Moreover that non-noble metal electrocatalysts tend to aggregate into larger particles during catalytic cycling.[241] In addition that, as shown in volcano curve at Chapter 1, inappropriate hydrogen adsorption energies of cobalt might be a reason of low catalytic activity and stability. Low ΔG_{H^*} value of Co slows down the hydrogen releasing step due to strong hydrogen bonding energy.
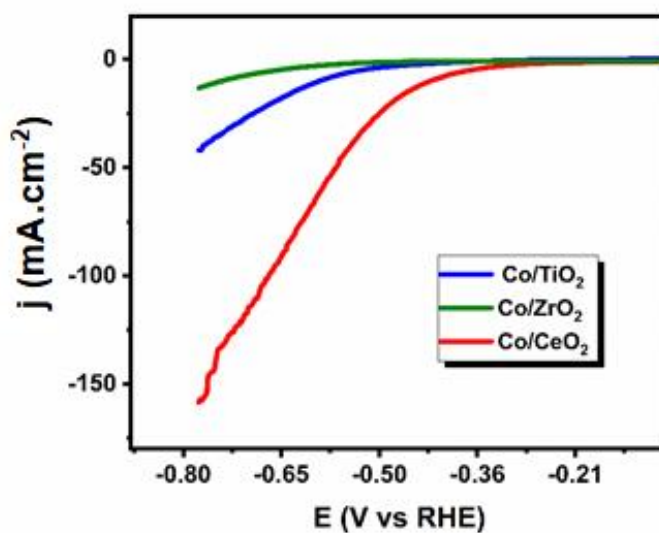
Figure 45. Consecutive LSV measurements of Co/CeO$_2$ in H$_2$SO$_4$ towards HER.

3.1.4. Conclusions about the performance of group 9B transition metal catalysts towards hydrogen evolution reaction

Since the experimental results so far obtained indicated that CeO_2 is better support material as compared to ZrO_2 and TiO_2, the electrocatalytic activity of CeO_2 supported metal nanoparticles towards HER are compared in terms of their onset potentials, Tafel slopes, exchange current densities, overpotential values and TOF values in Table 10.

Table 10. Tafel slopes, exchange current densities, overpotential values and TOF values of M/CeO_2 (M: Rh, Ir, Co) catalysts and commercial 10 % Pt/C catalyst.

	Tafel Slope $(mV.dec^{-1})$	j_0 $(mA.cm^{-2})$	η_0 vs. RHE (mV)	η_{10} (mV)	stability	TOF at -100 mV vs. RHE (s^{-1})
Rh/CeO₂	34.0	0.527	-25.0	-42.0	10000 cycles	1.56
Ir/CeO₂	38.7	2.69	-13.0	-23.0	20000 cycles	1.95
Co/CeO₂	188.0	0.0034	-384.0	-432.6	-	-
Pt/C	30.0	0.424	-19.0	37.0	1000 cycles	1.18

Inspection of Table 10 reveals that when the activity and stability of the metals are compared considering their onset potentials, overpotentials, exchange current densities and TOF values, it has been observed that iridium shows better performance in hydrogen evolution reactions.

Adsorption energy is one of the most important factors affecting the mechanism as well as the activity of electrocatalyst used for the HER during water splitting.[242] As described before, according to the Sabatier's principle, neither too high (slow adsorption) nor too low (slow desorption) adsorption energy should be preferred for an ideal catalyst.[243] To obtain optimum intermediate bond strength, Gibbs free energy of adsorbed hydrogen atom should be close to zero ($\Delta G_H \approx 0$).[244] The Volcano plot illustrating the principle of Sabatier predicts the catalyst activity at onset potential vs. ΔG_H in HER.[245] Pt which is on the top of the Volcano curve with a near zero ΔG_H value (-0.09 eV) has been widely

used for decades as an electrocatalyst for HER.[246] Ir, on the other hand, has Gibbs free adsorption energy of 0.03 eV which is even closer to zero than Pt in the Volcano plot.[247,32] Considering the volcano plot group 9b elements Rh and Ir were used as electro active metals catalyst with low ΔG values similar to Pt. Iridium and rhodium, on the other hand, have high cost and scarcity problems as well as stronger tendency to aggregation due to the higher atomization enthalpies ($\Delta H_{at,Ir}$=669.4 kJ.mol^{-1} $\Delta H_{at,Rh} =$ 556.5 kJ.mol^{-1} at 25°C).[248,249] Therefore, the use of supporting materials becomes crucial in order to maximize the active surface area while decreasing the amount of metal utilized.

In fact, the formation of highly dispersed metal nanoparticles on the oxide surfaces such as cerium, [90,237,250] zirconium[251] and titanium[252] oxides is thought to be a potential technique for producing an efficient electrocatalyst. In this regard, the choice of supporting material to stabilize iridium nanoparticles can dramatically affect the activity and stability of the electrocatalyst. Furthermore, it is well known that the metal-support interaction plays an important role in improving HER activity.[115] CeO_2 as a supporting material for the metal nanoparticles has attracted a great attention in electrocatalytic application.[253] The use of ceria in catalysis relies on the beneficial effect of noble metal-ceria interactions.[254] In addition, the redox behavior of CeO_2 in which Ce^{4+} and Ce^{3+} can easily be formed under oxidizing and reducing conditions can enhance the efficiency of metal nanoparticles.[255] Ceria also affects the catalyst performance by improving the dispersion of metal nanoparticles,[256] increasing the thermal stability of the support, [257] promoting the noble metal reduction-oxidation.[108] With all these properties, CeO_2 maintains smaller iridium nanoparticles and resists particle aggregation better than most of the metal oxides, i.e: ZrO_2, TiO_2.[258] Notably, thermodynamic ΔG_{H*} is not the only descriptor for HER activity trend, kinetic barrier is another important factor in determining the intrinsic HER activity of the electrocatalysts.[259] The presence of morphological defects such as oxygen vacancies has a beneficial effect on the reaction, lowering the barriers or stabilizing key intermediates.[260] The abundant oxygen vacancies in the ceria containing catalysts weaken H adsorption toward the optimum region and generating superior HER activity by facilitating water dissociation. [81, 261]

3.2. Electrocatalytic activity of MO$_2$ (M= Ti, Zr, Ce) supported rhodium, iridium and cobalt nanoparticles towards oxygen evolution reaction

Oxygen evolution reaction in acidic environment has been studied, but as stated in the literature, the catalysts were not found to be active in acid, since dissolution was observed in noble metals after certain potentials. [262-264] For this reason, OER studies were performed in 1.0 M KOH.

3.2.1. Electrocatalytic activity of Co NPs supported on MO$_2$

3.2.1.1. Effect of metal oxides on the performance of 4.0 % wt Co NPs catalysts

In this part of the study, the electrocatalytic activity of Co NPs toward OER were investigated. Three supporting metal oxides were used to prevent agglomeration and some effects on the electrocatalytic behavior of Co NPs were expected due to different physicochemical features of metal oxides. Inspection of our results (Figure 46) revealed a slight impact of CeO$_2$, ZrO$_2$ and TiO$_2$ on the electrocatalytic behavior (i.e Tafel slope, onset potential, over potential exchange current density), besides preventing agglomeration. However, the slight differences were found on the side of CeO$_2$ support (i.e. slightly lower Tafel slope, lower onset and oxidation potential and higher exchange current density). This slightly better performance of CeO$_2$ supported catalyst can be attributed to more favorable substrate–metal interaction via Ce(III) defects. These defects cause excess negative charge on the oxide surface and enhance the interaction between the metal and substrate. [90, 92, 265]
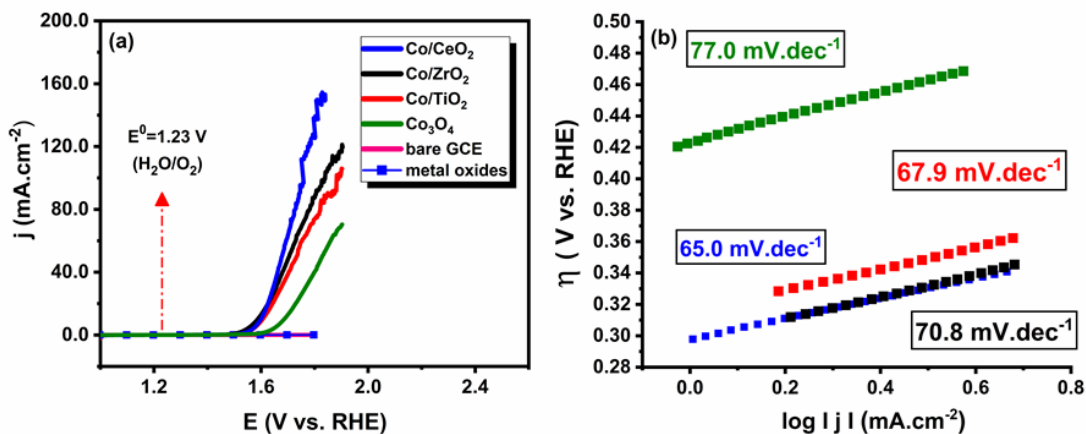
Figure 46. a) LSV curves of bare GCE, Co_3O_4, metal oxides (TiO_2, ZrO_2, and CeO_2), Co/TiO_2, Co/ZrO_2, and Co/CeO_2, and b) corresponding Tafel plots.

Table 11. Tafel slope, onset potential, overpotential, and exchange current density of synthesized catalysts and commercial Co_3O_4.

Catalysts	Tafel slope (mV.dec^{-1})	η_0 (V vs. RHE)	η_{10} (V vs. RHE)	j_0 (10^{-5}) (mA.cm^{-2})
Co/TiO_2	67.9	1.594	0.390	2.27
Co/ZrO_2	70.8	1.577	0.373	6.12
Co/CeO_2	65.0	1.575	0.365	7.67
Co_3O_4	77.0	1.655	0.455	1.49

85

3.2.1.2. Characterization of Co/TiO$_2$, Co/ZrO$_2$, Co/CeO$_2$

Highly dispersed cobalt nanoparticles with a uniform particle size were formed on TiO$_2$, ZrO$_2$, and CeO$_2$. The particle size distribution of Co NPs was investigated by TEM analyses and shown in Figure 47 (a)- Co/TiO$_2$, 47 (d)- Co/ZrO$_2$, and 47 (f)- Co/CeO$_2$. The content of the Co/MO$_2$ (M= Ti, Zr, Ce) catalysts was confirmed by TEM-EDX (Figure 47 (b), (d), and (h)), and the existence of Co, Ti, Zr, Ce, and O were proven. The mean particle size of highly dispersed Co NPs were found as 2.8 ± 0.4 nm (Figure 47.(c)), 2.6 ± 0.2 nm (Figure 47 (f)), and as 2.4 ± 0.2 nm (Figure 47 (i)) for Co/TiO$_2$, Co/ZrO$_2$, and Co/CeO$_2$, respectively.
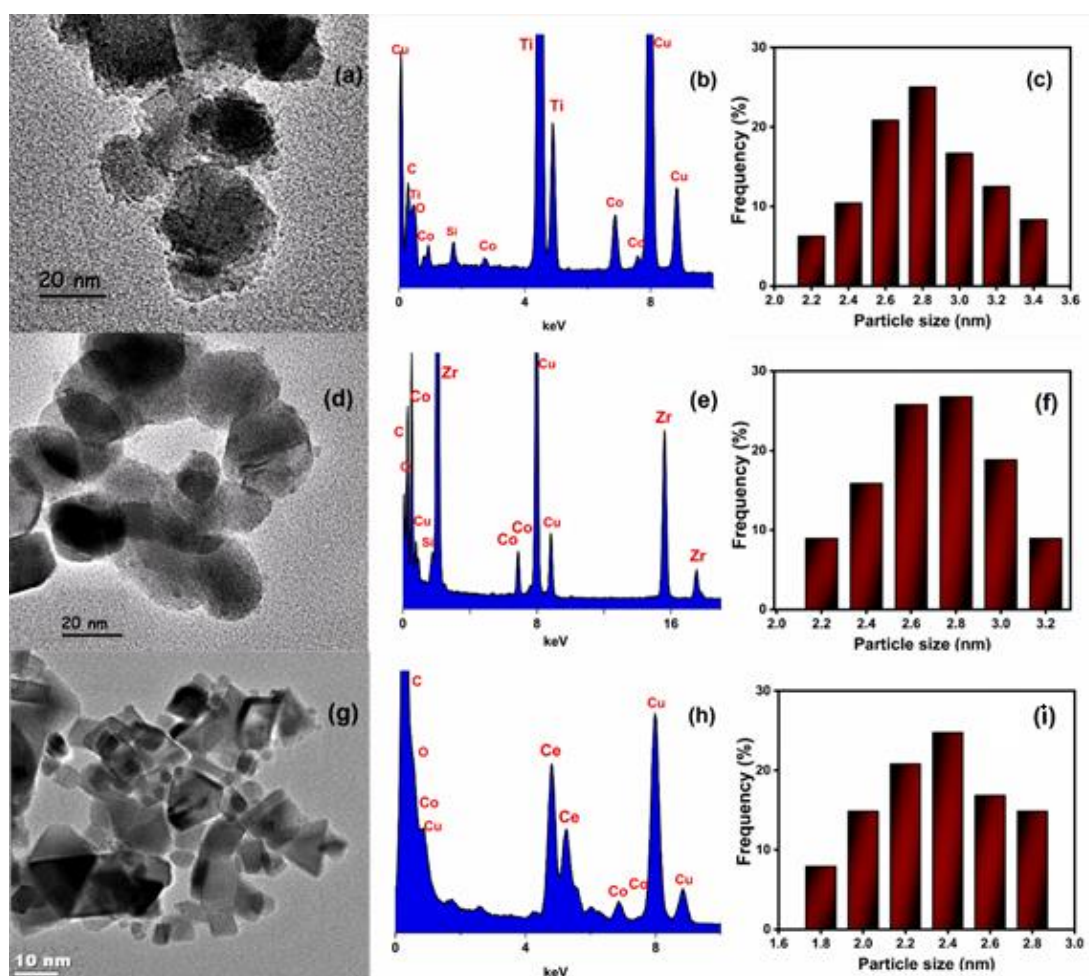
Figure 47. TEM images, TEM-EDX spectra and particle size histograms of a,b, and c) Co/TiO$_2$, d,e, and f) Co/ZrO$_2$ and g,h, and i) Co/CeO$_2$

The crystal structures of bare metal oxides and the cobalt-containing metal oxides (three catalysts and three supporting materials) were investigated by X-ray diffraction (XRD). Figure 48 shows the XRD patterns of Co/TiO_2, TiO_2, Co/ZrO_2, ZrO_2, Co/CeO_2, and CeO_2. In Figure 48 (a) and (b), the miller indices were indicated onto diffraction peaks. All these peaks confirmed that titania in the Co/TiO_2 catalyst was in the anatase phase. (Joint Committee on Powder Diffraction Standards (JCPDS) no. 1271)[266]. As shown in Figures 48 (c) and (d), diffraction peaks match the pure monoclinic phase of zirconia (JCPDS card no. 37-1484)[267]. The XRD pattern of the Co/CeO_2 and CeO_2 were depicted in Figure 48 (e)-(f) and shows that the crystal structure of CeO_2 nanoparticles is face-centered cubic and the high-intensity peaks are in good agreement with the JCPDS file No: 81-0792. [238] According to the XRD patterns of Co/MO_2 and MO_2, due to the low cobalt loading, there is no signal indicating the Co NPs. The crystallinity of MO_2 does not change after the impregnation of cobalt nanoparticles.
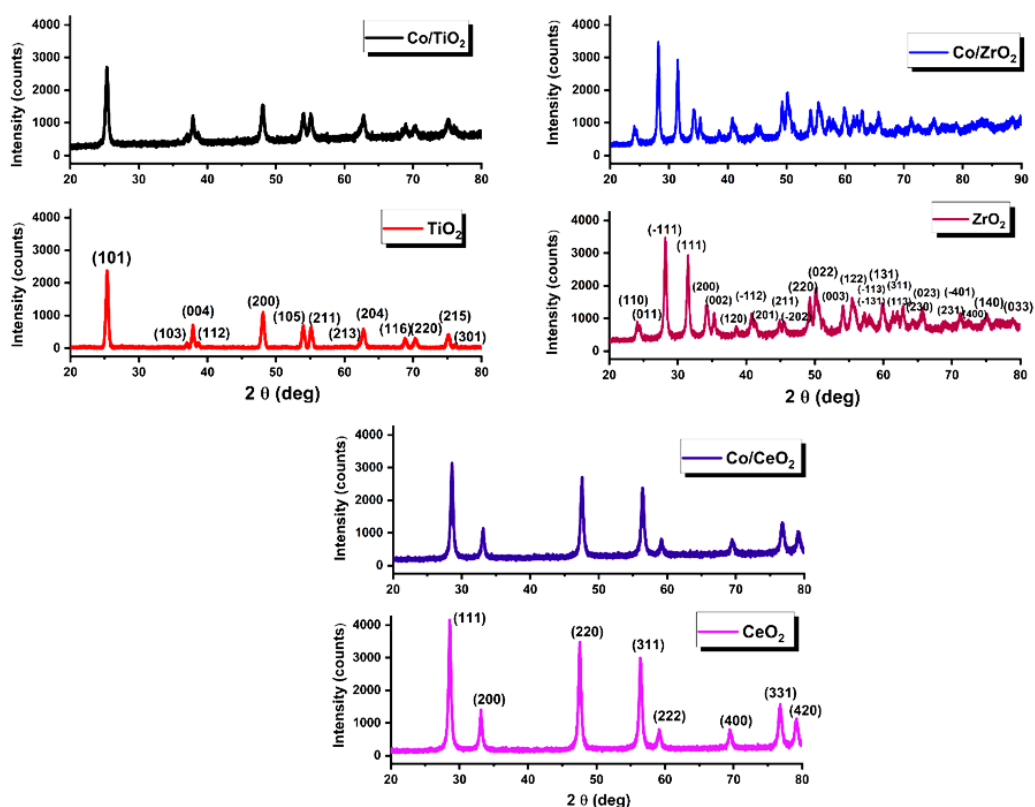
Figure 48. XRD patterns of Co/MO_2 and bare metal oxides.

3.2.1.3. Electrochemical studies of Co/TiO₂, Co/ZrO₂, Co/CeO₂

The electrochemical characteristics of the Co/TiO$_2$, Co/ZrO$_2$, and Co/CeO$_2$ were examined using a three-electrode cell in 1 M KOH solution at room temperature. The OER activity was determined via LSV at a 20 mV/s scan rate. At the scan rate lower than 20 mV/s, the catalyst surface blockage occurs by the evolved O$_2$ gas bubbles, which decreases the mass transfer capability. The resulting voltammograms of as-synthesized all three cobalt catalysts are represented in Figure 49 (a) together with the polarization curves of commercial Co$_3$O$_4$, bare GCE, and bare metal oxides (TiO$_2$, ZrO$_2$, and CeO$_2$) for comparison. As could be understood from Figure 49 (a) and (b), bare GCE and bare metal oxides exhibit no activity, and the synthesized catalysts show high activity towards OER. The order of activity of catalysts can be represented as Co/CeO$_2$ > Co/ZrO$_2$ > Co/TiO$_2$ > Co$_3$O$_4$ according to Tafel slopes which are 65.0, 67.9, 70.8, and 77.0 mV.dec^{-1}, respectively.
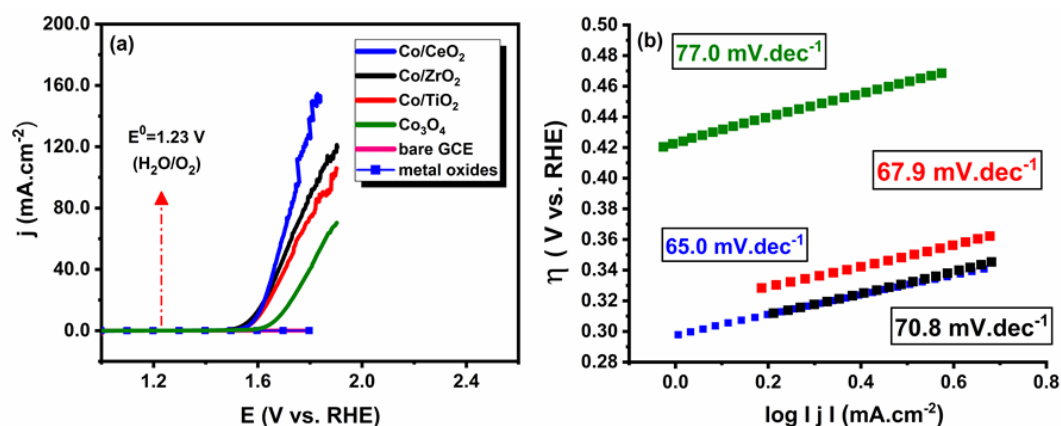
Figure 49. a) LSV curves of bare GCE, Co$_3$O$_4$, metal oxides (TiO$_2$, ZrO$_2$, and CeO$_2$), Co/TiO$_2$, Co/ZrO$_2$, and Co/CeO$_2$, and b) corresponding Tafel plots.

The activity of Co/CeO_2, Co/ZrO_2, and Co/TiO_2 are comparable with the reported electrocatalysts listed in Table 12, such as Fe_3O_4-Co_3S_4 NS (entry 7), Co_3O_4/CeO_2 NHs (Entry 9), CoP-based nanoneedle arrays on carbon cloth (entry 11), $NiCo_2O_4/Ti_4O_7$ (entry 14), Co9S8@NOSC-900 (entry 18), Co/Ce-Ni_3S_2/NF (entry 24). Although $Cu_{0.3}Co_{2.7}P$/NC (entry 1), $CoCr_2O_4$/CNS (entry 3), Fe_3O_4@Co_9S_8/rGO-2 (entry 6), Fe_3O_4-Co_3S_4 NS (entry 7), CoP hollow polyhedrons (entry 8) show better electrocatalytic activity in terms of Tafel slope and overpotential values, they have disadvantages considering their catalysts preparation methods. During the synthesis of Co/MO_2, there is no need to follow harsh techniques such as calcination at very high temperature (400-600 ºC), carbonization (800–900 ºC), phosphidation (300 ºC) pyrolization, solvothermal treatment (600 ºC) or annealing (300- 600ºC). An environmentally friendly and easy synthesis procedure requiring no high temperature is always preferred regarding the manufacturing process requirements and the environmental issues. Following a facile preparation method, including just simple impregnation and reduction steps at room temperature, Co/MO_2 (M= TiO_2, ZrO_2, and CeO_2) could be reproducibly synthesized and show excellent activity for OER.

Because the oxygen evolution reaction is highly irreversible, j_0 can hardly be determined from charge transfer resistance and found by extrapolating the Tafel line.[153] The high value of j_0 indicates that the initiation of reaction is easier. Co/CeO_2 shows excellent j_0 with the value of 7.67×10^{-5} mA.cm^{-2}, which is higher than the $Cu_{0.3}Co_{2.7}P$/NC (Entry1, j_0= 0.263×10^{-5}). Although $Cu_{0.3}Co_{2.7}P$/NC exhibits a low Tafel slope and overpotential, its exchange current density is 26.6 times lower than our catalyst. Pt catalysts also have 10^{-9} mA.cm^{-2} exchange current density for OER.[268] Thus, Co/MO_2 catalysts can be an excellent alternative to Pt with the non-noble metal content.

Table 12. Various Co based OER electrocatalysts reported in 1.0 M KOH.

Entry	Catalysts	particle size (nm)	Loading density ($\mu g.cm^{-2}$)	b ($mV.dec^{-1}$) (LSV)	η_0 (V vs. RHE)	η_{10} (V vs. RHE)	ref.
1	$Cu_{0.3}Co_{2.7}P/NC$	500	400	44.0	-	0.190	269
2	NiCo cages	400	-	50	-	0.380	270
3	$CoCr_2O_4/CNS$	5-15	-	51.0	1.470	0.326	271
4	$Co_2P/NPCNT$	55	750	53.0	1.500	0.370	272
5	$\alpha\text{-}Co_4Fe(OH)x$ NS	25	280	52.0	1.490	0.295	273
6	$Fe_3O_4@Co_9S_8/rGO\text{-}2$	350-500	250	54.5	~1.480	0.320	274
7	$Fe_3O_4\text{-}Co_3S_4$ NS	100–200	672	56.0	1.460	0.270	275
8	CoP hollow polyhedrons	700	102	57.0	1.530	0.400	276
9	Co_3O_4/CeO_2 NHs	8	-	60.0	~1.450	0.270	277
10	$Co_3O_4@C\text{–}MWCNTs$	6.2	325	62.0	1.500	0.320	278
11	CoP-based nanoneedle arrays on carbon cloth	3–15 nm	3300	62.0	-	0.281	279
12	**Co/CeO_2**	**2.4**	**107**	**65.0**	**1.575**	**0.365**	**This work**
13	$NiCo_2S_4$	100–150	70	64.0	1.450	0.337	280
14	$NiCo_2O_4/Ti_4O_7$	200-300	-	64.0	-	0.398	281
15	$CeO_2/Co(OH)_2$ HCs	18.6	-	66.0	1.650	0.410	282
16	**Co/TiO_2**	**2.8**	**107**	**67.9**	**1.594**	**0.390**	**This work**
17	$CNTs\text{-}Au@Co_3O_4$	3.86	--	68.0	1.560	0.350	283
18	$Co_9S_8@NOSC\text{-}900\ °C$	2-6	5000	68.0	1.400	0.340	284
19	$CeO_2(111)/Co_3O_4(110)$	150	-	68.1	~1.480	0.265	285
20	$Co\text{-}MOF@CNTs$	20-50	297	69.0	1.510	0.34	286
21	$CeO_2\text{-}Co_3O_4/CF$	100	-	70.0	-	0.103	287

Table 12 (continued).

22	Co/ZrO_2	2.6	107	70.8	1.577	0.373	This work
23	*N*-CG-CoO	10-30	-	71.0	1.300	~0.34	288
24	$Co/Ce-Ni_3S_2/NF$	5	2000	71.7	-	0.29@20	289
25	CP/CTs/Co-S	28	320	72.0	–	0.306	290
26	CoMo-H	300	500	75.0	~1.500	0.312	291
27	$SrNb_{0.1}Co_{0.7}Fe_{0.2}O_{3-\delta}$	-	-	76.0	1.490	0.420	292
28	CMO@CNTs	4.4	100	81.1	2.558	0.27	293
29	$Ag-NW@\alpha-Co(OH)_2$ NS	80-100	-	82.5	1.450	0.320	273
30	Ni foam-supported *N*-CNT@Co_3O_4	-	1200	84.0	1.470	0.310	294
31	$CuCo_2S_4$ NS	8-15	700	86.0	1.430	0.310	295
32	$Zn-CoSe_2$ NS	<100	-	88.0	1.340	0.356	296
33	$CoTe_2$@*N*-GC	10-30	1000	90.0	1.450	0.300	297
34	$Ni_{2.3\%}-CoS_2/CC$	50-100	970	119.0	–	0.270	298
35	$CeO_x/NiCo_2S_4/CC$	5	4000	126	-	0.270	299
36	$Co_{0.5}Fe_{0.5}S$@*N*-MC	20-40	100	159.0	~1.570	0.41	300

EIS measurements at controlled potentials are essential for understanding the mechanism of the OER. A series of EIS spectra for Co/TiO_2, Co/ZrO_2, and Co/CeO_2 recorded in the direction of increasing potential (650 to 700 mV vs. Hg/HgO) and resulting Nyquist plots are shown in Figure 50 (a), (c), and (e). The semicircles at low frequency region of the Nyquist plots, arises from the charge transfer resistance and are potential dependent. On the other hand, the semicircles at high frequency region (left semicircles) are potential independent and might be observed due to adsorbed species on GCEs or surface porosity[89]. The impedance results were fitted the equivalence circuit model depicted in chapter 1. In this circuit, uncompensated solution resistance and charge transfer resistance (R_{CT}) were represented as R_s and R_1, respectively.

Constant phase element-1 (CPE$_1$) represents the double layer capacitance (C$_{DL}$) and is applied due to the dispersion of capacitance frequency at the electrode/electrolyte interface. The resistance R$_2$ and the constant phase element-2 (CPE$_2$) symbolize the surface coverage relaxation of adsorbed intermediate in the mechanism of oxygen evolution reaction. [301]

The R$_{CT}$ is a total charge resistance for the overall rate of OER, and it decreases with the increasing potential, which means electron transfer kinetic increases when the applied potential increases. The basis of finding the Tafel slope is the steady-state polarization technique, and the logarithmic form of the applied potential and steady-state anodic current are used. The slope of log (1/R$_{CT}$) vs. overpotential graph gives the EIS Tafel slope. As seen in the Figure 50 (b), (d), and (e), for the Co/TiO$_2$, Co/ZrO$_2$, and Co/CeO$_2$, Tafel slopes were found as 70.12, 71.56, and 68.02 mV.dec^{-1}, respectively. These results are consistent with the values of 67.9, 70.8, and 65.0 mV.dec^{-1} obtained from the polarization curves. The EIS measurements of Co$_3$O$_4$ were also studied (Appendix Figure C6) and Tafel slope of Co$_3$O$_4$ was found as 83.51 mV.dec^{-1} from EIS. At the given potentials, there are little differences in the Tafel slopes, suggesting that similar intermediates and charging processes are involved in the rds of these catalysts. In the Bode plots given in Figure C7, single peaks between 100 MHz and 100 Hz were monitored, the peaks suggests that the formation of chemical intermediates dominate the OER mechanism.[302]
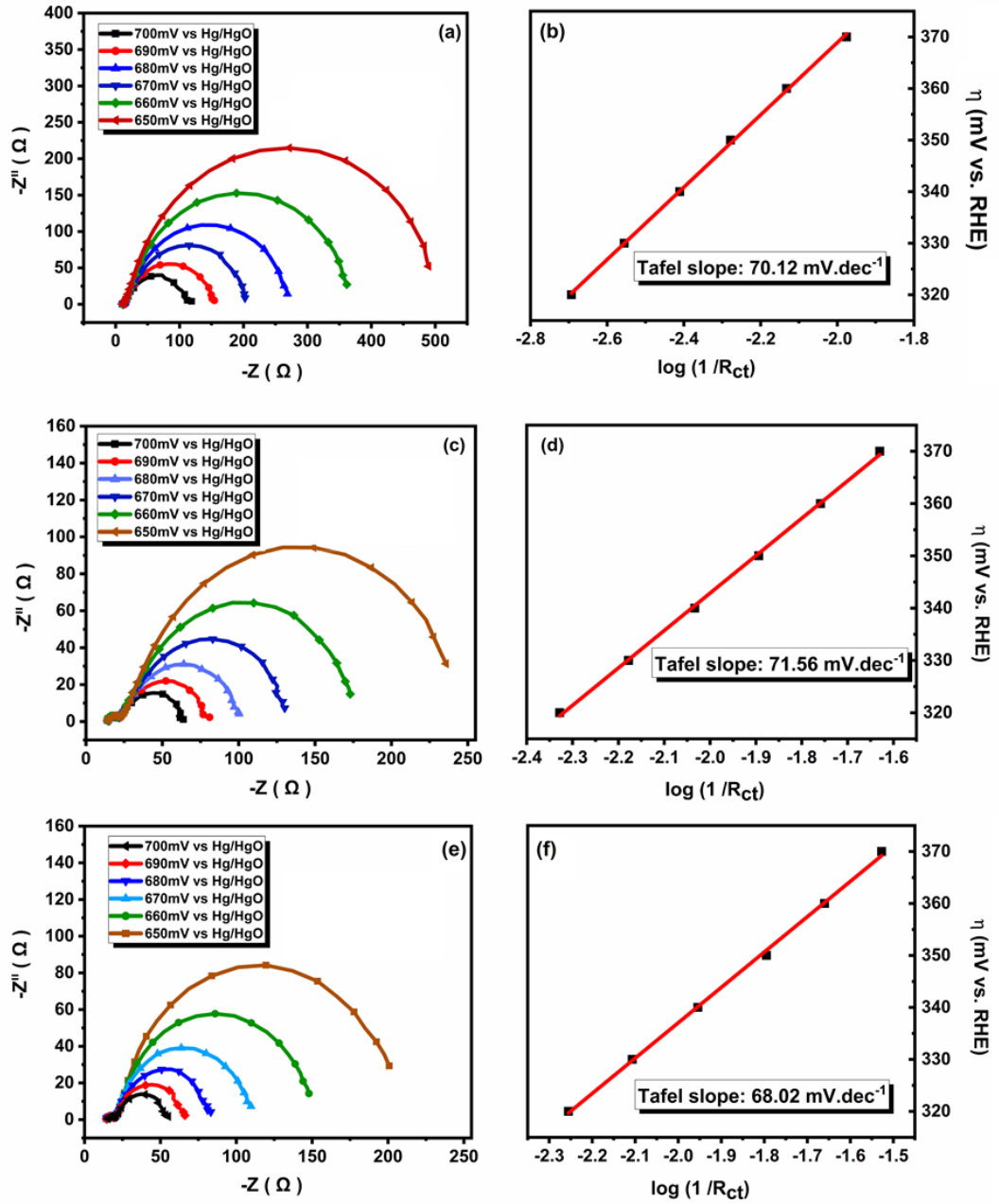
Figure 50. EIS measurement of a) Co/TiO$_2$, c) Co/ZrO$_2$, and e) Co/CeO$_2$ at a potential range between 650mV and 700 mV vs. Hg/HgO and b, c, and f) corresponding Tafel plots.

Another essential parameter to evaluate the catalyst activity is ECSA which is directly related to the particle size of the catalysts. The high ECSA value may result from the small particle size.[303] ECSA was estimated by the division of double-layer capacitance (could be found via CV or EIS) to the specific capacitance (C_s). C_s describes the ideal flat surface capacitance of the catalyst and different C_s values have been used in literature, such as 0.022, 0.04, and 0.130 $mF.cm^{-2}$ in alkaline media.[304] 40 $\mu F.cm^{-2}$ was chosen as C_s in this thesis. C_{DL} was firstly found from the CV experiment, the non-faradic region was determined as 0.17- 0.37 V vs. Hg/HgO. A plot of the anodic current as a function of scan rate yields a straight line and slope of this line equal to C_{DL}. The representative multi CV experiments were given in Figure 51 (a), (c), and (e) for Co/TiO$_2$, Co/ZrO$_2$, and Co/CeO$_2$, respectively and Appendix Figure C9 (a) for commercial Co$_3$O$_4$ catalyst. The C_{DL} measured from the scan-rate dependent CVs for the Co/TiO$_2$, Co/ZrO$_2$, Co/CeO$_2$, and Co$_3$O$_4$ catalysts are 0.225, 0.317, 0.446 mF, and 0.048 mF as represented in Figure 51 (b), (d), (f) and Appendix Figure C9 (b). For Co/TiO$_2$, Co/ZrO$_2$, and Co/CeO$_2$ catalysts, ECSA values were found as 5.62, 7.92, and 11.15 cm^2, respectively. For the Co/MO$_2$ catalysts, the active sites are only located on the cobalt nanoparticles. The increasing values of C_{DL} indicates the increasing number of electro-active cites which is in accordance with the decreasing average particle sizes of Co NPs obtained from TEM results (i.e. 2.84 ± 0.4 nm, 2.62 ± 0.2 nm and 2.42 ± 0.2 nm for Co/TiO$_2$, Co/ZrO$_2$, and Co/CeO$_2$, respectively). The highest activity, especially in terms of exchange current density, of Co/CeO$_2$ could be attributed to higher ECSA value and lowest activity of Co$_3$O$_4$ arise from the lowest ECSA (1.2 cm^2). C_{DL} values calculated from the highest point of the Nyquist curves at overpotentials require to reach 10 $mA.cm^{-2}$ also support the trends in the ECSA from CVs for Co/TiO$_2$, Co/ZrO$_2$, and Co/CeO$_2$ (Appendix Figure C. 8 and Table 13).

Table 13. Calculated double layer capacitance and ECSA values of Co/TiO$_2$, Co/ZrO$_2$, Co/CeO$_2$, and Co$_3$O$_4$ from the EIS and CV measurements

catalysts	C_{DL} from EIS at 690 mV (mF)	C_{DL} from CV (mF)	ECSA from EIS cm^2	ECSA from CV cm^2
Co/CeO$_2$	0.414	0.446	10.35	11.15
Co/ZrO$_2$	0.274	0.317	6.85	7.93
Co/TiO$_2$	0.180	0.225	4.50	5.63
Co$_3$O$_4$	0.044	0.048	1.10	1.20
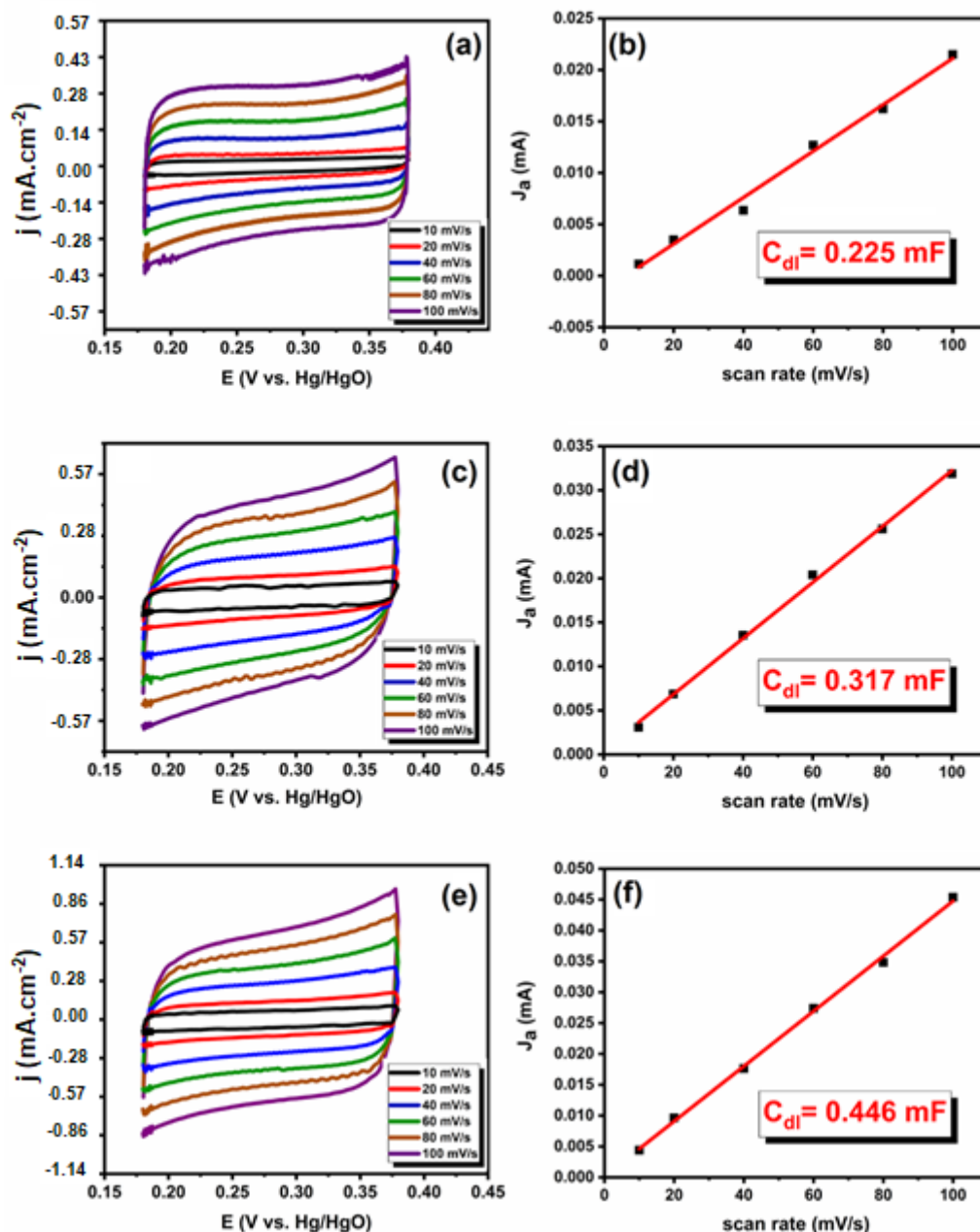
Figure 51. Representative multi-scan CV experiments for a) Co/TiO₂, c) Co/ZrO₂, e) Co/CeO₂ at different scan rates (10, 20, 40, 60, 80, and 100 mV/s) for C_{DL} determination in 1.0 M KOH; b,d,f) corresponding capacitive current versus scan rate plots at 0.27 V (vs. Hg/HgO) for Co/TiO₂, Co/ZrO₂, and Co/CeO₂, respectively.

To further evaluate the intrinsic activity of Co/TiO$_2$, Co/ZrO$_2$, and Co/CeO$_2$ catalysts, TOF values were calculated, and the results are given in Figure 52. The required overpotentials of Co/TiO$_2$, Co/ZrO$_2$, and Co/CeO$_2$ to reach the same TOF value (0.0063 s^{-1}) are 361, 353, and 349 mV, respectively. All these values are lower than the overpotential for the commercial Co$_3$O$_4$ catalyst (419 mV) for the 0.0063 s^{-1}, which may be attributed to the small particle size of Co NPs on the metal oxides. The smaller particle sizes provide more electroactive sites, and TOF may increase with the decreasing particle size. Among our catalyst and commercial Co$_3$O$_4$, Co/CeO$_2$ has the highest TOF value at the same overpotential with 2.4 ± 0.2 nm particle size and 11.15 cm^{-2} ECSA. Moreover, TOF values of Co/MO$_2$ (M: Ce, Ti, and Zr) summarized in Table 14 are comparable to the reported catalysts such as Ag NW@Co NS$_3$ (0.016s^{-1} at η = 300mV),[273] Co-NS (0.003s^{-1} at η = 300mV),[305] NiCo-LDH (0.002 s^{-1} at η =419mV),[306] Au@Co$_3$O$_4$ (0.015 s^{-1} at η= 350mV),[307] 20% wt. Pt/C (0.0053 s^{-1} at η = 350 mV)[308] and Fe–Co$_3$O$_4$@Fe–Co–Bi/CC (0.14 s^{-1} @ 400 mV) [309]. Considering the TOF values, the OER performance of Co/TiO$_2$, Co/ZrO$_2$, and Co/CeO$_2$ is promising as compared to the performance of reported Co containing catalysts.

Table 14. TOF values of Co/TiO$_2$, Co/ZrO$_2$, Co/CeO$_2$, and commercial Co$_3$O$_4$ at different overpotentials and current densities.

catalyst	current density (mA.cm^{-2})	TOF s^{-1}	overpotential mV vs. RHE
Co/TiO$_2$	5	0.0063	361
	10	0.014	385
	50	0.065	442
	77	0.1	469
	153	0.2	561
Co/ZrO$_2$	5	0.0063	353
	10	0.014	371
	50	0.065	431
	77	0.1	458
	153	0.2	526
Co/CeO$_2$	5	0.0063	349
	10	0.014	369
	50	0.065	409
	77	0.1	417
	153	0.2	453
Co$_3$O$_4$	5	0.0063	419
	10	0.014	445
	50	0.065	555
	77	0.1	645
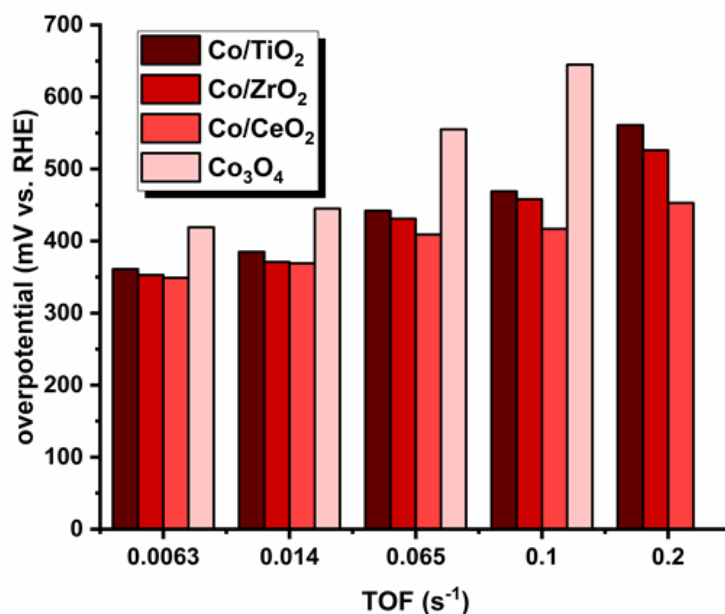
Figure 52. TOF values of Co/TiO_2, Co/ZrO_2, Co/CeO_2, and commercial Co_3O_4 at different overpotentials.

Stability is an important parameter while evaluating the OER performance of the catalysts. The stability tests of Co/MO_2 catalysts and commercial Co_3O_4 were performed employing chronopotentiometry measurements (insets of Figure 53). The constant current (0.7 mA) was applied to all three catalysts during 10800 s. LSVs of Co/TiO_2, Co/ZrO_2, and Co/CeO_2 were taken before and after stability measurements and shown in Figure 53 a-c, respectively. Moreover that durability of commercial Co_3O_4 catalyst was also performed for 1 h and LSV curves taken before and after stability test were given in Appendix Figure A13. As seen in Figure 53 (a), (b), and (c), there is a noticeable electrocatalytic activity loss for Co/TiO_2 and Co/ZrO_2 while the Co/CeO_2 keeps its electrocatalytic activity during the 3 hours stability test. The reason of higher stability of Co/CeO_2 than the other catalysts might be the better metal support interaction and large amount of oxygen vacancy provided by CeO_2.[310- 313]

There is a small change in the onset potential and the overpotentials required to achieve 10 $mA.cm^{-2}$ (35 mV shift) and the calculated Tafel slopes remain nearly same for Co/CeO_2 (only increased by 3.3 $mV.dec^{-1}$) after 3 hours stability measurement. On the other hand, Co/ZrO_2 shows better performance than Co/TiO_2, the anodic shifts of the onset potentials are 40 and 50 mV, the overpotential shifts are 50 and 62 mV and the changes of theTafel slopes are 11.5 and 21.5 $mV.dec^{-1}$ for Co/ZrO_2 and Co/TiO_2, respectively.

The decrease in the performance of the catalysts could be resulted from the accumulation of bubbles on the surface of the electrode. The bubbles causes the surface blockage and the electrical resistance increase with the formation of the dead area which consequently deteriorate the catalytic activity.[314] Note that although there is no loss of catalytic activity in the first hour period for the Co/MO_2 catalysts, the overpotential of commercial Co_3O_4 at 10 mA.cm^{-2} shifted 26.0 mV, and the Tafel slope increases by 12.0 mV.dec^{-1} after the one hour stability test (Appendix Figure C10). These activity differences after stability measurements show that the usage of supporting materials contributes to the durability of the material on the basis of metal support interaction. The stabilities of Co/MO_2 catalysts are comparable with the literature, such as $CoWO_4$[315], Co_3O_4/CNW[316,] and Ni–Cu nanoclusters on TiO_2 nanoparticles[317].
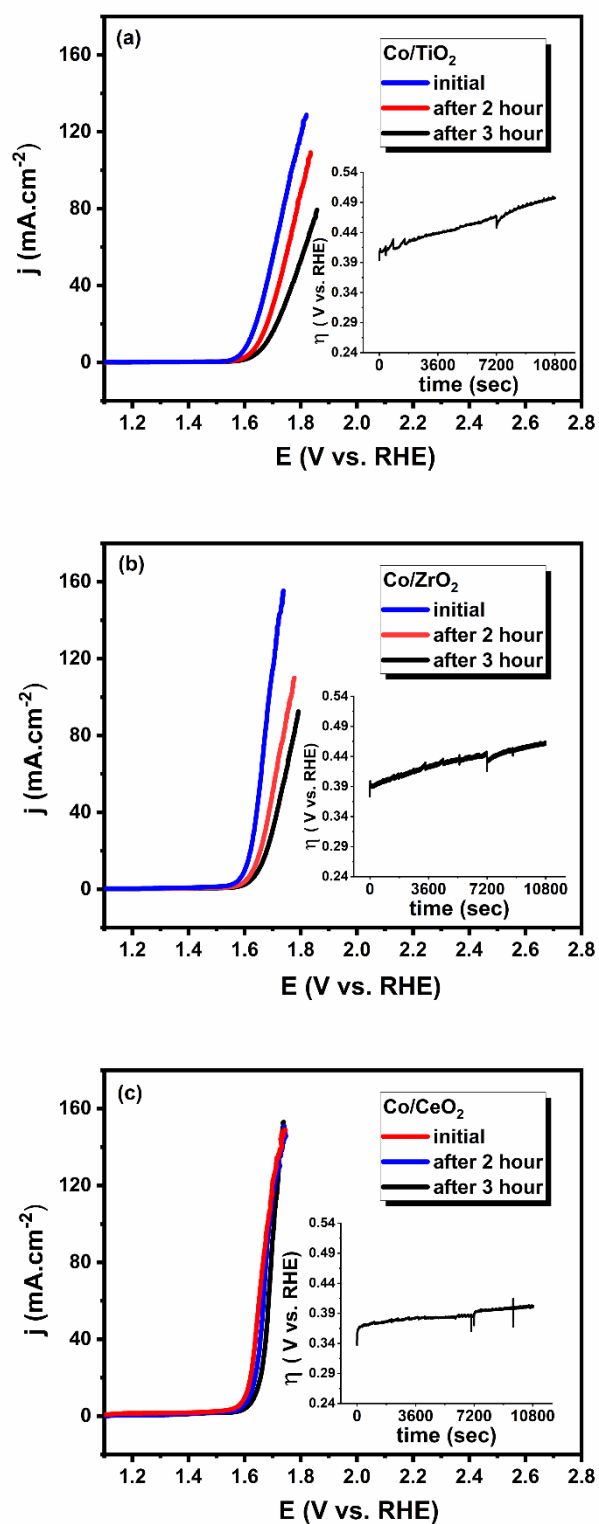
Figure 53. The polarization curves of a) Co/TiO_2 b) Co/ZrO_2 and c) Co/CeO_2 at the beginning and after 3-hour chronopotentiometry experiment (inset Figure) at 10 $mA.cm^{-2}$ in 1.0 M KOH.

The electrochemical OER activity was further studied at various temperatures. Figure 54 (a), (c), and (e) compile Tafel analyses of the catalysts at 304, 309, 314, 319, 324, and 329 K in 1.0 M KOH. At the same potential value, the current increases with the increasing temperature due to increasing migration rate of current carrying ions in the lower viscous medium. As shown in the Figures mentioned above, there is a linear relationship between log |j| vs. overpotential, and the Tafel slopes remain nearly the same for all the applied temperatures. The apparent thermal activation energies were found from the Arrhenius plot derived from the Arrhenius equation given below:

$$\log j_0 = \log (FKC) - E_a / 2.303RT$$

where T is the temperature (K), R is the gas constant (8.314 J mol^{-1} K^{-1}), E_a is the apparent activation energy (J.mol^{-1}), 'C' is the concentration of the reactant (constant), 'K' is Kohlrausch coefficient (dimensionless), 'F' is Faraday's constant, and 'j$_0$' is exchange current density (mA.cm^{-2}).[318] The activation energy reveals the kinetic barriers involved in the OER process and from the slope of the Arrhenius plots (Figure 54 b, d, and f), the apparent thermal activation energies were calculated as 30.156 kJ.mol^{-1}, 24.838 kJ.mol^{-1}, and 31.803 kJ.mol^{-1} for Co/TiO$_2$, Co/ZrO$_2$, and Co/CeO$_2$, respectively. These experimentally determined activation energies are in good agreement with the reported OER catalysts in alkaline environments such as NiFeOx/NF (25 ± 12 kJ mol^{-1}),[319] NiCoOx (71 kJ.mol^{-1}),[320] Ni–Fe hydroxide (18.1 kJ mol^{-1}),[321] and La$_{1-x}$Sr$_x$CoO$_3$ (LSC04) (35 kJ.mol^{-1})[322]. The apparent thermal activation energies of Co/MO$_2$ catalysts did not follow a regular trend however, the similar values imply that the active sites of the catalysts are nearly identical.[323]

The electrochemical OER mechanism is complex and consists of many consecutive reactions steps both chemical steps such as association or dissociation reaction and electron transfer steps. Transfer coefficient value is important indicator for the determination of rate determining step (RDS) of the OER mechanism. The transfer coefficients (α) could be calculated for different temperatures by using the formula: b= 2.303RT/αF where; b is the tafel slope (V.dec^{-1}), R is the universal gas constant constant (J.K^{-1} mol^{-1}), T is the temperature (K), F is the Faraday constant (96485 C).[39,36]

Bockris and Reddy[152] derive also the transfer coefficient as $\alpha_a = (n_b/\upsilon)+(n_r\beta)$ for a multiple electron reaction where n_b represents the number of electrons transferred back to the electrode before the RDS, υ is the number of RDSs taken place in the overall reaction, n_r is the number of transferred electrons in each occurance of the RDS and β is symmetry factor (β is generally assumed 0.5). If the chemical reaction after a one electron transfer reaction is RDS, the value of n_r is equal to 0 and the values of n_b and υ are 1. Hence, transfer coefficient become unity and Tafel slope is 60 mV.dec^{-1}.[16] As seen in Table 15, the estimated values of transfer coefficients increases from ~0.9 to ~1.0 for all three catalysts with increasing temperature. According to the both calculated transfer coefficient and the Tafel slope values, the second reaction step (M–OH + OH$^-$ → M–O$^-$ + H$_2$O) of the OER mechanism proposed by Krasil'shchikov path could be considered as the rate determining step for Co/MO$_2$ (M=Ti, Zr, Ce) catalysts in alkaline medium.[38]

Table 15. Tafel slopes and transfer coefficients of Co/MO$_2$ (M: Ti, Zr, Ce) catalysts at different temperatures.

Temperature K	Co/TiO$_2$		Co/ZrO$_2$		Co/CeO$_2$	
	Tafel slopes (V.dec^{-1})	α_a	Tafel slopes (V.dec^{-1})	α_a	Tafel slopes (V.dec^{-1})	α_a
304	0.067	0.90	0.069	0.87	0.066	0.91
309	0.065	0.95	0.068	0.89	0.066	0.93
314	0.058	1.07	0.065	0.94	0.066	0.94
319	0.058	1.09	0.065	0.96	0.067	0.94
324	0.057	1.12	0.065	0.99	0.066	0.97
329	0.057	1.14	0.063	1.03	0.065	1.00
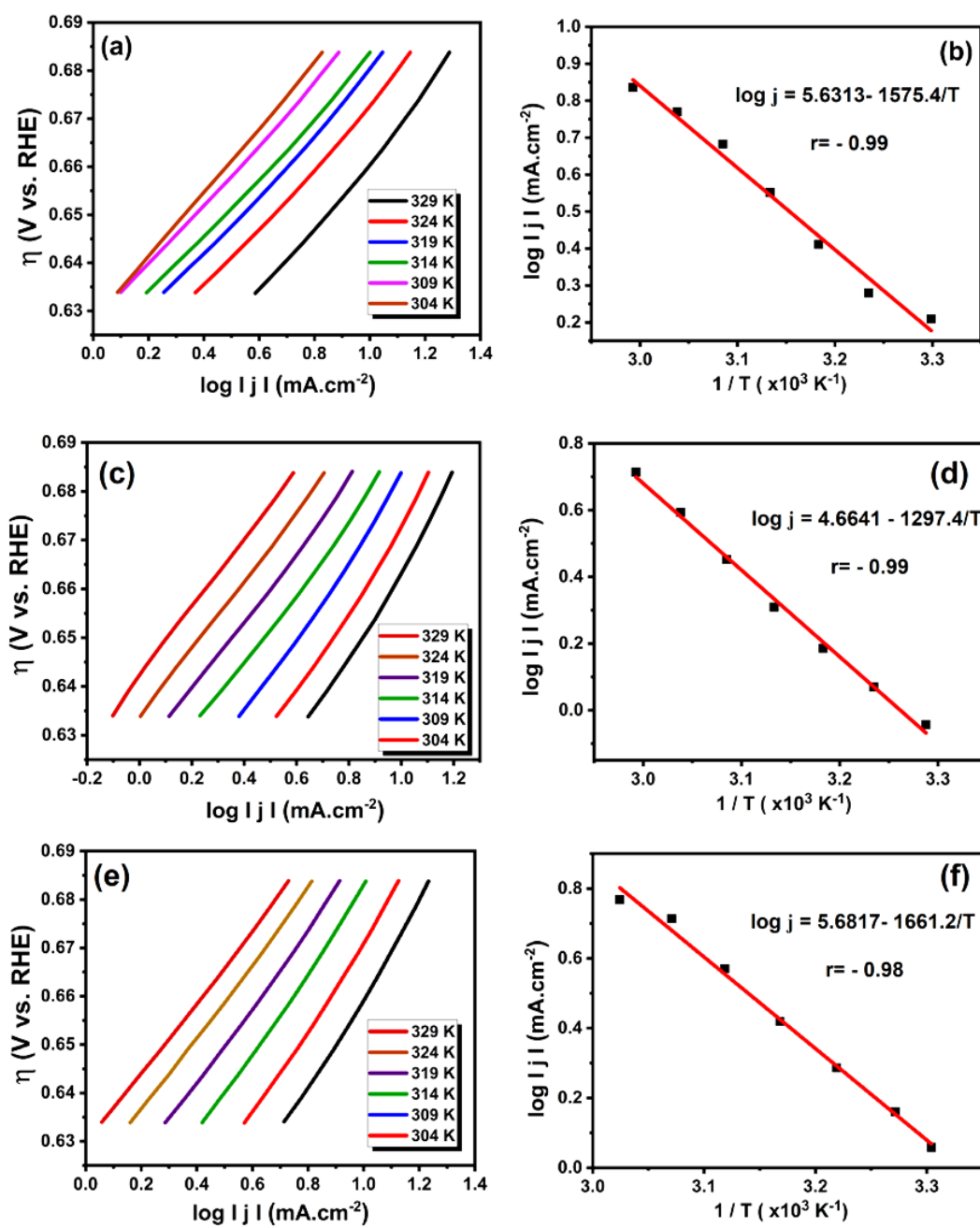
Figure 54. Tafel curves of the a) Co/TiO$_2$, c) Co/ZrO$_2$ and e) Co/CeO$_2$ at different temperatures in 1.0 M KOH and b, d, f) corresponding Arrhenius plots.

To understand the effect of hydroxyl ion concentration on OER performance, the polarization curves were taken for Co/TiO$_2$ (Figure 55(a)), Co/ZrO$_2$ (Figure 55 (b)), and Co/CeO$_2$ (Figure 55 (c)) at 0.2 M, 0.4 M, 0.6 M, 0.8 M and 1.0 M KOH solutions. The results given in Figure 55 show that the highest current densities are achieved in 1.0 M KOH solution. The lower activity at low KOH concentration may be attributed to the insufficient OH$^-$ adsorption on the active sites of the cobalt catalysts. The transfer of the OH$^-$ ions from the bulk electrolyte to the electrochemical double layer was mostly hindered by the high charge transport resistance.[324] OH$^-$ transfer becomes easier between bulk and electrochemical double layer when the OH$^-$ concentration increases, which results in the decrease of the Tafel slope value gradually (Table C. 2). On the other hand, at higher OH$^-$ concentrations greater than 1.0 M, the generated O$_2$ covers and blocks the catalysts' active sites, which causes high ionic transport resistance. The charge transport limitation can be observed at high electrolyte concentrations.
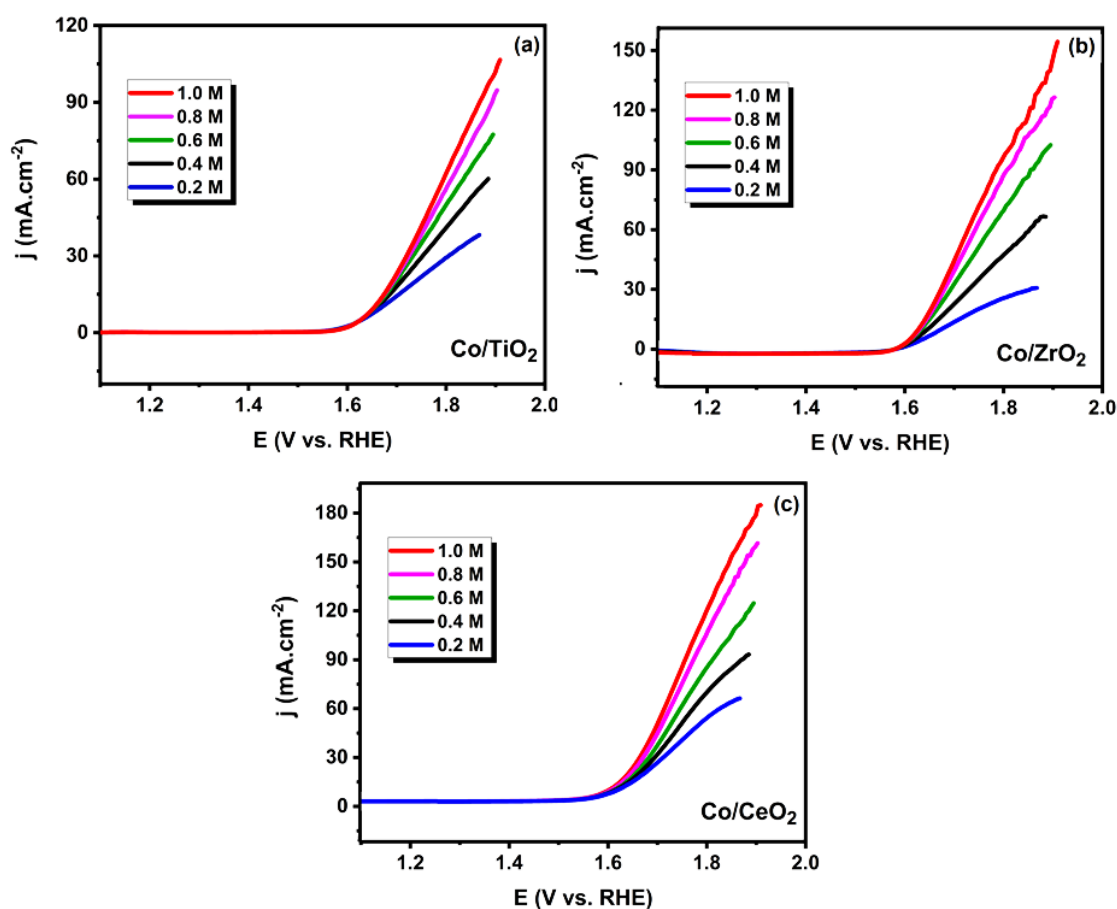
Figure 55. LSV curves of (a) Co/TiO$_2$, (b) Co/ZrO$_2$, (c) Co/CeO$_2$ at 0.2, 0.4, 0.6, 0.8, and 1.0 M KOH solution.

The Faradaic efficiency during OER was calculated via chronoamperometry experiment using a Hoffman apparatus which consists of working electrode, counter electrode and reference electrode. Applying the control potential coulometry method at 900 mV vs. Hg/HgO, both the charge passing through the system and the amount of produced O_2 gas were measured for 1 h. The theoretical and the experimental results were found to be consistent, and the related efficiencies were found as 95%, 96.1%, and 92.6% for Co/TiO_2, Co/ZrO_2, and Co/CeO_2, respectively (Figure 56). The Faradaic efficiency results of Co/MO_2 catalysts are comparable to that of the other cobalt-containing catalysts tested in an alkaline medium in the literature, such as CoS-DNA (90.28%) [325], $NiCo_2S_4$ (95.8%) [280], $CuO_x@Co_3O_4$ (95%),[326] $Fe_{0.25}$–CoMoCH/NF (97.7%),[327] CoGel1-derived xerogel1 (91.72%),[328] $Co_3O_4/Co_{0.85}Se/Co_9Se_8$ (82%),[329] $MoO_2/CoC_2O_4\cdot2H_2O$ (~90%),[330] $C_{12}H_{10}CoN_2O_4$ (91.78%), [331] $Cu_xCo_{3-x}O_4$ ($x = 0.95$, annealed at 200 °C) (93%),[332] NiCo-POM/Ni (96±5%) [333].
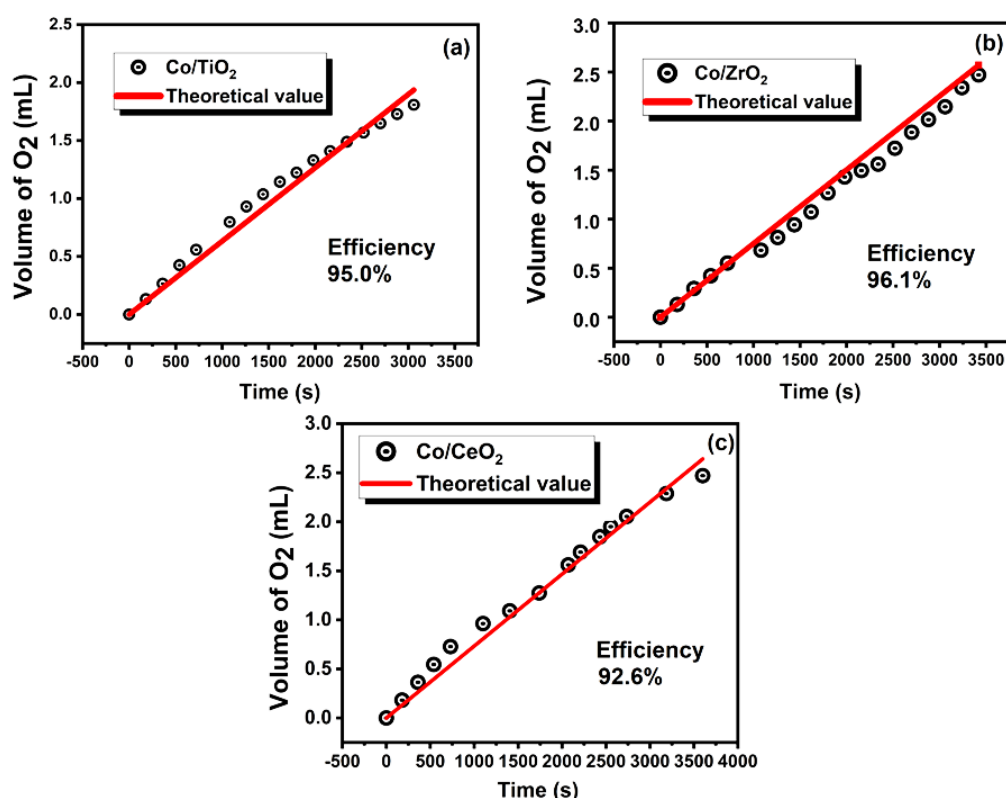
Figure 56. Faradic efficiency of (a) Co/TiO_2, (b) Co/ZrO_2, (c) Co/CeO_2 for 1 h.

3.2.1.4. Outlook of the synthesis, characterization and electrochemical studies of Co/TiO₂, Co/ZrO₂, Co/CeO₂

In this part of the thesis, Co nanoparticles were successfully impregnated onto the titania, zirconia, and ceria surfaces by the environmentally friendly method to increase the performance of the cobalt for OER. With the conductive support materials, the rate of the charge transfer and the electrochemically active surface areas were increased via decreasing charge transfer resistance and decreasing the particle size. Without using any high temperature needed steps such as carbonization, phosphidation, pyrolization, or annealing, Co/MO_2 (M= CeO_2, ZrO_2, and TiO_2) could be reproducibly synthesized and show excellent activity for OER. All three catalysts exhibited impressive performance for the oxygen evolution reaction in an alkaline environment with low overpotentials (0.368, 0.371, and 0.385 V), low Tafel slopes (65.0, 67.9, and 70.8 mV.dec^{-1}), high exchange current densities, high TOF values, and considerable durabilities. Although the commercial Co_3O_4 loses its activity to a great extent after the stability test, for the Co/CeO_2, Co/ZrO_2, and Co/CeO_2, no noticeable change was observed in Tafel slopes and overvoltages. Considering all parameters Co/MO_2 (M= CeO_2, ZrO_2, and TiO_2) show higher activity and stability than commercial Co_3O_4. The enhanced OER activity in Co/MO_2 (M= CeO_2, ZrO_2, and TiO_2) catalysts appears to originate from smaller R_{CT}, smaller particle size and higher electrochemical active sites than commercial Co_3O_4 and more disordered atomic arrangement. Among those three catalysts, because of the highest ECSA, Co/CeO_2 was found to have slightly better performance, especially in terms of exchange current density. According to the Tafel slopes, onset and overpotentials, exchange current densities, TOFs, Faradaic efficiencies, and stabilities, Co impregnated metal oxides (especially Co/CeO_2, Co/ZrO_2, and Co/CeO_2) catalysts could be a promising class of electrocatalysts for OER. This work also opens up an avenue for designing inexpensive, earth-abundant, and highly active OER electrocatalysts via using different non-noble metals or changing supporting materials.

3.2.2. Electrocatalytic activity of Ir NPs supported on MO$_2$

3.2.2.1. Effect of metal oxides on the performance of Ir catalysts

Before starting the detailed investigation, different supporting materials were combined with Ir metal to find the best Ir containg catalyst towards oxygen evolution reaction. According to the LSV curves in Figure 57, ceria was found to be best supporting material among titania, and zirconia. Although Ir/CeO$_2$, Ir/ZrO$_2$ and Ir/TiO$_2$ were prepared using the same amount of supporting materials by following the same procedure as explained in the experimental part, it was observed that iridium adhered better to the ceria surface based on the ICP results. Ir content of the prepared catalysts were determined as 2.44%, 1.13% and 0.63% wt. Ir for Ir/CeO$_2$, Ir/ZrO$_2$ and Ir/TiO$_2$, respectively.
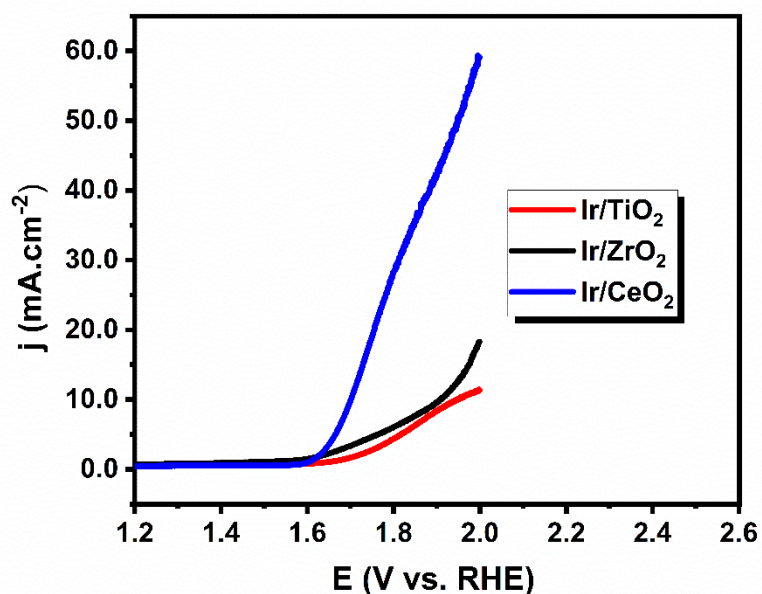
Figure 57. LSV curves of Ir/CeO$_2$, Ir/ZrO$_2$, Ir/TiO$_2$ in 1.0 M KOH.

3.2.2.2. Characterization of Ir/TiO₂, Ir/ZrO₂, Ir/CeO₂

Previously synthesis Ir NPs were used for OER studies. Characterization details of Ir/TiO$_2$, Ir/ZrO$_2$, Ir/CeO$_2$ were given in '3.1.2.3. Characterization of Ir/CeO$_2$'

3.2.2.3. Electrochemical studies of Ir/TiO₂, Ir/ZrO₂, Ir/CeO₂

The LSV curves of three iridium catalysts were represented in Figure 58 to investigate the electrochemical properties of the Ir@CeO$_2$, Ir@TiO$_2$, and Ir@ZrO$_2$ towards OER at RT in 1.0 M KOH. The voltammograms of metal oxides (TiO$_2$, ZrO$_2$, and CeO$_2$) on GCE and bare GCE were also given for comparison sake. As seen in Figure 60, bare MO$_2$'s and bare GCE were found to be inactive while the synthesized Iridium catalysts (Ir@CeO$_2$, Ir@TiO$_2$, and Ir@ZrO$_2$) were found to show activity towards OER. Based on the Tafel slopes, the activity order can be represented as Ir@CeO$_2$ (93.4 mV.dec^{-1}) > Ir@ZrO$_2$ (281.0 mV.dec^{-1}) > Ir@TiO$_2$ (292.3 mV.dec^{-1}).
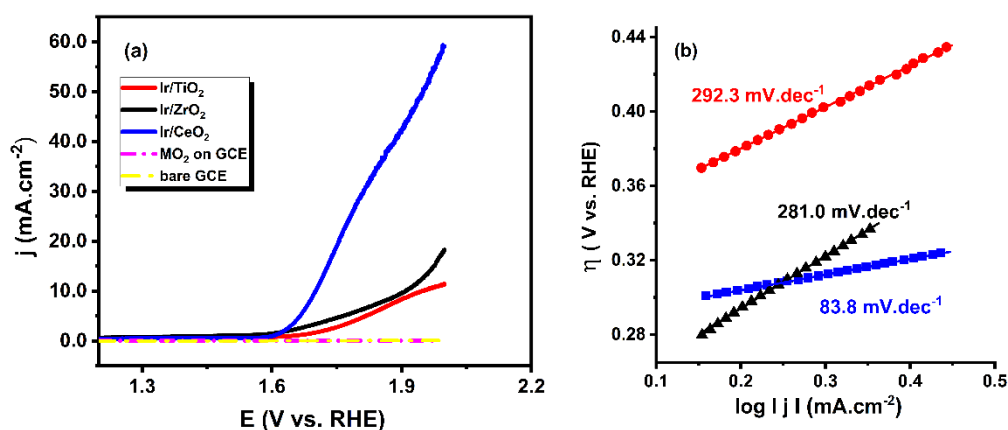
Figure 58. a) IR corrected LSV curves for bare GCE, metal oxides on GCE (MO$_2$:CeO$_2$, TiO$_2$, and ZrO$_2$), Ir@TiO$_2$, Ir@ZrO$_2$, and Ir@CeO$_2$, b)Tafel slope analysis of corresponding electrocatalysts

As given in Table 16, the onset potentials of these three catalysts were found to be quite similar (1.552, 1.554, and 1.598 V vs RHE for Ir/CeO$_2$, Ir/ZrO$_2$, and Ir/TiO$_2$, respectively). However, the overpotential (η_{10} = 0.379 V vs. RHE) and Tafel slope (b= 93.4 mV.dec^{-1}) values of Ir/CeO$_2$ were found to be highly better than the values belonging to Ir/ZrO$_2$ (η_{10} = 0.600 V vs. RHE and b= 281.0 mV.dec^{-1}) and Ir/TiO$_2$ (η_{10} = 0.640 V vs. RHE and b= 292.3 mV.dec^{-1}).

107

In practice j_0 is not the most suitable figure of merit to compare electrocatalysts since small differences in the Tafel slopes, compounded with a long extrapolation over more than 200 mV could yield distorted results. It would be best to compare the performance by means of the potential at a fixed small current density. Thus, the onset potential and overpotential values are better Figure of merits, especially if very different electrocatalysts exhibiting different Tafel slopes were compared. Considering all the onset potentials (η_0), Tafel slopes, and overpotentials at 10 mA.cm^{-2} (η_{10}) represented in Table 16, Ir/CeO$_2$ provides the highest activity among Ir/ZrO$_2$, Ir/TiO$_2$. The reason of the higher activity of the Ir/CeO$_2$ could be the more favorable metal support interaction due to the defects of Ce(III). These defects might enhance the metal substrate interaction by causing excess negative charge on the surface of oxide.[81,92, 265]

Table 16. Tafel slopes, onset and overpotential values at 10 mA.cm^{-2} of as-synthesized catalysts.

catalysts	η_0 (V vs. RHE)	η_{10} (V vs. RHE)	b (mv.dec^{-1})	j_0 (mA.cm^{-2})
Ir/CeO$_2$	1.552	0.379	93.4	0.0004
Ir/ZrO$_2$	1.554	0.600	281.0	0.1423
Ir/TiO$_2$	1.598	0.640	292.3	0.0959

Compared to the iridium based catalysts previously reported in the literature shown in Table 17, Ir@CeO$_2$ shows promising results considering the Ir amounts, Tafel slopes, onset potentials, and overvoltage values that must be applied to reach a current density of 10 mAcm^{-2}. Although there are catalysts that perform better than Ir@CeO$_2$ among the catalysts listed in Table 17, it can be said that Ir@CeO$_2$ has more advantages when the synthesis methods are compared. The synthesis steps of most of the catalysts require high temperatures (400-900 ºC), harsh steps such as calcination (Entry 10), annealing (Entry 19), pyrolization (Entry 7) and harmful chemicals, however, in the synthesis of Ir@CeO$_2$ the reaction temperature was kept at room temperature and water was preferred as a solvent.

Table 17. Several Ir-containing OER electrocatalysts reported in alkaline media.

entry	Catalysts	Loading density ($\mu g.cm^{-2}$)	mass activity at 10 mA cm^{-2} (A.mg$_{ir}^{-1}$)	b (mV.dec^{-1}) (LSV)	η_0 (V vs. RHE)	η_{10} (V vs. RHE)	ref.
1	**Ir@CeO₂**	**51.6**	**0.118**	**93.4**	**1.552**	**0.379**	**This work**
2	Ir@Co₄N NF	285	0.65@ 1.6 V vs. RHE	94.5	~1.50	0.310	334
3	IrO₂	-	0.01	47.7	-	0.380	335
4	Co@Ir@NC10%	-	0.50	73.8		0.280	336
5	Ir@Ni oxide	64	0.47	44.0	-	0.264	337
6	Ti/Ir$_{0.05}$Co$_{0.05}$Sb$_{0.1}$Sn$_{0.8}$O$_x$	-	-	53.0	-	0.416	338
7	Ir-MnOx/N-C	-	3.71	47.0	-	0.250	339
8	Ir-Cu	-	0.12	38.0		0.340	340
9	Ni-(Ebonex/Ir)	-	0.03	56.3	-	0.367	341
10	Ir(III)–Co(II) organophosphonate (1@600)	-	-	59.1	-	0.317	342
11	Ir$_{0.25}$W$_{0.75}$	-	-	85.0	-	0.309	343
12	Ir	-	-	-	-	0.430	146
13	IrO₂@NiO/NF	2000		41.8	~1.50	0.278	344
14	Ir-CoxNi1-xO/NF	-	-	48.0	~1.48	0.260	345
15	Ir-NiCo LDH	-	-	41.2	~1.45	0.192	346
16	₉₀PtOy-₁₀IrO₂	-	-	55.0	1.521	0.480	347
17	IrNi/ZNC	-	-	85.0	~1.52	0.322	348
18	IrO₂@Ir-MOF	20.4	~0.5	110.6	1.36	0.284	349
19	Ir@NG-750	280	-	64.0	~1.45	0.273	350
20	NiFeIr$_{0.03}$/Ni	-	-	44.6	~1.45	0.200	351
21	Ba$_{0.9}$Sr$_{0.1}$Co$_{0.8}$Fe$_{0.1}$Ir$_{0.1}$O$_{3-\delta}$	425	.	61.2	~1.50	0.300	352
22	Pt–IrO₂/CC	36.6	-	35.0	~1.50	0.209	353

Table 17 (continued)

23	NiIr@N-C/NF	800	-	82.2	~1.55	0.329@50	354
24	Ir-NR/C	14	0.374@1.5 V vs. RHE	60.3	~1.52	0.296	355
25	FF–NaCl–Ir–P	-	-	44.4	~1.45	0.169	356
26	Ir_{16}–PdCu/C	-	1.01@1.5 V vs. RHE	48.9	~1.55	0.284	357
27	Ir_{SA}-N_2iP	-	12@1.5 V vs. RHE	90.1	~1.40	0.149	358
28	FeIr@NF	-	-	64.8	~1.50	0.220	359
29	Ir–Co(OH)$_2$-5	-	-	69.9	~1.45	0.262	360
30	Ir-Ni(OH)$_2$ nanocage	-	-	75.5	1.42	0.243	361
31	Ir-Te NWs	142.85	-	38.1	~1.47	0.248	362

The turnover frequency (TOF) data were determined to further analyze the intrinsic activity of the Ir@CeO$_2$ catalyst. The overpotentials required to get the TOF values 0.048 s^{-1} [(at 5 mA.cm^{-2}), 0.096 s^{-1} (at 10 mA.cm^{-2}), and 0.480 s^{-1} (at 50 mA.cm^{-2}) are 344, 379, and 631 mV, respectively. The TOF results of Ir@CeO$_2$ are similar to the catalysts reported in the literature. For example NiFeIr$_{0.03}$/Ni exhibit ~0.0505 s^{-1} value at 270 mV. [351] In fact, it can be said that the TOF values of the Ir@CeO$_2$ catalyst with ultralow noble metal loading are at least 3 times higher when compared to catalysts containing earth abundant metals such as Ni-Co-LDH (at 419mV TOF= 0.002 s^{-1}) [306], Au@Co$_3$O$_4$ (at 350 mV TOF= 0.015 s^{-1}),[307] CoNS (at 300mV TOF= 0.003s^{-1})[305].

To understand the OER mechanism via determining the Tafel slope, EIS is also an important method since the data can just represent the charge transfer kinetics of the electrode reaction without accounting for resistance of catalyst. The Nyquist plots of Ir@CeO$_2$ given in Figure 61 were recorded from 700 mV to 800 mV with 20 mV interval in 1.0 M KOH. There are two semicircles in a Nyquist plot of Ir@CeO$_2$. Small semicircles can be seen due to porosity of surface or adsorbed species on GCEs in the high frequency range, and they are potential independent. On the other hand, in the low frequency region, the semicircles become smaller and smaller due to the charge transfer resistance as the applied potential increases.

The EIS results were fitted the equivalence circuit model given in and inset of Figure 59. Total charge transfer resistance (R_{CT}) for oxygen evolution reactions decreases with increasing potential, indicating that the transfer kinetics of electrons increase as the potential applied increases.

One of the aim of the EIS method is determining the Tafel slope which can be found from the slope of log ($1/R_{CT}$) vs. η plot. Tafel slopes from polarization curves support the results from EIS. As seen in Figure 61 (b), Tafel slope of Ir@CeO$_2$ was found as 91.13 mV.dec^{-1} and this value is consistent with the result obtained from the LSV curves (93.4 mV.dec^{-1}). At the Ir@CeO$_2$-electrolyte interface, interfacial charge-transfer mechanism dominates the Bode plot (Figure C.11). The relaxation, which is associated to the charge transfer kinetics, is attributed to the single peak in the Bode plot. [363,364] The phase angle maximum in the Bode plot decreased to lower values with increasing applied potentials while the R_{CT} and the time constant decrease indicating a faster charge transfer process at the Ir@CeO$_2$–electrolyte interface (Figure C11 (a) and (b)).[365] These changes in Bode and Nyquist plots were attributed to the OER process, which had an onset potential of 1.55 V.
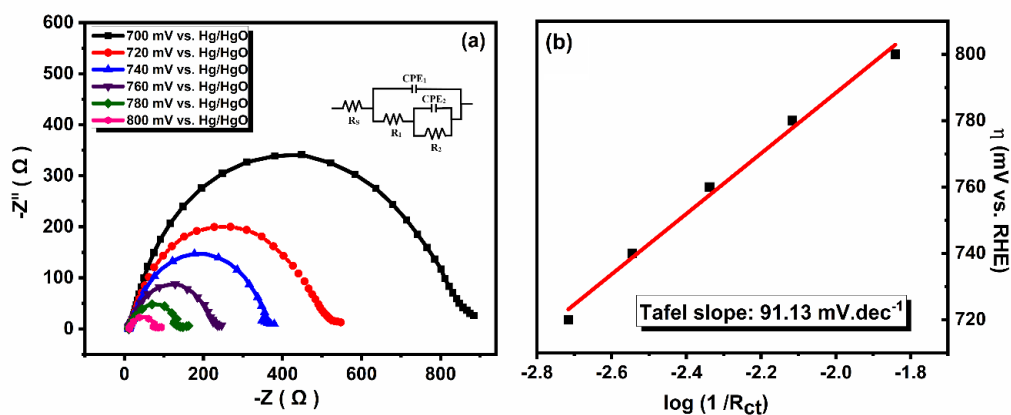
Figure 59. a) Electrochemical impedance spectroscopy results of Ir@CeO$_2$ at 700mV - 800 mV vs. Hg/HgO potential range and b) Tafel graph obtained using the data from EIS.

ECSA was estimated by dividing the double-layer capacitance (which can be determined from EIS (Figure 59 (a)) or CV (Figure 60 (a)) by the C_s (0.04 mF.cm^{-2} in alkaline media[304]). First of all, C_{DL} was calculated from the non-faradic area of the CV (0.10- 0.20 V vs. Hg/HgO). Graphing the j_a as a function of scan rate provides a straight line with a slope equal to C_{DL}. Multiple CV experiment for Ir@CeO$_2$ was given in Figure 60 (a). As shown in Figure 60 (b), the C_{DL} for Ir@CeO$_2$ was found to be 0.026 mF. For Ir/CeO$_2$ catalyst, ECSA value was found as 0.65 cm^2 in 1 M KOH. Secondly, the C_{DL} estimated from the highest point of the Nyquist curve at overpotential required to reach 10 mA.cm^{-2} was found to be the same as the C_{DL} obtained from CV.
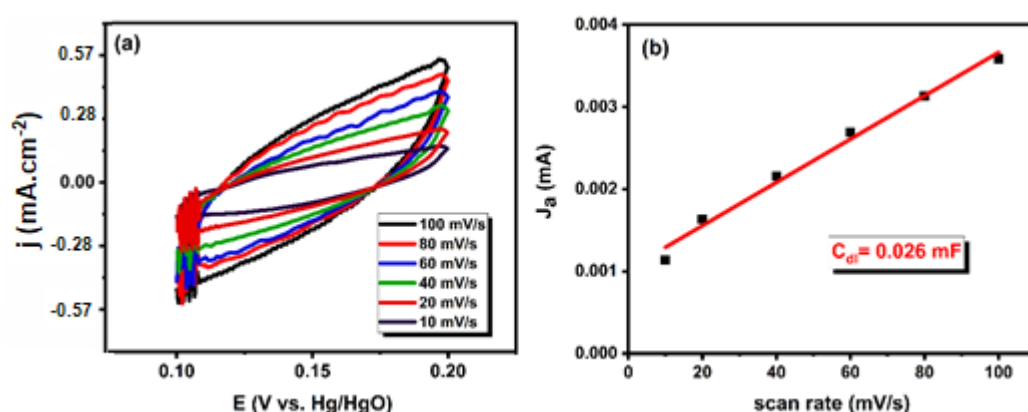
Figure 60. a) The multi-scan CV curves of Ir@CeO$_2$ acquired in 1.0 M KOH at different scanning rates from 10, to 120 mVs^{-1} and b) current densities as a function of scanning rates with the slope corresponding to the C_{DL} value.

The electrochemical OER activity was further investigated at different temperatures. The Tafel analyses of Ir@CeO$_2$ in 1.0 M KOH at 299, 304, 309, 314, 319, 324, and 329 K are shown in Figure 61 (a). The currents at the same potential value increase with the increasing temperature due to an increase in the current carrying ions' migration rate in the lower viscous medium. The Tafel slopes are approximately the same for all of the applied temperatures and there is a linear relationship between the logarithm of |j| and η, as seen in the Figure 61 (a). The apparent thermal activation energies were determined using Arrhenius plot, which was obtained from the Arrhenius equation given in Appendix C Table A3.

The activation energy indicates the kinetic barriers involved in the OER mechanism, and the apparent thermal activation energy for Ir@CeO_2 was determined as 37.476 kJ.mol^{-1} based on the slope of the Arrhenius plots (Figure 61 (b)). It is noteworthy that the observed E_a value for OER on Ir@CeO_2 (37.476 kJ.mol^{-1} at E=720 mV vs. Hg/HgO) are lower when compared to the catalysts in the literature such as Fe_3O_4 (E_a = 109 kJ mol^{-1}) [366], $NiCoO_x$ (E_a = 71 kJ.mol^{-1})[320], $CoFe_{1.2}Cr_{0.8}O_4$ (E_a = 67.3 kJ mol^{-1} at E=560 mV)[367], Adams-RuO_2 (E_a = 49±1 kJ mol^{-1})[368], $Cu_{0.9}Co_{2.1}O_4$ (E_a = 45.19 kJ mol^{-1})[369], oxide coated $Co_{50}Ni_{25}Si_{15}B_{10}$ amorphous alloy (E_a= 40 kJ mol^{-1})[370], $La_{0.6}Cu_{0.4}CoO_3$ (E_a= 46 kJmol^{-1})[323] but it was higher than those $NiFeO_x$/NF (25 ± 12 kJmol^{-1}), [319] and NiFe hydroxide (18.1 kJ.mol^{-1})[321].
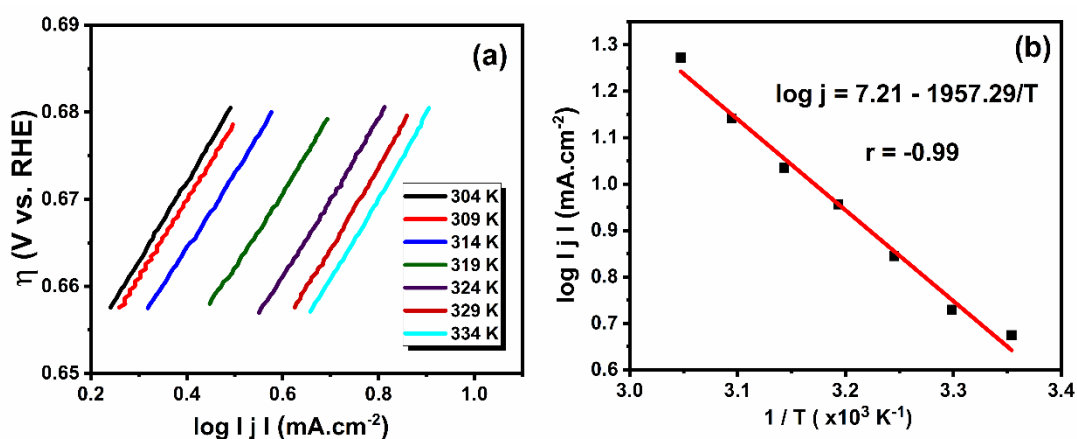
Figure 61. Tafel plots of the Ir/CeO_2 catalyst in 1.0 M KOH at various temperatures (a) and the related Arrhenius plot (b).

The transfer coefficient of Ir/CeO_2 was calculated as described in the OER section '*3.2.1.3.Electrochemical studies of Co/TiO₂, Co/ZrO₂, Co/CeO₂*' and the definitions of terms were given in the relevant part. Table 18 shows that while there is an increase in the predicted values of the transfer coefficients with the increase of the reaction temperature. On the other hand, the Tafel slope values decrease at high temperatures. The calculated transfer coefficients and the Tafel slope values indicate that the lattice oxygen process (Table Appendix C4) becomes more competitive with the oxygen-evolving mechanism for Ir/CeO_2. The lattice oxygen evolution process has been linked to enhanced OER activity and catalyst dissolution on metal oxide structures. The inclusion of the lattice oxygen in the OER may have a major impact on the electrochemical stability of iridium oxide.[371] According to this mechanism, the

removal of a lattice oxygen atom during OER creates an oxygen vacancy. This defect in the lattice structure can either be repaired by a reoxidation step or cause the iridium atoms to dissolve.[41] Due to the thermodynamic instability of the oxygen atoms in the metal oxide lattice, any metal oxides can become unstable under the oxidizing conditions of the OER.

According to the Tafel slope values, the rate determining step of the oxygen formation mechanism for Ir/CeO$_2$ in alkaline medium can be considered as the third reaction step (M–O$^-$ + OH$^-$ → M–O-O-H$^-$ + e$^-$) proposed by Krasil'shchikov. (see introduction chapter for the recommended route) [38,372]

Table 18. Transfer coefficients and Tafel slopes of Ir/CeO$_2$ at different temperatures.

Temperature K	Ir/CeO$_2$	
	Tafel slopes (V.dec^{-1})	α_a
298	0.0934	0.6335
303	0.0914	0.6582
308	0.0887	0.6894
313	0.0864	0.7193
318	0.0852	0.7410
323	0.0848	0.7562

The stability along the reaction is a critical factor for the evaluation of the electrocatalytic performance of the catalysts in OER. Therefore, chronopotentiometry experiments were carried out to conduct the stability tests for the Ir/CeO$_2$ catalyst (see Figure 62b). During 1 h, a constant current with a 0.7 mA value was applied to the Ir/CeO$_2$ catalyst. Figure 62 shows the LSVs of Ir/CeO$_2$ recorded before and after stability measurements. As seen in Figure 62a, there is a noticeable electrocatalytic activity loss for Ir/CeO$_2$ during the 1 hour stability test. After the stability experiment of the Ir/CeO$_2$ catalyst, anodic shifts of 39 mV and 119 mV were recorded in the onset and overpotential values, respectively, and the change in Tafel slope was determined to be 46.6 mV.dec^{-1}. As can be seen from the Figure 62b, there is a negligible change in the potential in the first 40 minutes. The fluctuation in the potential value at about the 40th minute may be attributed to both the formation of the oxygen bubbles on the surface and the desorption of them from the surface of the electrode. In fact, gas

bubbles periodically nucleate, grow, and finally detach from the surface. As a result of this detachment, it was observed that the catalytic activity was greatly reduced by taking into account the overvoltage corresponding to the value of 10 mA.cm^{-2}. The decrease in the catalyst performance might be caused by the buildup of bubbles on the surface of the electrode.[373] The bubbles generate surface obstruction and the formation of the dead region, which causes the electrical resistance, and thus they deteriorate the activity of the catalyst.[314] Another reason for the catalytic activity loss could be the dissolution of iridium metal during the oxygen evolution.[41,374] OER competes with the lattice oxygen evolution reaction (LOER) and, under the anodic potential circumstances, LOER is thought to be the major cause of catalyst instability.[375,376,377]
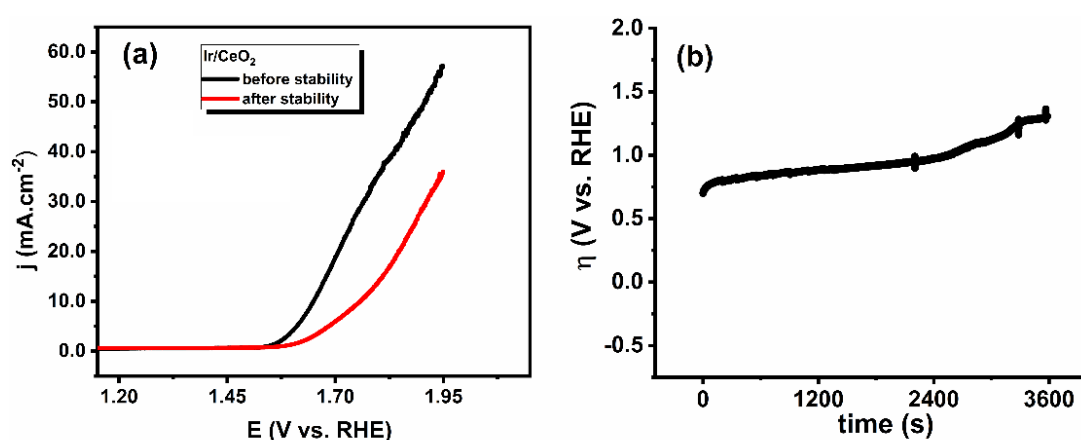
Figure 62. (a) Voltammograms taken before and after the stability test of Ir@CeO$_2$ (b) Chronopotentiometry measurement in 1.0 M KOH at 10 mA.cm^{-2}

The polarization curves for Ir/CeO$_2$ (Figure 63 (a)) were collected at 0.2 , 0.4 , 0.6 , 0.8 , and 1.0 M KOH solutions to investigate the influence of the concentration of hydroxyl ions on OER performance. Figure 63 (a) indicated that the highest current density was obtained in 1.0 M KOH solution among the other solutions. The low activity at low KOH concentrations might be attributed to inadequate OH$^-$ adsorption on the active sites of iridium catalyst. The high charge transport resistance hampers the movement of hydroxyl ions from the bulk electrolyte to the electrochemical double layer. [324] When the concentration of hydroxyl ions increases, OH$^-$ transfer between the the electrochemical double layer and bulk solution becomes easier, resulting in a gradual decrease in the Tafel slope values (Figure 63 (b)).

However, at high concentration of hydroxyl ions which are higher than 1.0 M, the active sites of the catalyst could be blocked by the evolved O_2 gas, which may result in a significant ionic transport resistance at high electrolyte concentrations, and thus, the charge transport restriction might be observed.
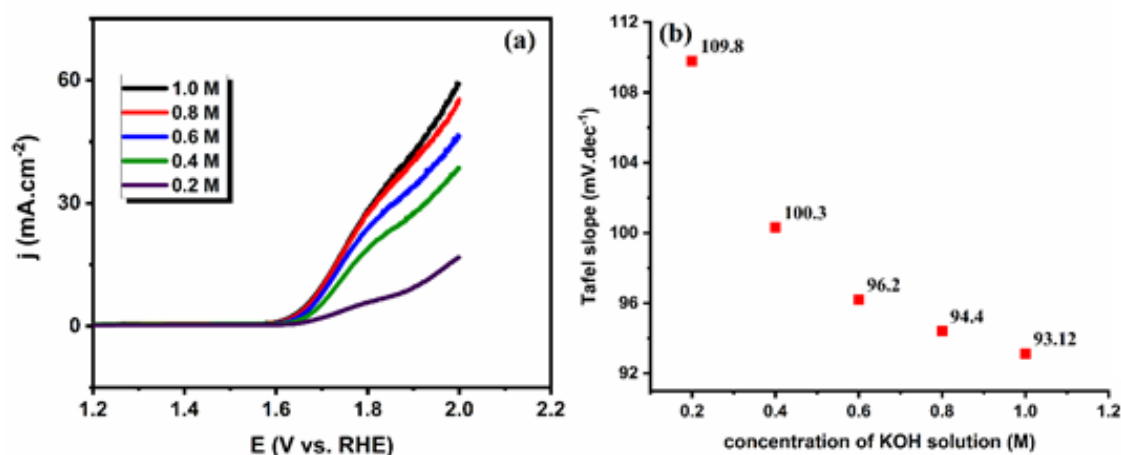
Figure 63. a) LSV curves of Ir/CeO$_2$ and b)corresponding Tafel slopes at different KOH solutions.

3.2.2.4. Outlook of the synthesis, characterization and electrochemical studies of Ir/TiO$_2$, Ir/ZrO$_2$, Ir/CeO$_2$

To investigate the performance of the iridium for OER, Ir nanoparticles were effectively impregnated onto the surface of metal oxides (MO$_2$: TiO$_2$, ZrO$_2$, and CeO$_2$) supports. The electrochemically active surface areas and the rate of charge transfer were improved with conductive support materials by lowering charge resistance and reducing particle size. As prepared iridium catalysts were found to be show activity towards OER. The onset potentials of these catalysts were found quite similar (1.552, 1.554, and 1.598 V vs RHE for Ir/CeO$_2$, Ir/ZrO$_2$, and Ir/TiO$_2$, respectively) however, the overpotential (η_{10} = 0.379 V vs. RHE) and Tafel slope (b= 93.4 mV.dec^{-1}) values of Ir/CeO$_2$ were found highly better than the values to Ir/ZrO$_2$ (η_{10} = 0.600 V vs. RHE and b= 281.0 mV.dec^{-1}) and Ir/TiO$_2$ (η_{10} = 0.640 V vs. RHE and b= 292.3 mV.dec^{-1}). The reason of the higher activity of the Ir/CeO$_2$ could be the more favorable metal support interaction due to the defects of Ce(III). These defects might enhance the metal substrate interaction by causing excess negative charge on the surface of oxide. On the

116

other hand, there is a noticeable electrocatalytic activity loss for Ir/CeO_2 during stability test especially after 2400 s. The reason of the catalytic activity loss could be the dissolution of iridium metal during the oxygen evolution.[374] OER compete with the LOER and under anodic potential circumstances, LOER is thought to be the major cause of catalyst instability. Moreover that, the instability of Ir/CeO_2 could also be associated with blockage caused by bubbles accumulating on the surface.

3.2.3. Electrocatalytic activity of Rh NPs supported on MO_2

3.2.3.1. Effect of metal oxides on the performance of Rh catalysts

Since the ceria as a supporting material shows the best performance when combining with noble metals in our studies so far, only Rh/CeO_2 has been studied for OER in alkaline media. 4% Rh/CeO_2 catalyst prepared for HER was used for OER studies. Their characterizations were reviewed under the subheading '3.1.1.5. Characterization of Rh/CeO_2'.

3.2.3.2. Electrochemical studies of Rh/CeO_2

Rhodium metal was found to be unstable in alkaline solution. Rh in Rh/CeO_2 tends to dissolve at high potentials. The onset potential of the OER also corresponds to the potential at which dissolution begins. As seen in Figure 64, Rh/CeO_2 loses almost all of its activity in alkaline medium in 10 scans. The onset potential of Rh/CeO_2 at the first scan was found as 1.726 V, the overpotential that require to reach 10 $mA.cm^{-2}$ is 560 mV vs. RHE (the potential is equal to 1.790 V vs. RHE) and the Tafel slope was calculated as 152 $mV.dec^{-1}$.
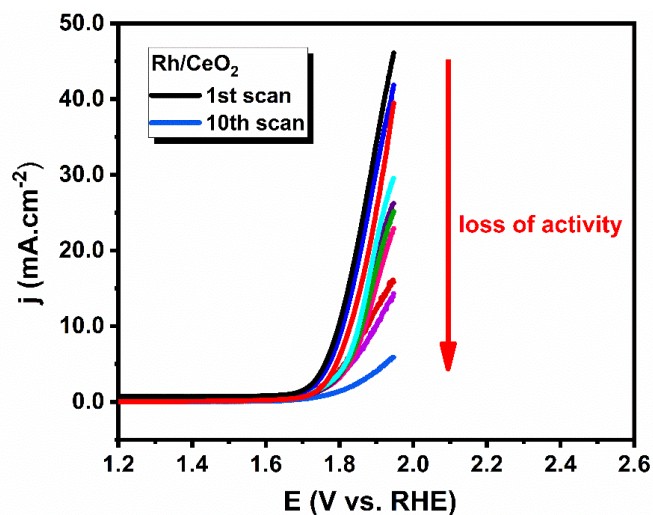
Figure 64. LSV scans of Rh/CeO$_2$ in 1.0 M KOH

The electroactive surface area of Rh/CeO$_2$ was estimated from multi CV experiment and found to be extremely low (0.425 cm^2) (Figure 65).
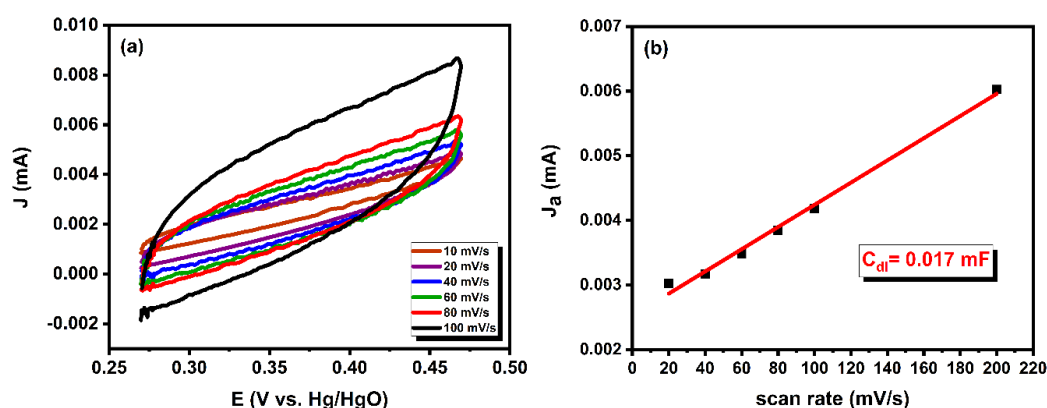
Figure 65. (a) The multi-scan CV curves of Rh@CeO$_2$ acquired in 1.0 M KOH at different scanning rates from 10, to 100 mVs^{-1} and (b) current densities as a function of scanning rates with the slope corresponding to the C$_{DL}$ value.

In aqueous electrolytes, three situations may be identified based on the selected potential and pH: (a) the metal is assumed to be immune to corrosion if the potential is below the metal oxidation potential; (b) at higher potentials, it can be passivated/protected by development of a stable oxide layer; or (c) it dissolves. Since the onset potential of Rh/CeO$_2$ for OER is above the unstable oxide formation potential, dissolution occurred from these three states and Rh/CeO$_2$ could not be used as an active catalyst in the OER.

3.2.4. Conclusions about the performance of group 9B transition metal catalysts towards oxygen evolution reaction

Although the dissolution problem of noble metals is more common in an acidic environment during oxygen evolution reactions, it also occurs in an alkaline environment. In the literature, dissolution phenomena of noble metals have been investigated by pearbaux diagrams[378], thermodynamic[376] and kinetic experiments[379]. The surface processes during the OER and correlated changes of the oxidation states lead to dissolution. During the non-equilibrium process of the OER, the oxidation states of metal catalysts are continuously changed. Accordingly, the dissolution rate is a question of OER mechanisms and kinetics.

As represented in Table 19, among the Co, Rh and Ir metals, Co was found to show high activity and stability in OER, while Rh and Ir metals were found to be active but not stable. Since the onset potential of Rh/CeO_2 is about 200 mV ahead of Ir/CeO_2, Rh loses its activity to a great extent compared to Ir as of the first scan. The reason why iridium loses its activity after applying a constant current of 10 $mA.cm^2$ for about 40 minutes is that the accumulation of bubbles on the surface increase the surface resistance and require more and more potential to generate 10 $mA.cm^2$ current. As the required potential increases, the amount of dissolution increases and accordingly the iridium loses its activity. On the other hand, all three cobalt catalysts (Co/CeO_2, Co/ZrO_2 and Co/TiO_2) exhibited impressive performance for the oxygen evolution reaction in an alkaline environment with low overpotentials (0.368, 0.371, and 0.385 V), low Tafel slopes (65.0, 67.9, and 70.8 $mV.dec^{-1}$), high TOF values, and considerable durabilities. The enhanced OER activity in Co/MO_2 (M= CeO_2, ZrO_2, and TiO_2) catalysts appears to originate from smaller R_{CT}, smaller particle size and higher electrochemical active sites than commercial Co_3O_4 and eis.

Among those three cobalt based catalysts, because of the highest ECSA, Co/CeO_2 was found to have slightly better performance.

Table 19. Comparison of the OER performance of the metals

Catalysts	Tafel slope (mV.dec^{-1})	η_0 (V vs. RHE)	η_{10} (V vs. RHE)	ECSA (cm^2)	durations of the stability tests	after stability experiments		
						η_0	η_{10}	Tafel
Co/TiO$_2$	67.9	1.594	0.390	5.63	3h	1.644	0.452	89.4
Co/ZrO$_2$	70.8	1.577	0.373	7.93	3h	1.617	0.423	82.3
Co/CeO$_2$	65.0	1.575	0.365	11.15	3h	1.610	0.400	68.3
Co$_3$O$_4$	77.0	1.655	0.455	1.20	1h	1.665	0.481	89.0
Ir/TiO$_2$	292.3	1.598	0.640	-	1h	-	-	-
Ir/ZrO$_2$	281.0	1.554	0.600	-	1h	-	-	-
Ir/CeO$_2$	93.4	1.552	0.379	0.65	1h	1.591	0.498	140.0
Rh/CeO$_2$	152.0	1.726	0.560	0.43	-	-	-	-

In addition to the OER performances of metals in the alkaline media, HER performances have also been studied and the results were given in Table 20. The cell potentials were calculated and catalysts were not found suitable for overall water splitting. In the literature, higher current densities have been obtained at lower cell potentials for example, the 3D core-shell heterostructure of WS$_2$@Co$_3$S$_4$ NW/CC can deliver 100 mA cm^{-2} at a cell voltage of 1.56 V in alkaline solution for overall water splitting.[380]

Table 20. Required cell potentials for the overall water splitting. (Potentials were given as V vs. Hg/HgO in the table)

catalysts	η_0 (HER)	η_{10} (HER)	η_0 (OER)	η_{10} (OER)	E_{cell} according to onset potentials (V)	E_{cell} according to overpotentials (V)
Ir/CeO$_2$	-1.324	-1.370	0.637	0.694	1.961	2.064
Co/CeO$_2$	-1.370	-1.441	0.660	0.680	2.030	2.121

CHAPTER 4

CONCLUSION

At the beginning of the detailed investigations of the catalysts, the factors affecting the activity of rhodium nanoparticles towards hydrogen evolution reactions were examined. The counter electrode effect, the effect of the supporting metal oxide, the effect of the loading amount and the effect of the loading density on the working electrode were investigated.

Pt wire and graphite rod were used comparatively as counter electrodes in the electrochemical cell to observe whether there was metal dissolution in acidic media. Electrocatalytic activity of 0.5 % Rh/TiO_2 modified GCE was investigated by recording polarization curves in 0.5 M H_2SO_4 solution. Since the electrocatalytic activity of the modified electrode was found to be improved gradually after potential cycling between -0.5 and 0.5 V vs. Ag/AgCl when using Pt wire, Rh/TiO_2 modified GCE was subjected to the potential cycling until no more change was noted in the onset potential.

- ➢ The results show that there were Pt dissolution and deposition on surface of the Rh/TiO_2 during 2000 cycle pretreatment.
- ➢ The increase in the activity of catalyst were attributed to cathodic deposition of Pt originating from anodic dissolution of Pt counter electrode.
- ➢ It was also found that, besides metal-support interaction metal-metal interactions are also important in HER. Therefore, the observed improvement in the electrocatalytic activity of Rh/TiO_2 can be attributed not only to Pt deposition but also Rh-Pt interaction.
- ➢ By using very low amount of Rh, highly good results can be obtained and these results are due to the bimetallic relationship of Pt with Rh.

- Rh/TiO$_2$-2000 shows superior electrocatalytic activity in 0.5 M H$_2$SO$_4$ solution for HER with ultralow mass loading of Rh (3.79 µg.cm^{-2}). Rh/TiO$_2$-2000 provides very low Tafel slope (32 mV.dec^{-1}), low overpotential (37 mV@ -10 mA.cm^{-2}), high exchange current density (0.686 mA.cm^{-2}) and high TOF values (11.45 s^{-1}).

- The Faradaic efficiency of Rh/TiO$_2$-2000 was found as 94% after applying 18000 mC. The Tafel slope and overpotential at -10 mA.cm^{-2} values are found to be nearly the same with the one obtained by using benchmark Pt/C catalyst (75 µg.cm^{-2}).

- Rh/TiO$_2$-2000 provides higher j$_0$ (0.686 mA.cm^{-2}) than that of Pt/C catalyst (0.541 mA.cm^{-2}). Rh/TiO$_2$-2000 on GCE provides high stability even after 10000 cycle in HER. There is no noticeable change in the onset potential (29 mV), overpotential (40 mV@ -10 mA.cm^{-2}), and Tafel slope (33.1 mV.dec^{-1}) after the stability test. [89]

The Pt counter electrode was replaced by graphite electrodes and improvement after treatment was not observed when using graphite rod as a counter electrode and catalyst lost some of its electrochemical activity. Graphite electrode was used as a counter electrode during the HER studies in order to prevent platinum contamination and to evaluate the HER performance of group 9B metals in the acidic environment.

After observing the counter electrode effect, the effect of the supporting metal oxide, the effect of the loading amount and the effect of the loading density on the working electrode were studied.

- Ceria was found to be the better supporting material than TiO$_2$, ZrO$_2$, HfO$_2$, Al$_2$O$_3$, and SiO$_2$ towards HER in acidic media. Activity order was determined as CeO$_2$ > TiO$_2$> ZrO$_2$> Al$_2$O$_3$> HfO$_2$ > SiO$_2$.

- It was found that the % loading (2% - 5%) did not significantly affect the catalytic activity when the loading density was kept constant.

- It was also observed that when the loading density was increased, the pouring of the catalyst increased and accordingly the stability decreased.

- Considering all the results, 4% loading and 85.7 µg.cm^{-2} loading density were chosen for the other catalysts .

The findings of the HER studies can be summarized as follows,

➢ Rhodium and iridium based NPs were successfully formed on the surface of metal oxides by simple impregnation technique and characterized by TEM, TEM-EDX, XRD and ICP-OES.

➢ Among these catalysts, Ir/CeO_2 and Rh/CeO_2 have been found very efficient electrocatalysts for HER in acidic environment.

➢ Electrochemical tests were performed without using any binder such as nafion and graphene.

➢ Rh/CeO_2 provides a low Tafel slope value (34 $mV.dec^{-1}$) and high exchange current density (0.527 $mA.cm^{-2}$) with a low overpotential of 42 mV at j = 10 $mA.cm^{-2}$. Rh/CeO_2 with a very low mass loading 85 $\mu g.cm^{-2}$ provides also exceptional electrocatalytic activity and durability even after 10 000 cycle.

➢ Ir/CeO_2 provides -13 mV onset potential, -23 mV overpotential at 10 $mA.cm^{-2}$, 2.69 $mA.cm^{-2}$ exchange current density and 38.7 $mV.dec^{-1}$ Tafel slope values which were better than the ones obtained by Ir/TiO_2 and Ir/ZrO_2.

➢ Ir/CeO_2 shows higher intrinsic electrocatalytic activity (TOF= 1.95s^{-1} at 100 mV) than that of Rh/CeO_2 (TOF= 1.18 s^{-1} at 100 mV) and commercial Pt/C (TOF= 1.18 s^{-1} at 100 mV) due to the higher electroactive surface area.

➢ The electrocatalytic stability test shows that Ir/CeO_2 exhibits an outstanding stability for HER in 0.5 M H_2SO_4 even after 20 000 CV cycles. The Tafel slopes determined before and after stability test are found to be nearly the same.

➢ Among the catalysts, although Rh/CeO_2 has relatively lower Tafel slope, Ir/CeO_2 was found more efficient and stable than Rh/CeO_2. Co/CeO_2 shows very low activity and stability due to the low $M-H_{ads}$ energy.

➢ Although Co/CeO_2 showed better activity than Co/ZrO_2 and Co/TiO_2, it was observed that it could not maintain this activity. Co/CeO_2 lost its activity to a large extent even in the 2nd and 3rd LSV measurements taken consecutively. The reason of this activity loss could be explained via corrosion or dissolution of non-noble metal electrocatalysts under strong acidic conditions

➢ For Co/CeO_2, the rate determining step is adsorption step (Volmer step). For both Rh/CeO_2 and Ir/CeO_2, rate is determined by chemical or electrochemical desorption step.

> Considering the high stability, facile preparation method and low metal loading binder free Ir/CeO_2 and Rh/CeO_2 were found promising electrocatalyst for hydrogen evolution from water splitting and it will provide significant contribution in the field. [88, 237]

As compared with HER, OER has more sluggish kinetic with the four-electron transfer. M-OH, M-O, and M-OOH (where M represents the active sites on the surface) adsorption intermediates occur during the reaction in an alkaline environment. Electrochemical water splitting kinetic is seriously slow down due to considerable energy barriers causing from HER with two-electron transfer and OER with four-electron transfer reactions. Group 9B metals impregnated on metal oxides were also studied in OER to increase the rate of water splitting by decreasing onset potential, overpotential and Tafel slope.

The findings of the OER studies can be summarized as follows,

> Co nanoparticles have successfully impregnated onto the titania, zirconia, and ceria surfaces by the facile and environmentally friendly method to increase the performance of the cobalt for OER.

> The rate of the charge transfer was increased via decreasing charge transfer resistance and the electrochemically active surface areas was increased also by decreasing the particle size with the conductive supporting materials.

> Without using any high temperature needed steps such as carbonization, phosphidation, pyrolization, or annealing, Co/MO_2 (M= Ce, Zr, and Ti) could be reproducibly synthesized and show excellent activity for OER.

> Co/CeO_2, Co/ZrO_2, and Co/TiO_2 catalysts exhibited impressive performance for the oxygen evolution reaction in an alkaline environment with low overpotentials (0.365, 0.373, and 0.390 V), low Tafel slopes (65.0, 70.8, and 67.9 $mV.dec^{-1}$).

> Although the commercial Co_3O_4 loses its activity to a great extent after the stability test, for the Co/CeO_2, Co/ZrO_2, and Co/TiO_2, no noticeable change was observed in Tafel slopes and overvoltages.

- The enhanced OER activity in Co/MO_2 (M= Ce, Zr, and Ti) catalysts appears to originate from smaller R_{CT}, smaller particle size and higher electrochemical active sites than commercial Co_3O_4.

- Among those Co/MO_2 catalysts, because of the highest ECSA, Co/CeO_2 was found to have slightly better performance, especially in terms of exchange current density.

- According to the Tafel slopes, onset and overpotentials, exchange current densities, TOFs, Faradaic efficiencies, and stabilities, we believe that Co impregnated metal oxides (Co/CeO_2, Co/ZrO_2, and Co/CeO_2) catalysts could be a promising class of electrocatalysts for OER. [381]

- This work also opens up an avenue for designing inexpensive, earth-abundant, and highly active OER electrocatalysts via using different non-noble metals or changing supporting materials.

- As prepared iridium catalysts were found to show activity towards OER. The onset potentials of these three Ir@MO_2 (M= Ti, Zr, and Ce) catalyst were found quite similar (~1.55 V vs. RHE) however overpotential (η_{10} = 0.379 V vs. RHE) and Tafel slope (b= 93.4 $mV.dec^{-1}$) values of Ir@CeO_2 were found highly better than the values belongs to Ir@ZrO_2 (η_{10} = 0.600 V vs. RHE and b= 281.0 $mV.dec^{-1}$) and Ir@TiO_2 (η_{10} = 0.640 V vs. RHE and b= 292.3 $mV.dec^{-1}$). [382]

- The reason of the higher activity of the Ir@CeO_2 could be the more favorable metal support interaction due to the defects of Ce(III). These defects might enhance the metal substrate interaction by causing excess negative charge on the surface of oxide.

- A noticeable electrocatalytic activity loss was observed for Ir@CeO_2 during stability test especially after 2400 sec. The reason of the catalytic activity loss were attributed to the dissolution of iridium metal during the oxygen evolution.[382]

- OER also compete with the LOER and under anodic potential circumstances, LOER is thought to be the another cause of catalyst instability.

- The instability of Ir@CeO_2 could also be associated with blockage caused by bubbles accumulating on the surface.

➤ Nevertheless, Ir@CeO$_2$ could be a promising class of electrocatalysts for OER with the low overpotential and Tafel slope, and increased durability.

This thesis provided a rational, fairly easy and eco-friendly way to obtain high-performance electrocatalysts by attaching small amounts of noble or non noble metal onto supporting transition metal oxides. Moreover, this research offers up an avenue for obtaining cost the effective and high performance water splitting electrocatalysts by utilizing alternative noble or earth-abundant metals or modifying the supporting materials.

For the future work, the reaction mechanisms and the rate determining steps can be investigated in detail via computational analysis. Moreover, with this synthesis approach new catalysts can be synthesized and used for the other applications such as supercapacitors, CO$_2$ reduction and waste-water treatment.

REFERENCES

1   Chen, W.-F.; Muckerman, J. T.; Fujita, E. Recent Developments in Transition Metal Carbides and Nitrides as Hydrogen Evolution Electrocatalysts. *Chem. Commun.* **2013**, *49* (79), 8896. https://doi.org/10.1039/c3cc44076a.

2   Lewis, N. S.; Nocera, D. G. Powering the Planet: Chemical Challenges in Solar Energy Utilization. *Proc. Natl. Acad. Sci. U.S.A.* **2006**, *103* (43), 15729–15735. https://doi.org/10.1073/pnas.0603395103.

3   Demirbaş, A. Hydrogen and Boron as Recent Alternative Motor Fuels. *Energy Sources* **2005**, *27* (8), 741–748. https://doi.org/10.1080/00908310490450836.

4   Balat, M.; Balat, M. Political, Economic and Environmental Impacts of Biomass-Based Hydrogen. *Int. J. of Hydrog. Energy* **2009**, *34* (9), 3589–3603. https://doi.org/10.1016/j.ijhydene.2009.02.067.

5   Singh, S.; Jain, S.; Ps, V.; Tiwari, A. K.; Nouni, M. R.; Pandey, J. K.; Goel, S. Hydrogen: A Sustainable Fuel for Future of the Transport Sector. *Renew. Sust. Energ. Rev.* **2015**, *51*, 623–633. https://doi.org/10.1016/j.rser.2015.06.040.

6   V., D. Steam Reforming of Sunflower Oil for Hydrogen Gas Production. *Helia* **2007**, *30* (46), 103–132. https://doi.org/10.2298/HEL0746103D.

7   Jensen, J. 5 - Chemical Storage. In *Energy Storage*; Jensen, J., Ed.; Elsevier, 1980; 23–47. https://doi.org/10.1016/B978-0-408-01225-6.50009-2.

8   Ryu, Y.-K.; Kim, K.-L.; Lee, C.-H. Adsorption and Desorption of *n* -Hexane, Methyl Ethyl Ketone, and Toluene on an Activated Carbon Fiber from Supercritical Carbon Dioxide. *Ind. Eng. Chem. Res.* **2000**, *39* (7), 2510–2518. https://doi.org/10.1021/ie990673u.

9   Trasatti, S. Water Electrolysis: Who First? *Journal of Electroanalytical Chemistry* **1999**, *476* (1), 90–91. https://doi.org/10.1016/S0022-0728(99)00364-2.

10   Kenndler, E. Capillary Electrophoresis and Its Basic Principles in Historical Retrospect. Part 2. Electrophoresis of Ions: The Period from Its Discovery in 1800 till Faraday's Lines of Electric Force in the 1840s. *Substantia* **2021**, *5* (2), 97–120. https://doi.org/10.36253/Substantia-1312.

11   Tafel, J. Über Die Polarisation Bei Kathodischer Wasserstoffentwicklung. *Zeitschrift für Physikalische Chemie* **1905**, *50U* (1), 641–712. https://doi.org/10.1515/zpch-1905-5043.

12   Grigoriev, S. A.; Fateev, V. N. Hydrogen Production by Water Electrolysis. In Hydrogen Production Technologies; John Wiley & Sons, Ltd, 2017; 231–276. https://doi.org/10.1002/9781119283676.ch6.

13   Shiva Kumar, S.; Himabindu, V. Hydrogen Production by PEM Water Electrolysis – A Review. *Materials Science for Energy Technologies* **2019**, *2* (3), 442–454. https://doi.org/10.1016/j.mset.2019.03.002.

14   Wang, S.; Lu, A.; Zhong, C.-J. Hydrogen Production from Water Electrolysis: Role of Catalysts. *Nano Convergence* **2021**, *8* (1), 4. https://doi.org/10.1186/s40580-021-00254-x.

15   Danilovic, N.; Subbaraman, R.; Strmcnik, D.; Stamenkovic, V.; Markovic, N. Electrocatalysis of the HER in Acid and Alkaline Media. *J Serb Chem Soc* **2013**, *78* (12), 2007–2015. https://doi.org/10.2298/JSC131118136D.

16   Suen, N.-T.; Hung, S.-F.; Quan, Q.; Zhang, N.; Xu, Y.-J.; Chen, H. M. Electrocatalysis for the Oxygen Evolution Reaction: Recent Development and Future Perspectives. *Chem. Soc. Rev.* **2017**, *46* (2), 337–365. https://doi.org/10.1039/C6CS00328A.

17   LeRoy, R. L.; Bowen, C. T.; LeRoy, D. J. The Thermodynamics of Aqueous Water Electrolysis. *J. Electrochem. Soc.* **1980**, *127* (9), 1954–1962. https://doi.org/10.1149/1.2130044.

18 LeRoy, R. L. Industrial Water Electrolysis: Present and Future. *Int. J. of Hydrog. Energy* **1983**, *8* (6), 401–417. https://doi.org/10.1016/0360-3199(83)90162-3.

19 Joo, J.; Kim, T.; Lee, J.; Choi, S.-I.; Lee, K. Morphology-Controlled Metal Sulfides and Phosphides for Electrochemical Water Splitting. *Adv. Mater.* **2019**, *31* (14), 1806682. https://doi.org/10.1002/adma.201806682.

20 Gupta, S.; Patel, M. K.; Miotello, A.; Patel, N. Metal Boride-Based Catalysts for Electrochemical Water-Splitting: A Review. *Adv. Funct. Mater.* **2020**, *30* (1), 1906481. https://doi.org/10.1002/adfm.201906481.

21 Norskov, J. K.; Christensen, C. H. Toward Efficient Hydrogen Production at Surfaces. *Science* **2006**, *312* (5778), 1322–1323. https://doi.org/10.1126/science.1127180.

22 Ooka, H.; Huang, J.; Exner, K. S. The Sabatier Principle in Electrocatalysis: Basics, Limitations, and Extensions. *Front. Energy Res.* **2021**, *9*. https://doi.org/10.3389/fenrg.2021.654460

23 Cook, T. R.; Dogutan, D. K.; Reece, S. Y.; Surendranath, Y.; Teets, T. S.; Nocera, D. G. Solar Energy Supply and Storage for the Legacy and Nonlegacy Worlds. *Chem. Rev.* **2010**, *110* (11), 6474–6502. https://doi.org/10.1021/cr100246c.

24 Parsons, R. The Rate of Electrolytic Hydrogen Evolution and the Heat of Adsorption of Hydrogen. *Trans. Faraday Soc.* **1958**, *54* (0), 1053–1063. https://doi.org/10.1039/TF9585401053.

25 Seh, Z. W.; Kibsgaard, J.; Dickens, C. F.; Chorkendorff, I.; Nørskov, J. K.; Jaramillo, T. F. Combining Theory and Experiment in Electrocatalysis: Insights into Materials Design. *Science* **2017**, *355* (6321), eaad4998. https://doi.org/10.1126/science.aad4998.

26 Trasatti, S. Work Function, Electronegativity, and Electrochemical Behaviour of Metals: III. Electrolytic Hydrogen Evolution in Acid Solutions. *J. Electroanal. Chem. Interfacial Electrochem.* **1972**, *39* (1), 163–184. https://doi.org/10.1016/S0022-0728(72)80485-6.

27 Zhu, J.; Hu, L.; Zhao, P.; Lee, L. Y. S.; Wong, K.-Y. Recent Advances in Electrocatalytic Hydrogen Evolution Using Nanoparticles. *Chem. Rev.* **2020**, *120* (2), 851–918. https://doi.org/10.1021/acs.chemrev.9b00248.

28 Medford, A. J.; Vojvodic, A.; Hummelshøj, J. S.; Voss, J.; Abild-Pedersen, F.; Studt, F.; Bligaard, T.; Nilsson, A.; Nørskov, J. K. From the Sabatier Principle to a Predictive Theory of Transition-Metal Heterogeneous Catalysis. *J. Catal.* **2015**, *328*, 36–42. https://doi.org/10.1016/j.jcat.2014.12.033.

29 McKone, J. R.; Warren, E. L.; Bierman, M. J.; Boettcher, S. W.; Brunschwig, B. S.; Lewis, N. S.; Gray, H. B. Evaluation of Pt, Ni, and Ni–Mo Electrocatalysts for Hydrogen Evolution on Crystalline Si Electrodes. *Energy Environ. Sci.* **2011**, *4* (9), 3573. https://doi.org/10.1039/c1ee01488a.

30 Mahmood, J.; Li, F.; Jung, S.-M.; Okyay, M. S.; Ahmad, I.; Kim, S.-J.; Park, N.; Jeong, H. Y.; Baek, J.-B. An Efficient and PH-Universal Ruthenium-Based Catalyst for the Hydrogen Evolution Reaction. *Nature Nanotech.* **2017**, *12* (5), 441–446. https://doi.org/10.1038/nnano.2016.304.

31 Vesborg, P. C. K.; Seger, B.; Chorkendorff, I. Recent Development in Hydrogen Evolution Reaction Catalysts and Their Practical Implementation. *J. Phys. Chem. Lett.* **2015**, *6* (6), 951–957. https://doi.org/10.1021/acs.jpclett.5b00306.

32 Zeng, M.; Li, Y. Recent Advances in Heterogeneous Electrocatalysts for the Hydrogen Evolution Reaction. *J. Mater. Chem. A* **2015**, *3* (29), 14942–14962. https://doi.org/10.1039/C5TA02974K.

33 Greeley, J.; Jaramillo, T. F.; Bonde, J.; Chorkendorff, I.; Nørskov, J. K. Computational High-Throughput Screening of Electrocatalytic Materials for Hydrogen Evolution. *Nature Mater.* **2006**, *5* (11), 909–913. https://doi.org/10.1038/nmat1752.

34 Hu, M.; Ming, M.; Xu, C.; Wang, Y.; Zhang, Y.; Gao, D.; Bi, J.; Fan, G. Towards High-Efficiency Hydrogen Production through in Situ Formation of Well-Dispersed Rhodium Nanoclusters. *ChemSusChem* **2018**, *11* (18), 3253–3258. https://doi.org/10.1002/cssc.201801204.

35 Wu, L.; Xi, Z.; Sun, S. Well-Defined Metal Nanoparticles for Electrocatalysis. In *Studies in SurfaceScience and Catalysis*; Elsevier, **2017**; Vol. 177, 123–148. https://doi.org/10.1016/B978-0-12-805090-3.00004-8.

36 Spanos, I.; Masa, J.; Zeradjanin, A.; Schlögl, R. The Effect of Iron Impurities on Transition Metal Catalysts for the Oxygen Evolution Reaction in Alkaline Environment: Activity Mediators or Active Sites? *Catal. Lett.* **2020**. https://doi.org/10.1007/s10562-020-03478-4.

37 Li, X.; Zhao, L.; Yu, J.; Liu, X.; Zhang, X.; Liu, H.; Zhou, W. Water Splitting: From Electrode to Green Energy System. *Nano-Micro Lett.* **2020**, *12* (1), 131. https://doi.org/10.1007/s40820-020-00469-3.

38 Iwakura, C.; Fukuda, K.; Tamura, H. The Anodic Evolution of Oxygen on Platinum Oxide Electrode in Alkaline Solutions. *Electrochim. Acta* **1976**, *21* (7), 501–508. https://doi.org/10.1016/0013-4686(76)85139-0.

39 Negahdar, L.; Zeng, F.; Palkovits, S.; Broicher, C.; Palkovits, R. Mechanistic Aspects of the Electrocatalytic Oxygen Evolution Reaction over Ni−Co Oxides. *ChemElectroChem* **2019**, *6* (22), 5588–5595. https://doi.org/10.1002/celc.201901265

40 Lyons, M. E. G.; Brandon, M. P. Redox Switching and Oxygen Evolution Electrocatalysis in Polymeric Iron Oxyhydroxide Films. *Phys. Chem. Chem. Phys.* **2009**, *11* (13), 2203. https://doi.org/10.1039/b815338h.

41 Dam, A. P.; Papakonstantinou, G.; Sundmacher, K. On the Role of Microkinetic Network Structure in the Interplay between Oxygen Evolution Reaction and Catalyst Dissolution. *Sci. Rep.* **2020**, *10* (1), 14140. https://doi.org/10.1038/s41598-020-69723-3.

42 Matsumoto, Y.; Sato, E. Electrocatalytic Properties of Transition Metal Oxides for Oxygen Evolution Reaction. *Mater. Chem. Phys.* **1986**, *14* (5), 397–426. https://doi.org/10.1016/0254-0584(86)90045-3.

43 Bockris, J. O. Kinetics of Activation Controlled Consecutive Electrochemical Reactions: Anodic Evolution of Oxygen. *J. Chem. Phys.* **1956**, *24* (4), 817–827. https://doi.org/10.1063/1.1742616.

44 Fabbri, E.; Habereder, A.; Waltar, K.; Kötz, R.; Schmidt, T. J. Developments and Perspectives of Oxide-Based Catalysts for the Oxygen Evolution Reaction. *Catal. Sci. Technol.* **2014**, *4* (11), 3800–3821. https://doi.org/10.1039/C4CY00669K.

45 Wade, W. H.; Hackerman, N. Anodic Phenomena at an Iron Electrode. *Trans. Faraday Soc.* **1957**, *53*, 1636. https://doi.org/10.1039/tf9575301636.

46 W. E. O'Grady, C. Iwakura, J. Huang, E. Yeager, in *Proc. Symp. on Electrocatalysis* (Ed: M. W. Breiter), *The Electrochemical Society*, Princeton, NJ **1974**, 286.

47 Zhang, H.; Maijenburg, A. W.; Li, X.; Schweizer, S. L.; Wehrspohn, R. B. Bifunctional Heterostructured Transition Metal Phosphides for Efficient Electrochemical Water Splitting. *Advanced Functional Materials* **2020**, *30* (34), 2003261. https://doi.org/10.1002/adfm.202003261.

48 Bockris, J. O.; Otagawa, T. The Electrocatalysis of Oxygen Evolution on Perovskites. *J. Electrochem. Soc.* **1984**, *131* (2), 290. https://doi.org/10.1149/1.2115565.

49 Guo, Q.; Mao, J.; Huang, J.; Wang, Z.; Zhang, Y.; Hu, J.; Dong, J.; Sathasivam, S.; Zhao, Y.; Xing, G.; Pan, H.; Lai, Y.; Tang, Y. Reducing Oxygen Evolution Reaction Overpotential in Cobalt-Based Electrocatalysts via Optimizing the "Microparticles-in-Spider Web" Electrode Configurations. *Small* **2020**, *16* (8), 1907029. https://doi.org/10.1002/smll.201907029.

50 Hona, R. K.; Karki, S. B.; Ramezanipour, F. Oxide Electrocatalysts Based on Earth-Abundant Metals for Both Hydrogen- and Oxygen-Evolution Reactions. *ACS Sustain. Chem. Eng.* **2020**, *8* (31), 11549–11557. https://doi.org/10.1021/acssuschemeng.0c02498.

51 Dickens, C. F.; Montoya, J. H.; Kulkarni, A. R.; Bajdich, M.; Nørskov, J. K. An Electronic Structure Descriptor for Oxygen Reactivity at Metal and Metal-Oxide Surfaces. *Surf. Sci.* **2019**, *681*, 122–129. https://doi.org/10.1016/j.susc.2018.11.019.

52 Reier, T.; Oezaslan, M.; Strasser, P. Electrocatalytic Oxygen Evolution Reaction (OER) on Ru, Ir, and Pt Catalysts: A Comparative Study of Nanoparticles and Bulk Materials. *ACS Catal.* **2012**, *2* (8), 1765–1772. https://doi.org/10.1021/cs3003098.

53 Li, Y.; Li, F.-M.; Meng, X.-Y.; Li, S.-N.; Zeng, J.-H.; Chen, Y. Ultrathin Co_3O_4 Nanomeshes for the Oxygen Evolution Reaction. *ACS Catal.* **2018**, *8* (3), 1913–1920. https://doi.org/10.1021/acscatal.7b03949.

54 Jamesh, M. I. Recent Progress on Earth Abundant Hydrogen Evolution Reaction and Oxygen Evolution Reaction Bifunctional Electrocatalyst for Overall Water Splitting in Alkaline Media. *J. Power Sources* **2016**, *333*, 213–236. https://doi.org/10.1016/j.jpowsour.2016.09.161.

55 Zhu, K.; Li, M.; Li, X.; Zhu, X.; Wang, J.; Yang, W. Enhancement of Oxygen Evolution Performance through Synergetic Action between NiFe Metal Core and $NiFeO_x$ Shell. *Chem. Commun.* **2016**, *52* (79), 11803–11806. https://doi.org/10.1039/C6CC04951F.

56 Tong, Y.; Chen, P.; Zhou, T.; Xu, K.; Chu, W.; Wu, C.; Xie, Y. A Bifunctional Hybrid Electrocatalyst for Oxygen Reduction and Evolution: Cobalt Oxide Nanoparticles Strongly Coupled to B,N-Decorated Graphene. *Angew. Chem. Int. Ed.* **2017**, *56* (25), 7121–7125. https://doi.org/10.1002/anie.201702430.

57 Chen, Z.; Kronawitter, C. X.; Koel, B. E. Facet-Dependent Activity and Stability of Co_3O_4 Nanocrystals towards the Oxygen Evolution Reaction. *Phys. Chem. Chem. Phys.* **2015**, *17* (43), 29387–29393. https://doi.org/10.1039/C5CP02876K.

58 Flores, C. L. I.; Balela, M. D. L. Electrocatalytic Oxygen Evolution Reaction of Hierarchical Micro/Nanostructured Mixed Transition Cobalt Oxide in Alkaline Medium. *J. Solid State Electrochem.* **2020**, *24* (4), 891–904. https://doi.org/10.1007/s10008-020-04530-4.

59 Paul, B.; Bhanja, P.; Sharma, S.; Yamauchi, Y.; Alothman, Z. A.; Wang, Z.-L.; Bal, R.; Bhaumik, A. Morphologically Controlled Cobalt Oxide Nanoparticles for Efficient Oxygen Evolution Reaction. *J. Colloid Interface Sci.* **2021**, *582*, 322–332. https://doi.org/10.1016/j.jcis.2020.08.029.

60 Khan, M. A.; Zhao, H.; Zou, W.; Chen, Z.; Cao, W.; Fang, J.; Xu, J.; Zhang, L.; Zhang, J. Recent Progresses in Electrocatalysts for Water Electrolysis. *Electrochem. Energ. Rev.* **2018**, *1* (4), 483–530. https://doi.org/10.1007/s41918-018-0014-z.

61 Charles, V.; Anumah, A. O.; Adegoke, K. A.; Adesina, M. O.; Ebuka Ikegwuonu, P.; Gaya, N. A.; Ogwuche, S.; Yakubu, M. O. Progress and Challenges Pertaining to the Earthly-Abundant Electrocatalytic Materials for Oxygen Evolution Reaction. *Sustain. Mater. Technol* **2021**, e00252. https://doi.org/10.1016/j.susmat.2021.e00252.

62 Tong, L.; P. Thummel, R. Mononuclear Ruthenium Polypyridine Complexes That Catalyze Water Oxidation. *Chem. Sci* **2016**, *7* (11), 6591–6603. https://doi.org/10.1039/C6SC02766K.

63 Mahmood, N.; Yao, Y.; Zhang, J.; Pan, L.; Zhang, X.; Zou, J. Electrocatalysts for Hydrogen Evolution in Alkaline Electrolytes: Mechanisms, Challenges, and Prospective Solutions. *Adv Sci (Weinh)* **2017**, *5* (2), 1700464. https://doi.org/10.1002/advs.201700464.

64 Muthudineshkumar, R.; Anand, R. Anaerobic Digestion of Various Feedstocks for Second-Generation Biofuel Production. In *Advances in Eco-Fuels for a Sustainable Environment*; Elsevier, **2019**; 157–185. https://doi.org/10.1016/B978-0-08-102728-8.00006-1.

65 Kakaei, K.; Esrafili, M. D.; Ehsani, A. Introduction to Catalysis. In *Interface Science and Technology*; Elsevier, **2019**; Vol. 27, 1–21. https://doi.org/10.1016/B978-0-12-814523-4.00001-0.

66 Argyle, M. D.; Bartholomew, C. H. Heterogeneous Catalyst Deactivation and Regeneration: A Review. *Catalysts* **2015**, *5* (1), 145–269. https://doi.org/10.3390/catal5010145.

67 Özkar, S. Enhancement of Catalytic Activity by Increasing Surface Area in Heterogeneous Catalysis. *Appl. Surf. Sci.* **2009**, *256* (5), 1272–1277. https://doi.org/10.1016/j.apsusc.2009.10.036.

68 Cole-Hamilton, D. J., Tooze, R. P., *Catalyst Separation, Recovery and Recycling: Chemistry and Process Design*; Eds.; Catalysis by Metal Complexes; Springer: Dordrecht, **2006**.

69 Kvitek, L.; Prucek, R.; Panacek, A.; Soukupova, J. Physicochemical Aspects of Metal Nanoparticle Preparation. In *Engineered Nanomaterials - Health and Safety*; Marius Avramescu, S., Akhtar, K., Fierascu, I., Bahadar Khan, S., Ali, F., M. Asiri, A., Eds.; IntechOpen, **2020**. https://doi.org/10.5772/intechopen.89954.

70 Liu, L.; Corma, A. Metal Catalysts for Heterogeneous Catalysis: From Single Atoms to Nanoclusters and Nanoparticles. *Chem. Rev.* **2018**, *118* (10), 4981–5079. https://doi.org/10.1021/acs.chemrev.7b00776.

71 Jakhar, M.; Kumar, A.; Ahluwalia, P. K.; Tankeshwar, K.; Pandey, R. Engineering 2D Materials for Photocatalytic Water-Splitting from a Theoretical Perspective. *Materials* **2022**, *15* (6), 2221. https://doi.org/10.3390/ma15062221.

72 Rodrigues, T. S.; Silva, A. G. M. da; Camargo, P. H. C. Nanocatalysis by Noble Metal Nanoparticles: Controlled Synthesis for the Optimization and Understanding of Activities. *J. Mater. Chem. A* **2019**, *7* (11), 5857–5874. https://doi.org/10.1039/C9TA00074G.

73 El-Eskandarany, M. S.; Al-Hazza, A.; Al-Hajji, L. A.; Ali, N.; Al-Duweesh, A. A.; Banyan, M.; Al-Ajmi, F. Mechanical Milling: A Superior Nanotechnological Tool for Fabrication of Nanocrystalline and Nanocomposite Materials. *J. Nanomater.* **2021**, *11* (10), 2484. https://doi.org/10.3390/nano11102484.

74 Khan, I.; Saeed, K.; Khan, I. Nanoparticles: Properties, Applications and Toxicities. *Arab. J. Chem.* **2019**, *12* (7), 908–931. https://doi.org/10.1016/j.arabjc.2017.05.011.

75 Li, Z.; Wang, Y.; Yu, Q. Significant Parameters in the Optimization of Synthesis of Silver Nanoparticles by Chemical Reduction Method. *J. of Materi Eng and Perform* **2010**, *19* (2), 252–256. https://doi.org/10.1007/s11665-009-9486-7.

76 Singh, K. R.; Nayak, V.; Sarkar, T.; Singh, R. P. Cerium Oxide Nanoparticles: Properties, Biosynthesis and Biomedical Application. *RSC Adv.* **2020**, *10* (45), 27194–27214. https://doi.org/10.1039/D0RA04736H.

77 Xu, C.; Ming, M.; Wang, Q.; Yang, C.; Fan, G.; Wang, Y.; Gao, D.; Bi, J.; Zhang, Y. Facile Synthesis of Effective Ru Nanoparticles on Carbon by Adsorption-Low Temperature Pyrolysis Strategy for Hydrogen Evolution. *J. Mater. Chem. A* **2018**, *6* (29), 14380–14386. https://doi.org/10.1039/C8TA03572E.

78 Demir, E.; Akbayrak, S.; Önal, A. M.; Özkar, S. Titania, Zirconia and Hafnia Supported Ruthenium(0) Nanoparticles: Highly Active Hydrogen Evolution Catalysts. *J. Colloid Interface Sci.* **2018**, *531*, 570–577. https://doi.org/10.1016/j.jcis.2018.07.085.

79 Song, F.; Li, W.; Sun, Y. Metal–Organic Frameworks and Their Derivatives for Photocatalytic Water Splitting. *Inorganics* **2017**, *5* (3), 40. https://doi.org/10.3390/inorganics5030040.

80 Winterbottom, J. M., King, M. B., *Reactor Design for Chemical Engineers*; Eds.; Stanley Thornes: Cheltenham, U.K, 1999.

81 Ruiz Puigdollers, A.; Schlexer, P.; Tosoni, S.; Pacchioni, G. Increasing Oxide Reducibility: The Role of Metal/Oxide Interfaces in the Formation of Oxygen Vacancies. *ACS Catal.* **2017**, *7* (10), 6493–6513. https://doi.org/10.1021/acscatal.7b01913.

82 Ferrari, A. M.; Pacchioni, G. Electronic Structure of F and V Centers on the MgO Surface. *J. Phys. Chem.* **1995**, *99* (46), 17010–17018. https://doi.org/10.1021/j100046a029.

83 Pacchioni, G.; Freund, H. Electron Transfer at Oxide Surfaces. The MgO Paradigm: From Defects to Ultrathin Films. *Chem. Rev.* **2013**, *113* (6), 4035–4072. https://doi.org/10.1021/cr3002017.

84 Schlicht, S.; Büttner, P.; Bachmann, J. Highly Active Ir/TiO$_2$ Electrodes for the Oxygen Evolution Reaction Using Atomic Layer Deposition on Ordered Porous Substrates. *ACS Appl. Energy Mater.* **2019**, *2* (3), 2344–2349. https://doi.org/10.1021/acsaem.9b00402.

85 Abbas, M.; Haq, T. ul; Arshad, S. N.; Zaheer, M. Fabrication of Cobalt Doped Titania for Enhanced Oxygen Evolution Reaction. *Molecular Catalysis* **2020**, *488*, 110894. https://doi.org/10.1016/j.mcat.2020.110894.

86 Liu, B.; Wang, S.; Wang, C.; Chen, Y.; Ma, B.; Zhang, J. Surface Morphology and Electrochemical Properties of RuO2-Doped Ti/IrO2-ZrO2 Anodes for Oxygen Evolution Reaction. *J. Alloys Compd.* **2019**, *778*, 593–602. https://doi.org/10.1016/j.jallcom.2018.11.191.

87 Li, L.; Hu, Z.; Tao, L.; Xu, J.; Yu, J. C. Efficient Electronic Transport in Partially Disordered Co$_3$O$_4$ Nanosheets for Electrocatalytic Oxygen Evolution Reaction. *ACS Appl. Energy Mater.* **2020**, *3* (3), 3071–3081. https://doi.org/10.1021/acsaem.0c00190.

88 Akbayrak, M.; Önal, A. M. Binder- Free Iridium Based Electrocatalysts: Facile Preparation, High Activity and Outstanding Stability for Hydrogen Evolution Reaction in Acidic Medium. *J. Colloid Interface Sci.* **2020**, *580*, 11–20. https://doi.org/10.1016/j.jcis.2020.06.117.

89 Akbayrak, M.; Önal, A. M. High Durability and Electrocatalytic Activity Toward Hydrogen Evolution Reaction with Ultralow Rhodium Loading on Titania. *J. Electrochem. Soc.* **2020**, *167* (15), 156501. https://doi.org/10.1149/1945-7111/abb9cf.

90 Demir, E.; Akbayrak, S.; Önal, A. M.; Özkar, S. Ceria Supported Ruthenium(0) Nanoparticles: Highly Efficient Catalysts in Oxygen Evolution Reaction. *J. Colloid Interface Sci.* **2019**, *534*, 704–710. https://doi.org/10.1016/j.jcis.2018.09.075.

91 Kodiyath, R.; V. Ramesh, G.; Manikandan, M.; Ueda, S.; Fujita, T.; Abe, H. Intermetallic Pd $_3$ *X* (*X* = Ti and Zr) Nanocrystals for Electro-Oxidation of Alcohols and Formic Acid in Alkaline and Acidic Media. *Sci. Technol. Adv. Mater.* **2020**, *21* (1), 573–583. https://doi.org/10.1080/14686996.2020.1789437.

92 Akbayrak, S.; Taneroğlu, O.; Özkar, S. Nanoceria Supported Cobalt(0) Nanoparticles: A Magnetically Separable and Reusable Catalyst in Hydrogen Generation from the Hydrolysis of Ammonia Borane. *New J. Chem.* **2017**, *41* (14), 6546–6552. https://doi.org/10.1039/C7NJ01035D.

93 Bagheri, S.; Muhd Julkapli, N.; Bee Abd Hamid, S. Titanium Dioxide as a Catalyst Support in Heterogeneous Catalysis. *Sci. World J.* **2014**, *2014*, 1–21. https://doi.org/10.1155/2014/727496.

94 Zhang, Q.; Joo, J.-B.; Lu, Z.; Dahl, M.; Oliveira, D. Q. L.; Ye, M.; Yin, Y. Self-Assembly and Photocatalysis of Mesoporous TiO2 Nanocrystal Clusters. *Nano Res.* **2011**, *4* (1), 103–114. https://doi.org/10.1007/s12274-010-0058-9.

95 Mori, K.; Miyawaki, K.; Yamashita, H. Ru and Ru–Ni Nanoparticles on TiO2 Support as Extremely Active Catalysts for Hydrogen Production from Ammonia–Borane. *ACS Catal.* **2016**, *6* (5), 3128–3135. https://doi.org/10.1021/acscatal.6b00715.

96 Kouva, S.; Honkala, K.; Lefferts, L.; Kanervo, J. Review: Monoclinic Zirconia, Its Surface Sites and Their Interaction with Carbon Monoxide. *Catal. Sci. Technol.* **2015**, *5* (7), 3473–3490. https://doi.org/10.1039/C5CY00330J.

97 Saridag, S.; Tak, O.; Alniacik, G. Basic Properties and Types of Zirconia: An Overview. *World Journal of Stomatology* **2013**, *2* (3), 40–47. https://doi.org/10.5321/wjs.v2.i3.40.

98 Younis, A.; Chu, D.; Li, S. Cerium Oxide Nanostructures and Their Applications; *IntechOpen* **2016**, 53-68. https://doi.org/10.5772/65937.

99 Fadzil, N. A. M.; Rahim, M. H. A.; Maniam, G. P. Brief Review of Ceria and Modified Ceria: Synthesis and Application. *Mater. Res. Express* **2018**, *5* (8), 085019. https://doi.org/10.1088/2053-1591/aad2b5.

100 Xu, C.; Qu, X. Cerium Oxide Nanoparticle: A Remarkably Versatile Rare Earth Nanomaterial for Biological Applications. *NPG Asia Mater* **2014**, *6* (3), e90–e90. https://doi.org/10.1038/am.2013.88.

101 Melchionna, M.; Fornasiero, P. The Role of Ceria-Based Nanostructured Materials in Energy Applications. *Mater. Today* **2014**, *17* (7), 349–357. https://doi.org/10.1016/j.mattod.2014.05.005.

102 Vinodkumar, T.; Rao, B. G.; Reddy, B. M. Influence of Isovalent and Aliovalent Dopants on the Reactivity of Cerium Oxide for Catalytic Applications. *Catal. Today* **2015**, *253*, 57–64. https://doi.org/10.1016/j.cattod.2015.01.044.

103 Gupta, A.; Waghmare, U. V.; Hegde, M. S. Correlation of Oxygen Storage Capacity and Structural Distortion in Transition-Metal-, Noble-Metal-, and Rare-Earth-Ion-Substituted CeO_2 from First Principles Calculation. *Chem. Mater.* **2010**, *22* (18), 5184–5198. https://doi.org/10.1021/cm101145d.

104 Jaiswal, N.; Tanwar, K.; Suman, R.; Kumar, D.; Upadhyay, S.; Parkash, O. A Brief Review on Ceria Based Solid Electrolytes for Solid Oxide Fuel Cells. *J. Alloys Compd.* **2019**, *781*, 984–1005. https://doi.org/10.1016/j.jallcom.2018.12.015.

105 Pan, C.; Zhang, D.; Shi, L. CTAB Assisted Hydrothermal Synthesis, Controlled Conversion and CO Oxidation Properties of CeO2 Nanoplates, Nanotubes, and Nanorods. *J. Solid State Chem.* **2008**, *181* (6), 1298–1306. https://doi.org/10.1016/j.jssc.2008.02.011.

106 Tang, Z.-R.; Zhang, Y.; Xu, Y.-J. A Facile and High-Yield Approach to Synthesize One-Dimensional CeO2 Nanotubes with Well-Shaped Hollow Interior as a Photocatalyst for Degradation of Toxic Pollutants. *RSC Adv.* **2011**, *1* (9), 1772–1777. https://doi.org/10.1039/C1RA00518A.

107 Tonbul, Y.; Akbayrak, S.; Özkar, S. Palladium(0) Nanoparticles Supported on Ceria: Highly Active and Reusable Catalyst in Hydrogen Generation from the Hydrolysis of Ammonia Borane. *Int. J. of Hydrog. Energy* **2016**, *41* (26), 11154–11162. https://doi.org/10.1016/j.ijhydene.2016.04.058.

108 Trovarelli, A. Catalytic Properties of Ceria and CeO_2 -Containing Materials. *Catal. Rev. Sci. Eng.* **1996**, *38* (4), 439–520. https://doi.org/10.1080/01614949608006464.

109 Hughes, A. E.; Haque, N.; Northey, S. A.; Giddey, S. Platinum Group Metals: A Review of Resources, Production and Usage with a Focus on Catalysts. *Resources* **2021**, *10* (9), 93. https://doi.org/10.3390/resources10090093.

110 Rossell, M. D.; Caparrós, F. J.; Angurell, I.; Muller, G.; Llorca, J.; Seco, M.; Rossell, O. Magnetite-Supported Palladium Single-Atoms Do Not Catalyse the Hydrogenation of Alkenes but Small Clusters Do. *Catal. Sci. Technol.* **2016**, *6* (12), 4081–4085. https://doi.org/10.1039/C6CY00596A.

111 Guan, H.; Lin, J.; Qiao, B.; Yang, X.; Li, L.; Miao, S.; Liu, J.; Wang, A.; Wang, X.; Zhang, T. Catalytically Active Rh Sub-Nanoclusters on TiO_2 for CO Oxidation at Cryogenic Temperatures. *Angew. Chem. Int. Ed.* **2016**, *55* (8), 2820–2824. https://doi.org/10.1002/anie.201510643.

112 Shimizu, K.; Satsuma, A.; Hattori, T. Catalytic Performance of Ag–Al$_2$O$_3$ Catalyst for the Selective Catalytic Reduction of NO by Higher Hydrocarbons. *Appl. Catal. B: Environ* **2000**, *25* (4), 239–247. https://doi.org/10.1016/S0926-3373(99)00135-6.

113 Li, Y.; Zhang, Y.; Qian, K.; Huang, W. Metal–Support Interactions in Metal/Oxide Catalysts and Oxide–Metal Interactions in Oxide/Metal Inverse Catalysts. *ACS Catal.* **2022**, *12* (2), 1268–1287. https://doi.org/10.1021/acscatal.1c04854.

114 Fally, F.; Perrichon, V.; Vidal, H.; Kaspar, J.; Blanco, G.; Pintado, J. M.; Bernal, S.; Colon, G.; Daturi, M.; Lavalley, J. C. Modification of the Oxygen Storage Capacity of CeO2–ZrO2 Mixed Oxides after Redox Cycling Aging. *Catal. Today* **2000**, *59* (3–4), 373–386. https://doi.org/10.1016/S0920-5861(00)00302-3.

115 Acerbi, N.; Golunski, S.; Tsang, S. C.; Daly, H.; Hardacre, C.; Smith, R.; Collier, P. Promotion of Ceria Catalysts by Precious Metals: Changes in Nature of the Interaction under Reducing and Oxidizing Conditions. *J. Phys. Chem. C* **2012**, *116* (25), 13569–13583. https://doi.org/10.1021/jp212233u.

116 van Deelen, T. W.; Hernández Mejía, C.; de Jong, K. P. Control of Metal-Support Interactions in Heterogeneous Catalysts to Enhance Activity and Selectivity. *Nat Catal* **2019**, *2* (11), 955–970. https://doi.org/10.1038/s41929-019-0364-x.

117 Tauster, S. J.; Fung, S. C.; Garten, R. L. Strong Metal-Support Interactions. Group 8 Noble Metals Supported on Titanium Dioxide. *J. Am. Chem. Soc.* **1978**, *100* (1), 170–175. https://doi.org/10.1021/ja00469a029.

118 Tauster, S. J.; Fung, S. C.; Baker, R. T. K.; Horsley, J. A. Strong Interactions in Supported-Metal Catalysts. *Science* **1981**, *211* (4487), 1121–1125. https://doi.org/10.1126/science.211.4487.1121.

119 Penner, S.; Armbrüster, M. Formation of Intermetallic Compounds by Reactive Metal–Support Interaction: A Frequently Encountered Phenomenon in Catalysis. *ChemCatChem* **2015**, *7* (3), 374–392. https://doi.org/10.1002/cctc.201402635.

120 Ahmadi, M.; Mistry, H.; Roldan Cuenya, B. Tailoring the Catalytic Properties of Metal Nanoparticles via Support Interactions. *J. Phys. Chem. Lett.* **2016**, *7* (17), 3519–3533. https://doi.org/10.1021/acs.jpclett.6b01198.

121 Lou, Y.; Xu, J.; Zhang, Y.; Pan, C.; Dong, Y.; Zhu, Y. Metal-Support Interaction for Heterogeneous Catalysis: From Nanoparticles to Single Atoms. *Mater. Today Nano* **2020**, *12*, 100093. https://doi.org/10.1016/j.mtnano.2020.100093.

122 Ro, I.; Resasco, J.; Christopher, P. Approaches for Understanding and Controlling Interfacial Effects in Oxide-Supported Metal Catalysts. *ACS Catal.* **2018**, *8* (8), 7368–7387. https://doi.org/10.1021/acscatal.8b02071.

123 Li, S.; Xu, Y.; Chen, Y.; Li, W.; Lin, L.; Li, M.; Deng, Y.; Wang, X.; Ge, B.; Yang, C.; Yao, S.; Xie, J.; Li, Y.; Liu, X.; Ma, D. Tuning the Selectivity of Catalytic Carbon Dioxide Hydrogenation over Iridium/Cerium Oxide Catalysts with a Strong Metal-Support Interaction. *Angew. Chem. Int. Ed.* **2017**, *56* (36), 10761–10765. https://doi.org/10.1002/anie.201705002.

124 Inzelt, G. Chronoamperometry, Chronocoulometry, and Chronopotentiometry. In *Encyclopedia of Applied Electrochemistry*; Kreysa, G., Ota, K., Savinell, R. F., Eds.; Springer: New York, NY, **2014**; 207–214. https://doi.org/10.1007/978-1-4419-6996-5_217.

125 Bond, A. M. 2.15 - Electrochemistry: General Introduction. In *Comprehensive Coordination Chemistry II*; McCleverty, J. A., Meyer, T. J., Eds.; Pergamon: Oxford, **2003**; 197–222. https://doi.org/10.1016/B0-08-043748-6/01117-8.

126 Pajkossy, T.; Jurczakowski, R. Electrochemical Impedance Spectroscopy in Interfacial Studies. *Current Opinion in Electrochemistry* **2017**, *1* (1), 53–58. https://doi.org/10.1016/j.coelec.2017.01.006.

127 Jiao, K.; Wang, B.; Du, Q.; Wang, Y.; Zhang, G.; Yang, Z.; Deng, H.; Xie, X. Chapter 3 - Experimental Characterization and Diagnostics. In *Water and Thermal Management of Proton Exchange Membrane Fuel Cells*; Jiao, K., Wang, B., Du, Q., Wang, Y., Zhang, G., Yang, Z., Deng, H., Xie, X., Eds.; Elsevier, **2021**; 67–120. https://doi.org/10.1016/B978-0-323-91116-0.00003-1.

128 Zhang, J.; Zhang, H.; Wu, J.; Zhang, J. Chapter 10 - High-Temperature PEM Fuel Cells. In *Pem Fuel Cell Testing and Diagnosis*; Zhang, J., Zhang, H., Wu, J., Zhang, J., Eds.; Elsevier: Amsterdam, **2013**; pp 243–282. https://doi.org/10.1016/B978-0-444-53688-4.00010-3.

129 Napporn, T. W.; Holade, Y.; Kokoh, B.; Mitsushima, S.; Mayer, K.; Eichberger, B.; Hacker, V. Chapter 9 - Electrochemical Measurement Methods and Characterization on the Cell Level. In *Fuel Cells and Hydrogen*; Hacker, V., Mitsushima, S., Eds.; Elsevier, **2018**; 175–214. https://doi.org/10.1016/B978-0-12-811459-9.00009-8.

130 Vrubel, H.; Moehl, T.; Grätzel, M.; Hu, X. Revealing and Accelerating Slow Electron Transport in Amorphous Molybdenum Sulphide Particles for Hydrogen Evolution Reaction. *Chem. Commun.* **2013**, *49* (79), 8985–8987. https://doi.org/10.1039/C3CC45416A.

131 Choi, W.; Shin, H.-C.; Kim, J. M.; Choi, J.-Y.; Yoon, W.-S. Modeling and Applications of Electrochemical Impedance Spectroscopy (EIS) for Lithium-Ion Batteries. *J. Electrochem. Sci. Technol* **2020**, *11* (1), 1–13. https://doi.org/10.33961/jecst.2019.00528.

132 Hernández, S.; Ottone, C.; Varetti, S.; Fontana, M.; Pugliese, D.; Saracco, G.; Bonelli, B.; Armandi, M. Spin-Coated vs. Electrodeposited Mn Oxide Films as Water Oxidation Catalysts. *Materials* **2016**, *9* (4), 296. https://doi.org/10.3390/ma9040296.

133 Park, S.-J.; Seo, M.-K. Chapter 1 - Intermolecular Force. In *Interface Science and Technology*; Park, S.-J., Seo, M.-K., Eds.; Interface Science and Composites; Elsevier, **2011**; Vol. 18, 1–57. https://doi.org/10.1016/B978-0-12-375049-5.00001-3.

134 Panda, P. K.; Grigoriev, A.; Mishra, Y. K.; Ahuja, R. Progress in Supercapacitors: Roles of Two Dimensional Nanotubular Materials. *Nanoscale Adv.* **2020**, *2* (1), 70–108. https://doi.org/10.1039/C9NA00307J.

135 Kurzweil, P. CAPACITORS | Electrostatic Solid-State Capacitors. In *Encyclopedia of Electrochemical Power Sources*; Garche, J., Ed.; Elsevier: Amsterdam, **2009**; 600–606. https://doi.org/10.1016/B978-044452745-5.00351-8.

136 Zhao, X.; He, X.; Yin, F.; Chen, B.; Li, G.; Yin, H. Cobalt-Molybdenum Carbide@graphitic Carbon Nanocomposites: Metallic Cobalt Promotes the Electrochemical Hydrogen Evolution Reaction. *Int. J. Hydrogen Energy* **2018**, 43 (49), 22243–22252. https://doi.org/10.1016/j.ijhydene.2018.10.085

137 Gamburg, Y. D.; Zangari, G. Introduction to Electrodeposition: Basic Terms and Fundamental Concepts. In *Theory and Practice of Metal Electrodeposition*; Springer New York: New York, NY, 2011; 1–25. https://doi.org/10.1007/978-1-4419-9669-5_1.

138 Mayet, N.; Servat, K.; Kokoh, K.B.; Napporn, T.W. Probing the Surface of Noble Metals Electrochemically by Underpotential Deposition of Transition Metals. *Surfaces* **2019**, *2*, 257-276. https://doi.org/10.3390/surfaces2020020

139 Sundén, B. Chapter 2 - Electrochemistry and Thermodynamics. In *Hydrogen, Batteries and Fuel Cells*; Sundén, B., Ed.; Academic Press, **2019**; 15–36. https://doi.org/10.1016/B978-0-12-816950-6.00002-6.

140 Kumsa, D. W.; Bhadra, N.; Hudak, E. M.; Kelley, S. C.; Untereker, D. F.; Mortimer, J. T. Electron transfer processes occurring on platinum neural stimulating electrodes: a tutorial on the i(Ve) profile. *J. Neural Eng.* **2016**, *13* (5), 052001. https://doi.org/10.1088/1741-2560/13/5/052001.

141 Bard, A. J.; Faulkner, L. R. *Electrochemical Methods: Fundamentals and Applications*, 2nd ed.; Wiley: New York, 2001.

142 Srinivasan, S. Electrode/Electrolyte Interfaces: Structure And Kinetics Of Charge Transfer. In *Fuel Cells: From Fundamentals to Applications*; Srinivasan, S., Ed.; Springer US: Boston, MA, **2006**; 27–92. https://doi.org/10.1007/0-387-35402-6_2.

143 Panero, S. ELECTROCHEMICAL THEORY | Thermodynamics. In *Encyclopedia of Electrochemical Power Sources*; Garche, J., Ed.; Elsevier: Amsterdam, **2009**; 1–7. https://doi.org/10.1016/B978-044452745-5.00033-2.

144 Appel, A. M.; Helm, M. L. Determining the Overpotential for a Molecular Electrocatalyst. *ACS Catal.* **2014**, *4* (2), 630–633. https://doi.org/10.1021/cs401013v.

145 Zou, X.; Zhang, Y. Noble Metal-Free Hydrogen Evolution Catalysts for Water Splitting. *Chem. Soc. Rev.* **2015**, *44* (15), 5148–5180. https://doi.org/10.1039/C4CS00448E.

146   McCrory, C. C. L.; Jung, S.; Ferrer, I. M.; Chatman, S. M.; Peters, J. C.; Jaramillo, T. F. Benchmarking Hydrogen Evolving Reaction and Oxygen Evolving Reaction Electrocatalysts for Solar Water Splitting Devices. *J. Am. Chem. Soc.* **2015**, *137* (13), 4347–4357. https://doi.org/10.1021/ja510442p.

147 McCrory, C. C. L.; Jung, S.; Peters, J. C.; Jaramillo, T. F. Benchmarking Heterogeneous Electrocatalysts for the Oxygen Evolution Reaction. *J. Am. Chem. Soc.* **2013**, *135* (45), 16977–16987. https://doi.org/10.1021/ja407115p.

148 Fukumoto, T.; Endo, N.; Mori, K.; Tachikawa, Y.; Matsuda, J.; Taniguchi, S.; Sasaki, K. Exchange Current Density of Solid Oxide Electrolysis Cell Electrodes. *Meet. Abstr.* **2021**, *MA2021-03* (1), 282. https://doi.org/10.1149/MA2021-031282mtgabs.

149 Peled, E.; Menkin, S. Review—SEI: Past, Present and Future. *J. Electrochem. Soc.* **2017**, *164* (7), A1703. https://doi.org/10.1149/2.1441707jes.

150   Fang, Y.-H.; Liu, Z.-P. Tafel Kinetics of Electrocatalytic Reactions: From Experiment to First-Principles. *ACS Catal.* **2014**, *4* (12), 4364–4376. https://doi.org/10.1021/cs501312v.

151 Ko, Y.-J.; Cho, J.-M.; Kim, I.; Jeong, D. S.; Lee, K.-S.; Park, J.-K.; Baik, Y.-J.; Choi, H.-J.; Lee, W.-S. Tungsten Carbide Nanowalls as Electrocatalyst for Hydrogen Evolution Reaction: New Approach to Durability Issue. *Appl. Catal. B: Environ* **2017**, *203*, 684–691. https://doi.org/10.1016/j.apcatb.2016.10.085.

152 Bockris, J.O.; Reddy, A.K.N. Electrochemistry. In: Modern Electrochemistry. **1970** , 1-44, Springer, Boston, MA. https://doi.org/10.1007/978-1-4615-8600-5_1

153 Trasatti,S. ELECTROCHEMICAL THEORY | Oxygen Evolution, Editor(s): Jürgen Garche, Encyclopedia of Electrochemical Power Sources, Elsevier, 2009, 49-55, ISBN 9780444527455, https://doi.org/10.1016/B978-044452745-5.00023-X

154 Gasteiger, H. A.; Kocha, S. S.; Sompalli, B.; Wagner, F. T. Activity Benchmarks and Requirements for Pt, Pt-Alloy, and Non-Pt Oxygen Reduction Catalysts for PEMFCs. *Appl. Catal. B: Environ* **2005**, *56* (1), 9–35. https://doi.org/10.1016/j.apcatb.2004.06.021.

155 Kuhl, K. P.; Cave, E. R.; Abram, D. N.; Jaramillo, T. F. New Insights into the Electrochemical Reduction of Carbon Dioxide on Metallic Copper Surfaces. *Energy Environ. Sci.* **2012**, *5* (5), 7050–7059. https://doi.org/10.1039/C2EE21234J.

156 Creus, J.; Drouet, S.; Suriñach, S.; Lecante, P.; Collière, V.; Poteau, R.; Philippot, K.; García-Antón, J.; Sala, X. Ligand-Capped Ru Nanoparticles as Efficient Electrocatalyst for the Hydrogen Evolution Reaction. ACS Catal. **2018**, 8 (12), 11094–11102. https://doi.org/10.1021/acscatal.8b03053

157 Kocabas, S., Cetin, A., Önal, A.M. et al. Chromium substituted iron oxide nanowires as affordable electrocatalysts for oxygen evolution reaction. *J.* Nanopart. Res.2019, 21, (143). https://doi.org/10.1007/s11051-019-4591-5.

158 Yan, Y.; Xia, B. Y.; Zhao, B.; Wang, X. A Review on Noble-Metal-Free Bifunctional Heterogeneous Catalysts for Overall Electrochemical Water Splitting. J. Mater. Chem. A 2016, 4 (45), 17587–17603. https://doi.org/10.1039/C6TA08075H.

159 Li, X.; Zhao, L.; Yu, J.; Liu, X.; Zhang, X.; Liu, H.; Zhou, W. Water Splitting: From Electrode to Green Energy System. *Nano-Micro Lett.* **2020**, *12* (1), 131. https://doi.org/10.1007/s40820-020-00469-3.

160 Zeng, M.; Li, Y. Recent Advances in Heterogeneous Electrocatalysts for the Hydrogen Evolution Reaction. *J. Mater. Chem. A* **2015**, *3* (29), 14942–14962. https://doi.org/10.1039/C5TA02974K.

161 Li, F.; Han, G.-F.; Noh, H.-J.; Jeon, J.-P.; Ahmad, I.; Chen, S.; Yang, C.; Bu, Y.; Fu, Z.; Lu, Y.; Baek, J.-B. Balancing Hydrogen Adsorption/Desorption by Orbital Modulation for Efficient Hydrogen Evolution Catalysis. *Nat Commun* **2019**, *10* (1), 4060. https://doi.org/10.1038/s41467-019-12012-z.

162 Pu, Z.; Zhao, J.; Amiinu, I. S.; Li, W.; Wang, M.; He, D.; Mu, S. A Universal Synthesis Strategy for P-Rich Noble Metal Diphosphide-Based Electrocatalysts for the Hydrogen Evolution Reaction. *Energy Environ. Sci.* 2019, *12* (3), 952–957. https://doi.org/10.1039/C9EE00197B.

163 Mahmood, J.; Anjum, M. A. R.; Shin, S.-H.; Ahmad, I.; Noh, H.-J.; Kim, S.-J.; Jeong, H. Y.; Lee, J. S.; Baek, J.-B. Encapsulating Iridium Nanoparticles Inside a 3D Cage-Like Organic Network as an Efficient and Durable Catalyst for the Hydrogen Evolution Reaction. *Adv. Mater.* **2018**, *30* (52), 1805606. https://doi.org/10.1002/adma.201805606.

164 Jiang, B.; Wang, T.; Cheng, Y.; Liao, F.; Wu, K.; Shao, M. Ir/g-C$_3$N$_4$/Nitrogen-Doped Graphene Nanocomposites as Bifunctional Electrocatalysts for Overall Water Splitting in Acidic Electrolytes. *ACS Appl. Mater. Interfaces* **2018**, *10* (45), 39161–39167. https://doi.org/10.1021/acsami.8b11970.

165 Sheng, M.; Jiang, B.; Wu, B.; Liao, F.; Fan, X.; Lin, H.; Li, Y.; Lifshitz, Y.; Lee, S.-T.; Shao, M. Approaching the Volcano Top: Iridium/Silicon Nanocomposites as Efficient Electrocatalysts for the Hydrogen Evolution Reaction. *ACS Nano* **2019**, *13* (3), 2786–2794. https://doi.org/10.1021/acsnano.8b07572.

166 Zhang, L.; Liu, L.; Wang, H.; Shen, H.; Cheng, Q.; Yan, C.; Park, S. Electrodeposition of Rhodium Nanowires Arrays and Their Morphology-Dependent Hydrogen Evolution Activity. *Nanomaterials* **2017**, *7* (5), 103. https://doi.org/10.3390/nano7050103.

167 Yoon, D.; Seo, B.; Lee, J.; Nam, K. S.; Kim, B.; Park, S.; Baik, H.; Joo, S. H.; Lee, K. Facet-Controlled Hollow Rh2S3 Hexagonal Nanoprisms as Highly Active and Structurally Robust Catalysts toward Hydrogen Evolution Reaction. *Energy Environ. Sci.* **2016**, *9* (3), 850–856. https://doi.org/10.1039/C5EE03456F.

168 Jiang, B.; Yang, L.; Liao, F.; Sheng, M.; Zhao, H.; Lin, H.; Shao, M. A Stepwise-Designed Rh-Au-Si Nanocomposite That Surpasses Pt/C Hydrogen Evolution Activity at High Overpotentials. *Nano Res.* **2017**, *10* (5), 1749–1755. https://doi.org/10.1007/s12274-017-1447-0.

169 Du, J.; Wang, X.; Li, C.; Liu, X.-Y.; Gu, L.; Liang, H.-P. Hollow Rh Nanoparticles with Nanoporous Shell as Efficient Electrocatalyst for Hydrogen Evolution Reaction. *Electrochimica Acta* **2018**, *282*, 853–859. https://doi.org/10.1016/j.electacta.2018.06.126.

170 Pu, Z.; Amiinu, I. S.; He, D.; Wang, M.; Li, G.; Mu, S. Activating Rhodium Phosphide-Based Catalysts for the PH-Universal Hydrogen Evolution Reaction. *Nanoscale* **2018**, *10* (26), 12407–12412. https://doi.org/10.1039/C8NR02854K.

171 Duan, H.; Li, D.; Tang, Y.; He, Y.; Ji, S.; Wang, R.; Lv, H.; Lopes, P. P.; Paulikas, A. P.; Li, H.; Mao, S. X.; Wang, C.; Markovic, N. M.; Li, J.; Stamenkovic, V. R.; Li, Y. High-Performance Rh $_2$ P Electrocatalyst for Efficient Water Splitting. *J. Am. Chem. Soc.* **2017**, *139* (15), 5494–5502. https://doi.org/10.1021/jacs.7b01376.

172 Hu, M.; Ming, M.; Xu, C.; Wang, Y.; Zhang, Y.; Gao, D.; Bi, J.; Fan, G. Towards High-Efficiency Hydrogen Production through in Situ Formation of Well-Dispersed Rhodium Nanoclusters. *ChemSusChem* **2018**, *11* (18), 3253–3258. https://doi.org/10.1002/cssc.201801204.

173 Yang, F.; Zhao, Y.; Du, Y.; Chen, Y.; Cheng, G.; Chen, S.; Luo, W. A Monodisperse Rh2P-Based Electrocatalyst for Highly Efficient and PH-Universal Hydrogen Evolution Reaction. *Adv. Energy Mater.* **2018**, *8* (18), 1703489. https://doi.org/10.1002/aenm.201703489.

174 Hona, R. K.; Karki, S. B.; Ramezanipour, F. Oxide Electrocatalysts Based on Earth-Abundant Metals for Both Hydrogen- and Oxygen-Evolution Reactions. *ACS Sustain. Chem. Eng.* **2020**, *8* (31), 11549–11557. https://doi.org/10.1021/acssuschemeng.0c02498.

175 Song, J.; Zhu, C.; Xu, B. Z.; Fu, S.; Engelhard, M. H.; Ye, R.; Du, D.; Beckman, S. P.; Lin, Y. Bimetallic Cobalt-Based Phosphide Zeolitic Imidazolate Framework: CoP_x Phase-Dependent Electrical Conductivity and Hydrogen Atom Adsorption Energy for Efficient Overall Water Splitting. *Adv. Energy Mater.* **2017**, *7* (2), 1601555. https://doi.org/10.1002/aenm.201601555.

176 Al-Mamun, M.; Su, X.; Zhang, H.; Yin, H.; Liu, P.; Yang, H.; Wang, D.; Tang, Z.; Wang, Y.; Zhao, H. Strongly Coupled $CoCr_2O_4$/Carbon Nanosheets as High Performance Electrocatalysts for Oxygen Evolution Reaction. *Small* **2016**, *12* (21), 2866–2871. https://doi.org/10.1002/smll.201600549.

177 Yang, J.; Zhu, G.; Liu, Y.; Xia, J.; Ji, Z.; Shen, X.; Wu, S. Fe_3O_4-Decorated Co_9S_8 Nanoparticles In Situ Grown on Reduced Graphene Oxide: A New and Efficient Electrocatalyst for Oxygen Evolution Reaction. *Adv. Funct. Mater.* **2016**, *26* (26), 4712–4721. https://doi.org/10.1002/adfm.201600674.

178 Liu, M.; Li, J. Cobalt Phosphide Hollow Polyhedron as Efficient Bifunctional Electrocatalysts for the Evolution Reaction of Hydrogen and Oxygen. *ACS Appl. Mater. Interfaces* **2016**, *8* (3), 2158–2165. https://doi.org/10.1021/acsami.5b10727.

179 Zhu, Y.; Zhou, W.; Chen, Z.-G.; Chen, Y.; Su, C.; Tadé, M. O.; Shao, Z. $SrNb_{0.1}Co_{0.7}Fe_{0.2}O_{3-\delta}$ Perovskite as a Next-Generation Electrocatalyst for Oxygen Evolution in Alkaline Solution. *Angew. Chem. Int. Ed.* **2015**, *54* (13), 3897–3901. https://doi.org/10.1002/anie.201408998.

180 Huang, S.; Meng, Y.; He, S.; Goswami, A.; Wu, Q.; Li, J.; Tong, S.; Asefa, T.; Wu, M. N-, O-, and S-Tridoped Carbon-Encapsulated Co_9S_8 Nanomaterials: Efficient Bifunctional Electrocatalysts for Overall Water Splitting. *Adv. Funct. Mater.* **2017**, *27* (17), 1606585. https://doi.org/10.1002/adfm.201606585.

181   Charles, V.; Anumah, A. O.; Adegoke, K. A.; Adesina, M. O.; Ebuka Ikegwuonu, P.; Gaya, N. A.; Ogwuche, S.; Yakubu, M. O. Progress and Challenges Pertaining to the Earthly-Abundant Electrocatalytic Materials for Oxygen Evolution Reaction. *Sustain. Mater. Technol* **2021**, e00252. https://doi.org/10.1016/j.susmat.2021.e00252.

182 Tamizhdurai, P.; Sakthinathan, S.; Chen, S.-M.; Shanthi, K.; Sivasanker, S.; Sangeetha, P. Environmentally Friendly Synthesis of CeO_2 Nanoparticles for the Catalytic Oxidation of Benzyl Alcohol to Benzaldehyde and Selective Detection of Nitrite. *Sci. Rep.* **2017**, *7* (1), 46372. https://doi.org/10.1038/srep46372.

183   Sultan, S.; Ha, M.; Kim, D. Y.; Tiwari, J. N.; Myung, C. W.; Meena, A.; Shin, T. J.; Chae, K. H.; Kim, K. S. Superb Water Splitting Activity of the Electrocatalyst Fe3Co(PO4)4 Designed with Computation Aid. *Nat Commun* **2019**, *10* (1), 5195. https://doi.org/10.1038/s41467-019-13050-3.

184 Cherevko, S.; Zeradjanin, A. R.; Keeley, G. P.; Mayrhofer, K. J. J. A Comparative Study on Gold and Platinum Dissolution in Acidic and Alkaline Media. *J. Electrochem. Soc.* **2014**, *161* (12), H822–H830. https://doi.org/10.1149/2.0881412jes.

185 Zhang, C.; Hong, Y.; Dai, R.; Lin, X.; Long, L.-S.; Wang, C.; Lin, W. Highly Active Hydrogen Evolution Electrodes via Co-Deposition of Platinum and Polyoxometalates. *ACS Appl. Mater. Interfaces* **2015**, *7* (21), 11648–11653. https://doi.org/10.1021/acsami.5b02899.

186 Lotfi, N.; Shahrabi, T.; Yaghoubinezhad, Y.; Darband, Gh. B. Direct Electrodeposition of Platinum Nanoparticles@graphene Oxide@nickel-Copper@nickel Foam Electrode as a Durable and Cost-Effective Catalyst with Remarkable Performance for Electrochemical Hydrogen Evolution Reaction. *Appl. Surf. Sci.* **2020**, *505*, 144571. https://doi.org/10.1016/j.apsusc.2019.144571.

187 Shang, X.; Dong, B.; Chai, Y.-M.; Liu, C.-G. In-Situ Electrochemical Activation Designed Hybrid Electrocatalysts for Water Electrolysis. *Science Bulletin* **2018**, *63* (13), 853–876. https://doi.org/10.1016/j.scib.2018.05.014.

188 Kulesza, P. J.; Lu, W.; Faulkner, L. R. Cathodic Fabrication of Platinum Microparticles via Anodic Dissolution of a Platinum Counter-Electrode: Electrocatalytic Probing and Surface Analysis of Dispersed Platinum. *Journal of Electroanalytical Chemistry* **1992**, *336* (1), 35–44. https://doi.org/10.1016/0022-0728(92)80260-B.

189 Xing, L.; Hossain, M. A.; Tian, M.; Beauchemin, D.; Adjemian, K. T.; Jerkiewicz, G. Platinum Electro-Dissolution in Acidic Media upon Potential Cycling. *Electrocatalysis* **2014**, *5* (1), 96–112. https://doi.org/10.1007/s12678-013-0167-9.

190 Zhou, W.; Jia, J.; Lu, J.; Yang, L.; Hou, D.; Li, G.; Chen, S. Recent Developments of Carbon-Based Electrocatalysts for Hydrogen Evolution Reaction. *Nano Energy* **2016**, *28*, 29–43. https://doi.org/10.1016/j.nanoen.2016.08.027.

191 Dong, G.; Fang, M.; Wang, H.; Yip, S.; Cheung, H.-Y.; Wang, F.; Wong, C.-Y.; Chu, S. T.; Ho, J. C. Insight into the Electrochemical Activation of Carbon-Based Cathodes for Hydrogen Evolution Reaction. *J. Mater. Chem. A* **2015**, *3* (24), 13080–13086. https://doi.org/10.1039/C5TA02551F.

192 Rand, D. A. J.; Woods, R. A Study of the Dissolution of Platinum, Palladium, Rhodium and Gold Electrodes in 1 m Sulphuric Acid by Cyclic Voltammetry. *J. Electroanal. Chem. Interfacial Electrochem.* **1972**, *35* (1), 209–218. https://doi.org/10.1016/S0022-0728(72)80308-5.

193 Alayoglu, S.; Eichhorn, B. Rh−Pt Bimetallic Catalysts: Synthesis, Characterization, and Catalysis of Core−Shell, Alloy, and Monometallic Nanoparticles. *J. Am. Chem. Soc.* **2008**, *130* (51), 17479–17486. https://doi.org/10.1021/ja8061425.

194 Powell, C. J. Recommended Auger Parameters for 42 Elemental Solids. *Journal of Electron Spectroscopy and Related Phenomena* **2012**, *185* (1), 1–3. https://doi.org/10.1016/j.elspec.2011.12.001.

195 Rohan, R.; Pareek, K.; Chen, Z.; Cai, W.; Zhang, Y.; Xu, G.; Gao, Z.; Cheng, H. A High Performance Polysiloxane-Based Single Ion Conducting Polymeric Electrolyte Membrane for Application in Lithium Ion Batteries. *J. Mater. Chem. A* **2015**, *3* (40), 20267–20276. https://doi.org/10.1039/C5TA02628H.

196 Masud, J.; Van Nguyen, T.; Singh, N.; McFarland, E.; Ikenberry, M.; Hohn, K.; Pan, C.-J.; Hwang, B.-J. A Rh $_x$ S $_y$ /C Catalyst for the Hydrogen Oxidation and Hydrogen Evolution Reactions in HBr. *J. Electrochem. Soc.* **2015**, *162* (4), F455–F462. https://doi.org/10.1149/2.0901504jes.

197 Yao, Q.; Lu, Z.-H.; Jia, Y.; Chen, X.; Liu, X. In Situ Facile Synthesis of Rh Nanoparticles Supported on Carbon Nanotubes as Highly Active Catalysts for H2 Generation from NH3BH3 Hydrolysis. *Int. J. of Hydrog. Energy* **2015**, *5* (40), 2207–2215. https://doi.org/10.1016/j.ijhydene.2014.12.047.

198 Wang, G.; Jing, S.; Tan, Y. Branched Pd@Rh Core@shell Nanocrystals with Exposed Rh {100} Facets: An Effective Electrocatalyst for Hydrazine Electro-Oxidation. *Sci Rep* **2017**, *7* (1), 16465. https://doi.org/10.1038/s41598-017-16776-6.

199 Zhu, L.; Lin, H.; Li, Y.; Liao, F.; Lifshitz, Y.; Sheng, M.; Lee, S.-T.; Shao, M. A Rhodium/Silicon Co-Electrocatalyst Design Concept to Surpass Platinum Hydrogen Evolution Activity at High Overpotentials. *Nat Commun* **2016**, *7* (1), 12272. https://doi.org/10.1038/ncomms12272.

200 Yoon, D.; Seo, B.; Lee, J.; Nam, K. S.; Kim, B.; Park, S.; Baik, H.; Joo, S. H.; Lee, K. Facet-Controlled Hollow Rh2S3 Hexagonal Nanoprisms as Highly Active and Structurally Robust Catalysts toward Hydrogen Evolution Reaction. *Energy Environ. Sci.* **2016**, *9* (3), 850–856. https://doi.org/10.1039/C5EE03456F.

201 Zhu, Y.; Yuan, M.; Deng, L.; Ming, R.; Zhang, A.; Yang, M.; Chai, B.; Ren, Z. High-Efficiency Electrochemical Hydrogen Evolution Based on the Intermetallic Pt2Si Compound Prepared by Magnetron-Sputtering. *RSC Adv.* **2017**, *7* (3), 1553–1560. https://doi.org/10.1039/C6RA24754G.

202 Kim, T.; Park, J.; Jin, H.; Oh, A.; Baik, H.; Joo, S. H.; Lee, K. A Facet-Controlled Rh3Pb2S2 Nanocage as an Efficient and Robust Electrocatalyst toward the Hydrogen Evolution Reaction. *Nanoscale* **2018**, *10* (21), 9845–9850. https://doi.org/10.1039/C8NR02091D.

203 Zhang, C.-C.; Li, M.; Wang, Z.-K.; Jiang, Y.-R.; Liu, H.-R.; Yang, Y.-G.; Gao, X.-Y.; Ma, H. Passivated Perovskite Crystallization and Stability in Organic–Inorganic Halide Solar Cells by Doping a Donor Polymer. *J. Mater. Chem. A* **2017**, *5* (6), 2572–2579. https://doi.org/10.1039/C6TA08970D.

204 Nguyen, N.-A.; Nguyen, V.-T.; Shin, S.; Choi, H.-S. NiRh Nanosponges with Highly Efficient Electrocatalytic Performance for Hydrogen Evolution Reaction. *J. Alloys Compd.* **2019**, *789*, 163–173. https://doi.org/10.1016/j.jallcom.2019.03.003.

205 Zhang, L.; Liu, L.; Wang, H.; Shen, H.; Cheng, Q.; Yan, C.; Park, S. Electrodeposition of Rhodium Nanowires Arrays and Their Morphology-Dependent Hydrogen Evolution Activity. *Nanomaterials* **2017**, *7* (5), 103. https://doi.org/10.3390/nano7050103.

206 Jiang, B.; Yang, L.; Liao, F.; Sheng, M.; Zhao, H.; Lin, H.; Shao, M. A Stepwise-Designed Rh-Au-Si Nanocomposite That Surpasses Pt/C Hydrogen Evolution Activity at High Overpotentials. *Nano Res.* **2017**, *10* (5), 1749–1755. https://doi.org/10.1007/s12274-017-1447-0.

207 Du, J.; Wang, X.; Li, C.; Liu, X.-Y.; Gu, L.; Liang, H.-P. Hollow Rh Nanoparticles with Nanoporous Shell as Efficient Electrocatalyst for Hydrogen Evolution Reaction. *Electrochim. Acta* **2018**, *282*, 853–859. https://doi.org/10.1016/j.electacta.2018.06.126.

208 Pu, Z.; Amiinu, I. S.; He, D.; Wang, M.; Li, G.; Mu, S. Activating Rhodium Phosphide-Based Catalysts for the PH-Universal Hydrogen Evolution Reaction. *Nanoscale* **2018**, *10* (26), 12407–12412. https://doi.org/10.1039/C8NR02854K.

209 Duan, H.; Li, D.; Tang, Y.; He, Y.; Ji, S.; Wang, R.; Lv, H.; Lopes, P. P.; Paulikas, A. P.; Li, H.; Mao, S. X.; Wang, C.; Markovic, N. M.; Li, J.; Stamenkovic, V. R.; Li, Y. High-Performance Rh $_2$ P Electrocatalyst for Efficient Water Splitting. *J. Am. Chem. Soc.* **2017**, *139* (15), 5494–5502. https://doi.org/10.1021/jacs.7b01376.

210 Yang, F.; Zhao, Y.; Du, Y.; Chen, Y.; Cheng, G.; Chen, S.; Luo, W. A Monodisperse Rh2P-Based Electrocatalyst for Highly Efficient and pH-Universal Hydrogen Evolution Reaction. *Advanced Energy Materials* **2018**, *8* (18), 1703489. https://doi.org/10.1002/aenm.201703489.

211 Gu, Q.; Gao, Z.; Yu, S.; Xue, C. Constructing Ru/TiO$_2$ Heteronanostructures Toward Enhanced Photocatalytic Water Splitting via a RuO$_2$/TiO$_2$ Heterojunction and Ru/TiO2 Schottky Junction. *Advanced Materials Interfaces* **2016**, *3* (4), 1500631. https://doi.org/10.1002/admi.201500631.

212 Bernsmeier, D.; Bernicke, M.; Ortel, E.; Bergmann, A.; Lippitz, A.; Nissen, J.; Schmack, R.; Strasser, P.; Polte, J.; Kraehnert, R. Nafion-Free Carbon-Supported Electrocatalysts with Superior Hydrogen Evolution Reaction Performance by Soft Templating. *ChemElectroChem* **2017**, *4* (1), 221–229. https://doi.org/10.1002/celc.201600444.

213 Chen, Z.; Lu, J.; Ai, Y.; Ji, Y.; Adschiri, T.; Wan, L. Ruthenium/Graphene-like Layered Carbon Composite as an Efficient Hydrogen Evolution Reaction Electrocatalyst. *ACS Appl. Mater. Interfaces* **2016**, *8* (51), 35132–35137. https://doi.org/10.1021/acsami.6b09331.

214 Pu, Z.; Amiinu, I. S.; Kou, Z.; Li, W.; Mu, S. RuP2-Based Catalysts with Platinum-like Activity and Higher Durability for the Hydrogen Evolution Reaction at All PH Values. *Angewandte Chemie International Edition* **2017**, *56* (38), 11559–11564. https://doi.org/10.1002/anie.201704911.

215 Franco, D. V.; Silva, L. M. D.; Jardim, W. F.; Boodts, J. F. C. Influence of the Electrolyte Composition on the Kinetics of the Oxygen Evolution Reaction and Ozone Production Processes. *J. Braz. Chem. Soc.* **2006**, *17*, 446–757. https://doi.org/10.1590/S0103-50532006000400017

216 Pu, Z.; Zhao, J.; Amiinu, I. S.; Li, W.; Wang, M.; He, D.; Mu, S. A Universal Synthesis Strategy for P-Rich Noble Metal Diphosphide-Based Electrocatalysts for the Hydrogen Evolution Reaction. *Energy Environ. Sci.* **2019**, *12* (3), 952–957. https://doi.org/10.1039/C9EE00197B.

217 Mahmood, J.; Anjum, M. A. R.; Shin, S.-H.; Ahmad, I.; Noh, H.-J.; Kim, S.-J.; Jeong, H. Y.; Lee, J. S.; Baek, J.-B. Encapsulating Iridium Nanoparticles Inside a 3D Cage-Like Organic Network as an Efficient and Durable Catalyst for the Hydrogen Evolution Reaction. *Adv. Mater.* **2018**, *30* (52), 1805606. https://doi.org/10.1002/adma.201805606.

218 Jiang, B.; Wang, T.; Cheng, Y.; Liao, F.; Wu, K.; Shao, M. Ir/g-C_3N_4/Nitrogen-Doped Graphene Nanocomposites as Bifunctional Electrocatalysts for Overall Water Splitting in Acidic Electrolytes. *ACS Appl. Mater. Interfaces* **2018**, *10* (45), 39161–39167. https://doi.org/10.1021/acsami.8b11970.

219 Sun, X.; Liu, F.; Chen, X.; Li, C.; Yu, J.; Pan, M. Iridium-Doped ZIFs-Derived Porous Carbon-Coated IrCo Alloy as Competent Bifunctional Catalyst for Overall Water Splitting in Acid Medium. *Electrochim. Acta* **2019**, *307*, 206–213. https://doi.org/10.1016/j.electacta.2019.03.179.

220 Jiang, P.; Chen, J.; Wang, C.; Yang, K.; Gong, S.; Liu, S.; Lin, Z.; Li, M.; Xia, G.; Yang, Y.; Su, J.; Chen, Q. Tuning the Activity of Carbon for Electrocatalytic Hydrogen Evolution via an Iridium-Cobalt Alloy Core Encapsulated in Nitrogen-Doped Carbon Cages. *Adv. Mater.* **2018**, *30* (9), 1705324. https://doi.org/10.1002/adma.201705324.

221 Kim, S.; Jung, H.; Lee, C.; Kim, M. H.; Lee, Y. Comparative Study on Hydrogen Evolution Reaction Activity of Electrospun Nanofibers with Diverse Metallic Ir and IrO$_2$ Composition Ratios. *ACS Sustain. Chem. Eng.* **2019**, *7* (9), 8613–8620. https://doi.org/10.1021/acssuschemeng.9b00402.

222 Luo, F.; Hu, H.; Zhao, X.; Yang, Z.; Zhang, Q.; Xu, J.; Kaneko, T.; Yoshida, Y.; Zhu, C.; Cai, W. Robust and Stable Acidic Overall Water Splitting on Ir Single Atoms. *Nano Lett.* **2020**, *20* (3), 2120–2128. https://doi.org/10.1021/acs.nanolett.0c00127.

223 Ming, M.; Zhang, Y.; He, C.; Zhao, L.; Niu, S.; Fan, G.; Hu, J. Room-Temperature Sustainable Synthesis of Selected Platinum Group Metal (PGM = Ir, Rh, and Ru) Nanocatalysts Well-Dispersed on Porous Carbon for Efficient Hydrogen Evolution and Oxidation. *Small* **2019**, *15* (49), 1903057. https://doi.org/10.1002/smll.201903057.

224 Zhu, M.; Shao, Q.; Qian, Y.; Huang, X. Superior Overall Water Splitting Electrocatalysis in Acidic Conditions Enabled by Bimetallic Ir-Ag Nanotubes. *Nano Energy* **2019**, *56*, 330–337. https://doi.org/10.1016/j.nanoen.2018.11.023.

225 Gong, S.; Wang, C.; Jiang, P.; Yang, K.; Lu, J.; Huang, M.; Chen, S.; Wang, J.; Chen, Q. O Species-Decorated Graphene Shell Encapsulating Iridium–Nickel Alloy as an Efficient Electrocatalyst towards Hydrogen Evolution Reaction. *J. Mater. Chem. A* **2019**, *7* (25), 15079–15088. https://doi.org/10.1039/C9TA04361F.

226 Kundu, M. K.; Mishra, R.; Bhowmik, T.; Kanrar, S.; Barman, S. Three-Dimensional Hierarchically Porous Iridium Oxide-Nitrogen Doped Carbon Hybrid: An Efficient Bifunctional Catalyst for Oxygen Evolution and Hydrogen Evolution Reaction in Acid. *Int. J. Hydrogen Energy* **2020**, *45* (11), 6036–6046. https://doi.org/10.1016/j.ijhydene.2019.12.186.

227 Liao, F.; Jiang, B.; Shen, W.; Chen, Y.; Li, Y.; Shen, Y.; Yin, K.; Shao, M. Ir-Au Bimetallic Nanoparticle Modified Silicon Nanowires with Ultralow Content of Ir for Hydrogen Evolution Reaction. *ChemCatChem* **2019**, *11* (8), 2126–2130. https://doi.org/10.1002/cctc.201900241.

228 Zhang, J.; Chen, Z.; Liu, C.; Zhao, J.; Liu, S.; Rao, D.; Nie, A.; Chen, Y.; Deng, Y.; Hu, W. Hierarchical Iridium-Based Multimetallic Alloy with Double-Core-Shell Architecture for Efficient Overall Water Splitting. *Sci. China Mater.* **2020**, *63* (2), 249–257. https://doi.org/10.1007/s40843-019-1176-6.

229 Roy, S. B.; Akbar, K.; Jeon, J. H.; Jerng, S.-K.; Truong, L.; Kim, K.; Yi, Y.; Chun, S.-H. Iridium on Vertical Graphene as an All-Round Catalyst for Robust Water Splitting Reactions. *J. Mater. Chem. A* **2019**, *7* (36), 20590–20596. https://doi.org/10.1039/C9TA07388D.

230 Wang, Z.; Li, M.; Yu, J.; Ge, X.; Liu, Y.; Wang, W. Low-Iridium-Content IrNiTa Metallic Glass Films as Intrinsically Active Catalysts for Hydrogen Evolution Reaction. *Adv. Mater.* **2020**, *32* (4), 1906384. https://doi.org/10.1002/adma.201906384.

231 Fan, K.; He, M.; Dharanipragada, N. V. R. A.; Kuang, P.; Jia, Y.; Fan, L.; Inge, A. K.; Zhang, B.; Sun, L.; Yu, J. Amorphous WO_3 Induced Lattice Distortion for a Low-Cost and High-Efficient Electrocatalyst for Overall Water Splitting in Acid. *Sustainable Energy Fuels* **2020**. https://doi.org/10.1039/C9SE01282F.

232 Yang, X.; Li, Y.; Deng, L.; Li, W.; Ren, Z.; Yang, M.; Yang, X.; Zhu, Y. Synthesis and Characterization of an IrO_2–Fe_2O_3 Electrocatalyst for the Hydrogen Evolution Reaction in Acidic Water Electrolysis. *RSC Adv.* **2017**, *7* (33), 20252–20258. https://doi.org/10.1039/C7RA01533J.

233 Yuan, M.; Zhu, Y.; Deng, L.; Ming, R.; Zhang, A.; Li, W.; Chai, B.; Ren, Z. IrO_2–TiO_2 Electrocatalysts for the Hydrogen Evolution Reaction in Acidic Water Electrolysis without Activation. *New J. Chem.* **2017**, *41* (14), 6152–6159. https://doi.org/10.1039/C7NJ00756F.

234 Karfa, P.; Majhi, K. C.; Madhuri, R. Shape-Dependent Electrocatalytic Activity of Iridium Oxide Decorated Erbium Pyrosilicate toward the Hydrogen Evolution Reaction over the Entire PH Range. *ACS Catal.* **2018**, *8* (9), 8830–8843. https://doi.org/10.1021/acscatal.8b01363.

235 Drouet, S.; Creus, J.; Collière, V.; Amiens, C.; García-Antón, J.; Sala, X.; Philippot, K. A Porous Ru Nanomaterial as an Efficient Electrocatalyst for the Hydrogen Evolution Reaction under Acidic and Neutral Conditions. *Chem. Commun.* **2017**, *53* (85), 11713–11716. https://doi.org/10.1039/C7CC05615J.

236 Cui, E.; Hou, G.; Shao, R.; Guan, R. Facet-Dependent Activity of Pt Nanoparticles as Cocatalyst on TiO_2 Photocatalyst for Dye-Sensitized Visible-Light Hydrogen Generation. *J. of Nanomat.* **2016**, *2016*, 1–7. https://doi.org/10.1155/2016/3469393.

237 Akbayrak, M.; Önal, A. M. Efficient Ceria-Supported Rhodium Nanoparticles as an Electrocatalyst for Hydrogen Evolution. *J. Electrochem. Soc.* **2019**, *166* (16), H897–H903. https://doi.org/10.1149/2.0701916jes.

238 Sebastiammal, S.; Fathima, A. L.; Shally, V.; Jayam, G. Effect of Calcination Temperature on Pure Cerium Oxide Nanoparticles by Precipitation Method. **2018**, *6* (2), 7.

239 Yakusheva, E. A.; Gorichev, I. G.; Atanasyan, T. K.; Lainer, Yu. A. Kinetics of Dissolution of Cobalt Oxides in Acidic Media. *Russ. Metall.* **2010**, *2010* (1), 18–23. https://doi.org/10.1134/S0036029510010040.

240 Fu, T.; Wang, M.; Cai, W.; Cui, Y.; Gao, F.; Peng, L.; Chen, W.; Ding, W. Acid-Resistant Catalysis without Use of Noble Metals: Carbon Nitride with Underlying Nickel. *ACS Catal.* **2014**, *4* (8), 2536–2543. https://doi.org/10.1021/cs500523k.

241 Wu, H.; Feng, C.; Zhang, L.; Zhang, J.; Wilkinson, D. P. Non-Noble Metal Electrocatalysts for the Hydrogen Evolution Reaction in Water Electrolysis. *Electrochem. Energ. Rev.* **2021**, *4* (3), 473–507. https://doi.org/10.1007/s41918-020-00086-z.

242 Li, F.; Han, G.-F.; Noh, H.-J.; Jeon, J.-P.; Ahmad, I.; Chen, S.; Yang, C.; Bu, Y.; Fu, Z.; Lu, Y.; Baek, J.-B. Balancing Hydrogen Adsorption/Desorption by Orbital Modulation for Efficient Hydrogen Evolution Catalysis. *Nat Commun* **2019**, *10* (1), 4060. https://doi.org/10.1038/s41467-019-12012-z.

243 Sarkar, S.; Peter, S. C. An Overview on Pd-Based Electrocatalysts for the Hydrogen Evolution Reaction. *Inorg. Chem. Front.* **2018**, *5* (9), 2060–2080. https://doi.org/10.1039/C8QI00042E.

244 Yang, L.; Liu, P.; Li, J.; Xiang, B. Two-Dimensional Material Molybdenum Disulfides as Electrocatalysts for Hydrogen Evolution. *Catalysts* **2017**, *7* (10), 285. https://doi.org/10.3390/catal7100285.

245 Quaino, P.; Juarez, F.; Santos, E.; Schmickler, W. Volcano Plots in Hydrogen Electrocatalysis – Uses and Abuses. *Beilstein J. Nanotechnol.* **2014**, *5*, 846–854. https://doi.org/10.3762/bjnano.5.96.

246 Ojha, K.; Saha, S.; Dagar, P.; Ganguli, A. K. Nanocatalysts for Hydrogen Evolution Reactions. *Phys. Chem. Chem. Phys.* **2018**, *20* (10), 6777–6799. https://doi.org/10.1039/C7CP06316D.

247 Nørskov, J. K.; Bligaard, T.; Logadottir, A.; Kitchin, J. R.; Chen, J. G.; Pandelov, S.; Stimming, U. Trends in the Exchange Current for Hydrogen Evolution. *J. Electrochem. Soc.* **2005**, *152* (3), J23. https://doi.org/10.1149/1.1856988.

248 Sheng, M.; Jiang, B.; Wu, B.; Liao, F.; Fan, X.; Lin, H.; Li, Y.; Lifshitz, Y.; Lee, S.-T.; Shao, M. Approaching the Volcano Top: Iridium/Silicon Nanocomposites as Efficient Electrocatalysts for the Hydrogen Evolution Reaction. *ACS Nano* **2019**, *13* (3), 2786–2794. https://doi.org/10.1021/acsnano.8b07572.

249 Batsanov, S. S.; Batsanov, A. S. *Introduction to Structural Chemistry*; Springer Netherlands: Dordrecht, **2012**. https://doi.org/10.1007/978-94-007-4771-5.

250 Akbayrak, S. Rhodium(0) Nanoparticles Supported on Ceria as Catalysts in Hydrogenation of Neat Benzene at Room Temperature. *J. Colloid Interface Sci.* **2018**, *530*, 459–464. https://doi.org/10.1016/j.jcis.2018.07.011.

251 Tonbul, Y.; Akbayrak, S.; Özkar, S. Nanozirconia Supported Ruthenium(0) Nanoparticles: Highly Active and Reusable Catalyst in Hydrolytic Dehydrogenation of Ammonia Borane. *J. Colloid Interface Sci.* **2018**, *513*, 287–294. https://doi.org/10.1016/j.jcis.2017.11.037.

252 El-Bery, H. M.; Matsushita, Y.; Abdel-moneim, A. Fabrication of Efficient TiO$_2$-RGO Heterojunction Composites for Hydrogen Generation via Water-Splitting: Comparison between RGO, Au and Pt Reduction Sites. *Appl. Surf. Sci.* **2017**, *423*, 185–196. https://doi.org/10.1016/j.apsusc.2017.06.130.

253 Wang, J.; Xiao, X.; Liu, Y.; Pan, K.; Pang, H.; Wei, S. The Application of CeO$_2$-Based Materials in Electrocatalysis. *J. Mater. Chem. A* **2019**, *7* (30), 17675–17702. https://doi.org/10.1039/C9TA04804A.

254 Bernal, S.; Calvino, J. J.; Cauqui, M. A.; Gatica, J. M.; Larese, C.; Pérez Omil, J. A.; Pintado, J. M. Some Recent Results on Metal/Support Interaction Effects in NM/CeO$_2$ (NM: Noble Metal) Catalysts. *Catal. Today* **1999**, *50* (2), 175–206. https://doi.org/10.1016/S0920-5861(98)00503-3.

255 Garcia, X.; Soler, L.; Divins, N. J.; Vendrell, X.; Serrano, I.; Lucentini, I.; Prat, J.; Solano, E.; Tallarida, M.; Escudero, C.; Llorca, J. Ceria-Based Catalysts Studied by Near Ambient Pressure X-Ray Photoelectron Spectroscopy: A Review. *Catalysts* **2020**, *10* (3), 286. https://doi.org/10.3390/catal10030286.

256 Hemmingson, S. L.; James, T. E.; Feeley, G. M.; Tilson, A. M.; Campbell, C. T. Adsorption and Adhesion of Au on Reduced CeO$_2$ (111) Surfaces at 300 and 100 K. *J. Phys. Chem. C* **2016**, *120* (22), 12113–12124. https://doi.org/10.1021/acs.jpcc.6b03789.

257 Penner, S.; Wang, D.; Podloucky, R.; Schlögl, R.; Hayek, K. Rh and Pt Nanoparticles Supported by CeO$_2$: Metal–Support Interaction upon High-Temperature Reduction Observed by Electron Microscopy. *Phys. Chem. Chem. Phys.* **2004**, *6* (22), 5244–5249. https://doi.org/10.1039/B410124C.

258 Bruix, A.; Rodriguez, J. A.; Ramírez, P. J.; Senanayake, S. D.; Evans, J.; Park, J. B.; Stacchiola, D.; Liu, P.; Hrbek, J.; Illas, F. A New Type of Strong Metal–Support Interaction and the Production of H_2 through the Transformation of Water on Pt/CeO$_2$ (111) and Pt/CeO$_x$/TiO$_2$ (110) Catalysts. *J. Am. Chem. Soc.* **2012**, *134* (21), 8968–8974. https://doi.org/10.1021/ja302070k.

259 Zhang, S.; Zhang, X.; Rui, Y.; Wang, R.; Li, X. Recent Advances in Non-Precious Metal Electrocatalysts for PH-Universal Hydrogen Evolution Reaction. *Green Energy & Environment* **2021**, *6* (4), 458–478. https://doi.org/10.1016/j.gee.2020.10.013.

260 Schlexer, P.; Ruiz Puigdollers, A.; Pacchioni, G. Role of Metal/Oxide Interfaces in Enhancing the Local Oxide Reducibility. *Top Catal* **2019**, *62* (17–20), 1192–1201. https://doi.org/10.1007/s11244-018-1056-5.

261 Campbell, C. T.; Peden, C. H. F. Oxygen Vacancies and Catalysis on Ceria Surfaces. *Science* **2005**, *309* (5735), 713–714. https://doi.org/10.1126/science.1113955.

262 Cherevko, S.; Zeradjanin, A. R.; Topalov, A. A.; Kulyk, N.; Katsounaros, I.; Mayrhofer, K. J. J. Dissolution of Noble Metals during Oxygen Evolution in Acidic Media. *ChemCatChem* **2014**, *6* (8), 2219–2223. https://doi.org/10.1002/cctc.201402194.

263 Roy, C.; Rao, R. R.; Stoerzinger, K. A.; Hwang, J.; Rossmeisl, J.; Chorkendorff, I.; Shao-Horn, Y.; Stephens, I. E. L. Trends in Activity and Dissolution on RuO2 under Oxygen Evolution Conditions: Particles versus Well-Defined Extended Surfaces. *ACS Energy Lett.* **2018**, *3* (9), 2045–2051. https://doi.org/10.1021/acsenergylett.8b01178.

264 Kasian, O.; Grote, J.-P.; Geiger, S.; Cherevko, S.; Mayrhofer, K. J. J. The Common Intermediates of Oxygen Evolution and Dissolution Reactions during Water Electrolysis on Iridium. *Angew. Chem. Int. Ed.* **2018**, *57* (9), 2488–2491. https://doi.org/10.1002/anie.201709652.

265 Parastaev, A.; Muravev, V.; Huertas Osta, E.; van Hoof, A. J. F.; Kimpel, T. F.; Kosinov, N.; Hensen, E. J. M. Boosting CO2 Hydrogenation via Size-Dependent Metal–Support Interactions in Cobalt/Ceria-Based Catalysts. *Nat Catal* **2020**, *3* (6), 526–533. https://doi.org/10.1038/s41929-020-0459-4.

266 Bahar, M.; Gholami, M.; Azim-Araghi, M. E. Sol–Gel Synthesized Titania Nanoparticles Deposited on Porous Polycrystalline Silicon: Improved Carbon Dioxide Sensor Properties. *Materials Science in Semiconductor Processing* **2014**, *26*, 491–500. https://doi.org/10.1016/j.mssp.2014.05.035.

267 Guo, C.; Wang, P.; Liao, S.; Si, H.; Chen, S.; Fan, G.; Wang, Z. Morphology-Controllable Hydrothermal Synthesis of Zirconia with the Assistance of a Rosin-Based Surfactant. *Applied Sciences* **2019**, *9* (19), 4145. https://doi.org/10.3390/app9194145.

268 Abderezzak, B. 2 - Charge Transfer Phenomena, Introduction to Transfer Phenomena in PEM Fuel Cell, Elsevier, **2018**, 53-83, ISBN 9781785482915, https://doi.org/10.1016/B978-1-78548-291-5.50002-0

269 Song, J.; Zhu, C.; Xu, B. Z.; Fu, S.; Engelhard, M. H.; Ye, R.; Du, D.; Beckman, S. P.; Lin, Y. Bimetallic Cobalt-Based Phosphide Zeolitic Imidazolate Framework: CoP $_x$ Phase-Dependent Electrical Conductivity and Hydrogen Atom Adsorption Energy for Efficient Overall Water Splitting. *Adv. Energy Mater.* **2017**, *7* (2), 1601555. https://doi.org/10.1002/aenm.201601555.

270 Han, L.; Yu, X.-Y.; Lou, X. W. D. Formation of Prussian-Blue-Analog Nanocages via a Direct Etching Method and Their Conversion into Ni-Co-Mixed Oxide for Enhanced Oxygen Evolution. *Adv. Mater.* **2016**, *28* (23), 4601–4605. https://doi.org/10.1002/adma.201506315.

271 Al-Mamun, M.; Su, X.; Zhang, H.; Yin, H.; Liu, P.; Yang, H.; Wang, D.; Tang, Z.; Wang, Y.; Zhao, H. Strongly Coupled $CoCr_2O_4$/Carbon Nanosheets as High Performance Electrocatalysts for Oxygen Evolution Reaction. *Small* **2016**, *12* (21), 2866–2871. https://doi.org/10.1002/smll.201600549.

272 Das, D.; Das, A.; Reghunath, M.; Nanda, K. K. Phosphine-Free Avenue to Co_2P Nanoparticle Encapsulated N,P Co-Doped CNTs: A Novel Non-Enzymatic Glucose Sensor and an Efficient Electrocatalyst for Oxygen Evolution Reaction. *Green Chem.* **2017**, *19* (5), 1327–1335. https://doi.org/10.1039/C7GC00084G.

273 Jin, H.; Mao, S.; Zhan, G.; Xu, F.; Bao, X.; Wang, Y. Fe Incorporated α-Co(OH)$_2$ Nanosheets with Remarkably Improved Activity towards the Oxygen Evolution Reaction. *J. Mater. Chem. A* **2017**, *5* (3), 1078–1084. https://doi.org/10.1039/C6TA09959A.

274 Yang, J.; Zhu, G.; Liu, Y.; Xia, J.; Ji, Z.; Shen, X.; Wu, S. Fe_3O_4-Decorated Co_9S_8 Nanoparticles In Situ Grown on Reduced Graphene Oxide: A New and Efficient Electrocatalyst for Oxygen Evolution Reaction. *Adv. Funct. Mater.* **2016**, *26* (26), 4712–4721. https://doi.org/10.1002/adfm.201600674.

275 Du, J.; Zhang, T.; Xing, J.; Xu, C. Hierarchical Porous Fe_3O_4/Co_3S_4 Nanosheets as an Efficient Electrocatalyst for the Oxygen Evolution Reaction. *J. Mater. Chem. A* **2017**, *5* (19), 9210–9216. https://doi.org/10.1039/C7TA02108A.

276 Liu, M.; Li, J. Cobalt Phosphide Hollow Polyhedron as Efficient Bifunctional Electrocatalysts for the Evolution Reaction of Hydrogen and Oxygen. *ACS Appl. Mater. Interfaces* **2016**, *8* (3), 2158–2165. https://doi.org/10.1021/acsami.5b10727.

277 Liu, Y.; Ma, C.; Zhang, Q.; Wang, W.; Pan, P.; Gu, L.; Xu, D.; Bao, J.; Dai, Z. 2D Electron Gas and Oxygen Vacancy Induced High Oxygen Evolution Performances for Advanced Co_3O_4/CeO_2 Nanohybrids. *Adv. Mater.* **2019**, *31* (21), 1900062. https://doi.org/10.1002/adma.201900062.

278 Li, X.; Fang, Y.; Lin, X.; Tian, M.; An, X.; Fu, Y.; Li, R.; Jin, J.; Ma, J. MOF Derived Co_3O_4 Nanoparticles Embedded in N-Doped Mesoporous Carbon Layer/MWCNT Hybrids: Extraordinary Bi-Functional Electrocatalysts for OER and ORR. *J. Mater. Chem. A* **2015**, *3* (33), 17392–17402. https://doi.org/10.1039/C5TA03900B.

163

279 Wang, P.; Song, F.; Amal, R.; Ng, Y. H.; Hu, X. Efficient Water Splitting Catalyzed by Cobalt Phosphide-Based Nanoneedle Arrays Supported on Carbon Cloth. *ChemSusChem* **2016**, *9* (5), 472–477. https://doi.org/10.1002/cssc.201501599.

280 Jiang, J.; Yan, C.; Zhao, X.; Luo, H.; Xue, Z.; Mu, T. A PEGylated Deep Eutectic Solvent for Controllable Solvothermal Synthesis of Porous $NiCo_2S_4$ for Efficient Oxygen Evolution Reaction. *Green Chem.* **2017**, *19* (13), 3023–3031. https://doi.org/10.1039/C7GC01012E.

281 Zheng, Z.; Geng, W.; Wang, Y.; Huang, Y.; Qi, T. $NiCo_2O_4$ Nanoflakes Supported on Titanium Suboxide as a Highly Efficient Electrocatalyst towards Oxygen Evolution Reaction. *Int. J. of Hydrog. Energy* **2017**, *42* (1), 119–124. https://doi.org/10.1016/j.ijhydene.2016.11.187.

282 Sung, M.-C.; Lee, G.-H.; Kim, D.-W. CeO2/Co(OH)2 Hybrid Electrocatalysts for Efficient Hydrogen and Oxygen Evolution Reaction. *J. Alloys Compd.* **2019**, *800*, 450–455. https://doi.org/10.1016/j.jallcom.2019.06.047.

283 Fang, Y.; Li, X.; Hu, Y.; Li, F.; Lin, X.; Tian, M.; An, X.; Fu, Y.; Jin, J.; Ma, J. Ultrasonication-Assisted Ultrafast Preparation of Multiwalled Carbon Nanotubes/Au/Co3O4 Tubular Hybrids as Superior Anode Materials for Oxygen Evolution Reaction. *J. Power Sources* **2015**, *300*, 285–293. https://doi.org/10.1016/j.jpowsour.2015.09.049.

284 Huang, S.; Meng, Y.; He, S.; Goswami, A.; Wu, Q.; Li, J.; Tong, S.; Asefa, T.; Wu, M. N-,O-, and S-Tridoped Carbon-Encapsulated Co_9S_8 Nanomaterials: Efficient Bifunctional Electrocatalysts for Overall Water Splitting. *Adv. Funct. Mater.* **2017**, *27* (17), 1606585. https://doi.org/10.1002/adfm.201606585.

285 Qiu, B.; Wang, C.; Zhang, N.; Cai, L.; Xiong, Y.; Chai, Y. CeO_2-Induced Interfacial Co^{2+} Octahedral Sites and Oxygen Vacancies for Water Oxidation. *ACS Catal.* **2019**, *9* (7), 6484–6490. https://doi.org/10.1021/acscatal.9b01819.

286 Fang, Y.; Li, X.; Li, F.; Lin, X.; Tian, M.; Long, X.; An, X.; Fu, Y.; Jin, J.; Ma, J. Self-Assembly of Cobalt-Centered Metal Organic Framework and Multiwalled Carbon Nanotubes Hybrids as a Highly Active and Corrosion-Resistant Bifunctional Oxygen Catalyst. *J. Power Sources* **2016**, *326*, 50–59. https://doi.org/10.1016/j.jpowsour.2016.06.114.

287 Yang, X.; Tao, Z.; Wu, Y.; Lin, W.; Zheng, J. Electrochemical Deposition of CeO_2 Nanocrystals on Co3O4 Nanoneedle Arrays for Efficient Oxygen Evolution. *J. Alloys Compd.* **2020**, *828*, 154394. https://doi.org/10.1016/j.jallcom.2020.154394.

288 Mao, S.; Wen, Z.; Huang, T.; Hou, Y.; Chen, J. High-Performance Bi-Functional Electrocatalysts of 3D Crumpled Graphene–Cobalt Oxide Nanohybrids for Oxygen Reduction and Evolution Reactions. *Energy Environ. Sci.* **2014**, *7* (2), 609–616. https://doi.org/10.1039/C3EE42696C.

289 Wu, X.; Zhang, T.; Wei, J.; Feng, P.; Yan, X.; Tang, Y. Facile Synthesis of Co and Ce Dual-Doped Ni_3S_2 Nanosheets on Ni Foam for Enhanced Oxygen Evolution Reaction. *Nano Res.* **2020**, *13* (8), 2130–2135. https://doi.org/10.1007/s12274-020-2819-4.

290 Wang, J.; Zhong, H.; Wang, Z.; Meng, F.; Zhang, X. Integrated Three-Dimensional Carbon Paper/Carbon Tubes/Cobalt-Sulfide Sheets as an Efficient Electrode for Overall Water Splitting. *ACS Nano* **2016**, *10* (2), 2342–2348. https://doi.org/10.1021/acsnano.5b07126.

291 Lyu, F.; Bai, Y.; Li, Z.; Xu, W.; Wang, Q.; Mao, J.; Wang, L.; Zhang, X.; Yin, Y. Self-Templated Fabrication of CoO-MoO_2 Nanocages for Enhanced Oxygen Evolution. *Adv. Funct. Mater.* **2017**, *27* (34), 1702324. https://doi.org/10.1002/adfm.201702324.

292 Zhu, Y.; Zhou, W.; Chen, Z.-G.; Chen, Y.; Su, C.; Tadé, M. O.; Shao, Z. $SrNb_{0.1}Co_{0.7}Fe_{0.2}O_{3-\delta}$ Perovskite as a Next-Generation Electrocatalyst for Oxygen Evolution in Alkaline Solution. *Angew. Chem. Int. Ed.* **2015**, *54* (13), 3897–3901. https://doi.org/10.1002/anie.201408998.

293 Ma, T.; Li, C.; Chen, X.; Cheng, F.; Chen, J. Spinel Cobalt–Manganese Oxide Supported on Non-Oxidized Carbon Nanotubes as a Highly Efficient Oxygen Reduction/Evolution Electrocatalyst. *Inorg. Chem. Front.* **2017**, *4* (10), 1628–1633. https://doi.org/10.1039/C7QI00367F.

294 Wu, J.; Liu, Y.; Geng, D.; Liu, H.; Meng, X. Cobalt Oxide Nanosheets Anchored onto Nitrogen-Doped Carbon Nanotubes as Dual Purpose Electrodes for Lithium-Ion Batteries and Oxygen Evolution Reaction. *Int J Energy Res* **2018**, *42* (2), 853–862. https://doi.org/10.1002/er.3862.

295 Chauhan, M.; Reddy, K. P.; Gopinath, C. S.; Deka, S. Copper Cobalt Sulfide Nanosheets Realizing a Promising Electrocatalytic Oxygen Evolution Reaction. *ACS Catal.* **2017**, *7* (9), 5871–5879. https://doi.org/10.1021/acscatal.7b01831.

296 Dong, Q.; Wang, Q.; Dai, Z.; Qiu, H.; Dong, X. MOF-Derived Zn-Doped CoSe$_2$ as an Efficient and Stable Free-Standing Catalyst for Oxygen Evolution Reaction. *ACS Appl. Mater. Interfaces* **2016**, *8* (40), 26902–26907. https://doi.org/10.1021/acsami.6b10160

297 Liu, M.; Lu, X.; Guo, C.; Wang, Z.; Li, Y.; Lin, Y.; Zhou, Y.; Wang, S.; Zhang, J. Architecting a Mesoporous N-Doped Graphitic Carbon Framework Encapsulating CoTe$_2$ as an Efficient Oxygen Evolution Electrocatalyst. *ACS Appl. Mater. Interfaces* **2017**, *9* (41), 36146–36153. https://doi.org/10.1021/acsami.7b09897.

298 Fang, W.; Liu, D.; Lu, Q.; Sun, X.; Asiri, A. M. Nickel Promoted Cobalt Disulfide Nanowire Array Supported on Carbon Cloth: An Efficient and Stable Bifunctional Electrocatalyst for Full Water Splitting. *Electrochem. Commun.* **2016**, *63*, 60–64. https://doi.org/10.1016/j.elecom.2015.10.010.

299 Wu, X.; Yang, Y.; Zhang, T.; Wang, B.; Xu, H.; Yan, X.; Tang, Y. CeO$_x$-Decorated Hierarchical NiCo$_2$S$_4$ Hollow Nanotubes Arrays for Enhanced Oxygen Evolution Reaction Electrocatalysis. *ACS Appl. Mater. Interfaces* **2019**, *11* (43), 39841–39847. https://doi.org/10.1021/acsami.9b12221.

300 Shen, M.; Ruan, C.; Chen, Y.; Jiang, C.; Ai, K.; Lu, L. Covalent Entrapment of Cobalt–Iron Sulfides in N-Doped Mesoporous Carbon: Extraordinary Bifunctional Electrocatalysts for Oxygen Reduction and Evolution Reactions. *ACS Appl. Mater. Interfaces* **2015**, *7* (2), 1207–1218. https://doi.org/10.1021/am507033x.

301 Doyle, R. L.; Lyons, M. E. G. Kinetics and Mechanistic Aspects of the Oxygen Evolution Reaction at Hydrous Iron Oxide Films in Base. *J. Electrochem. Soc.* **2013**, *160* (2), H142–H154. https://doi.org/10.1149/2.015303jes.

302 Swierk, J. R.; Klaus, S.; Trotochaud, L.; Bell, A. T.; Tilley, T. D. Electrochemical Study of the Energetics of the Oxygen Evolution Reaction at Nickel Iron (Oxy)Hydroxide Catalysts. *J. Phys. Chem. C* **2015**, *119* (33), 19022–19029. https://doi.org/10.1021/acs.jpcc.5b05861.

303 Hong, S.; Hwang, H.; Hwang, J. P.; Kim, J. W.; Lee, C. H.; Lee, J. The Effect of Morphological Difference and Hydride Incorporation on the Activity of Pd/C Catalysts in Direct Alkaline Formate Fuel Cell. *Catal. Today* **2021**, *359*, 28–34. https://doi.org/10.1016/j.cattod.2019.06.042.

304 Connor, P.; Schuch, J.; Kaiser, B.; Jaegermann, W. The Determination of Electrochemical Active Surface Area and Specific Capacity Revisited for the System MnO_x as an Oxygen Evolution Catalyst. *Z. Phys. Chem.* **2020**, *234* (5), 979–994. https://doi.org/10.1515/zpch-2019-1514.

305 Zhou, X.; Xia, Z.; Tian, Z.; Ma, Y.; Qu, Y. Ultrathin Porous Co_3O_4 Nanoplates as Highly Efficient Oxygen Evolution Catalysts. *J. Mater. Chem. A* **2015**, *3* (15), 8107–8114. https://doi.org/10.1039/C4TA07214F.

306 Jiang, J.; Zhang, A.; Li, L.; Ai, L. Nickel–Cobalt Layered Double Hydroxide Nanosheets as High-Performance Electrocatalyst for Oxygen Evolution Reaction. *J. Power Sources* **2015**, *278*, 445–451. https://doi.org/10.1016/j.jpowsour.2014.12.085.

307 Zhuang, Z.; Sheng, W.; Yan, Y. Synthesis of Monodispere Au@Co$_3$O$_4$ Core-Shell Nanocrystals and Their Enhanced Catalytic Activity for Oxygen Evolution Reaction. *Adv. Mater.* **2014**, *26* (23), 3950–3955. https://doi.org/10.1002/adma.201400336.

308 Gao, M.; Sheng, W.; Zhuang, Z.; Fang, Q.; Gu, S.; Jiang, J.; Yan, Y. Efficient Water Oxidation Using Nanostructured α-Nickel-Hydroxide as an Electrocatalyst. *J. Am. Chem. Soc.* **2014**, *136* (19), 7077–7084. https://doi.org/10.1021/ja502128j.

309 Zhu, G.; Ge, R.; Qu, F.; Du, G.; Asiri, A. M.; Yao, Y.; Sun, X. In Situ Surface Derivation of an Fe–Co–Bi Layer on an Fe-Doped Co $_3$ O $_4$ Nanoarray for Efficient Water Oxidation Electrocatalysis under near-Neutral Conditions. *J. Mater. Chem. A* **2017**, *5* (14), 6388–6392. https://doi.org/10.1039/C7TA00740J.

310 Song, X.-Z.; Zhu, W.-Y.; Wang, X.-F.; Tan, Z. Recent Advances of CeO2-Based Electrocatalysts for Oxygen and Hydrogen Evolution as Well as Nitrogen Reduction. *ChemElectroChem* **2021**, *8* (6), 996–1020. https://doi.org/10.1002/celc.202001614.

311 Cai, D.; Chen, B.; Huang, Z.; Zeng, X.; Xiao, J.; Zhou, S.-F.; Zhan, G. Metal Oxide/CeO$_2$ Nanocomposites Derived from Ce-Benzene Tricarboxylate (Ce-BTC) Adsorbing with Metal Acetylacetonate Complexes for Catalytic Oxidation of Carbon Monoxide. *RSC Adv.* **2021**, *11* (34), 21057–21065. https://doi.org/10.1039/D1RA03319K.

312 Obata, K.; Takanabe, K. A Permselective CeOx Coating To Improve the Stability of Oxygen Evolution Electrocatalysts. *Angewandte Chemie International Edition* **2018**, *57* (6), 1616–1620. https://doi.org/10.1002/anie.201712121.

313 Koga, H.; Hayashi, A.; Ato, Y.; Tada, K.; Hosokawa, S.; Tanaka, T.; Okumura, M. Effect of Ceria and Zirconia Supports on NO Reduction over Platinum-Group Metal Catalysts: A DFT Study with Comparative Experiments. *Catal. Today* **2019**, *332*, 236–244. https://doi.org/10.1016/j.cattod.2018.07.023.

314 El-Sayed, H. A.; Weiß, A.; Olbrich, L. F.; Putro, G. P.; Gasteiger, H. A. OER Catalyst Stability Investigation Using RDE Technique: A Stability Measure or an Artifact? *J. Electrochem. Soc.* **2019**, *166* (8), F458–F464. https://doi.org/10.1149/2.0301908jes.

315 Rani, B. J.; Ravi, G.; Ravichandran, S.; Ganesh, V.; Ameen, F.; Al-Sabri, A.; Yuvakkumar, R. Electrochemically Active XWO_4 (X = Co, Cu, Mn, Zn) Nanostructure for Water Splitting Applications. *Appl Nanosci* **2018**, *8* (5), 1241–1258. https://doi.org/10.1007/s13204-018-0780-2.

316 Liu, S.; Li, L.; Ahn, H. S.; Manthiram, A. Delineating the Roles of Co_3O_4 and N-Doped Carbon Nanoweb (CNW) in Bifunctional Co_3O_4/CNW Catalysts for Oxygen Reduction and Oxygen Evolution Reactions. *J. Mater. Chem. A* **2015**, *3* (21), 11615–11623. https://doi.org/10.1039/C5TA00661A.

317 Gautam, R. P.; Pan, H.; Chalyavi, F.; Tucker, M. J.; Barile, C. J. Nanostructured Ni–Cu Electrocatalysts for the Oxygen Evolution Reaction. *Catal. Sci. Technol.* **2020**, *10* (15), 4960–4967. https://doi.org/10.1039/D0CY00427H.

318 Wu, W.; Liu, J.; Johannes, N. Electrodeposition of Ir–Co Thin Films on Copper Foam as High-Performance Electrocatalysts for Efficient Water Splitting in Alkaline Medium. *Int. J. of Hydrog. Energy* **2021**, *46* (1), 609–621. https://doi.org/10.1016/j.ijhydene.2020.09.268.

319 Nurlaela, E.; Shinagawa, T.; Qureshi, M.; Dhawale, D. S.; Takanabe, K. Temperature Dependence of Electrocatalytic and Photocatalytic Oxygen Evolution Reaction Rates Using NiFe Oxide. *ACS Catal.* **2016**, *6* (3), 1713–1722. https://doi.org/10.1021/acscatal.5b02804.

320 Davidson,C.; Kissel, G.; Srinivasan, S. Electrode kinetics of the oxygen evolution reaction at $NiCo_2O_4$ from 30% KOH.: Dependence on temperature, J. Electroanal. Chem. Interfacial Electrochem., 132, **1982**, 129-135, https://doi.org/10.1016/0022-0728(82)85012-2.

321 Zhou, M.; Weng, Q.; Zhang, X.; Wang, X.; Xue, Y.; Zeng, X.; Bando, Y.; Golberg, D. In Situ Electrochemical Formation of Core–Shell Nickel–Iron Disulfide and Oxyhydroxide Heterostructured Catalysts for a Stable Oxygen Evolution Reaction and the Associated Mechanisms. *J. Mater. Chem. A* **2017**, *5* (9), 4335–4342. https://doi.org/10.1039/C6TA09366C.

322 Duan, Y.; Dubouis, N.; Huang, J.; Dalla Corte, D. A.; Pimenta, V.; Xu, Z. J.; Grimaud, A. Revealing the Impact of Electrolyte Composition for Co-Based Water Oxidation Catalysts by the Study of Reaction Kinetics Parameters. *ACS Catal.* **2020**, *10* (7), 4160–4170. https://doi.org/10.1021/acscatal.0c00490.

323 Yadav, M. K.; Lal, B.; Singh, N. K. Electrocatalytic Properties of $La_{1-X}Cu_xCoO_3$ ($0 \leq x \leq 0.8$) Film Electrodes for Oxygen Evolution in Alkaline Medium: Part II. A Comparative Study. *Indian J Chem.* **2019**, 8.

324 Li, G.-F.; Divinagracia, M.; Labata, M. F.; Ocon, J. D.; Abel Chuang, P.-Y. Electrolyte-Dependent Oxygen Evolution Reactions in Alkaline Media: Electrical Double Layer and Interfacial Interactions. *ACS Appl. Mater. Interfaces* **2019**, *11* (37), 33748–33758. https://doi.org/10.1021/acsami.9b06889.

325 Karthick, K.; Anantharaj, S.; Karthik, P. E.; Subramanian, B.; Kundu, S. Self-Assembled Molecular Hybrids of CoS-DNA for Enhanced Water Oxidation with Low Cobalt Content. *Inorg. Chem.* **2017**, *56* (11), 6734–6745. https://doi.org/10.1021/acs.inorgchem.7b00855.

326 Zhou, Q.; Li, T.-T.; Qian, J.; Hu, Y.; Guo, F.; Zheng, Y.-Q. Self-Supported Hierarchical CuO_x @Co_3O_4 Heterostructures as Efficient Bifunctional Electrocatalysts for Water Splitting. *J. Mater. Chem. A* **2018**, *6* (29), 14431–14439. https://doi.org/10.1039/C8TA03120G.

327 Cai, M.; Lu, X.; Zou, Z.; Guo, K.; Xi, P.; Xu, C. The Energy Level Regulation of CoMo Carbonate Hydroxide for the Enhanced Oxygen Evolution Reaction Activity. *ACS Sustain. Chem. Eng.* **2019**, *7* (6), 6161–6169. https://doi.org/10.1021/acssuschemeng.8b06360.

328 Saha, E.; Karthick, K.; Kundu, S.; Mitra, J. Electrocatalytic Oxygen Evolution in Acidic and Alkaline Media by a Multistimuli-Responsive Cobalt(II) Organogel. *ACS Sustain. Chem. Eng.* **2019**, *7* (19), 16094–16102. https://doi.org/10.1021/acssuschemeng.9b02858.

329 Ghosh, S.; Tudu, G.; Mondal, A.; Ganguli, S.; Inta, H. R.; Mahalingam, V. Inception of Co_3O_4 as Microstructural Support to Promote Alkaline Oxygen Evolution Reaction for $Co_{0.85}Se/Co_9Se_8$ Network. *Inorg. Chem.* **2020**, *59* (23), 17326–17339. https://doi.org/10.1021/acs.inorgchem.0c02618.

330 Ghosh, S.; Inta, H. R.; Ganguli, S.; Tudu, G.; Koppisetti, H. V. S. R. M.; Mahalingam, V. MoO_2 as a Propitious "Pore-Forming Additive" for Boosting the Water Oxidation Activity of Cobalt Oxalate Microrods. *J. Phys. Chem. C* **2020**, *124* (37), 20010–20020. https://doi.org/10.1021/acs.jpcc.0c05787.

331 Sahoo, M. K.; Samantara, A. K.; Behera, J. N. In Situ Transformed Cobalt Metal–Organic Framework Electrocatalysts for the Electrochemical Oxygen Evolution Reaction. *Inorg. Chem.* **2020**, *59* (17), 12252–12262. https://doi.org/10.1021/acs.inorgchem.0c01300.

332 Nath, N. C. D.; Jeong, H. W.; Han, D. S.; Park, H.; Lee, J.-J. Facile Electrochemical Synthesis of Highly Efficient Copper–Cobalt Oxide Nanostructures for Oxygen Evolution Reactions. *J. Electrochem. Soc.* **2020**, *167* (2), 026510. https://doi.org/10.1149/1945-7111/ab6a80.

333 Luo, W.; Hu, J.; Diao, H.; Schwarz, B.; Streb, C.; Song, Y.-F. Robust Polyoxometalate/Nickel Foam Composite Electrodes for Sustained Electrochemical Oxygen Evolution at High PH. *Angew. Chem. Int. Ed.* **2017**, *56* (18), 4941–4944. https://doi.org/10.1002/anie.201612232.

334 Cho, S.-H.; Yoon, K. R.; Shin, K.; Jung, J.-W.; Kim, C.; Cheong, J. Y.; Youn, D.-Y.; Song, S. W.; Henkelman, G.; Kim, I.-D. Synergistic Coupling of Metallic Cobalt Nitride Nanofibers and IrO_x Nanoparticle Catalysts for Stable Oxygen Evolution. *Chem. Mater.* **2018**, *30* (17), 5941–5950. https://doi.org/10.1021/acs.chemmater.8b02061.

335 Jung, S.; McCrory, C. C. L.; Ferrer, I. M.; Peters, J. C.; Jaramillo, T. F. Benchmarking Nanoparticulate Metal Oxide Electrocatalysts for the Alkaline Water Oxidation Reaction. *J. Mater. Chem. A* **2016**, *4* (8), 3068–3076. https://doi.org/10.1039/C5TA07586F.

336 Li, D.; Zong, Z.; Tang, Z.; Liu, Z.; Chen, S.; Tian, Y.; Wang, X. Total Water Splitting Catalyzed by Co@Ir Core–Shell Nanoparticles Encapsulated in Nitrogen-Doped Porous Carbon Derived from Metal–Organic Frameworks. *ACS Sustain. Chem. Eng.* **2018**, *6* (4), 5105–5114. https://doi.org/10.1021/acssuschemeng.7b04777.

337 Gong, L.; Ren, D.; Deng, Y.; Yeo, B. S. Efficient and Stable Evolution of Oxygen Using Pulse-Electrodeposited Ir/Ni Oxide Catalyst in Fe-Spiked KOH Electrolyte. *ACS Appl. Mater. Interfaces* **2016**, *8* (25), 15985–15990. https://doi.org/10.1021/acsami.6b01888.

338 Xie, Y.; Deng, Y.; Yang, C.; Zeng, Z.; Li, Y.; Chen, G. CoO Functionalized IrO2-Sb$_2$O$_5$-SnO$_2$ Anode with an Enhanced Activity and Stability for Electrocatalytic Oxygen Evolution. *J. Alloys Compd.* **2017**, *696*, 257–265. https://doi.org/10.1016/j.jallcom.2016.11.240.

339 Yan, N.; Detz, ctive Surface Functionalization Generating Site-Isolated Ir on a MnO $_x$ /N-Doped Carbon Composite R. J.; Govindarajan, N.; Koelewijn, J. M.; Hua, B.; Li, P.; Meijer, E. J.; Reek, J. N. H. Sele for Robust Electrocatalytic Water Oxidation. *J. Mater. Chem. A* **2019**, *7* (40), 23098–23104. https://doi.org/10.1039/C9TA08447A.

340 Pei, J.; Mao, J.; Liang, X.; Chen, C.; Peng, Q.; Wang, D.; Li, Y. Ir–Cu Nanoframes: One-Pot Synthesis and Efficient Electrocatalysts for Oxygen Evolution Reaction. *Chem. Commun.* **2016**, *52* (19), 3793–3796. https://doi.org/10.1039/C6CC00552G.

341 Jović, B. M.; Lačnjevac, U. Č.; Jović, V. D.; Gajić-Krstajić, Lj.; Kovač, J.; Poleti, D.; Krstajić, N. V. Ni-(Ebonex-Supported Ir) Composite Coatings as Electrocatalysts for Alkaline Water Electrolysis. Part II: Oxygen Evolution. *Int. J. of Hydrog. Energy* **2016**, *41* (45), 20502–20514. https://doi.org/10.1016/j.ijhydene.2016.08.226.

342 Liao, C.-H.; Fan, K.; Bao, S.-S.; Fan, H.; Wang, X.-Z.; Hu, Z.; Kurmoo, M.; Zheng, L.-M. From a Layered Iridium(III)–Cobalt(II) Organophosphonate to an Efficient Oxygen-Evolution-Reaction Electrocatalyst. *Chem. Commun.* **2019**, *55* (92), 13920–13923. https://doi.org/10.1039/C9CC06164A.

343 Fu, L.; Hu, X.; Li, Y.; Cheng, G.; Luo, W. IrW Nanobranches as an Advanced Electrocatalyst for PH-Universal Overall Water Splitting. *Nanoscale* **2019**, *11* (18), 8898–8905. https://doi.org/10.1039/C9NR01690B.

344 Liu, J.; Wang, Z.; Su, K.; Xv, D.; Zhao, D.; Li, J.; Tong, H.; Qian, D.; Yang, C.; Lu, Z. Self-Supported Hierarchical IrO_2 @NiO Nanoflake Arrays as an Efficient and Durable Catalyst for Electrochemical Oxygen Evolution. *ACS Appl. Mater. Interfaces* **2019**, *11* (29), 25854–25862. https://doi.org/10.1021/acsami.9b05785.

345 Li, X.; Xue, W.; Mo, R.; Yang, S.; Li, H.; Zhong, J. In Situ Growth of Minimal Ir-Incorporated $Co_xNi_{1-x}O$ Nanowire Arrays on Ni Foam with Improved Electrocatalytic Activity for Overall Water Splitting. *Chinese J. Catal.* **2019**, *40* (10), 1576–1584. https://doi.org/10.1016/S1872-2067(19)63414-5.

346 Fan, R.; Mu, Q.; Wei, Z.; Peng, Y.; Shen, M. Atomic Ir-Doped NiCo Layered Double Hydroxide as a Bifunctional Electrocatalyst for Highly Efficient and Durable Water Splitting. *J. Mater. Chem. A* **2020**, *8* (19), 9871–9881. https://doi.org/10.1039/D0TA03272G.

347 Kambir, O.; Pohan, L. A. G.; Kondro, K. H.; Ouattara, L. Study of Oxygen Evolution Reaction on Thermally Prepared $PtO_{y-(100-x)}$ IrO_2 Electrodes. *J. Electrochem. Sci. Eng.* **2020,** 14 (4) 347-360 http://dx.doi.org/10.5599/jese.806.

348 Chen, X.; Xu, M.; Li, S.; Li, C.; Sun, X.; Mu, S.; Yu, J. Ultrafine IrNi Bimetals Encapsulated in Zeolitic Imidazolate Frameworks-Derived Porous N-Doped Carbon for Boosting Oxygen Evolution in Both Alkaline and Acidic Electrolytes. *Adv. Mater. Interfaces* **2020**, *7* (24), 2001145. https://doi.org/10.1002/admi.202001145.

349 Fabricating nano-IrO2@amorphous Ir-MOF composites for efficient overall water splitting: a one-pot solvothermal approach J. Mater. Chem. A, 2020,8, 25687-25695 https://doi.org/10.1039/D0TA09168E

350 Zhang, Q.; Duan, Z.; Wang, Y.; Li, L.; Nan, B.; Guan, J. Atomically Dispersed Iridium Catalysts for Multifunctional Electrocatalysis. *J. Mater. Chem. A* **2020**, *8* (37), 19665–19673. https://doi.org/10.1039/D0TA05750A.

351 Luo, X.; Wei, X.; Zhong, H.; Wang, H.; Wu, Y.; Wang, Q.; Gu, W.; Gu, M.; Beckman, S. P.; Zhu, C. Single-Atom Ir-Anchored 3D Amorphous NiFe Nanowire@Nanosheets for Boosted Oxygen Evolution Reaction. *ACS Appl. Mater. Interfaces* **2020**, *12* (3), 3539–3546. https://doi.org/10.1021/acsami.9b17476.

352 Luo, Q.; Lin, D.; Zhan, W.; Zhang, W.; Tang, L.; Luo, J.; Gao, Z.; Jiang, P.; Wang, M.; Hao, L.; Tang, K. Hexagonal Perovskite Ba $_{0.9}$ Sr $_{0.1}$ Co $_{0.8}$ Fe $_{0.1}$ Ir $_{0.1}$ O $_{3-\delta}$ as an Efficient Electrocatalyst towards the Oxygen Evolution Reaction. *ACS Appl. Energy Mater.* **2020**, *3* (7), 7149–7158. https://doi.org/10.1021/acsaem.0c01192.

353 Li, L.; Wang, B.; Zhang, G.; Yang, G.; Yang, T.; Yang, S.; Yang, S. Electrochemically Modifying the Electronic Structure of IrO $_2$ Nanoparticles for Overall Electrochemical Water Splitting with Extensive Adaptability. *Adv. Energy Mater.* **2020**, *10* (30), 2001600. https://doi.org/10.1002/aenm.202001600.

354 Xu, Y.; Chai, X.; Liu, M.; Ren, T.; Yu, S.; Wang, Z.; Li, X.; Wang, L.; Wang, H. Two-Dimensional NiIr@N-Doped Carbon Nanocomposites Supported on Ni Foam for Electrocatalytic Overall Water Splitting. *Chem. Eur. J.* **2020**, *26* (63), 14496–14501. https://doi.org/10.1002/chem.202003473.

355 Luo, F.; Guo, L.; Xie, Y.; Xu, J.; Qu, K.; Yang, Z. Iridium Nanorods as a Robust and Stable Bifunctional Electrocatalyst for pH-Universal Water Splitting. *Appl. Catal. B: Environ* **2020**, *279*, 119394. https://doi.org/10.1016/j.apcatb.2020.119394.

356 Zhao, Z.; Jin, W.; Xu, L.; Wang, C.; Zhang, Y.; Wu, Z. Ultrafine Ir Nanoparticles Decorated on FeP/FeOOH with Abundant Interfaces *via* a Facile Corrosive Approach for Alkaline Water-Splitting. *J. Mater. Chem. A* **2021**, *9* (20), 12074–12079. https://doi.org/10.1039/D1TA02658E.

357 Qin, Y.; Wang, Z.; Yu, W.; Sun, Y.; Wang, D.; Lai, J.; Guo, S.; Wang, L. High Valence M-Incorporated PdCu Nanoparticles (M = Ir, Rh, Ru) for Water Electrolysis in Alkaline Solution. *Nano Lett.* **2021**, *21* (13), 5774–5781. https://doi.org/10.1021/acs.nanolett.1c01581.

358 Wang, Q.; Zhang, Z.; Cai, C.; Wang, M.; Zhao, Z. L.; Li, M.; Huang, X.; Han, S.; Zhou, H.; Feng, Z.; Li, L.; Li, J.; Xu, H.; Francisco, J. S.; Gu, M. Single Iridium Atom Doped Ni_2P Catalyst for Optimal Oxygen Evolution. *J. Am. Chem. Soc.* **2021**, *143* (34), 13605–13615. https://doi.org/10.1021/jacs.1c04682.

359 Chen, J.; Wang, Y.; Qian, G.; Yu, T.; Wang, Z.; Luo, L.; Shen, F.; Yin, S. In Situ Growth of Volcano-like FeIr Alloy on Nickel Foam as Efficient Bifunctional Catalyst for Overall Water Splitting at High Current Density. *Chemical Engineering Journal* **2021**, *421*, 129892. https://doi.org/10.1016/j.cej.2021.129892.

360 Li, Z.; Liu, D.; Lu, X.; Du, M.; Chen, Z.; Teng, J.; Sha, R.; Tian, L. Boosting Oxygen Evolution of Layered Double Hydroxide through Electronic Coupling with Ultralow Noble Metal Doping. *Dalton Trans.* **2022**, *51* (4), 1527–1532. https://doi.org/10.1039/D1DT03906G.

361 Guo, R.; Shi, W.; Wenzhu Liu; Yang, X.; Xie, Y.; Yang, T.; Xiao, J. Ultralow Noble Metals Doping Enables Metal-Organic Framework Derived Ni(OH)2nanocages as Efficient Water Oxidation Electrocatalysts. *Chemical Engineering Journal* **2022**, *429*, 132478. https://doi.org/10.1016/j.cej.2021.132478.

362 Li, L.; Wang, P.; Cheng, Z.; Shao, Q.; Huang, X. One-Dimensional Iridium-Based Nanowires for Efficient Water Electrooxidation and Beyond. *Nano Res.* **2022**, *15* (2), 1087–1093. https://doi.org/10.1007/s12274-021-3603-9.

363 Mugheri, A. Q.; Tahira, A.; Aftab, U.; Bhatti, A. L.; Memon, N. N.; Memon, J.-R.; Abro, M. I.; Shah, A. A.; Willander, M.; Hullio, A. A.; Ibupoto, Z. H. Efficient Tri-Metallic Oxides NiCo$_2$O$_4$/CuO for the Oxygen Evolution Reaction. *RSC Adv.* **2019**, *9* (72), 42387–42394. https://doi.org/10.1039/C9RA09351F.

364 Bhatti, A. L.; Aftab, U.; Tahira, A.; Abro, M. I.; Kashif samoon, M.; Aghem, M. H.; Bhatti, M. A.; HussainIbupoto, Z. Facile Doping of Nickel into Co$_3$O$_4$ Nanostructures to Make Them Efficient for Catalyzing the Oxygen Evolution Reaction. *RSC Adv.* **2020**, *10* (22), 12962–12969. https://doi.org/10.1039/D0RA00441C.

365 Moysiadou, A.; Lee, S.; Hsu, C.-S.; Chen, H. M.; Hu, X. Mechanism of Oxygen Evolution Catalyzed by Cobalt Oxyhydroxide: Cobalt Superoxide Species as a Key Intermediate and Dioxygen Release as a Rate-Determining Step. *J. Am. Chem. Soc.* **2020**, *142* (27), 11901–11914. https://doi.org/10.1021/jacs.0c04867.

366 Yoneda, Y. Fundamental Research on Anodic Reaction. II.* Activation Energy of Anodic Oxygen-producing Reaction on Some Electrode Materials in Aqueous Solution of N/10 Sodium Hydroxide. *Bull. Chem. Soc. Jpn.*, **1949,** 22, 266-274, https://doi.org/10.1246/bcsj.22.266

367 Singh, R. N.; Singh, N. K.; Singh, J. P. Electrocatalytic Properties of New Active Ternary Ferrite Film Anodes for O2 Evolution in Alkaline Medium. *Electrochim. Acta* **2002**, *47* (24), 3873–3879. https://doi.org/10.1016/S0013-4686(02)00354-7.

368 Mills, A.; Davies, H. L. Oxygen Evolution Redox Catalysis Using Ru-Adams. *Electrochim. Acta* **1992**, *37* (7), 1217–1225. https://doi.org/10.1016/0013-4686(92)85059-T.

369 Nikolov, I.; Darkaou, .; Zhecheva, E.; Stoyanova, R.; Dimitrov, N.; Vitanov, T . Electrocatalytic activity of spine1 related cobaltites $M_xCo_{3-x}O_4$ (M = Li, Ni, Cd in the oxygen evolution reaction *Journal of Electroanalytical Chemistry* 429, **1997**, 157- 168. https://doi.org/10.1016/S0022-0728(96)05013-9

370 Kessler, T.; Triaca, W. E.; Arvia, A. J. Kinetics and Mechanism of the Oxygen Evolution Reaction at Oxide-Coated Co-Ni Amorphous Alloy Electrodes. *J Appl Electrochem* **1994**, *24* (4). https://doi.org/10.1007/BF00242058.

371 Zagalskaya, A.; Evazzade, I.; Alexandrov, V. Ab Initio Thermodynamics and Kinetics of the Lattice Oxygen Evolution Reaction in Iridium Oxides. *ACS Energy Lett.* **2021**, *6* (3), 1124–1133. https://doi.org/10.1021/acsenergylett.1c00234.

372 Exner, K. S.; Over, H. Beyond the Rate-Determining Step in the Oxygen Evolution Reaction over a Single-Crystalline IrO2(110) Model Electrode: Kinetic Scaling Relations. *ACS Catal.* **2019**, *9* (8), 6755–6765. https://doi.org/10.1021/acscatal.9b01564.

373 Zeradjanin, A. R.; Masa, J.; Spanos, I.; Schlögl, R. Activity and Stability of Oxides During Oxygen Evolution Reaction---From Mechanistic Controversies Toward Relevant Electrocatalytic Descriptors. *Front. Energy Res.* **2021**, *8*, 613092. https://doi.org/10.3389/fenrg.2020.613092.

374 Fabbri, E.; Habereder, A.; Waltar, K.; Kötz, R.; Schmidt, T. J. Developments and Perspectives of Oxide-Based Catalysts for the Oxygen Evolution Reaction. *Catal. Sci. Technol.* **2014**, *4* (11), 3800–3821. https://doi.org/10.1039/C4CY00669K.

375 Exner, K. S. On the Lattice Oxygen Evolution Mechanism: Avoiding Pitfalls. *ChemCatChem* **2021**, *13* (19), 4066–4074. https://doi.org/10.1002/cctc.202101049.

376 Binninger, T.; Mohamed, R.; Waltar, K.; Fabbri, E.; Levecque, P.; Kötz, R.; Schmidt, T. J. Thermodynamic Explanation of the Universal Correlation between Oxygen Evolution Activity and Corrosion of Oxide Catalysts. *Sci Rep* **2015**, *5* (1), 12167. https://doi.org/10.1038/srep12167.

377 Fabbri, E.; Schmidt, T. J. Oxygen Evolution Reaction—The Enigma in Water Electrolysis. *ACS Catal.* **2018**, *8* (10), 9765–9774. https://doi.org/10.1021/acscatal.8b02712.

378 Parsons, R. Atlas of Electrochemical Equilibria in Aqueous Solutions. *J. Electroanal. Chem. Interfacial Electrochem.* **1967**, *13* (4), 471. https://doi.org/10.1016/0022-0728(67)80059-7.

379 Schalenbach, M.; Kasian, O.; Ledendecker, M.; Speck, F. D.; Mingers, A. M.; Mayrhofer, K. J. J.; Cherevko, S. The Electrochemical Dissolution of Noble Metals in Alkaline Media. *Electrocatalysis* **2018**, *9* (2), 153–161. https://doi.org/10.1007/s12678-017-0438-y.

380 Zhang, T.; Song, F.; Wang, Y.; Yuan, J.; Niu, L.; Wang, A.; Fang, K. Bifunctional WS_2@Co_3S_4 Core-Shell Nanowire Arrays for Efficient Water Splitting. *Electrochim. Acta* **2022**, *404*, 139648. https://doi.org/10.1016/j.electacta.2021.139648.

381 Akbayrak, M.; Önal, A. M. Metal Oxides Supported Cobalt Nanoparticles: Active Electrocatalysts for Oxygen Evolution Reaction. *Electrochim. Acta* **2021**, *393*, 139053. https://doi.org/10.1016/j.electacta.2021.139053.

382 Akbayrak, M.; Önal, A. M. The Utilization of Iridium Nanoparticles Impregnated on Metal Oxides (Ceria, Titania, and Zirconia) with a Simple and Ecologically Safe Synthesis Approach in Oxygen Evolution Reactions. *J. Electrochem. Soc.* **2022**, *169* (7), 076511. https://doi.org/10.1149/1945-7111/ac81fa.

APPENDICES

APPENDIX A

A.1. Synthesis, preparation and electrochemical studies of the catalysts for

the investigation of the activity towards HER

A.1.1. Rh/CeO$_2$ catalysts

400 mg of CeO$_2$ powder and 45.7 mg of RhCl$_3$.3H$_2$O were mixed in 100 mL distilled water and the mixture was stirred for 24 h at room temperature. Then, 10 mL of aqueous NaBH$_4$ solution (3.0 mM) was added to this slurry drop wise and the mixture was stirred for 1 h. After this period, Rh/CeO$_2$ nanoparticles were obtained and separated from the solution via centrifugation at 8000 rpm for 10 min. In order to remove residues coming from the solution, Rh/CeO$_2$ was washed with 50 mL water and dried under vacuum at 60°C for 12 h. Rh content of our catalyst was determined as 4.0% wt. using ICP-OES. XRD, TEM, TEM-EDX and XPS analyses were also performed for further characterization of Rh/CeO$_2$.

To modify GCEs, 37.5 mg of Rh/CeO$_2$ was sonicated for 1 h in 500.0 µL isopropanol and 2.0 µL aliquot of this dispersion was dropped onto previously cleaned GCE. The suspension was dried on GCE at room temperature for 1 h and Rh/CeO$_2$ on GCE was obtained. For comparison Pt/C on GCE was also prepared by following the same procedure given above using 15 mg of commercial Pt/C. Note that the amount of rhodium and platinum content on the GCE was kept constant as 85.7 µg.cm^{-2} for all measurements.

LSV was utilized to investigate the electrochemical activity of the modified electrodes in 0.5 M H_2SO_4 solution at 5 mV/s scan rate. The obtained potentials were optimized with respect to reversible hydrogen electrode (RHE) by using the following equation ($E_{vs\ RHE}$ = $E_{vs\ Ag/AgCl}$+ 0.210 + 0.059 pH) V. The electrochemical impedance spectroscopy (EIS) measurements were performed at various potentials in the frequency range of 0.1–100,000 Hz with an amplitude of 5 mV. The electrocatalytic stability of Rh/CeO_2 on GCE was tested by recording cycling voltammogram (CV) in 0.5 M H_2SO_4 solution in the range of -0.50 to +0.50 V vs. Ag/AgCl at a 50 mV.s^{-1} scan rate.

A.1.2. Rh/TiO$_2$ for the investigation of counter electrode effect

600 mg of TiO_2 powder and 7.78 mg of $RhCl_3.3H_2O$ salt were stirred together in 100 mL H_2O for 18 h at room temperature. 10 mL of 3.0 mM $NaBH_4$ (aq) solution was added drop wise to this mixture. After 1 hour stirring, Rh nanoparticles were successfully impregnated on TiO_2. After the centrifugation (10 min at 8000 rpm), washing (with 100 mL H_2O) and drying (under vacuum at 60 °C for 12 h) processes, 587 mg of Rh/TiO_2 was obtained. According to ICP-OES analysis, Rh metal content of Rh/TiO_2 was determined as 0.50% wt. To prepare the catalyst ink, 50 mg of Rh/TiO_2 and 400 µL Nafion solution were dispersed in 2 mL isopropanol by sonication for 2 hours. 2.5 µL of homogeneous ink was dropped onto cleaned GCE (diameter = 3.00 mm) and dried at RT for 3 h. Note that, for all tests, the Rh amount on GCE kept constant as 3.79 µg.cm^{-2} and for the control tests, Pt/C electrode was prepared by following the same procedure given above.

Linear sweep voltammetry method (LSV) with 20 mV/s scan rate in 0.5 M H_2SO_4 solution was used to investigate electrochemical behavior of catalysts on GCEs. The potentials obtained from polarization curves were reported against reversible hydrogen electrode (RHE) by adding a value of ($E^o_{Ag/AgCl}$ + 0.059 pH) V ($E^o_{Ag/AgCl}$ = 0.210 V). The EIS studies were conducted at -13, -23, -33 and -43 mV vs. RHE (frequency range: 0.1–100,000 Hz). Note that before electrocatalytic test of Rh/TiO_2, pretreatment has been performed by applying 2000 cycles between -0.5 and 0.5 V vs. Ag/AgCl. This potential range was also used to test electrocatalytic stability with a voltage scan rate of 50 mV.s^{-1}.

A.1.3. Ir containing catalysts

39.1 mg of $IrCl_3.xH_2O$ and 494.0 mg of ceria powder were stirred in 75 mL distilled water at room temperature (RT) for 24 h. Then, 10 mL of 40 mM $NaBH_4$ solution was added drop wise to this mixture and stirred for another 3 h. At the end of the stirring, Ir nanoparticles were successfully impregnated on ceria and Ir/CeO_2 was formed. Then, the obtained Ir/CeO_2 nanoparticles separated from solution by centrifugation method for 10 min, at 8000 rpm and dried at 60 °C for 12 hour under vacuum. Ir/ZrO_2 and Ir/TiO_2 nanoparticles were also obtained by the same experimental procedure. For comparison, Ir/CeO_2 samples with different iridium loadings were also prepared by changing the amount of $IrCl_3.xH_2O$. Ir content of the prepared catalysts were determined as 2.44%, 1.13% and 0.63% wt. Ir for Ir/CeO_2, Ir/ZrO_2 and Ir/TiO_2, respectively.

To modify GCEs, 61.5 mg of Ir/CeO_2, 133.0 mg of Ir/ZrO_2 and 238.0 mg Ir/TiO_2 were sonicated for 1 h in 500.0 μL isopropanol, separately. 2.0 μL of these aliquots were dropped onto previously cleaned GCEs. No nafion was used as a binder to attach the aliquots to surface of electrodes. Prepared GCEs were dried at RT for 1 hour and modified GCEs were ready to use for electrochemical studies.

For the all modified electrode, loading density of metals were kept constant as 85.7 μg.cm^{-2}. To study the electrochemical activity of the catalyst in 0.5 M H_2SO_4 environment, LSV was used at 5 mV/s scan rate. The obtained results were presented with respect to reversible hydrogen electrode (RHE). The conversion from Ag/AgCl to RHE was done by using the equation; $E_{vs\ RHE} = E_{vs\ Ag/AgCl} + 0.210 + 0.059$ pH. The EIS measurements were conducted at potential interval between 210 and 250 mV vs. Ag/AgCl (17 mV and 23 mV vs RHE) in the frequency range of 0.1– 100,000 Hz with an amplitude of 5 mV. The electrocatalytic stability tests of Ir/CeO_2 were conducted by recording CV in the range of −0.50 to +0.50 V vs. Ag/AgCl at a 50 mV.s^{-1} scan rate in 0.5 M H_2SO_4 solution.

A.2. Synthesis, preparation and electrochemical studies of the catalysts for the investigation of activity towards OER

A.2.1. Co containing catalysts

1 g of metal oxide (TiO_2, ZrO_2, or CeO_2) was stirred with the required amount of aqueous $CoCl_2 \cdot 6H_2O$ in 100 mL of deionized water for 24 h. Then, Co^{2+} ions were reduced using $NaBH_4$ solutions (mole of Co/ mole of $NaBH_4$ ratio is 1/5). The catalyst was centrifuged at 8000 rpm and washed with plenty of DI water to remove residues after reduction. The obtained Co/TiO_2, Co/ZrO_2, and Co/CeO_2 catalysts were characterized by ICP-OES, TEM, XRD, and XPS techniques. Loading of Co in the prepared catalyst were found as 4.1 % wt. by means of ICP- OES).

For the ink solutions, 445.0 µL of DMF, 5.0 µL of Nafion, and 37.0 mg catalyst were mixed and further dispersed via 1 h ultrasonication. Subsequently, 5.0 µL of the prepared ink solution was drop cast on the GCE and dried at room temperature overnight. Before beginning the measurements, the working electrodes were treated by oxidative constant current (0.071 mA.cm^{-2}) electrolysis for 10 s. After conditioning, the surface is covered with thin oxide layer. Therefore, Co/MO_2 can be considered as $CoOx/MO_2$.

LSV's were recorded in the range of 0.0- 1.0 V vs. Hg/HgO with a scan rate of 20 mV.s^{-1}. At the scan rate lower than 20 mVs^{-1}, the catalyst surface blockage occurs by the evolved O_2 gas bubbles, which decreases mass transfer capability. All the potentials were converted to the reversible hydrogen electrode at pH =14 [$E_{vs\,RHE} = E_{vs\,Hg/HgO} + 0.915$], and the LSV data were given after compensation for IR drop. The stability experiments were conducted by chronopotentiometry method in 1 M KOH solution at a constant current density of 10.0 mA cm^{-2}.

A.2.2. Ir containing catalysts

Synthesis of the Ir containig catalysts for the investigation of activity towards OER is same with the procedure in HER part. To determine the electrochemical activities of the synthesized iridium catalysts, surface of the GCE were modified with as-prepared electrocatalyst ink and used as a working electrode. Required amount of catalyst, Nafion (5.0 µL), and DMF (445.0 µL) were combined and sonicated during 1 h to obtain catalyst ink. Subsequently, 2.0 µL of the prepared ink was dropped onto the GCE (loading densities were kept constant as 51.58 $\mu g.cm^{-2}$ for all three catalyst) and dried overnight at RT. The working electrodes were pretreated during 100 s with constant current ($-6x10^{-4}$ A) just before the measurements started.

Table A1. Theoretical and experimental loading level of the prepared catalysts

	Loading Level (%)- Theoretical	Loading Level (%)- Experimental
Rh/TiO₂	4%	2.8±0.1
Rh/ZrO₂	4%	2.7±0.1
Rh/CeO₂	4%	4.1±0.1
Ir/TiO₂	4%	0.63±0.01
Ir/ZrO₂	4%	1.13±0.02
Ir/CeO₂	4%	2.44±0.02
Co/TiO₂	4%	4.2±0.2
Co/ZrO₂	4%	4.2±0.2
Co/CeO₂	4%	4.4±0.1

APPENDIX B

B. COUNTER ELECTRODE EFFECT Pt vs. CARBON ROD

B.1. Characterization of Rh/TiO$_2$

Titania (TiO$_2$) supported rhodium NPs (Rh/TiO$_2$) were prepared by impregnation and reduction of Rh^{3+} ions on TiO$_2$ surface and characterized by several analytical instruments. TEM analysis was performed to investigate the size of the Rh NPs. As seen in Figure B1 a and b, highly dispersed Rh NPs (the mean particle size= 2.54 ± 0.6 nm) were formed on titania (Rh particle size is in the range between 1.8 and 3.8 nm (Figure B1 (c)). TEM-EDX given in Fig B1 (d) confirms the presence of Rh NPs on the surface of TiO$_2$. However, due to the 0.5% wt. Rh loading, there is no peak belonging to the Rh NPs in the XRD spectra (Figure B2 (b)). According to the XRD results of TiO$_2$ and Rh/TiO$_2$, there is no change in crystal structure of titania after Rh impregnation (Figure B2 (a-b)).
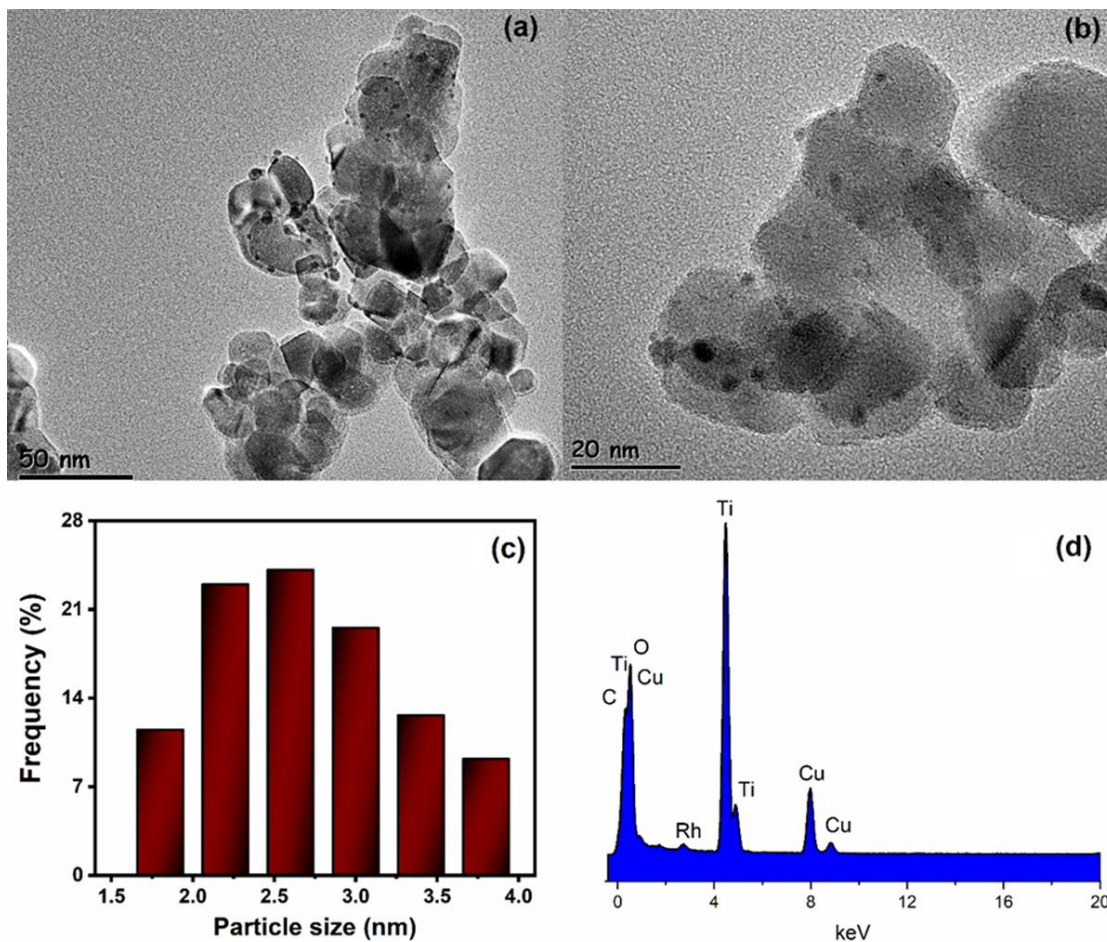
Figure B.1. TEM images of Rh/TiO$_2$ (a, b), the histogram showing the particle size distribution (c) and the corresponding TEM-EDX spectrum (d).
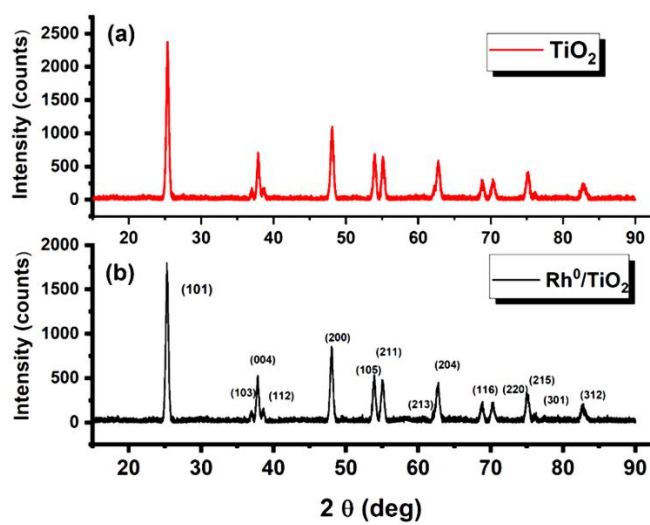
Figure B.2. Powder XRD patterns of a) TiO$_2$ and b) Rh/TiO$_2$ (0.50% wt. Rh).

The oxidation states of Rh NPs in Rh/TiO_2 were investigated with XPS analysis. As seen in Figure B.3 (a), the peaks which belong to $3d_{5/2}$ and $3d_{3/2}$ bands of metallic rhodium appear at 306.7 eV and 311.3 eV, respectively. On the other hand, the peaks at 308.2 eV and 312.7 eV show the oxides species of rhodium. The survey-scan XPS spectra of Rh/TiO_2 given in Figure B.3 (b) provides further evidence for the existence of Rh(0) NPs on TiO_2 nanopowder's surface.
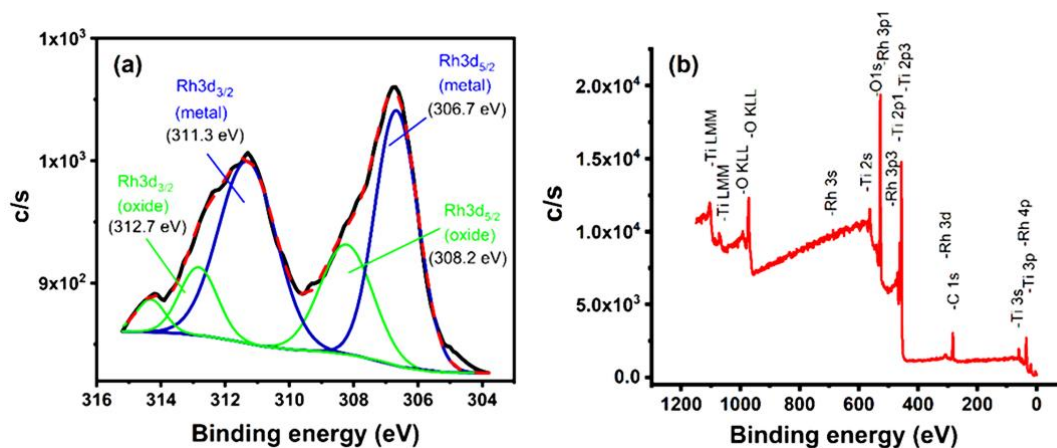
Figure B.3. (a) XPS spectrum of Rh 3d bands, (b) The survey-scan XPS spectrum of Rh/TiO_2.

The Pt loading on the electrode was measured by ICP-MS. Thermo X2 Series Inductively Coupled Plasma Mass Spectrometer was used for the determination of Pt in the solution. The surfaces of the prepared electrodes were digested by HNO_3 solution over 12 h. The amounts of metals in the solution were determined by ICP-MS, and then used to calculate the amounts of metals on the electrode. The amount of Pt deposited on Rh/TiO_2-GCE after 500, 1000 and 2000 cycles as 0.52, 6.38 and 17.94 mole/mole ratio, respectively.

B.2. Electrochemistry of Rh/TiO$_2$-2000

An inspection of Table B.1 reveals that the Tafel slope of Rh/TiO$_2$-2000 is closer to that of commercial 10% Pt/C (27 mV.dec^{-1}) (Figure B4) and comparable to the reported catalysts. Tafel slope is an important parameter to determine the mechanism of HER. The calculated Tafel slope (32 mV.dec^{-1}) for Rh/TiO$_2$-2000 modified GCE indicates that the HER mechanism fits to the Volmer–Tafel mechanism and the rate determining step is the electrochemical desorption of adsorbed hydrogen atoms. The overpotential (η) values at j=10 mA.cm^2 for R/TiO$_2$-2000 and TiO$_2$ were found as 37 mV and 104 mV vs. RHE. The lower η of Rh/TiO$_2$-2000 makes it superior over most of the reported Rh based catalyst.
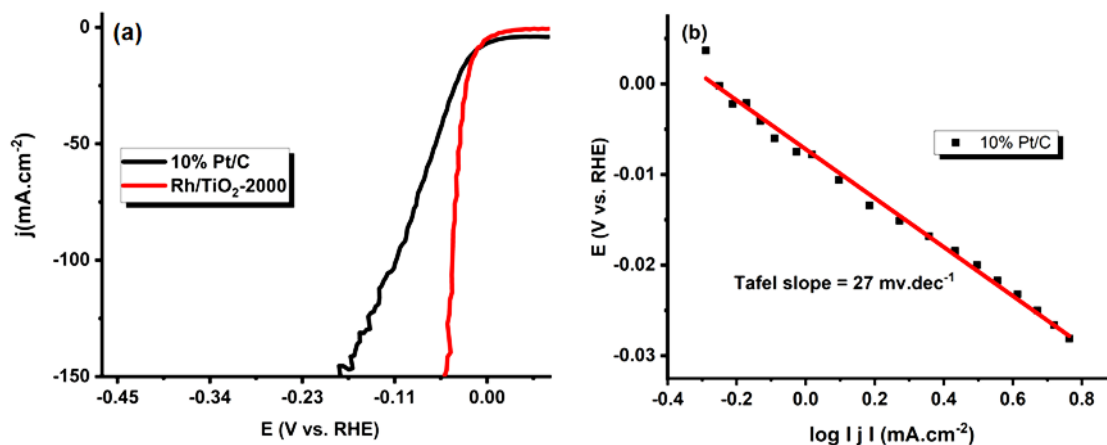
Figure B.4.. a) The polarization curve of Rh/TiO$_2$ modified GCE and 10% Pt/C in 0.5 M H$_2$SO$_4$ b) The corresponding Tafel plot of 10% Pt/C obtained from polarization curve.

The durability of Rh/TiO$_2$-2000 was tested by applying 10000 cyclic scans at a scan rate of 50 mV.s^{-1} in H$_2$SO$_4$ solution (0.5 M). The polarization curves which were obtained before and after the stability test (Figure B5) indicate that there is a negligible change in the onset potential (-29 mV), overpotential at j= 10 mA.cm^{-2} (40mV@-10) and Tafel slope (33.1 mV.dec^{-1}). According to these results, one may conclude that Rh/TiO$_2$-2000 is highly durable electrocatalyst and provides superior stability in HER as compared to the various Rh catalysts in literature.
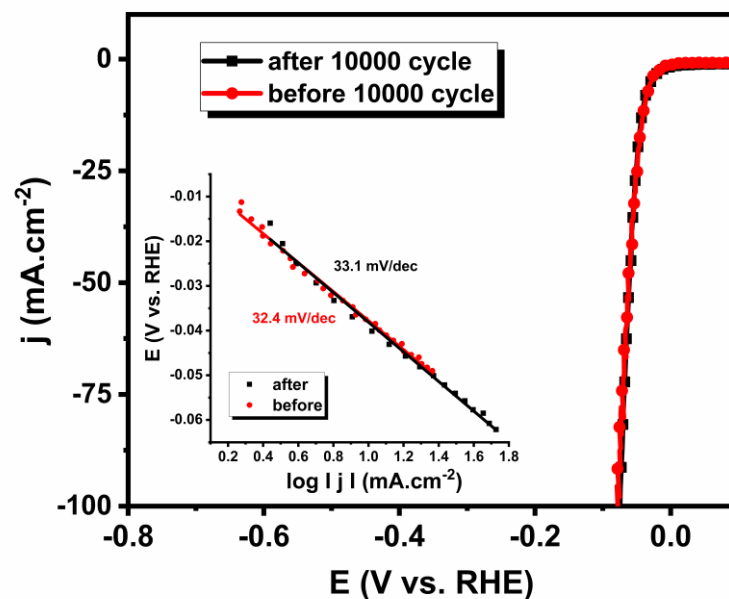
Figure B.5. The polarization curve of Rh/TiO$_2$ modified GCE before and after 10000 CV cycles in 0.5 M H$_2$SO$_4$ (10,000 cycles correspond to 55.5 h) Inset: The corresponding Tafel plot obtained from polarization curve.

To investigate the intrinsic activity of Rh/TiO$_2$-2000, the exchange current density (j$_0$) and TOF values were calculated. It was found that Rh/TiO$_2$-2000 provides an exchange current density of 0.686 mA.cm^{-2} which is superior as compared to the reported Rh based catalysts listed in Table 11. On the other hand, the TOF values calculated by copper under potential deposition (UPD) method for Rh/TiO$_2$-2000 in 1 M H$_2$SO$_4$ (Figure B.6) and they are found as 0.80, 1.44, and 11.45 s^{-1} at 20, 50, and 100 mV (vs. RHE), respectively (Figure B.6). Moreover, the TOF value was also calculated from chronopotantiometry. For this purpose, constant current was applied at overpotential of 100 mV for 1 h in 0.5 M H$_2$SO$_4$ then, the number moles of H$_2$ generated were divided to the number of moles of Rh on the electrode surface and the time. According to this calculation, TOF value was found to be 11.2 s^{-1} at an overpotential of 100 mV which is quite similar to the TOF value calculated from UPD method (Figure B.6). It was reported that Pt catalyst exhibits a TOF value of 0.8 s^{-1} at 0 V in HER which is the same as the TOF value obtained for Rh/TiO$_2$ -2000 at η = 20 mV.
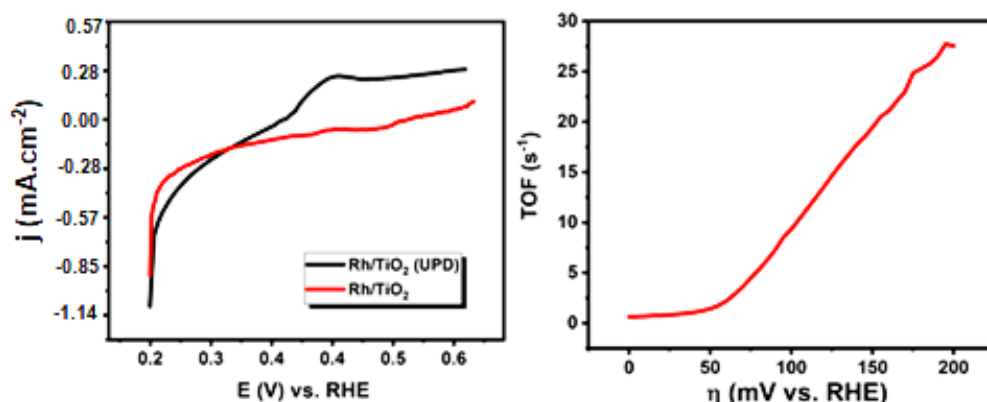
Figure B.6. a) Copper UPD in 1 M H_2SO_4 solution before (red line) and after (black line) of Rh/TiO_2 and b) TOF vs η (mV) graph of Rh/TiO_2 in 1 M H_2SO_4.

Electrochemical impedance spectroscopy (EIS) method was also studied to determine the electrocatalytic activity of Rh/TiO_2-2000 at the potential 240, 250, 260, and 270 mV vs. Ag/AgCl in 0.5 M H_2SO_4 (Figure B.6). From the η vs. log ($1/R_{CT}$) plot (Figure B.7b) , the Tafel slope value was calculated as 33 mV.dec^{-1} which is quite similar to the one derived from LSV curve. Moreover, the electrochemical surface area, ECSA, of Rh/TiO_2-2000 was determined as 15.35 cm^2 by dividing C_{DL} (found as $6.14*10^{-4}$ F C_{DL} from impedance curve at onset potential) to specific capacitance of flat electrode ($Cs \sim 40$ μFcm^{-2})
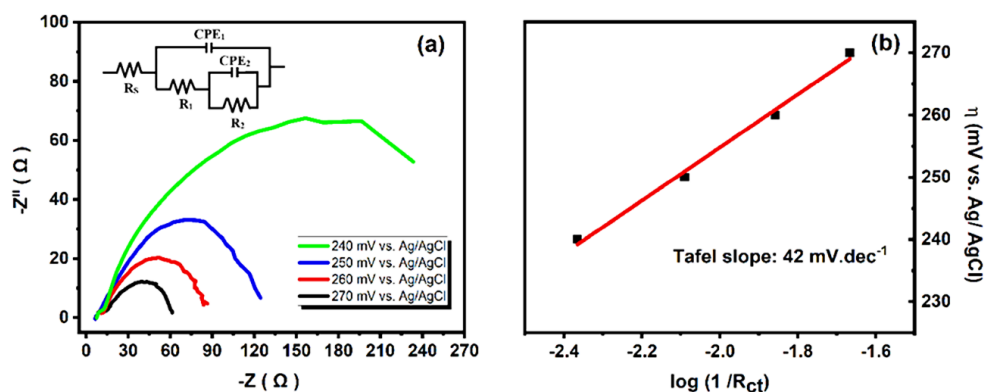
Figure B.7. a) The Nyquist plots for Rh/TiO_2 modified GCE at different overpotentials and b) Tafel plot of Rh/TiO_2 modified GCE, obtained using Rct from the EIS.

190

The HER activity of Rh/TiO$_2$-2000 was also calculated from chronopotantiometry. A constant current of 5.0 mA (corresponding to η=100 mV) was applied for 1 h at ~25 °C in 0.5 M H$_2$SO$_4$. The volume of the evolved H$_2$ gas from the water electrolysis was measured in a Hoffman electrolysis cell and followed as a function of time (Figure B.8). The Faradaic efficiency of Rh/TiO$_2$-2000 for HER was calculated as 94% after applying the charge of 18000 mC. The calculated yield is consistent with the theoretical one and also comparable to that of the reported catalysts.
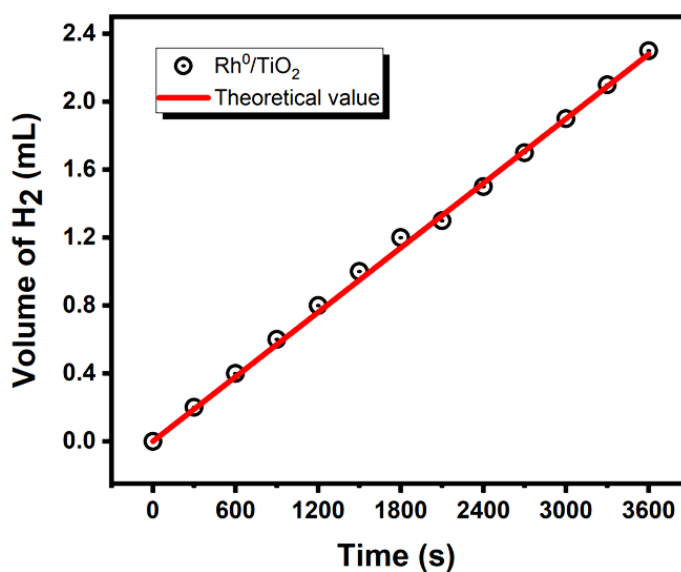
Figure B.8. Volume of H$_2$ versus time graph during the galvanostatic electrolysis of water using Rh/TiO$_2$ modified GCE in 0.5 M H$_2$SO$_4$. Theoretical value was calculated from the amount of electricity using the Faraday's relation and ideal gas equation. Efficiency 94.8%

In this study, rhodium nanoparticles on TiO_2 were successfully prepared by following a facile impregnation-reduction method. Afterwards, electrochemical Pt dissolution and deposition method was used by applying 2000 CV cycle treatment. The electrocatalytic activity of Rh/TiO_2-2000 on GCE with an ultralow mass loading of rhodium (3.79 μg.cm^{-2}) in HER was investigated in acidic media. The enhancements in activity of Rh/TiO_2 should be directly related to the changes in architectural configurations, which alter the electronic structures of the surface metals and/ or facilitate alternate reaction mechanisms relative to pure Pt. Some studies were designed to probe the electronic structures and nature of metal-metal bonding between the metal overlayers and the metallic substrates. The results showed that work functions of metallic films were altered from their bulk values due to the structural and electronic effects of the underlying metal host. Electron transfer between metal overlayers and their metallic hosts altered the metal-metal interactions and surface electronic structures. Lowering the energy of the metal overlayer's d-band center has a significant impact on the interactions of the metal overlayer with adsorbate molecules on the surface. The resulting changes in activation energies and bond enthalpies of adsorbates have dramatic effects on the catalytic activities.

Rh/TiO_2-2000 provides very low Tafel slope (32 mV.dec^{-1}), low overpotential (37 mV@ -10 mA.cm^{-2}), high exchange current density (0.686 mA.cm^{-2}) and high TOF value (11.45 s^{-1}). The Faradaic efficiency of Rh/TiO_2-2000 was found as 94% after applying 18000 mC. The Tafel slope and overpotential @ -10 mA.cm^{-2} values are found to be nearly the same with the one obtained by using benchmark Pt/C catalyst. Rh/TiO_2-2000 on GCE provides high stability even after 10000 cycles in HER. There is no noticeable change in the onset potential (29 mV), overpotential (40 mV@ -10 mA.cm^{-2}), and Tafel slope (33.1 mV.dec^{-1}) after the stability test.

SUPPORTING INFORMATION

Table C.1. Some of the preliminary studies to find suitable catalyst and metal amounts

Catalyst	Catalyst amount (mg)	Isopropanol amount (µL)	Nafion amount (µL)	Amount of Rh in 2 µL ink (µg)
0.5 % Rh/TiO$_2$	21.0	1000.0	10.0	0.21
0.5 % Rh/ZrO$_2$	21.0	1000.0	10.0	0.21
0.5 % Rh/HfO$_2$	21.0	1000.0	10.0	0.21
0.5 % Rh/Al$_2$O$_3$	21.0	1000.0	10.0	0.21
0.5 % Rh/SiO$_2$	21.0	1000.0	10.0	0.21
0.5 % Rh/CeO$_2$	21.0	1000.0	10.0	0.21
0.5 % Rh/CeO$_2$	105.0	1000.0	10.0	1.04
0.5 % Rh/CeO$_2$	150.0	300.0	-	5.00
2.0 % Rh/CeO$_2$	5.3	500.0	10.0	0.42
2.0 % Rh/CeO$_2$	62.0	100.0	50.0	16.53
2.0 % Rh/CeO$_2$	75.0	500.0	-	6.00
3.0 % Rh/CeO$_2$	50.0	500.0	-	6.00
4.0 % Rh/CeO₂	**37.5**	**500.0**	**-**	**6.00**
5.0 % Rh/CeO$_2$	30.0	500.0	-	6.00
4.0 % Rh/TiO$_2$	**37.5**	**500.0**	**-**	**6.00**
4.0 % Rh/ZrO$_2$	**37.5**	**500.0**	**-**	**6.00**
5.0 % Rh/CeO$_2$	30.0	1000.0	50.0	2.86
5.0 % Rh/Al$_2$O$_3$	30.0	500.0	25.0	5.71
10.0 % Pt/C	15.0	500.0	-	6.0
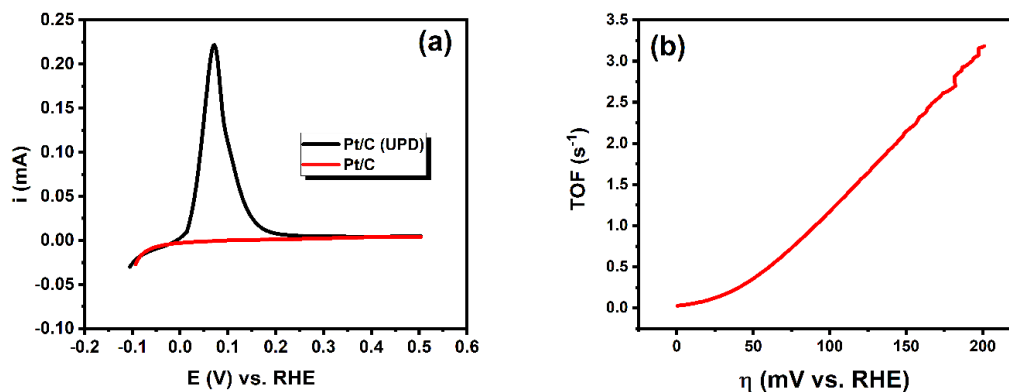
Figure C.1. a) Copper UPD of Pt/C in 1 M H_2SO_4 solution, b) TOF vs η (mV) graph of Rh/CeO$_2$ in 1 M H_2SO_4.
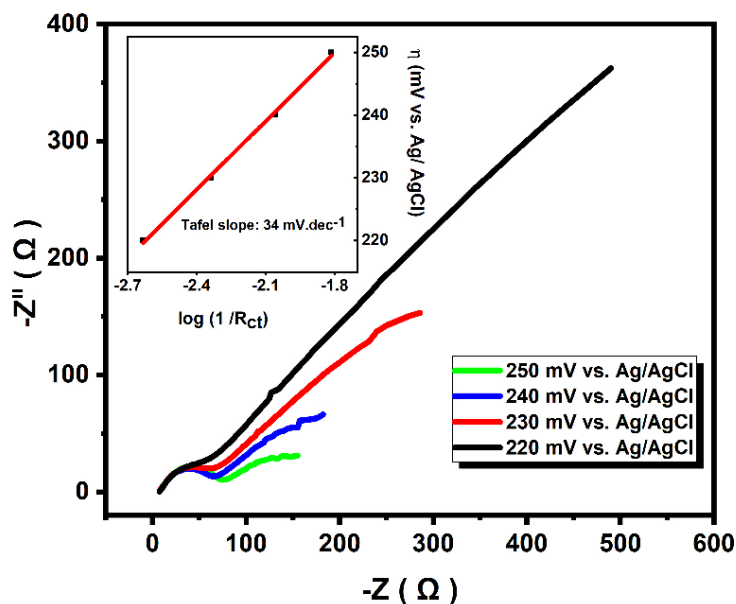
Figure C. 2. The Nyquist plots for Pt/C-GCE at different overpotentials (**inset:** Tafel plot of Pt/C-GCE, obtained using R_{CT} from the EIS)
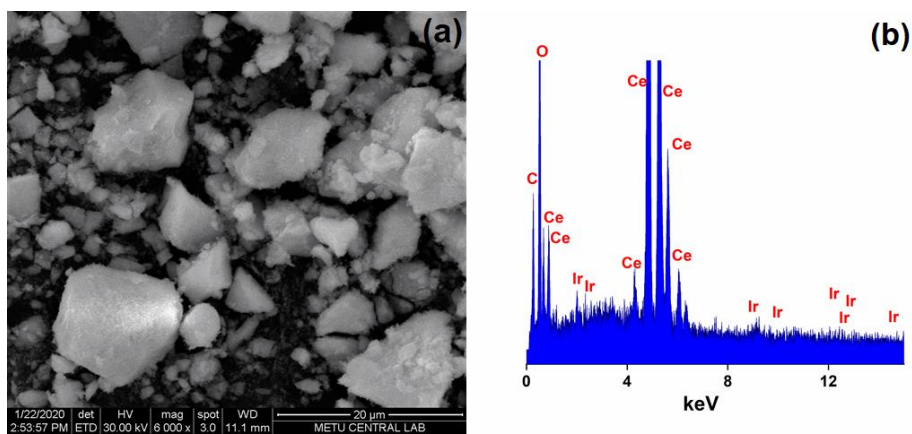
Figure C. 3. (a) SEM image and (b) SEM-EDX spectrum of Ir/CeO$_2$.
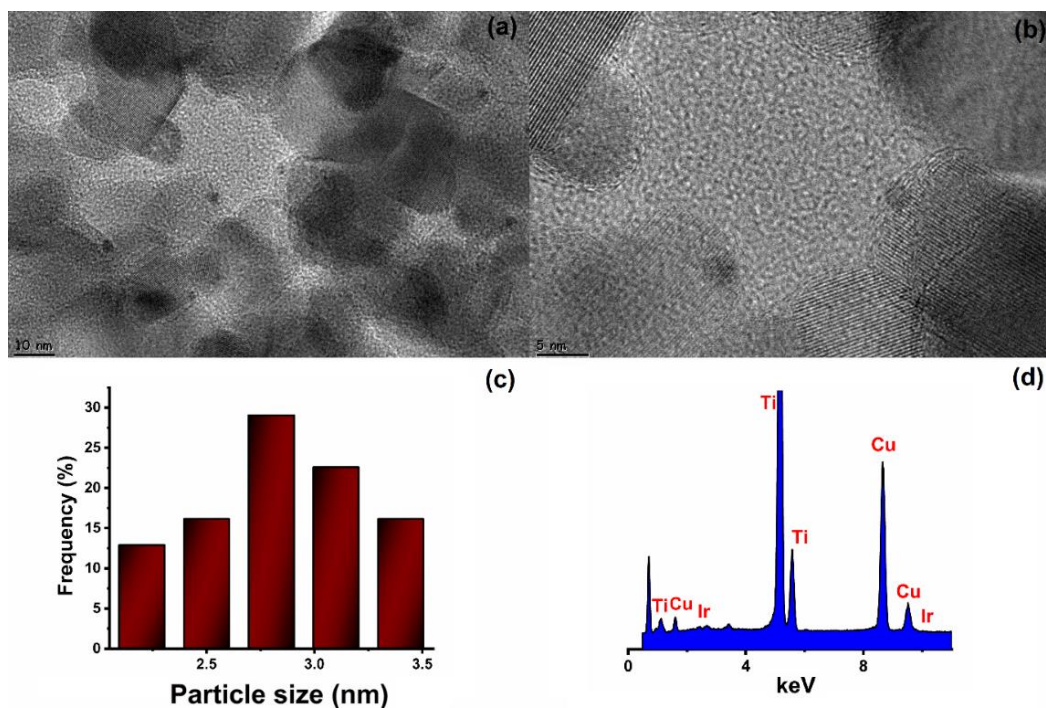
Figure C. 4. a, b) TEM images, c) the histogram and d) the corresponding TEM-EDX spectrum of Ir/TiO$_2$.
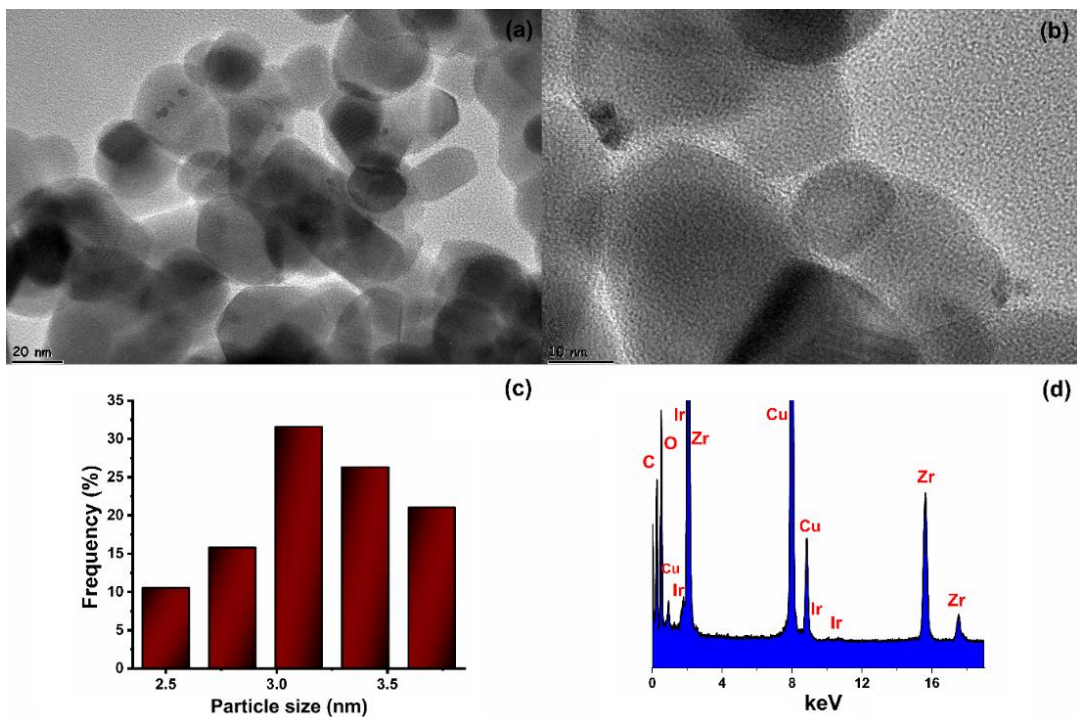
Figure C. 5. a, b) TEM images, c) the histogram and d) the corresponding TEM-EDX spectrum of Ir/ZrO$_2$.
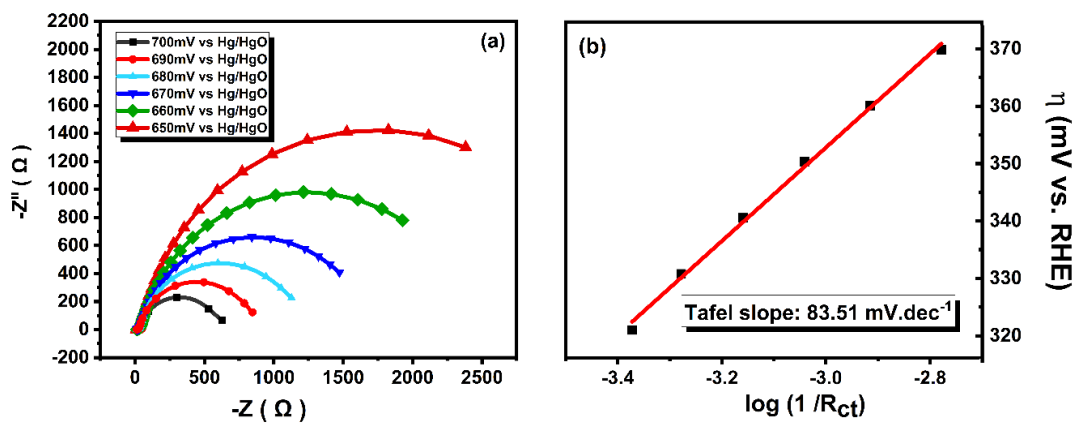
Figure C. 6. EIS measurement of Co$_3$O$_4$ at a potential range between 650 mV and 700 mV vs. Hg/HgO and corresponding Tafel plots.
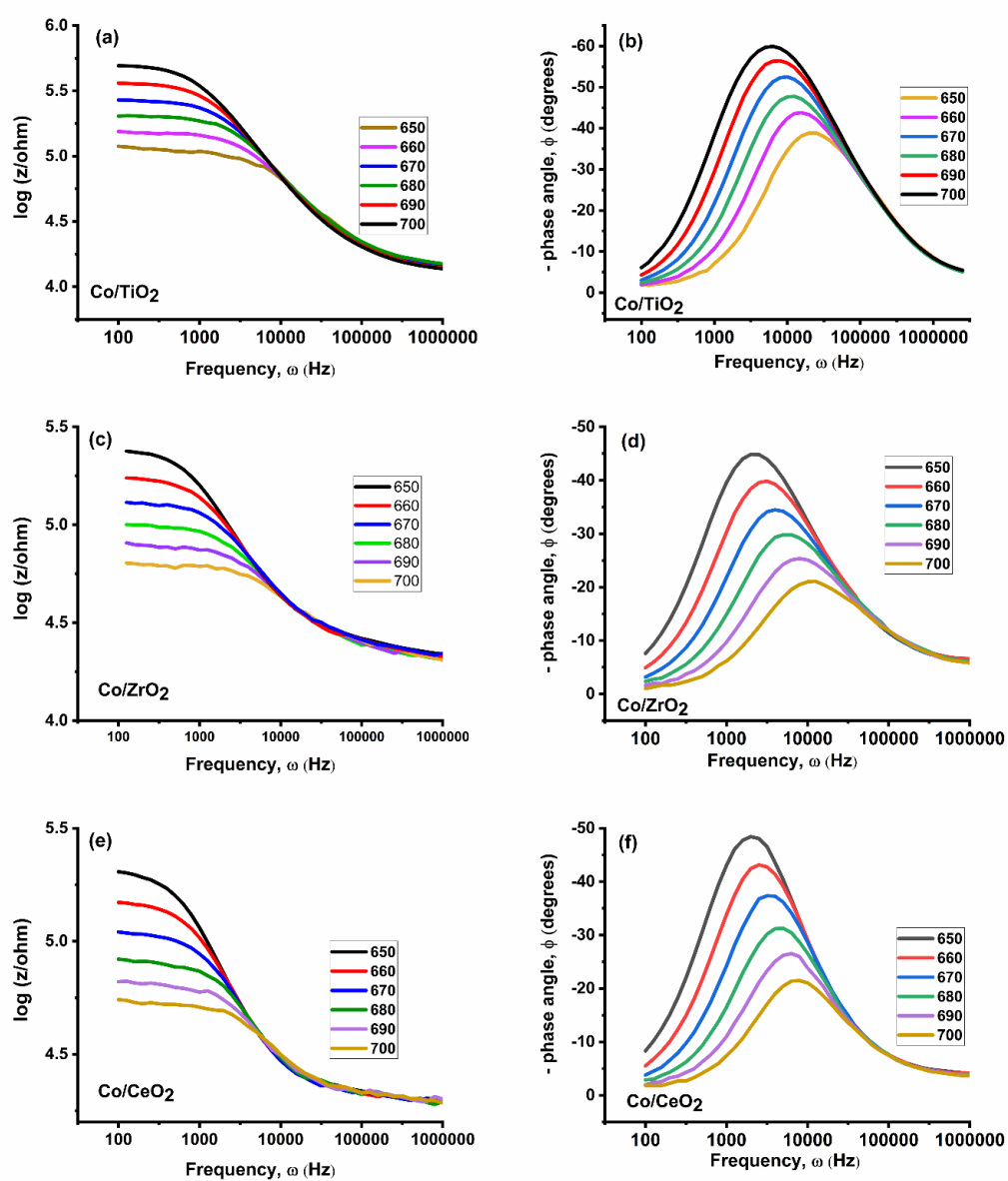
Figure C. 7. Representative Bode plots of Co/MO$_2$ (M= Ti, Zr, Ce) at a potential range between 650 mV and 700 mV vs. Hg/HgO.
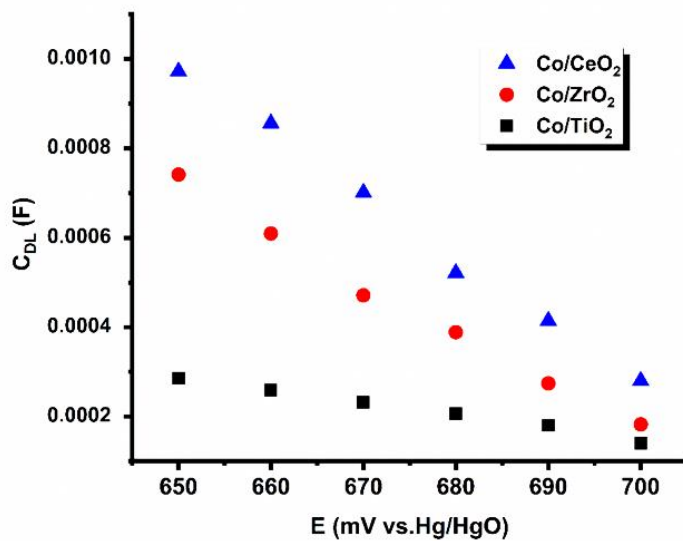
Figure C. 8. Double layer capacitance values at a given potentials from EIS.
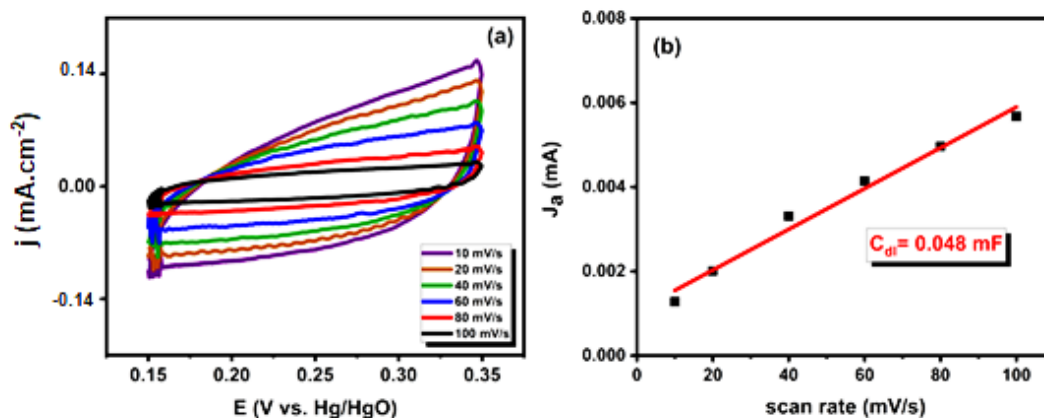
Figure C. 9. a) Representative multi CV experiment of Co_3O_4 at different scan rates (10, 20, 40, 60, 80, and 100 mV/s) for C_{DL} determination in 1.0 M KOH; and b) corresponding capacitive current versus scan rate plots at 0.27 V (vs. Hg/HgO).
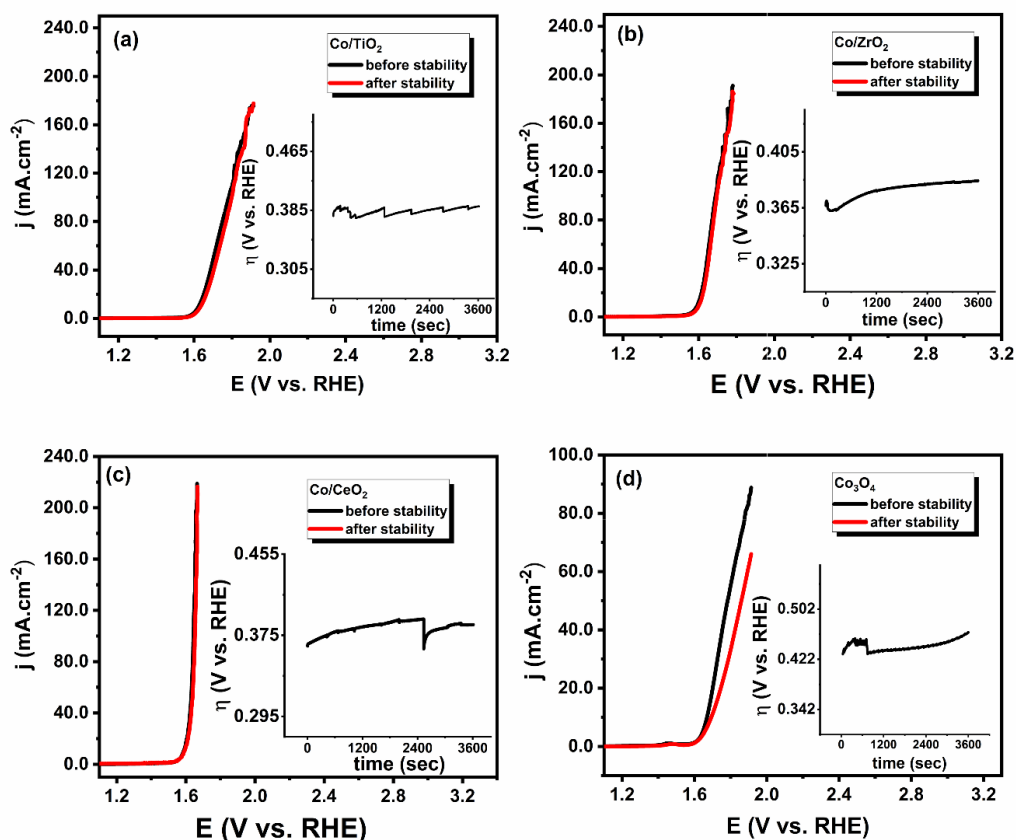
Figure C. 10. (a, b, c) The polarization curves of Co/MO$_2$ (M: Ti, Zr, Ce) and d) Co$_3$O$_4$ at the beginning and after 1-hour chronopotentiometry experiment (inset Figures) at 10 mA.cm^{-2} in 1.0 M KOH.

Table C. 2. Tafel slope values at different KOH concentrations for Co/TiO$_2$, Co/ZrO$_2$, and Co/CeO$_2$.

catalysts	Tafel slopes at 1.0 M	Tafel slopes at 0.8 M	Tafel slopes at 0.6 M	Tafel slopes at 0.4 M	Tafel slopes at 0.2 M
Co/TiO$_2$	67.0	70.0	75.0	82.0	95.0
Co/ZrO$_2$	70.5	72.0	76.0	83.0	104.0
Co/CeO$_2$	63.0	73.0	88.4	92.0	98.0
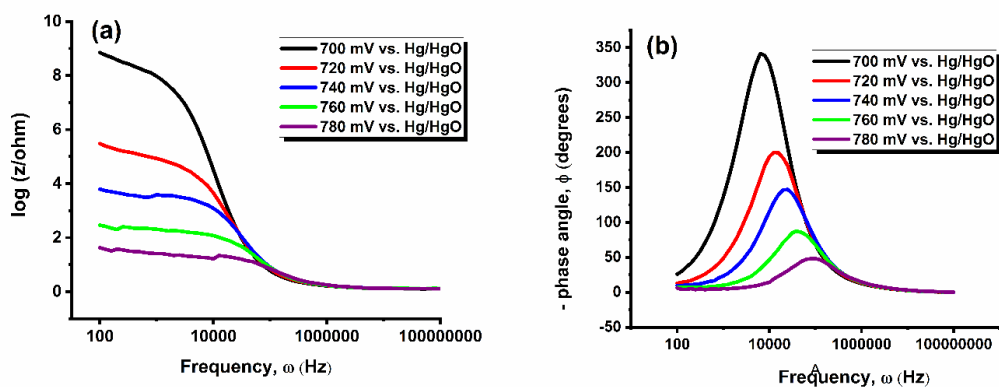
Figure C. 11. Representative Bode plots of Ir/CeO$_2$ at a potential range between 700 mV and 780 mV vs. Hg/HgO in 1.0 M KOH.

Table C. 3. Arrhenius equation, definitions and units of the terms in the formula.

log j$_k$= log (FKC)- Ea /2.303RT		
j$_k$	the kinetic current density	mA.cm^{-2}
F	Faraday's constant	96485 C
K	Kohlrausch coefficient	dimensionless
C	reactant concentration	mol.L^{-1}
E$_a$	the apparent activation energy	J.mol^{-1}
R	the gas constant	8.314 J mol^{-1} K^{-1}
T	the temperature	K

Table C. 4. Lattice oxygen evolution mechanism

$O_{lat} + H_2O \rightarrow O_{lat} - OH + H^+ + e^-$	(1)
$O_{lat} - OH \rightarrow V_O + O_{2(g)} + H^+ + e^-$	(2)
$V_O + H_2O \rightarrow O_{lat} - H + H^+ + e^-$	(3)
$O_{lat} - H \rightarrow O_{lat} + H^+ + e^-$	(4)

*In Equations (1)–(4), O_{lat} and V_O indicate an oxygen atom from the lattice and an oxygen vacancy, respectively

APPENDIX D

D.1. ELECTROCHEMICAL PROPERTIES OF METALS

D. 1. 1. Electrochemical properties of Rh, Ir, Co for hydrogen evolution reactıon

To examine the behavior of metals in 0.5 M H_2SO_4, the metals were deposited on the surface of GCE using an acid solution prepared with metal salt. The behavior of modified GCEs was observed using the DPV method. GCEs modified with metals were first oxidized from 0.0 V to 1.7 V in 0.5 M H_2SO_4, then reduced from 1.7 V to -1.5 V, and finally reoxidized to 0.0 V. For the DPV measurements following settings were used: step size= 2 mV, sample period= 0.2 s, pulse time= 0.05 s, and pulse size = 5mV.
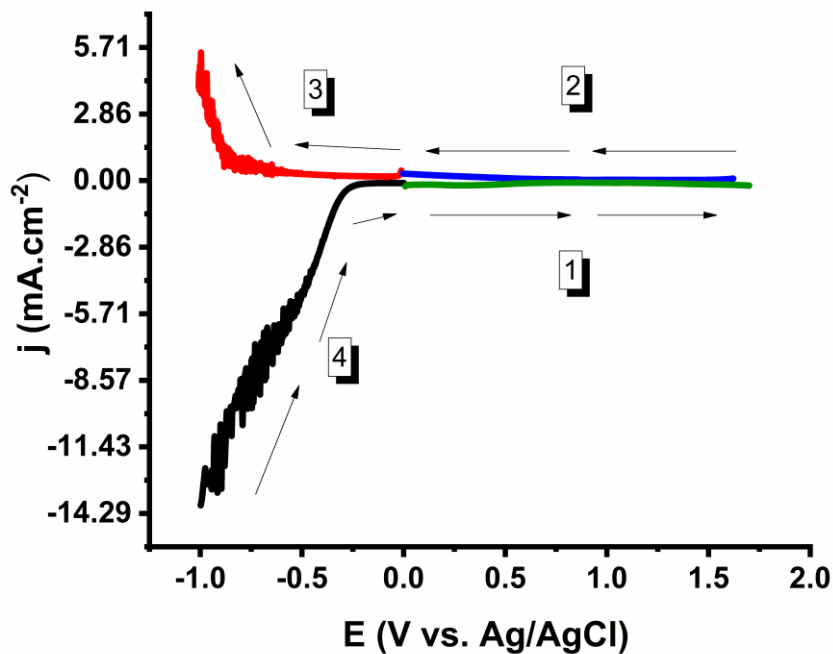
Figure D. 1. Differential pulse voltammograms of CoCl$_3$ in 0.5 M H$_2$SO$_4$
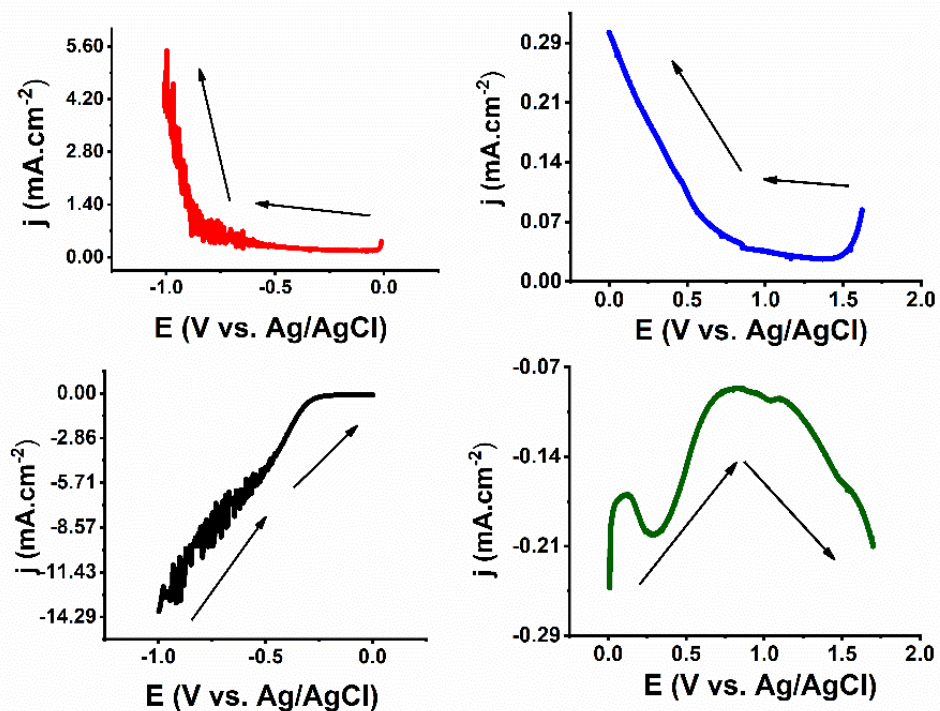
Figure D. 2. DPV plots of CoCl$_3$ examined as oxidation reduction-reoxidation in 0.5 M H$_2$SO$_4$
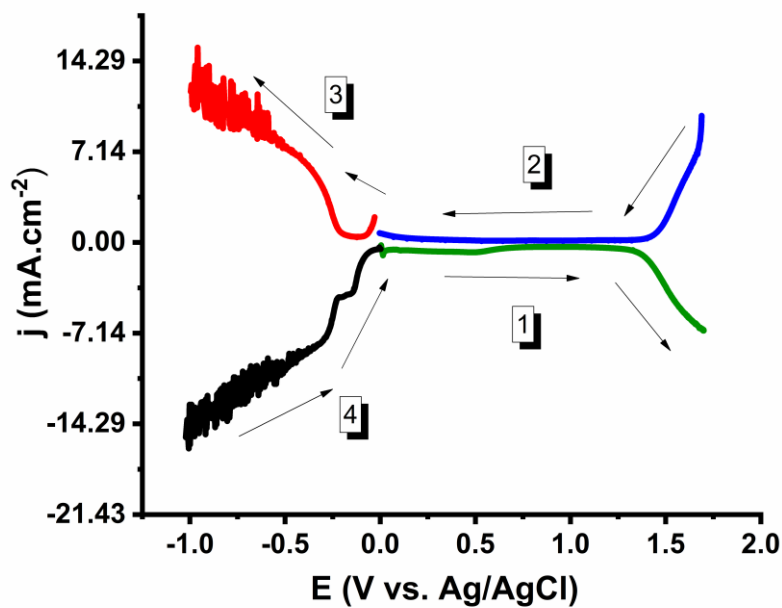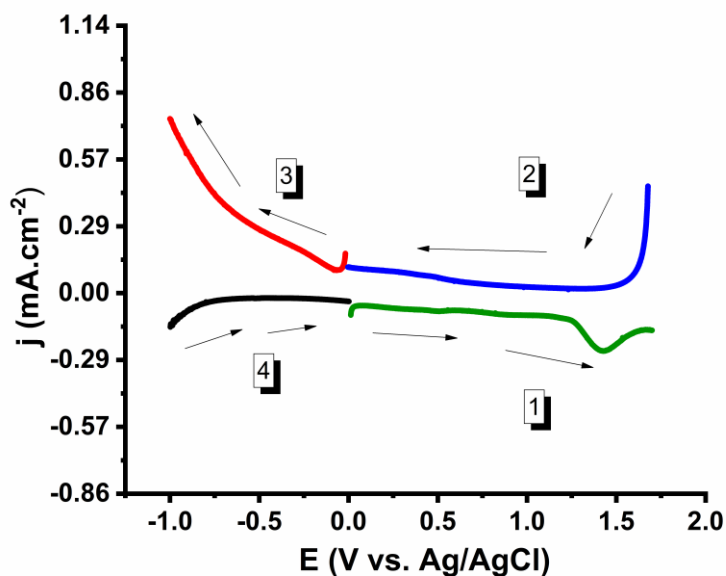
Figure D. 3. Differential pulse voltammograms of RhCl₃ in 0.5 M H₂SO₄
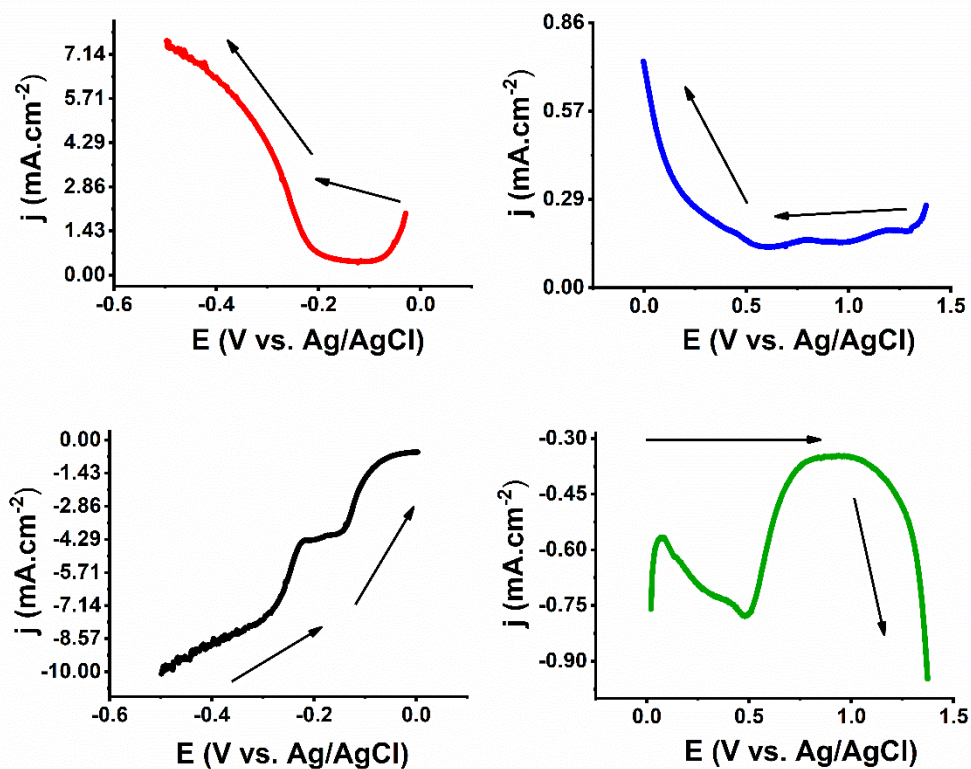
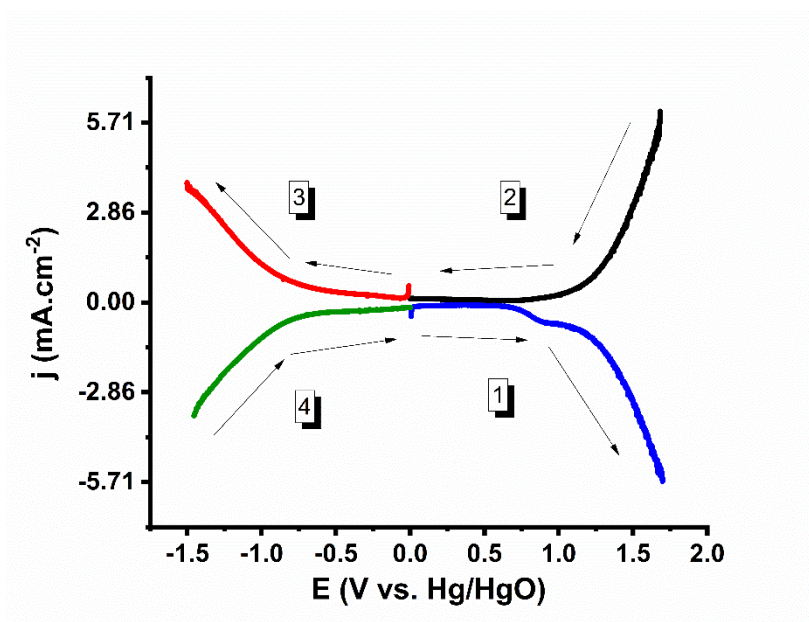**Figure D. 4.** DPV plots of RhCl₃ examined as oxidation reduction-reoxidation in 0.5 M H₂SO₄

Figure D. 5. Differential pulse voltammograms of IrCl$_3$ in 0.5 M H$_2$SO$_4$
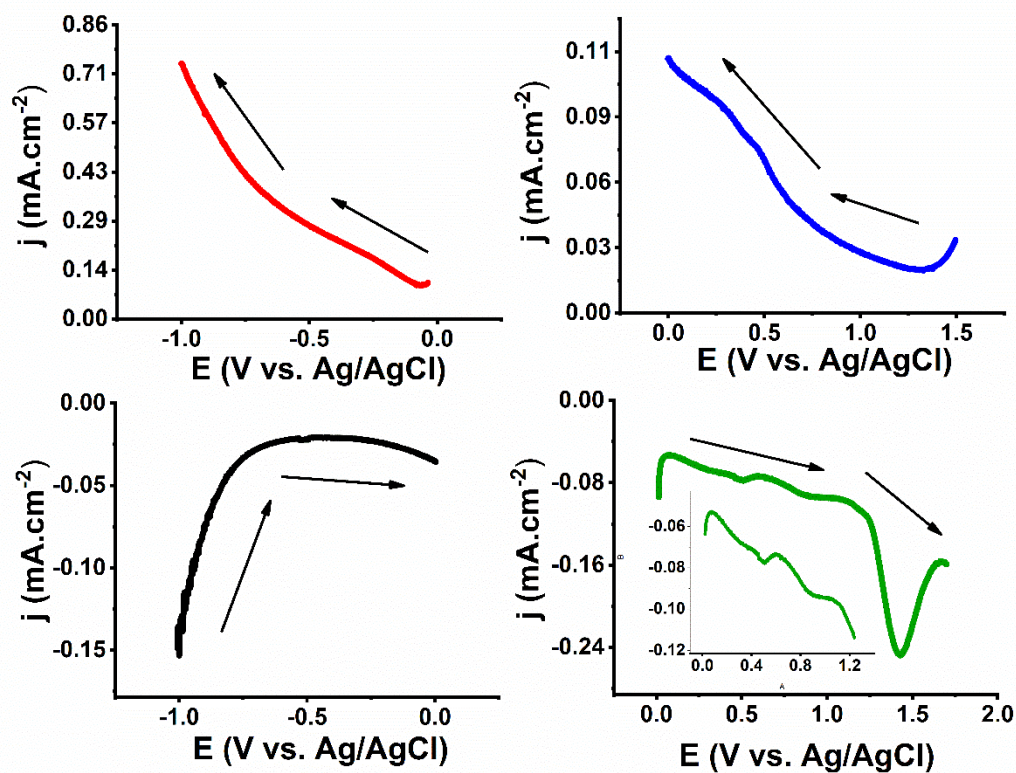
Figure D. 6. DPV plots of IrCl$_3$ examined as oxidation reduction-reoxidation in 0.5 M H$_2$SO$_4$

Table D. 1. Oxidation reduction potential of CoCl$_3$, RhCl$_3$ and IrCl$_3$ in 0.5 M H$_2$SO$_4$

|	Oxidation (1) V vs. Ag/AgCl	Reduction (2) V vs. Ag/AgCl	Reduction (3) V vs. Ag/AgCl	Oxidation (4) V vs. Ag/AgCl
CoCl$_3$	0.288 0.898 1.035 (onset) 1.480	1.484 0.657 0.450 0.173	-0.835	-0.285
RhCl$_3$	0.127 0.262 0.484 1.040(onset)	1.205 0.793 0.423 0.196	-0.061 -0.210	-0.279 -0.149
IrCl$_3$	0.282 0.514 0.877 1.178(Onset) 1.419	0.945 0.620 0.401 0.123	-0.079 -0.730	-0.722

D.2. Electrochemical properties of Rh, Ir, Co for oxygen evolution reaction

To examine the behavior of metals in 1.0 M KOH, the metals were deposited on the surface of GCE using an acid solution prepared with metal salt. The behavior of modified GCEs was observed using the DPV method. GCEs modified with metals were first oxidized from 0.0 V to 1.7 V in 1.0 M KOH, then reduced from 1.7 V to -1.5 V, and finally reoxidized to 0.0 V. For the DPV measurements following settings were used: step size= 2 mV, sample period= 0.2 s, pulse time= 0.05 s, and pulse size = 5mV.

Figure D. 7. Differential pulse voltammograms of CoCl$_3$ in 1.0 M KOH
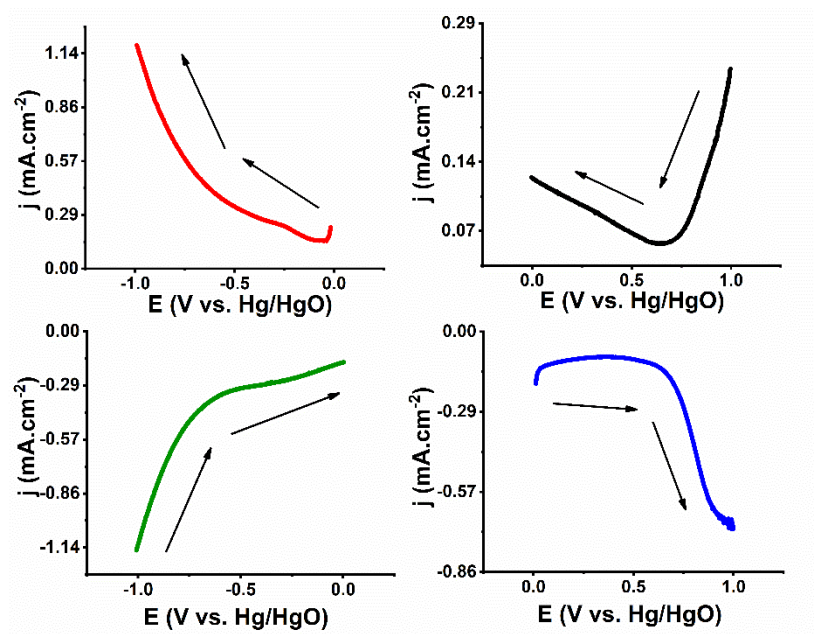
Figure D. 8. DPV plots of CoCl$_3$ examined as oxidation reduction-reoxidation in 1.0 M KOH
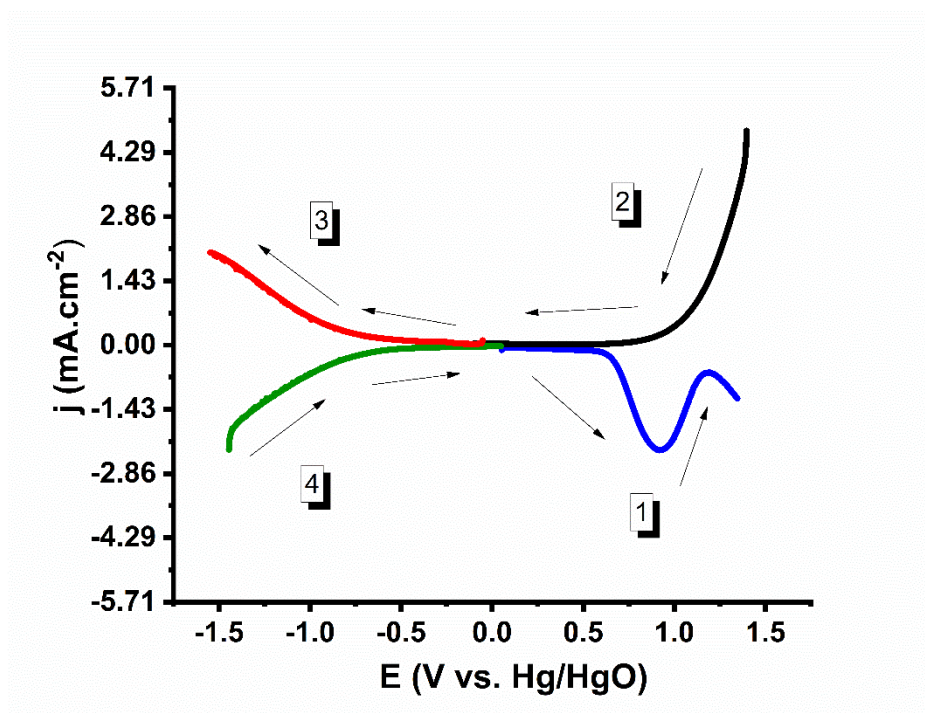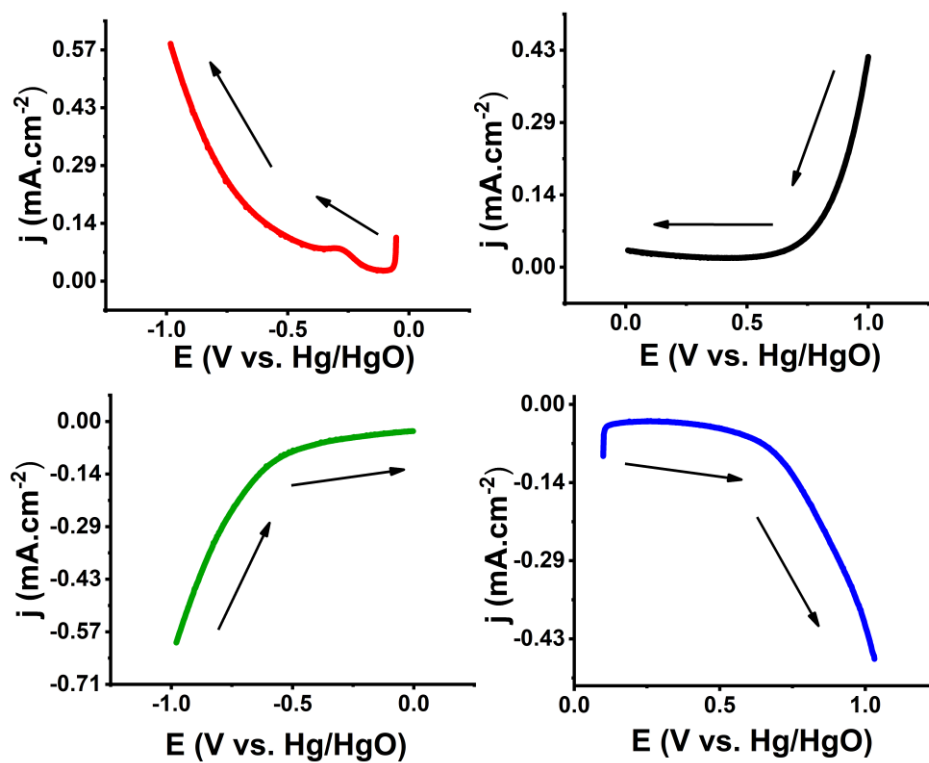
Figure D. 9. Differential pulse voltammograms of RhCl₃ in 1.0 M KOH

Figure D. 10. DPV plots of RhCl₃ examined as oxidation reduction-reoxidation in 1.0 M KOH
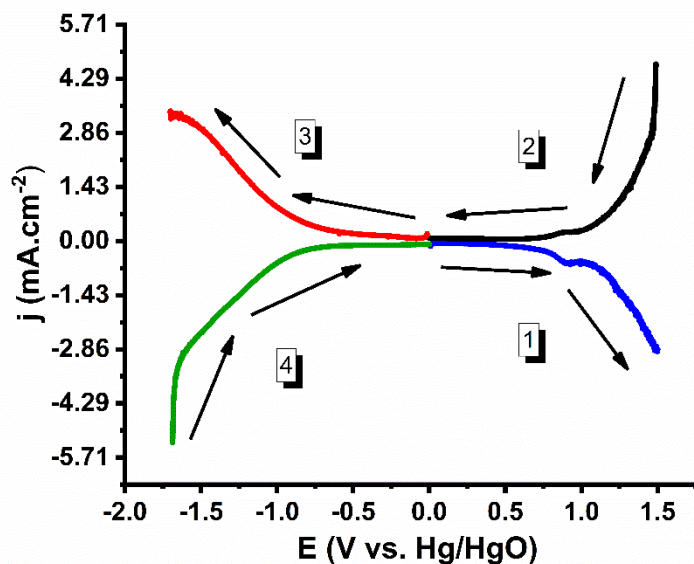
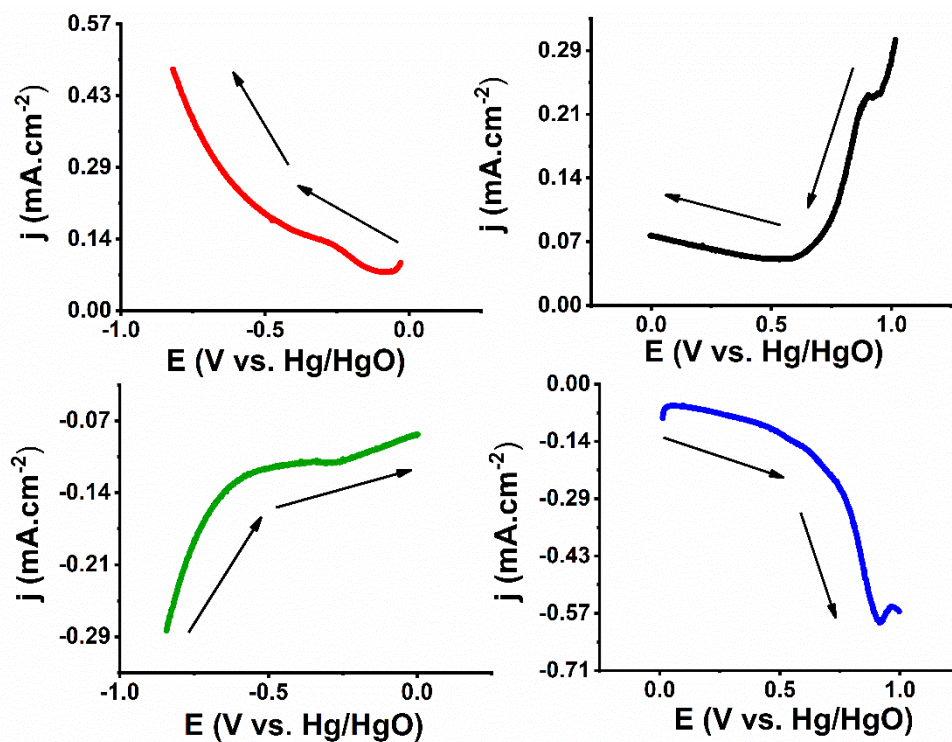**Figure D. 11.** Differential pulse voltammograms of IrCl$_3$ in 1.0 M KOH

Figure D. 12. DPV plots of IrCl$_3$ examined as oxidation reduction-reoxidation in 1.0 M KOH

Table D. 2. Oxidation reduction potential of $CoCl_3$, $RhCl_3$ and $IrCl_3$ in 1.0 M KOH

	Oxidation (1) V vs. Ag/AgCl	Reduction (2) V vs. Ag/AgCl	Reduction (3) V vs. Ag/AgCl	Oxidation (4) V vs. Ag/AgCl
$CoCl_3$	0.623	0.601	-0.265	-0.630
			-0.620 (onset)	-0.310
$RhCl_3$	0.676	0.679	-0.265	-0.560
$IrCl_3$	0.572	0.900	-0.265	-0.578
	0.907	0.608	-0.540	0.261

CURRICULUM VITAE

PERSONAL INFORMATION

Surname, Name: Akbayrak, Merve
Nationality: Turkish (TC)
Marital Status: Married
email: emerveakbayrak@gmail.com

EDUCATION

Degree	Institution	Year of Graduation
PhD	Middle East Technical University Department of Chemistry	2022
MSc	Middle East Technical University Department of Chemistry	2016
BSc	Middle East Technical University Department of Chemistry	2014

WORK EXPERIENCE

Year	Place	Enrollment
2015-Present	METU Chemistry	Teaching Assistant

PUBLICATIONS

(8) Akbayrak, M.; Önal, A. M. The Utilization of Iridium Nanoparticles Impregnated on Metal Oxides (Ceria, Titania, and Zirconia) with a Simple and Ecologically Safe Synthesis Approach in Oxygen Evolution Reactions. *J. Electrochem. Soc.* **2022**, *169* (7), 076511. https://doi.org/10.1149/1945-7111/ac81fa.

(7) Akbayrak, M.; Önal, A. M. Metal Oxides Supported Cobalt Nanoparticles: Active Electrocatalysts for Oxygen Evolution Reaction. *Electrochim. Acta* **2021**, *393*, 139053. https://doi.org/10.1016/j.electacta.2021.139053.

(6) Akbayrak, M.; Önal, A. M. High Durability and Electrocatalytic Activity Toward Hydrogen Evolution Reaction with Ultralow Rhodium Loading on Titania. *J. Electrochem. Soc.* **2020**, *167* (15), 156501. https://doi.org/10.1149/1945-7111/abb9cf.

(5) Akbayrak, M.; Önal, A. M. Binder- Free Iridium Based Electrocatalysts: Facile Preparation, High Activity and Outstanding Stability for Hydrogen Evolution Reaction in Acidic Medium. *J. Colloid Interface Sci.* **2020**, *580*, 11–20. https://doi.org/10.1016/j.jcis.2020.06.117.

(4) Akbayrak, M.; Önal, A. M. Efficient Ceria-Supported Rhodium Nanoparticles as an Electrocatalyst for Hydrogen Evolution. *J. Electrochem. Soc.* **2019**, *166* (16), H897–H903. https://doi.org/10.1149/2.0701916jes.

(3) Cansu-Ergun, E. G.; Akbayrak, M.; Akdag, A.; Önal, A. M. Effect of Thiophene Units on the Properties of Donor Acceptor Type Monomers and Polymers Bearing Thiophene-Benzothiadiazole- Scaffolds. *J. Electrochem. Soc.* **2016**, *163* (10), G153–G158. https://doi.org/10.1149/2.0711610jes.

(2) Akbayrak, M.; Cansu-Ergun, E. G.; Önal, A. M. Synthesis and Electro-Optical Properties of a New Copolymer Based on EDOT and Carbazole. *Designed Monomers and Polymers* **2016**, *19* (7), 679–687. https://doi.org/10.1080/15685551.2016.1209627.

(1) Akbayrak, M.; Önal, A. M. Synthesis and Electrochemical Polymerization of Diketopyrrolopyrrole Based Donor–Acceptor–Donor Monomers Containing 3,6- and 2,7-Linked Carbazoles. *Polym. Chem.* **2016**, *7* (39), 6110–6119. https://doi.org/10.1039/C6PY01489E.

CONFERENCES ATTENDED

- <u>Akbayrak Merve</u>, Önal Ahmet M. (2021). Iridium Nanoparticles on Ceria for Hydrogen Evolution Reaction in Acidic Medium, 3rd International Hydrogen Energy Conference and Exhibitions (Oral Presentation)

- <u>Akbayrak Merve</u>, Önal Ahmet M. (2021). Highly Durable Rhodium Nanoparticles Supported on Titania as an Electrocatalyst for Hydrogen Evolution Reaction via Electrochemical Water Splitting. 3rd International Hydrogen Energy Conference and Exhibitions (Poster Presentation)

- Önal Ahmet M., <u>Akbayrak Merve</u> (2018). Synthesis and Electrochemical Polymerization of Diketopyrrolopyrrole Based Donor–Acceptor–DonorMonomers Containing 3,6- and 2,7-linked Carbazoles. The 69th Annual Meeting of the International Society of Electrochemistry (Poster Presentation)

- <u>Akbayrak Merve</u>, Önal Ahmet M. (2016). Synthesis and Electropolymerization of New Hybrid Monomers Containing Carbazole Units. International Congress on Semiconductor Materials and Devices (ICSMD-2017) (Poster Presentation)

- <u>Akbayrak Merve</u>, Önal Ahmet M. (2017). Karbazol Birimleri İçeren Yeni Hibrit Monomerlerin Sentezi Ve Elektrokimyasal Polimerizasyonu. 29. National Chemistry Conference (Poster Presentation)

SUCCESSES AND AWARDS

- Middle East Technical University Thesis Award, 2017
- Güngör Gündüz Thesis Award, Middle East Technical University, 2017